Redox Mediators and Phase Transfer Catalysts for Metal-Oxygen Batteries

Alexander Thomas Robert Pateman

Oriel College

University of Oxford

A thesis submitted for the degree of

Doctor of Philosophy

Trinity 2021

Redox Mediators and Phase Transfer Catalysts for Metal-Oxygen Batteries

Minimising Decomposition on Charge and Understanding Redox Mediator Kinetics in Lithium-Oxygen Cells, and Improving Potassium-Oxygen Cell Discharge Capacity

Abstract

It is becoming increasingly clear that current lithium-ion battery technology does not possess a gravimetric energy density great enough to cater to the demands of our growing energy needs. By dispensing with the heavy cathode materials, metal-oxygen battery systems have far greater gravimetric energy densities, potentially enabling them to supersede lithium-ion technology and make the complete electrification of transport a viable endeavour.

Metal-oxygen batteries, however, are not without their limitations. Lithium-oxygen cells suffer from very large charging overpotentials, high levels of decomposition of cell components at all points of the cell cycle (particularly so on charge, due to the presence of singlet oxygen), and insoluble and insulating discharge products, which passivate the cathode leading to cell death. Potassium-oxygen cells, whilst displaying superior stability and smaller charging overpotentials, also form passivating discharge products. This thesis addresses a number of the issues and questions surrounding lithium- and potassium-oxygen cells.

Chapter 3 investigates the relationship between charging potential and the quantity of Li_2CO_3 arising from both ethereal electrolyte and carbon cathode decomposition. Use of *operando* electrochemical mass spectrometry and fluorescence spectroscopy reveals that formation of singlet oxygen only occurs above 3.31 V, with minimal quantities formed between 3.31 – 3.45 V. Low potential redox mediators are demonstrated to minimise cell decomposition by suppressing the charge potential below this level.

Chapter 4 details the synthesis and characterisation of novel redox mediators, identified through the use of DFT. The reaction kinetics of redox mediators with Li_2O_2 are investigated through the use of scanning electrochemical microscopy, revealing that said reaction kinetics are governed by Marcus theory.

Chapter 5 demonstrates the use of phenol as a protic phase transfer catalyst to increase the discharge capacity of potassium-oxygen cells, with *operando* electrochemical mass spectrometry revealing an electron to oxygen ratio of 1.02 on discharge, indicative of KO_2 formation.

A Note on the Impact of COVID-19

The national lockdown and resulting closure of University research buildings to non-COVID-19 related research in March 2020 until July 2020, followed by restricted access to the laboratories until my departure from Oxford at the end of August 2020, prevented the completion of a number of experiments for this thesis. This primarily affects **Chapter 5**, where the complete characterisation of the discharge products of potassium-oxygen cells with and without phenol, whilst using a solid electrolyte, was not possible.

The intended experiments include x-ray diffraction and Fourier transform infrared spectroscopy of the discharged cathodes and glass fibre separators used within potassium-oxygen cells, along with quantification of the discharge products through titration. This would need to be completed for cells discharged with and without phenol, whilst a solid electrolyte is in use to protect the potassium metal anode. Further discussion of these experiments may be found in **Section 5.3.8** (Future Experiments) on page 257 in **Chapter 5**.

Acknowledgements

I would like to begin by thanking Professor Peter G. Bruce for giving me this opportunity to study under his supervision in his world-leading research group and for the guidance and support that he has given me over the years. It has been an amazing experience and I am very grateful to have been welcomed into his outstanding academic family. My thanks also go to the EPSRC, who provided much of the funding that made completion of this thesis possible.

I owe much to Dr Lee Johnson, Dr Yuhui Chen and Dr Xiangwen Gao for their help in the early days of my DPhil, and to Dr Sunyhik Ahn and Dr Sixie Yang for their academic support in later years. I am grateful for the assistance of Dr Paul Adamson, Dr Erez Cohen, Dr Matthew Roberts, Mrs Zsofia Lazar and Mrs Miki Bennett with all the administrative tasks that have come along the way, and special thanks go to Dr Nadia Abdul-Karim for her tireless efforts in keeping the laboratory running smoothly.

To my friends in the laboratory, Dominic Spencer Jolly, Dr Gregory Rees, Gareth Hartley, Dominic Melvin, Ceren Zor, Johann Perera, Max Jenkins, Dominic Förstermann, Chloe Chau, Dr Stefanie Zekoll, Dr Samuel Wheeler, Dr Isaac Capone, Kevin Hurlbutt, Jack Fawdon, Dr Urmimala Maitra, Dr Andy Naylor, Dr James Somerville, Dr Adam Sobkowiak, Dr Jitti Kasemchainan, Dr Benjamin Bergner and Dr Christian Cuss; the time I have spent with you all has been incredibly special and I will forever cherish the camaraderie and good humour that you all brought to our

lunch and coffee breaks. Special thanks go to Dr Conrad Holc, who provided so much support in the early days and who helped me understand and develop the techniques I used over the years, and to Dr Robert House who, in addition to his great company, provided invaluable feedback and advice during the writing of this thesis. I am grateful also to those who did not play a direct role in my academic life, particularly the Orielensis, who helped to make Oxford my home.

Finally, I would like to thank my parents and family, whose love and support has enabled me to pursue this endeavour. Your encouragement and interest in my work has been essential, and I am forever grateful for your sound advice. It is to you, Mum and Dad, that I dedicate this thesis.

A. T. R. P.

11th April 2021, Oxford

Contents

List of Symbols

Symbols used throughout this work along with their definitions and typical units are listed below. Those symbols that appear only in **Chapter 2** for explanation of the techniques used, but which are not used in later Chapters, have been omitted. However, a full description of said symbols may be found when used in the relevant Sections.

Symbol	Definition	Typical Units
a	Electrode radius	cm
	Radius of molecule (idealised to a sphere)	cm
A	Absorbance	-
c	Concentration	mol dm^{-3} or M
D	Diffusion coefficient	cm^2 s^{-1}
e	Electron charge	C
E	Experimental potential	V
E^0	Formal potential of a redox couple	V
E_{cell}	Cell potential	V
E_a	Activation energy	kJ mol^{-1}
F	Faraday Constant	C mol^{-1}
G	Gibbs free energy	kJ mol^{-1}
i	Current	A
i_L	Limiting current	A
I	Intensity of Light	Lux
	Ionisation energy	eV
j	Current density	A cm^{-2}
j_o	Exchange current density	A cm^{-2}
k	Rate constant	cm s^{-1}
k_s	Standard rate constant for an electron transfer reaction	cm s^{-1}
k_{app}	Apparent heterogeneous rate constant for reaction between RM^+ and Li_2O_2	cm s^{-1}
L	Normalised distance of SECM electrode from substrate	-
m	Mass	g
n	Number of electrons transferred	-
N	Collection efficiency of rotating ring-disc electrode	-

Q	Charge or capacity	mAh or C
r_{glass}	Radius of insulator surrounding microdisc electrode	cm
R	Gas constant	J K^{-1} mol^{-1}
R_g	Ratio of insulator and electrode radius for a microelectrode	-
t	Time	s
T	Temperature	K or °C
v	Scan rate	mV s^{-1}
V_{vdW}	Van der Waals volume of a molecule	$Å^3$
x	Distance	cm
α	Transfer coefficient	-
β	Enhanced current factor for microelectrodes with small insulating sheaths	-
δ	Chemical shift	ppm
ε	Orbital energy	eV
ε_0	Permittivity of a vacuum	-
ε_{op}	Optical dielectric constant	-
η	Overpotential	V
σ	Product selectivity	-
$\varkappa$	Dimensionless rate constant for SECM feedback expressions	-
λ	Reorganisation energy	kJ mol^{-1}
Θ	Bragg angle	°

The subscripts 'a' and 'c' refer to anodic and cathodic reactions, respectively.

Abbreviations

Common abbreviations used throughout this work are listed below. Those abbreviations present in this work but not listed here are introduced when required.

ACN	Acetonitrile
CV	Cyclic Voltammogram
DMA	9,10-Dimethylanthracene
DME	Dimethoxyethane
DMHQ	1,4-Dimethyl-1,2,3,4-tetrahydroquinoxaline
DMPZ	5,10-Dihydro-5,10-dimethylphenazine
DMSO	Dimethyl Sulfoxide
FTIR	Fourier Transform Infrared Spectroscopy
GCMS	Gas Chromatography Mass Spectrometry
KTFSI	Potassium Bis(trifluoromethane)sulfonimide
LiTFSI	Lithium Bis(trifluoromethane)sulfonimide

MPO	10-Methyl-10*H*-phenoxazine
NMR	Nuclear Magnetic Resonance
OCV	Open Circuit Voltage (Potential)
OEMS	*Operando* Electrochemical Mass Spectrometry
RM	Redox Mediator
r.t	Room Temperature (298 K)
SECM	Scanning Electrochemical Microscopy
SERS	Surface Enhanced Raman Spectroscopy
TEGDME	Tetraethylene Glycol Dimethyl Ether
TEMPO	2,2,6,6-Tetramethyl-1-piperidinyloxy
TMPD	*N,N,N',N'*-Tetramethyl-*p*-phenylenediamine
UV-vis	Ultraviolet-Visible Absorption Spectroscopy
XRD	X-ray Diffraction

List of Figures

List of Tables

List of Schemes

Chapter 1

Introduction

Contents

1.1 The Case for Better Batteries

1.1.1 What is a Battery?

Since the early work of Volta, Daniell, Planté and others, we have developed a reliance upon portable electronics such that they are synonymous with modern living. Whilst to many the word "battery" suggests a single device, in more precise terms a battery is a combination of two or more voltaic cells, which produce electricity from an internal chemical reaction. Another important distinction to make is between a primary and a secondary cell, with the former being single use only whilst the latter is capable of being recharged once the store of energy has been depleted.[1]

1.1.2 Understanding the Lithium-Ion Battery

Lithium found its way into batteries, replacing toxic heavy metals such as lead and cadmium, due to its highly electropositive nature, with the Li^+/Li redox couple having a potential of -3.04 V against the standard hydrogen electrode (SHE). The greater the electrochemical potential difference between the positive and negative electrodes the greater the potential difference of the cell, which in turn leads to a greater cell energy. Lithium is also the third lightest element, which means that it has a high specific energy (energy per unit mass). The lithium-ion battery (LIB), developed by Goodenough in the 1980s, revolutionised the field of secondary batteries, with LIBs now being the main candidate for use in electric vehicles.[2-4]

In LIBs, the lithium ions are incorporated into intercalation electrodes; the negative electrode is typically graphite, with the structure Li_xC_6, whilst the positive electrode has the general structure $Li_{1-x}M^{M+}O_2$, where M is a transition metal (typically cobalt, nickel or iron). On discharge, the lithium cations are extracted from the negative electrode, pass through the electrolyte, then intercalate into the positive electrode, with the reverse process occurring during charge. This is represented by the equation:[2]

$$Li_xC_6 + Li_{1-x}M^{M+}O_2 \rightleftarrows 6C + LiM^{M+}O_2 \qquad \textbf{Eq. 1. 1}$$

Given there are only a finite number of lithium cations that may be incorporated into each electrode, there is a ceiling to how much charge LIBs may contain.

Despite their successful use in portable electronics, LIBs are not without their shortcomings. Whilst lithium metal may have a very high specific energy, its instability and reactivity towards the electrolyte has proven problematic in commercial cells, necessitating the need to use graphite intercalation electrodes. The specific energy of LIB intercalation electrodes is significantly reduced by the presence of carbon and transition metals, which add to the mass of the cell while not increasing the overall capacity. The transition metals of the positive electrode must also be mined at both high economic and environmental cost.[5] Lithium itself is an expensive material, having a market value of $100,000 per ton,[a] with the largest deposits found in politically unstable regions.[5, 6] In contrast, sodium and potassium metals are much cheaper

[a] Prices as of August 2020.

($3,000 and $13,000 per ton, respectively) and are more readily available.[5-7] Na-ion technology has received high levels of interest for static grid scale energy storage; since portability is not a requirement, the lower energy density of sodium is far outweighed by its relative cheapness and abundance.[8] A further issue is the formation of lithium dendrites, which pose a significant fire risk.[9]

1.1.3 The Need for Better Batteries

The improved performance of batteries has presented a vital opportunity to move away from fossil fuels in many applications, a change that is essential if we are to prevent further anthropogenic climate change.[10, 11] Transport is reliant on petroleum, made up of hydrocarbons and other organic compounds which, when burnt as fuel, release carbon dioxide and various other greenhouse gases into the atmosphere thus enhancing the greenhouse effect.[12] Electrification of transport is therefore an essential step in combatting anthropogenic climate change, as replacement of petroleum with batteries will allow the use of renewable energy sources (solar, wind, hydro) to power cars (batteries may be charged using these renewable energy sources).

Whilst LIBs have proven to be a very successful battery technology and are more than capable of supplying sufficient energy for most of our needs, ultimately even state-of-the-art LIBs with a specific energy of 387 Wh kg^{-1} do not provide enough energy to allow electric cars to cover more than a few hundred kilometres on a single charge.[10, 13] The Tesla Model S represents the higher end with a range of 500 km from

a single charge.[13] It is now generally accepted by automotive manufacturers that the performance of LIBs represents the greatest barrier to the complete electrification of transport and that a beyond Li-ion technology is required.[14]

There are a number of battery systems that can potentially supersede LIBs in electric vehicles, including alkali metal-air, lithium-sulfur and magnesium-ion. The non-aqueous lithium-air (Li-air) battery has a theoretical specific energy of 3,505 Wh kg^{-1} based on the mass of the discharge product lithium peroxide (Li_2O_2), making it a serious candidate to replace gasoline, with gasoline in automobiles having an approximate calculated specific energy of 1,700 Wh kg^{-1}.[b] The potassium-air (K-air) cell has a slightly lower specific energy of 935 Wh kg^{-1}, however it has its own advantages over the Li-air cell which will be discussed in **Section 1.6** on page 55.[5, 15] Whilst a practical cell will certainly have a lower specify energy than the theoretical value due to the mass of the electrodes, electrolyte and other components not involved in charge storage, there is a great potential for metal-air batteries to outperform all other battery technologies and contribute to a more sustainable future, justifying continued research into the systems.[10, 16]. **Figure 1.1** provides a comparison of the practical specific energies of different rechargeable batteries (that is to say, the specific energy once the mass of the current collectors, cell packaging and air purification systems etc. have been taken into account), whilst **Figure 1.2** provides a comparison of the specific energies of different metal-air cells.[10]

[b] While gasoline itself has a specific energy of 13,000 Wh kg^{-1}, the tank-to-wheel efficiency of 12.6% reduces this value significantly. Electric motors, by comparison, have an efficiency of closer to 90%.

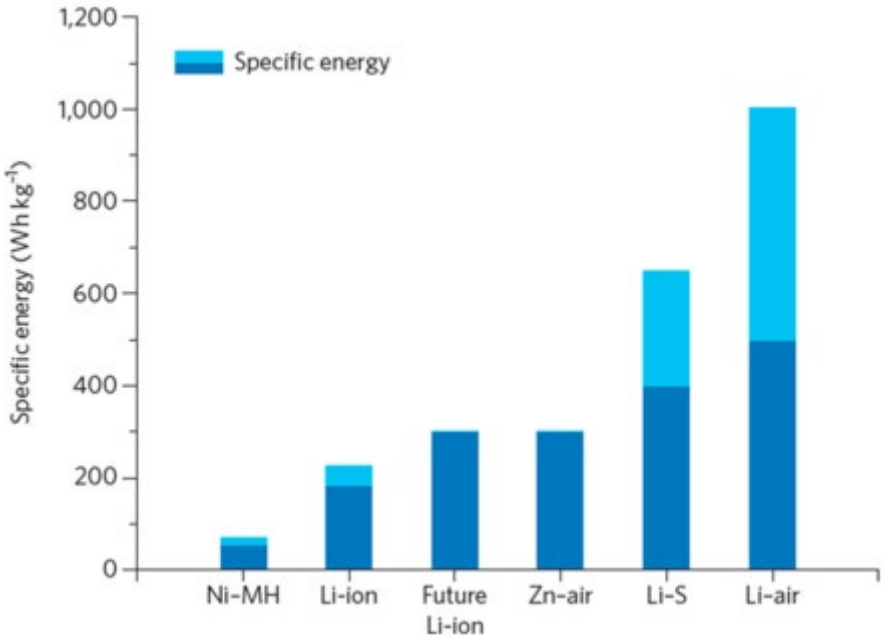

Fig. 1.1: Practical specific energies of a selection of secondary cell systems, where the light blue boxes indicate the range of recorded specific energies. Reproduced with permission. Copyright 2020, American Chemical Society.[10]

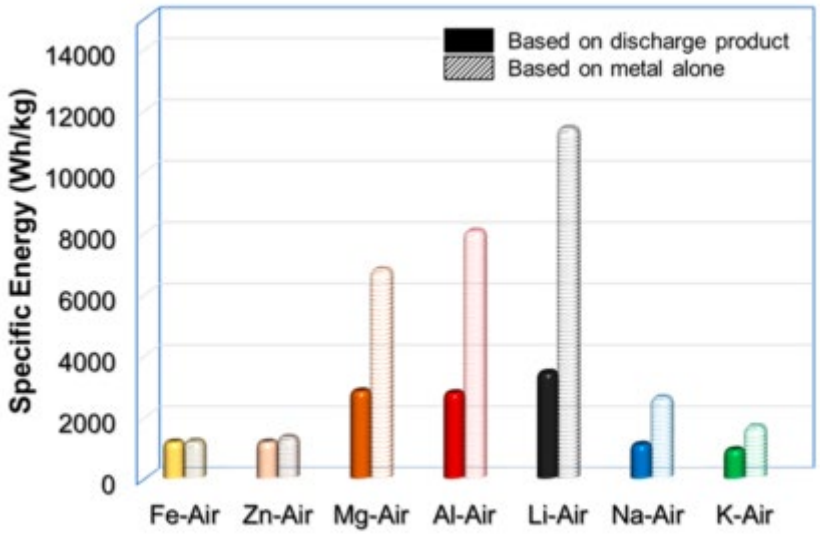

Fig. 1.2: Specific energies of different metal-air systems, based on (solid colour) the mass of the metal alone and (striped) the mass of the discharge product. Reproduced with permission. Copyright 2020, American Chemical Society.[10]

1.2 Operation of the Alkali Metal-Air Battery

1.2.1 Overall Discharge and Charge Reactions

This work focusses on both Li-air and K-air batteries in their non-aqueous forms which, whilst being similar in many respects, exhibit different discharge products (a typical cell design is discussed in greater detail in **Section 2.1.6.2** on page 88). During discharge in Li-air cells, O_2 gas enters the porous cathode[c] and undergoes a two-electron reduction to O_2^{2-} which combines with two lithium cations in the electrolyte to form lithium peroxide, Li_2O_2.[10] On charge, the process is reversed with O_2 being liberated, giving an overall reaction at the cathode of:

$$2Li^+ + O_2 + e^- \rightleftharpoons Li_2O_2 \qquad E^0 = 2.96\ V\ vs\ Li^+/\ Li \qquad \textbf{Eq. 1.2}$$

In K-air cells the O_2 undergoes only a single electron reduction to form a deposit of potassium superoxide, KO_2:[15]

$$K^+ + O_2 + e^- \rightleftharpoons KO_2 \qquad E^0 = 2.48\ V\ vs\ K^+/\ K \qquad \textbf{Eq. 1.3}$$

Unlike lithium superoxide, LiO_2, KO_2 is thermodynamically stable and so there is no driving force for the second oxygen reduction step without the application of a more negative potential.[15, 17] It is a combination of both the greater mass of K^+ compared to Li^+ and the single electron transfer to form KO_2 that results in the lower specific energy of K-air cells.[10]

[c] In the remainder of this work, the electrode termed the "cathode" is assigned from the perspective of cell discharge. Whilst it is recognised that when changing from discharge to charge the role of each electrode switches, such that on charge the original "cathode" becomes the positive electrode, all future uses of the term "cathode" will refer to the electrode at which O_2 is reduced on discharge and Li_2O_2/KO_2 oxidised on charge, regardless of whether cell discharge or charge is taking place.

It is worth noting that Li-air cells have been demonstrated using an aqueous electrolyte to form lithium hydroxide as the discharge product:[18]

$$2Li^+ + \tfrac{1}{2}O_2 + H_2O + 2e^- \rightleftharpoons 2LiOH \qquad E^0 = 3.44\ V\ vs\ Li^+/\ Li \qquad \textbf{Eq. 1.4}$$

In stark contrast to the non-aqueous Li-air cell, in aqueous conditions cleavage of the dioxygen double bond occurs, which typically requires the assistance of a heterogeneous catalyst such as platinum or manganese/cobalt oxides.[19-24] Furthermore, the lithium metal counter electrode must be protected from the electrolyte (with which it reacts violently) by a Li^+-conducting solid.[25, 26]

The ultimate aim for metal-air batteries is to use O_2 extracted from the ambient atmosphere, removing the need for a storage tank to be incorporated into the design of the vehicle.[27] However, many of the components of ambient air, particularly H_2O and CO_2, are found to have a deleterious effect on the non-aqueous chemistry, and so in laboratory settings pure O_2 is employed.[28-31] It is therefore more accurate to refer to these systems as metal-oxygen (M-O_2) cells, which is the nomenclature that shall be used hereon in. An illustration of the operation of Li-ion, aqueous and non-aqueous Li-O_2, and Li-S cells may be found in **Figure 1.3**.

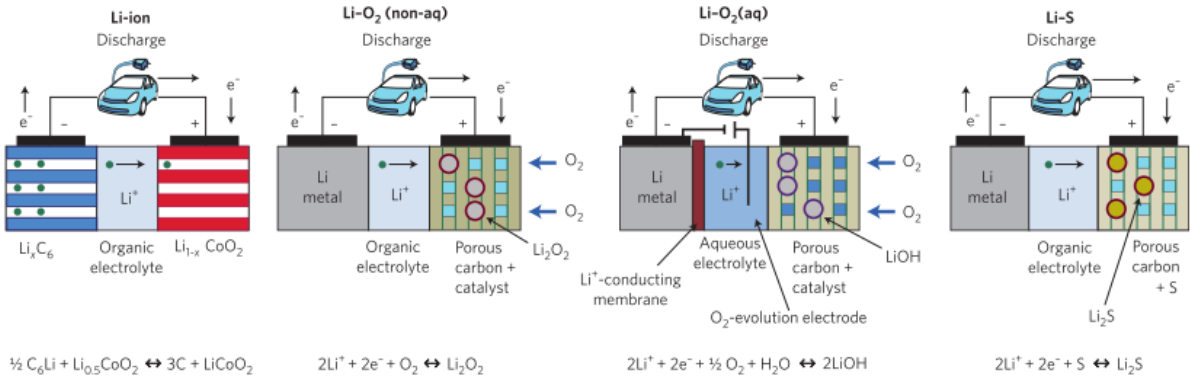

Fig. 1.3: Illustrative diagrams of Li-ion, non-aqueous and aqueous Li-O_2, and Li-S cells. Reproduced with permission. Copyright 2012, Springer Nature.[16]

While the mechanism for the oxygen reduction reaction (ORR) in aqueous electrolytes has been extensively studied and is now well understood, the same cannot be said for ORR (or indeed the oxygen evolution reaction, OER) in non-aqueous electrolytes. In non-aqueous electrolytes the oxygen undergoes a two-electron reduction to form O_2^{2-}, with each electron gained in a separate step. In the presence of lithium cations, the first reduction results in lithium superoxide, LiO_2, (**Equations 1.5** and **1.6**) which is then further reduced and combines with another Li^+ to form Li_2O_2 (**Equation 1.7**). LiO_2 may also disproportionate, forming Li_2O_2 and O_2 (**Equation 1.8**).

$$O_2 + e^- \rightarrow O_2^- \qquad \textbf{Eq. 1.5}$$

$$O_2^- + Li^+ \rightarrow LiO_2 \qquad \textbf{Eq. 1.6}$$

$$LiO_2 + Li^+ + e^- \rightarrow Li_2O_2 \qquad \textbf{Eq. 1.7}$$

$$2LiO_2 \rightarrow Li_2O_2 + O_2 \qquad \textbf{Eq. 1.8}$$

The Li_2O_2 forms an electrically insulating deposit on the cathode surface, which eventually passivates the cathode causing cell death.[32, 33] Consequently, many studies considering how passivation may be prevented have been conducted, with the choice of solvent and additives being of great importance.

It has been observed that there are two different mechanisms for O_2 reduction to form Li_2O_2; a surface formation and a solution formation mechanism. McCloskey *et al.* suggested that, given the discharge products LiO_2 and Li_2O_2 are insoluble in the solvent used (dimethoxyethane (DME)), their formation occurs on the surface of the carbon cathode where they remain affixed.[32]

Building on the work by Sawyer *et al.*, studies by Laoire *et al.* found that in tetrabutylammonium (TBA^+) salt solutions O_2 reduction to superoxide is reversible, whereas the second reduction to peroxide is irreversible at low potentials.[34-36] This was attributed to the weak interaction between TBA^+ and the solvents used (DME, tetraethylene glycol dimethyl ether (TEGDME), acetonitrile (ACN) and dimethyl sulfoxide (DMSO)), due to TBA^+ having a large radius (0.494 nm in DMSO) and low charge density. By invoking Pearson's Hard Soft Acid Base theory (HSAB)[d], Laoire *et al.* postulated that the characteristics resulting in weak solvation make TBA^+ a soft acid (and effectively a naked cation); this allows TBA^+ to stabilise O_2^- (a soft base) by forming an ion pair in the solvent.[36, 37] The creation of this ion pair slows down the

[d] Hard Soft Acid Base theory states that hard acids form strong bonds with hard bases, while soft acids form strong bonds with soft bases. A "hard" species has a small radius, has a high charge state and is weakly polarisable whereas a "soft" species is large, has a low charge state and is strongly polarisable. R. Pearson, *J. Am. Chem. Soc.* 1963, **85**, 22, 3533–3539.

second reduction to peroxide, resulting in the observed reversibility of the O_2/O_2^- couple.

In contrast to TBA^+, Li^+ is a hard acid according to HSAB theory due to its small radius and high charge density (Na^+ is also a hard acid, whereas K^+ is soft).[37] Consequently, Li^+ has a strong affinity for peroxide (a hard base due to its -2 charge). Li^+ also interacts more strongly than TBA^+ with solvents, with each Li^+ solvated by an average of four solvent molecules, resulting in the formation of solvent separated ion pairs. The greater the Gutmann donor number (DN) of the solvent, where a higher DN indicates greater Lewis basicity, the greater the strength of the Li^+-solvent interactions, according to the order DMSO > ACN > DME > TEGDME, with a stronger Li^+-solvent interaction leading to the Li^+ becoming a softer acid.[e] Superoxide is a relatively soft base, and so due to its low affinity for Li^+ in low DN solvents it is relatively unstable meaning it will undergo either a fast second reduction or disproportionation to peroxide. However, strong Li^+ solvation by high DN solvents means the O_2^- is stabilised and so exists for longer.[36]

The work by Johnson *et al.* presents the discharge mechanisms suggested by McCloskey and Laoire as being limiting cases of the same mechanism, where the initial intermediate is controlled by solvation of LiO_2.[38] At low discharge overpotentials, O_2

[e] The Gutmann Donor Number provides a quantitative measure of the Lewis basicity of a species. It is defined as the enthalpy of formation (in kcal) of the 1:1 adduct between the species and $SbCL_5$ in a highly diluted solution of dichloromethane. V. Gutmann, Coordination Chemistry Reviews, 1976, **18**, 225-255.

is reduced to form LiO_2, which can be dissolved in the electrolyte or adsorbed on the cathode surface according to the theoretical equilibrium:

$$LiO_2^* \rightleftharpoons Li^+_{(sol)} + O^-_{2(sol)} + \text{ion pairs} + \text{higher aggregates} \qquad \textbf{Eq. 1.9}$$

where * indicates surface-adsorbed LiO_2. In high donor number solvents the Li^+ is strongly solvated resulting in the formation of soluble O_2^-.[39] Conversely, in low donor number solvents the Li^+ is more weakly solvated leading to a Li^+-coupled electron transfer reaction and an adsorbed LiO_2. This means that in low donor number solvents the LiO_2 can disproportionate or undergo a second reduction on the electrode surface to form Li_2O_2 as a surface layer on the cathode, whereas in high donor number solvents disproportionation of LiO_2 dominates, resulting in precipitation of Li_2O_2 in solution. Disproportionation was confirmed as a mechanistic step through the addition of KO_2 to a solution containing a Li^+ salt, such as $LiClO_4$, leading to the precipitation of Li_2O_2.[38, 40, 41] Chemical formation of Li_2O_2 from KO_2 is only possible through disproportionation. The rate of disproportionation is discussed in the work of Laoire *et al.*, with solvents such as DME, which have an intermediate donor number, exhibiting both surface and solution pathways at low overpotentials.[36] In all solvents at high overpotentials the second reduction of LiO_2 or O_2^- to Li_2O_2 via the surface mechanism dominates.[38] **Figure 1.4** illustrates this unified mechanism for Li_2O_2 formation.

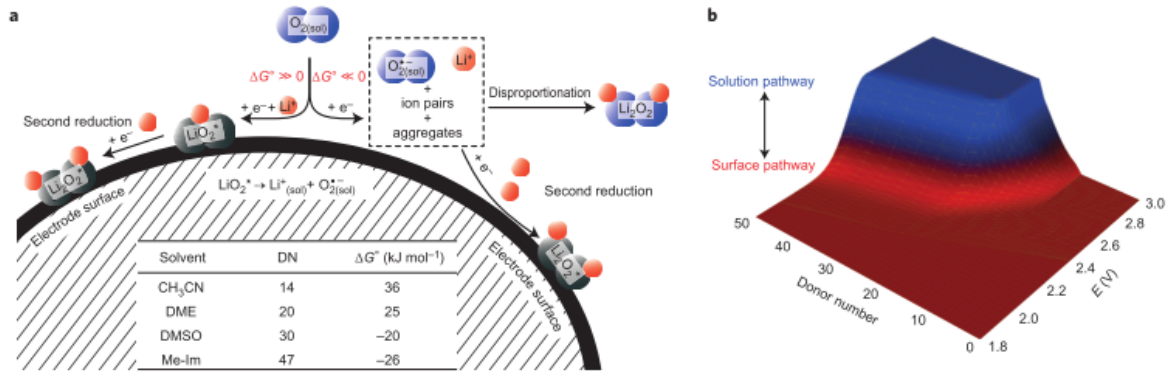

Fig. 1.4: a. Illustration of the O_2 reduction mechanism and **b.** the effect of solvent donor number and potential on the discharge pathway followed. Reproduced with permission. Copyright 2014, Springer Nature.[38]

The Gibbs free energy of the theoretical reaction in **Equation 1.9** determines whether LiO_2 is solvated or adsorbed on the surface of the cathode; if the free energy is positive then a surface mechanism will proceed. This is reflected in the cyclic voltammetry of 1-methylimidazole (Me-Im) and DMSO (high DN solvents), which display two reduction peaks, whilst ACN and DME (low DN solvents) have only one, in agreement with Laoire *et al.*[36, 38]

An understanding of the unified mechanism for ORR in the non-aqueous Li-O_2 battery provides a means of selecting solvents that will delay cell death by directing Li_2O_2 growth in solution, rather than as a passivating layer of the cathode surface. The benefits of a high DN solvent are evident in **Figure 1.5**, where the discharge capacity afforded by Me-Im vastly outperforms ACN and DME, with DNs of 47, 14 and 20, respectively.

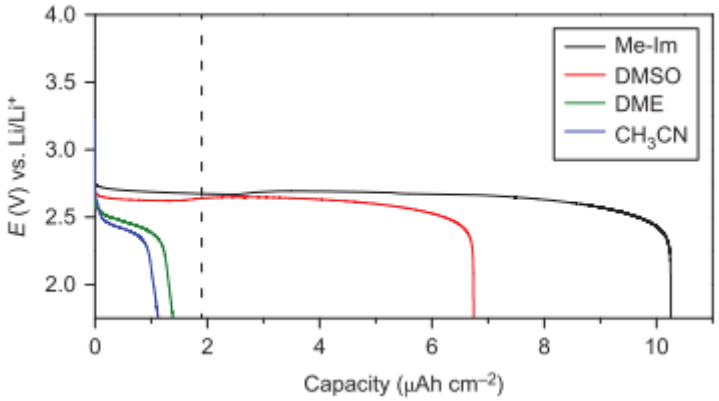

Fig. 1.5: Discharge profiles for cells with electrolyte solvents of Me-Im (black), DMSO (red), DME (green) and ACN (blue). Reproduced with permission. Copyright 2024, Springer Nature.[38]

It was also found that the cathode surface can influence the mechanism of Li_2O_2 formation, with defects in the carbon cathode found to stabilise surface-adsorbed LiO_2, preventing surface-mediated disproportionation and further reduction to Li_2O_2.[42] This has the effect of favouring the solution pathway for Li_2O_2 formation. In addition, O_2 chemisorption is not required for the first electron transfer to occur, with the implication being that this step is not dependent upon the cathode structure.

A range of morphologies of Li_2O_2 is possible during ORR, depending on whether surface (film formation) or solution (toroid formation) dominates, with each morphology having a possible effect on the charge process.[43, 44] The quantity of Li_2O_2 present in the cell at the end of discharge is also dependent upon the type of cathode used.[45]

1.2.3 Oxygen Evolution Reaction

When charging a Li-O_2 cell it is necessary to convert all the Li_2O_2 into O_2. On first observation, there are two theoretical reaction pathways for OER. Firstly, Li_2O_2 may be oxidised to LiO_2, which may then be further oxidised to O_2. Alternatively, Li_2O_2 may be directly oxidised to O_2. Laoire *et al.* suggested that OER occurs via direct oxidation of Li_2O_2 to form Li^+ and O_2, as evidenced by cyclic voltammetry studies. These show only a single anodic peak, in contrast to two peaks for the reduction pathway. If the LiO_2 intermediate were present on charge, two oxidation peaks would be expected. Peng *et al.* investigated whether LiO_2 existed as a charge intermediate using *in situ* surface enhanced Raman spectroscopy (SERS) measurements. After generating Li_2O_2 at 2.00 V the potential was switched to 3.75 V, however there was no evidence of LiO_2 formation.

Lu *et al.* proposed that OER occurs in two distinct stages.[46] The first stage occurs at low overpotentials, where the voltage profile is sloping and is relatively insensitive to charge rates and catalysts, attributed to the delithiation of the outer part of the Li_2O_2 to form lithium deficient $Li_{2-x}O_2$, which can then disproportionate to form O_2. The second stage occurs at high overpotentials and is sensitive to charging rate and catalysts, attributed to bulk oxidation of Li_2O_2 particles. Using *operando* x-ray diffraction (XRD), Ganapathy *et al.* again observed two stages of Li_2O_2 oxidation.[47] At low potentials amorphous Li_2O_2 is oxidised, whereas at high potentials crystalline Li_2O_2 is oxidised, with smaller crystals of Li_2O_2 found to decompose first. Both studies observe O_2 evolution from $Li_{2-x}O_2$ from the start of charge.[46, 47]

Wang *et al.* provide evidence for a unified charge mechanism analogous to that proposed by Johnson *et al.* for discharge.[48] The DN of the solvent was found to determine whether charge proceeded via the lithium deficient $Li_{2-x}O_2$ species (the surface route) or LiO_2 (solution route), with LiO_2 detected in DMSO but not in TEGDME using a rotating ring disc electrode (RRDE). X-ray absorption near edge structure spectroscopy has also allowed for detection of LiO_2 on charge in high DN solvents.[49] Further discussion of the charging mechanism for Li-O_2 cells may be found in **Chapter 3**.

1.3 Performance and Decomposition of Li-O_2 Battery Components

Numerous organic solvents and cathode materials have been tested for use in Li-O_2 cells, with varying degrees of success. The counter electrode, salts and polymer binders present are also susceptible to decomposition. This Section provides an overview of previously investigated materials, along with their reactions during cell cycling.

1.3.1 Electrolyte Degradation

The choice of electrolyte within a Li-O_2 cell is of great importance. The electrolyte must be stable against both the counter electrode and the cathode, and must not decompose at the operating potential of the cell. Furthermore, the electrolyte must be stable against any of the chemical species formed within the cell during discharge and charge. The electrolyte is composed of both a solvent and a lithium-containing salt

such as lithium bis(trifluoromethane)sulfonimide (LiTFSI) or lithium perchlorate ($LiClO_4$). There is some argument to be made that a degree of electrolyte decomposition may be beneficial to cell performance, particularly when resulting in the formation of a solid electrolyte interphase (SEI) on the lithium counter electrode surface.[50, 51] This SEI acts as a protective barrier mitigating further decomposition, a topic that will be revisited briefly **Section 1.4.1.6** (page 45).

Early work on Li-O_2 drew inspiration from LIBs, where organic carbonate solvents such as propylene carbonate were used to great success, with reports of carbonate-based Li-O_2 cells achieving specific energies of more than 1,000 Wh kg^{-1}, based on total electrode mass, sustained over more than 100 cycles.[11, 52, 53] However, it was subsequently shown that carbonate species were the predominant discharge product, with little to no Li_2O_2 produced.[54, 55] Both LiO_2 and Li_2O_2 have been shown to be reactive towards carbonate solvents, with superoxide initiating a series of radical reactions.[54, 56]

The unsuitability of carbonate solvents led to interest in ether solvents, in particular DME and TEGDME. Unlike many solvents, ethers are compatible with a lithium counter electrode, are stable to electrochemical oxidation up to 4.75 V (although this has been disputed), have low cost, are safe and, for ethers of sufficiently high molecular weight (such as TEGDME), have low volatility.[2, 57-59] The low volatility of TEGDME means that cells can be open to an O_2 atmosphere without loss of solvent.[60] Furthermore, Li_2O_2 has been demonstrated to be the predominant discharge product, although some Li_2CO_3 also forms.[57, 61] While there have been reports of ethers

not forming Li_2CO_3 as determined by time-of-flight secondary ion mass spectrometry, this is likely to be a false negative since the measurements were taken once the cell had polarised above the 3.82 V required to electrooxidise Li_2CO_3.[62, 63]

Ethers undergo decomposition when subjected to the conditions of a working Li-O_2 cell, with Freunberger *et al.* observing a mixture of lithium carbonate, formate and acetate, along with polyether chains, forming over five cycles. Formation of these side products was attributed to an initial hydrogen abstraction by superoxide, following a reaction scheme reproduced in **Figure 1.6**.[57] However, computational work by Bryantsev *et al.* found that the activation energy of such reactions is prohibitively high, and that ether decomposition proceeds via initial reaction with O_2 followed by attack by O_2^-.[64] Initial attack by O_2 is supported by comparison of TEGDME samples after exposure to O_2 for four hours or six days, with the latter displaying significantly impaired electrochemistry.[65] It has been suggested that ether decomposition results in the formation of alkene and alcohol moieties, which may then undergo further reaction within the cell.[66, 67] Additional decomposition species observed include alkoxides, aldehydes and shorter chain ethers.[58, 68, 69] Regardless of the nature of the attacking species, it is generally accepted that ether decomposition begins with abstraction of a hydrogen atom from either the α- or β-carbons, with attack at each position giving rise to different products.[70] Following abstraction of a hydrogen atom to form a carbon radical, a further hydrogen abstraction from a neighbouring methylene to form an alkene is highly exergonic.[71]

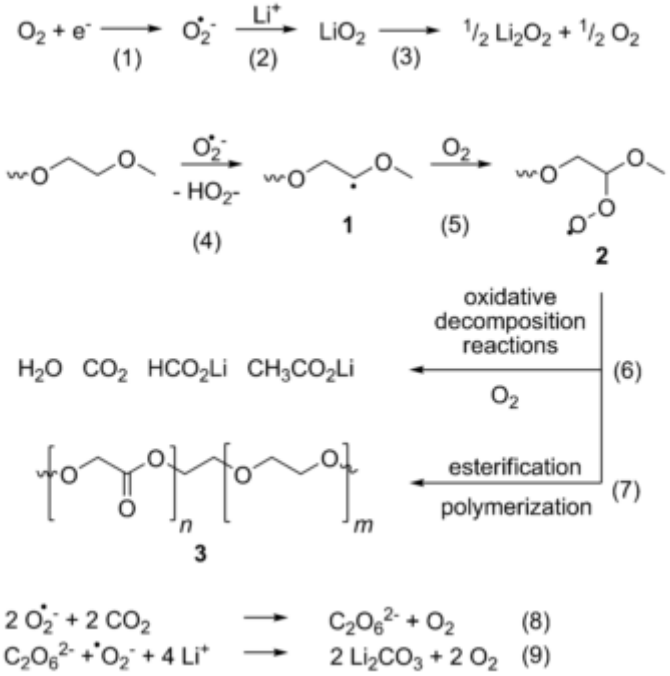

Fig. 1.6: Suggested mechanism for decomposition reactions of ethers during Li-O_2 cell discharge. Reproduced with permission. Copyright 2011, John Wiley and Sons.[57]

Given that ether decomposition begins with hydrogen abstraction, computational work replaced these atoms with fluorine to improve stability. No stable O-F compounds (resulting from fluorine abstraction by oxygen-containing species) were found, and so it was concluded that a fully fluorinated ether would be stable to autoxidation.[71] Whilst fluorinated ethers exhibit high O_2 solubility, due to their low polarity Li^+ solvation is potentially problematic and so use with a Li^+-solvating cosolvent may be necessary. A 1:1 mixture of 1,1,2,2-tetrafluoroethyl-2,2,3,3-tetrafluoropropyl ether and 3.4 M LiTFSI in TEGDME was successfully used and found to have high electrochemical stability.[72, 73]

Fluoroethers have the additional benefit of being resistant to fire, thereby increasing the safety of devices.[72]

Replacement of hydrogens with methyl groups by Adams *et al.* was exceptionally successful in minimising the level of solvent decomposition, with the total amount of $^{12}CO_2$ evolved on charge decreasing by approximately 90% when 2,3-dimethyl-2,3-dimethoxybutane was employed as a solvent compared to DME.[74] The use of a fully-methylated cyclic ether also provided excellent results, with negligible levels of CO_2 detected when exposed to superoxide or singlet oxygen (a full discussion of singlet oxygen in Li-O_2 cells may be found in **Section 1.5** on page 49).[75] Both of these works give a clear indication that hydrogen abstraction is a key step in ether decomposition.

DMSO was of interest as a solvent due to its low volatility, good O_2 diffusivity and high conductivity (2.11 mS cm^{-1}), along with facilitating high capacities of 9,400 mAh cm^{-2} when used in conjunction with a Ketjen black carbon cathode.[36, 76] In addition to being able to stabilise superoxide during discharge, theoretical and experimental work by Schroeder *et al.* suggested that DMSO is stable in contact with Li_2O_2 even after seven months of storage, with Mozhzhukhina *et al.* similarly observing no appreciable decomposition over two months.[38, 77, 78] However, a number of studies contradict this work, with Younesi *et al.* demonstrating that DMSO in contact with Li_2O_2 decomposes to carbonate species after only two days.[79]

Sharon *et al.* suggested that, when using gold electrodes during electrochemical quartz microcrystal microbalance experiments, DMSO was stable during ORR and OER, with other works further suggesting DMSO stability during ORR.[78, 80] Similarly, cells containing a DMSO-based electrolyte have been shown to display capacity retention of more than 95% after 100 cycles using a nanoporous gold (NPG) electrode.[81] However, given the high mass and price of gold it is an unsuitable electrode material for commercial cells. Substituting the gold for activated carbon cathodes, however, resulted in side products forming from the reaction between DMSO and the nucleophilic and basic O_2^{2-} and O_2^- species formed during ORR, with attack centred on the polar sulfinyl functional group and weakly acidic α-hydrogen on the methyl group. The dimsyl anion that forms may also undergo autoxidation in the presence of Li^+ to form Li_2SO_4. The occurrence of increased DMSO decomposition when using a carbon cathode was attributed to the greater surface area of the carbon compared to the gold, leading to more solution reaction of DMSO with solvated species. In contrast, the lower surface area of gold leads to rapid precipitation of soluble species (with species in the solid state less reactive than those in solution).[80] DMSO has been shown to electrochemically decompose on charging above 4.2 V (with the use of a platinum electrode resulting in decomposition from 3.5 V, suggesting that platinum catalyses the occurring decomposition reaction).[78, 82]

Following their studies involving DMSO, Xu *et al.* investigated tetramethylene sulfone (TMS) as a potential solvent.[83] TMS has a much lower volatility and greater resistance to chemical oxidation than DMSO, along with low toxicity and greater safety

compared to other available solvents. High capacity and good rate performance were observed using TMS, along with Li_2O_2 as the main discharge product. Whilst Barde *et al.* also found Li_2O_2 formation and decomposition to be the major reactions in TMS, this was only so for the first five cycles, after which the capacity began to decrease. This was attributed to an increase in Li_2CO_3 believed to originate from decomposition of the sulfone, as verified by the use of a NPG electrode.[84]

Computational studies by Laino *et al.* show that ACN has a strong interaction with Li_2O_2 and has the potential to undergo nucleophilic attack by O_2^{2-} due to the small intermolecular distance between the nitrile carbon and the peroxide (2.458 Å).[71] The more sterically bulky pivalonitrile (2,2-dimethylpropanenitrile) was found to have a similar interaction with the peroxide surface as ACN. However, x-ray photoelectron spectroscopy (XPS) analysis of a Li_2O_2 surface showed no degradation of the ACN solvent after two days.[79] It has also been determined computationally that ACN is stable towards superoxide, however treatment with KO_2 of 96.5% purity resulted in a slow decomposition reaction (attributed to the presence of hydroxide impurities).[85] It is vital to note, however, that ACN is incompatible with lithium metal as it reacts to form LiCN, which may then react with weak acids to liberate toxic hydrogen cyanide gas. As a consequence, ACN may only ever be used in the cathode compartment of a dual electrolyte cell.[71]

Chen *et al.* investigated dimethylformamide (DMF) as a solvent for Li-O_2 cells as it had previously been used as a solvent for O_2 reduction, finding it to be stable to O_2^- when TBA^+ was employed as the cation. However, despite Li_2O_2 formation and

decomposition being the major reactions on the first cycle, by the fifth cycle significant quantities of Li_2CO_3, lithium formate and lithium acetate had formed at the cathode.[86] In addition, DMF is unstable towards lithium metal and so, similarly to ACN, the counter electrode will need to be protected by a Li^+-conducting solid. To solve the issue of amide instability towards the counter electrode, Bryantsev *et al.* suggested substituting acidic hydrogens, increasing steric bulk and incorporating aromaticity as methods of reducing the reactivity of DMF.[64] Fluorinated amides such as *N*,*N*-dimethyltrifluoroacetamide (DMTFA) were found to form a stable SEI between the lithium metal and the electrolyte. Use of XPS revealed insoluble LiF to have formed on the lithium surface through the reductive defluorination of α-fluorinated amides by the lithium metal, providing a passivating protective layer of sufficiently low resistance to allow good Li^+ conductivity. However, DMTFA was found to be unstable towards the reactive O_2 species formed at the cathode, and so was deemed unsuitable for use over extended cycling.[87]

A range of other solvent systems have been investigated for use in Li-O_2 cells, to varying degrees of success. Use of *N*,*N*-dimethylproplyeneurea (DMPU) approximately doubles the achievable discharge capacity compared to the analogous TEGDME system, providing a charging potential plateau at 3.4 V on the first cycle. However, DMPU was found to decompose on charge, attributed to solvent reaction with superoxide.[88] Sharon *et al.* synthesised the solvent 2,4-dimethoxy-2,4-dimethylpentan-3-one which was found to be resistant to nucleophilic attack by reduced oxygen species. Whilst some degree of electrolyte

decomposition was detected after cell failure on the 49th cycle, the cell failure itself was attributed to degradation of the lithium counter electrode, rather than passivation of the cathode or solvent decomposition.[89] Ionic liquids and mixtures of ionic liquids and organic solvents have also been demonstrated as solvents for Li-O_2 cells.[90-98]

Bringing together this Section with **Section 1.2** (page 7), Khetan *et al.* summarised a number of common solvents in terms of their stability towards nucleophilic attack by superoxide and their ability to solvate LiO_2. It was found that there is an inverse correlation between the two descriptors, with solvents that are good at solvating LiO_2 also being the ones most susceptible to nucleophilic attack (**Figure 1.7).**[99] This highlights one of the key issues facing Li-O_2 cells; currently there are few organic solvents that are both stable during cell cycling and facilitate solution-based LiO_2 growth. With ethereal solvents demonstrating the greatest stability to nucleophilic attack, alternative methods of obtaining solution-based discharge to maximise capacity are necessary.

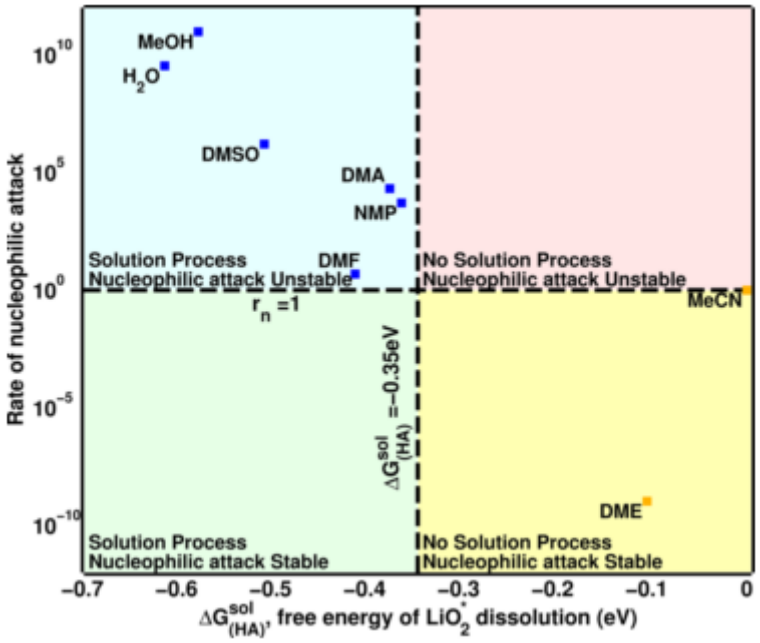

Fig. 1.7: Comparison of the stability of solvents to nucleophilic attack (hydrogen abstraction) and their ability to solvate LiO_2. Reproduced with permission. Copyright 2015, American Chemical Society.[100]

1.3.2 Cathodes

The requirements of a cathode material for M-O_2 cells are stability in the presence of the reactive oxygen species generated during cycling and stability at the high potentials experienced on charge. The ideal choice for the cathode should also have high conductivity, low mass and low cost. Whilst carbon is used almost exclusively as the cathode material in this work, attention shall also be given briefly to a selection of non-carbon cathode materials in **Section 1.3.2.2** (page 29), to give an overview of the range of materials explored by the field to date.

1.3.2.1 Carbon Cathodes

Whilst carbon may be the most desirable material to use as the cathode, it is well documented that it is not stable under the operating conditions of the Li-O_2 cell, particularly during charge. By utilising ^{13}C isotopic labelling of the cathode, Ottakam Thotiyl *et al.* were able to separate the $^{12}CO_2$ resulting from electrolyte decomposition from the $^{13}CO_2$ originating from the cathode.[101] It was found that, on discharge, the main product is Li_2O_2 and that the main side reactions involve the electrolyte (DMSO or TEGDME) rather than the cathode. The predominant side product is Li_2CO_3, with some lithium carboxylates present (the quantity of carboxylates increases if a hydrophilic carbon or TEGDME is used, discussed further on page 27). On charge, it was found that carbon decomposition begins above 3.5 V, but only after discharge has occurred (the presence of Li_2O_2 being necessary for carbon cathode decomposition to occur). The $Li_2{}^{13}CO_3$ produced is oxidised at high potentials to form $^{13}CO_2$, which can be measured using *operando* electrochemical mass spectrometry (OEMS).

It is thermodynamically favourable for Li_2O_2 to react chemically with carbon; however, when Li_2O_2 was mixed directly with carbon only 0.1% of the carbon decomposed to form Li_2CO_3. As such, it was concluded by Ottakam Thotiyl *et al.* that chemical reaction between Li_2O_2 and carbon was not the main decomposition pathway, although it does account for a small amount of $Li_2{}^{13}CO_3$ at the end of discharge.[101] McCloskey *et al.* proposed that Li_2O_2 reacts chemically during discharge to form a thin film of Li_2CO_3 at the interface between the Li_2O_2 and the carbon cathode, with an approximately equivalent monolayer forming between the Li_2O_2 and the ether-based

electrolyte. Li_2O_2 is only metastable on carbon due to the highly exothermic, and hence exergonic, nature of the reaction between the two:

$$Li_2O_2 + C + \frac{1}{2}O_2 \rightarrow Li_2CO_3 \qquad \Delta G = -542.4\ \text{kJ mol}^{-1} \qquad \textbf{Eq. 1.10}$$

$$2Li_2O_2 + C \rightarrow Li_2CO_3 + Li_2O \qquad \Delta G = -533.6\ \text{kJ mol}^{-1} \qquad \textbf{Eq. 1.11}$$

where ΔG is the Gibbs free energy for the reaction at 300 K.[102] During charge, these Li_2CO_3 deposits combine to form an insulating layer between the cathode and the decreasing quantity of Li_2O_2, causing an increase in the overpotential in order to maintain the same current. This continues until the potential is sufficiently positive to allow electrooxidation of the Li_2CO_3 to give CO_2. This is shown schematically in **Figure 1.8**.[102]

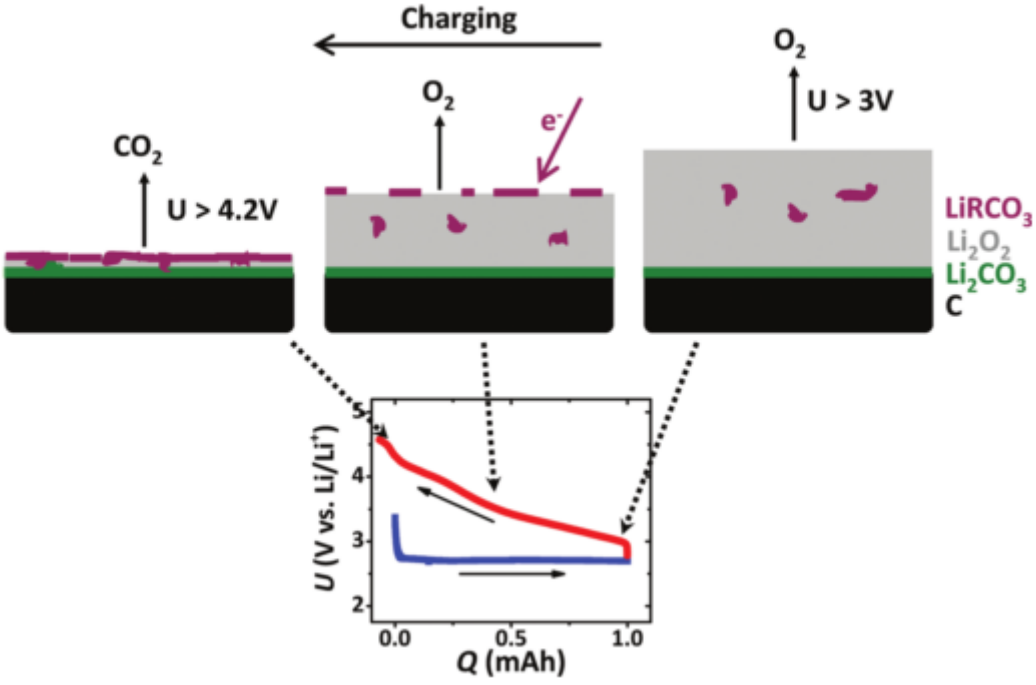

Fig. 1.8: Illustration of the formation of Li_2CO_3 layers originating from electrolyte (purple) and cathode (green) decomposition during discharge and charge. Reproduced with permission. Copyright 2012, American Chemical Society.[102]

Leskes *et al.* used solid state NMR to confirm that the major discharge products with a carbon cathode are Li_2O_2 and Li_2CO_3 by using ^6Li, ^7Li and ^{17}O quadrupole nuclei and monitoring the change in spectra during cell cycling.[103, 104] The rapid decrease in ^{17}O spectra intensity by approximately 80% led to the conclusion that the reaction:

$$3Li_2O_2 + 2C \rightarrow 2Li_2CO_3 + 2Li^+ + 2e^- \qquad \textbf{Eq. 1.12}$$

was occurring. There was also suggestion that LiOH forms during discharge.

There is a difference in stability between hydrophobic and hydrophilic carbons, with the former being more stable than the latter. The use of hydrophobic carbon results in approximately six-times less $Li_2{}^{12}CO_3$ formation than when hydrophilic carbon is employed, speculated as being due to the higher density of C-O, COOH and C-OH groups on the hydrophilic carbon surface that promote electrolyte decomposition.[101] Carbon-carbon double bonds and aromatic systems activated by the presence of oxygenated functional groups and associated defects also promote the formation of carbonate species. This occurs as superoxide species can readily react with these functional groups, notable forming epoxy intermediates.[105]

Xiao *et al.* compared the specific capacities of several different commercially available carbons, with the achievable capacity depending on the pore volume and surface area.[106] Ketjen black exhibited the highest specific capacity at 851 mAh g^{-1} at 0.05 mA cm^{-2}. Carbon loading was found to also affect the capacity obtained, with the optimum loading of Ketjen black being 15.1 mg cm^{-2}. Ma *et al.* further found that

mesopores are more effective than micropores in a achieving high discharge capacity and greater pore filling by Li_2O_2, with pore volume being more important than surface area.[107] Ordered mesoporous carbons (OMCs) have high surface areas and lead to low charging potentials. Park *et al.* found that OMCs with pore sizes of 6 nm and 17 nm diameters resulted in a less positive charging potential above 500 mAh g^{-1} compared to Super P (carbon black obtained from TIMCAL), with both having an energy efficiency approximately 3% greater than Super P.[108] This was attributed to the smaller Li_2O_2 particle size caused by the constraints of the small pores, leading to lower Li_2O_2 crystallinity.

Multiwalled carbon nanotubes, described as a catalyst, were found to perform well in a Li-O_2 cell. This was suggested as being due to the graphitic structures of the nanotube surface, which can suppress the parasitic side reactions, and the large amount of space within the nanotubes in which to store Li_2O_2.[109] Mesoporous carbon nanocubes were observed to have a discharge capacity of 26,100 mAh g^{-1} (based on total mass of catalyst in the electrode), which was further increased when the nanocubes were functionalised with ruthenium.[110]

1.3.2.2 Non-Carbon Cathodes

One of the more hotly debated non-carbon cathode materials is NPG, first demonstrated by Peng *et al.* coupled with DMSO as the solvent.[81] As stated in **Section 1.3.1** on page 21, cells using a NPG cathode were found to retain 95% of their capacity

after 100 cycles and have more than 99% Li_2O_2 purity. The decomposition of Li_2O_2 also occurred below 4 V, with approximately 50% being oxidised below 3.3 V. McCloskey *et al.*, however, disagreed with these findings, with their work showing that NPG resulted in a smaller ORR/OER ratio than carbon, using an array of different electrolytes.[45] Su *et al.* showed through density functional theory calculations supported by experimental work that the surface crystal plane is the key factor in ORR and OER promotion in gold nanocrystals.[111] It was observed that trisoctahedral gold nanocrystals had the lowest charge overpotential of approximately 900 mV, and reported a reversible capacity of 20,298 mAh g^{-1} based on the mass of carbon in the cathode. The catalytic activity of the gold crystal planes was identified as increasing from (100) < (111) < (441) due to increasing density of catalytic sites, with the gold nanoparticles also successfully decomposing Li_2O_2 on charge.

A similarly controversial cathode material is titanium carbide (TiC), first reported by Ottakam Thotiyl *et al.* as providing Li_2O_2 of more than 99.5% purity during each discharge, with more than 98% capacity retention after 100 cycles.[112] It is thought that a thin TiO_2 surface layer (observed using XPS) is responsible for the stability of TiC. The results of Ottakam Thotiyl *et al.* suggest that TiC is a superior cathode material to NPG, due to the better cycling performance, lower cost and mass, and easier synthesis compared to NPG. However, thus far no other groups have been able to recreate the results detailed by Ottakam Thotiyl *et al.*, with McCloskey *et al.* finding that TiC cathodes exhibit poorer rechargeability than carbon cathodes on the first cycle.[113] Kundu *et al.* found that a TiO_2 layer greater than 2-3 nm on the TiC

surface completely inhibits the oxidation of Li_2O_2, whereas a TiO_2 layer less than 2 nm in thickness or native TiC allows effective Li_2O_2 oxidation and charge transfer.[114] Other carbide materials include silicon carbide (SiC), which was found not to form a surface oxide layer, and nanoporous Mo_2C.[112, 114, 115].

The decoration of a carbon or other conductive material support with catalytic nanoparticles is a very active area of research. Palladium nanoparticles on carbon nanotubes were found to accelerate the nucleation and growth of Li_2O_2, which was less crystalline than that deposited on non-functionalised carbon nanotubes, with the reduced crystallinity leading to improved conductivity of the Li_2O_2.[116, 117] The palladium nanoparticles reduced the degree of carbon decomposition by minimising the degree of contact between the carbon and Li_2O_2, due to Li_2O_2 preferentially forming on the palladium rather than the carbon. Using three dimensionally ordered mesoporous carbon decorated with palladium nanoparticles, Xie *et al.* were able to achieve 68 cycles compared to 16 without the nanoparticles.[118]

Ruthenium has also been used extensively, being combined with carbon nanotubes, and indium tin oxide, to great effect, achieving low overpotentials on charge and more than 100 cycles without capacity fade.[119-122] RuO_2 was also tested, with evidence suggesting that the RuO_2 surface is not completely passivated by Li_2O_2.[123, 124]

However, despite the promising results presented thus far, work by Ma *et al.* suggested that the use of noble metal catalysts such as palladium and ruthenium

mounted on carbon nanotubes results in poor cycling efficiency. This is due to the metals also promoting parasitic side reactions, with O_2 recovery efficiencies of 0.209 for palladium and 0.662 for ruthenium, compared to 0.654 for non-functionalised carbon nanotubes.[125] In addition, the high cost of noble metals makes them undesirable for use in a commercial battery setting.

Transition metal oxides, such as Co_3O_4 (as a mesoporous film on a nickel foam or in combination with silver and palladium), have been demonstrated to effectively catalyse the ORR and OER reactions in Li-O_2 cells.[126-128] CoO mesoporous spheres mounted on carbon appear to have better cycling performance than Co_3O_4 due to the more stable adsorption configuration of LiO_2 on the former compared to the latter, which reduces the amount of contact between LiO_2 and the supporting carbon.[129] Consequently, undesired side reactions were minimised during charge, with specific capacities of more than 4,000 mAh g^{-1} (based on the mass of CoO) having been recorded.[129, 130] To further reduce costs, a CoO nanoparticle with a cheap Fe_3O_4 core was developed, providing 50 cycles at 92.7% coulombic efficiency.[131] Ti_4O_7 was also investigated for its low mass and low cost compared to ruthenium.[132]

The cathode materials described thus far do not constitute an exhaustive list, with many other more complex materials including $ZnO/ZnFe_2O_4/C$ metal-organic frameworks, doped $La_{0.8}Sr_{0.2}Mn_{1-x}Ni_xO_3$ and chromium oxides having been investigated.[133-135] However, whilst these non-carbon cathode materials exhibit excellent stability and rate performance in Li-O_2 cells, they suffer from difficult fabrication methods, higher mass (thus lowering the specific energy) and higher costs

than carbon. The key advantage of Li-O_2 cells over LIBs is the greater specific energy; a high mass, expensive cathode will thus negate the benefits of Li-O_2 technology. Furthermore, as the depth of discharge is increased the catalytic ability of nanoparticles will decrease, as ever greater quantities of insoluble Li_2O_2 block the active sites. This reinforces the need for strategies to facilitate solution-based growth of Li_2O_2 to increase the viability of Li-O_2 cells.

1.3.3 Binders

A constituent part of many cathodes is an organic polymer which acts as a binder, to provide the cathode with structural integrity. The choice of polymer is important as they too are susceptible to attack by reactive species within the cell. Poly(vinylidene fluoride) was found to be unstable during both cycling and ball milling with KO_2, undergoing defluorination.[136-138] Poly(tetrafluoroethylene) and poly(propylene), however, were found to be stable to KO_2.[137] Construction of binder-free cathodes is also possible.[139-143]

1.3.4 Lithium Salts

Not all lithium salts are suitable for use in the supporting electrolyte. $LiPF_6$ (which is commonly used in LIBs) was found to decompose to form LiF, leading to HF in the presence of trace water (which is not only corrosive but also highly toxic).[144] Multiple studies have found LiTFSI and $LiCF_3SO_3$ to be stable.[144, 145] However, other reports

suggest that LiTFSI can indeed decompose to LiF, and that $LiClO_4$ is the only stable lithium salt for Li-O_2 applications (of those salts tested).[146]

1.4 Additives for Improved Cell Performance

1.4.1 Redox Mediators

Given the need for low overpotentials and reversible solution-based discharge, redox mediators (RMs) for Li-O_2 cells have received significant levels of attention in recent years. RMs are redox-active molecules that act as electron/hole shuttles between the O_2 (on discharge) or Li_2O_2 (on charge) and the cathode. These species act as electrocatalysts, being returned to their original state and available for further reactions once an O_2 molecule has been reduced or Li_2O_2 oxidised. A discharge RM needs to have a less positive potential than the 2.96 V equilibrium potential for Li_2O_2 oxidation/reduction, whereas a charge RM needs to have a more positive potential. The main advantage of these soluble catalysts over the insoluble catalysts discussed in the previous Sections is the former can reach the interior of a porous cathode pore, where they may either facilitate solution-based discharge (preventing passivation) or facilitate the decomposition of Li_2O_2 that is electrically disconnected from the cathode surface, thereby increasing the cycling efficiency of the cell.

1.4.1.1 Charge Redox Mediators

The ideal charge RM must have a redox potential slightly above that of the Li_2O_2 oxidation equilibrium potential. Any charge RM must be able to decompose Li_2O_2, and the kinetics of both RM oxidation and the reaction between the RM^+ and Li_2O_2 need to be sufficiently fast to maintain a constant current without further increase in the charging potential of the cell. Furthermore, the RM should also not react with any other component within the cell, including the counter electrode and the electrolyte (unless intentional formation of a protective SEI on the counter electrode is desired, discussed further in **Section 1.4.1.6** on page 45). Charge RMs operate by being oxidised directly at the cathode surface to form RM^+, which then diffuses into the solution to oxidise the Li_2O_2 particles, returning the RM^+ to its non-oxidised state.

The first use of charge RMs in Li-O_2 cells was described by Chase *et al.*, with Chen *et al.* soon after demonstrating the use of tetrathiafulvalene (TTF) to achieve 100 cycles at 300 mAh g^{-1}, with a charging plateau of approximately 3.45 V (**Figure 1.9** provides a comparison of cells with and without TTF).[147, 148] Excellent reversibility of Li_2O_2 formation and decomposition was observed, as given by the electron to O_2 ratios on discharge and charge of 2.02 and 2.03 respectively. However, by the 100th cycle the charge ratio had increased to 2.14, indicating that even with the use of TTF side reactions were still occurring (as further demonstrated by Bawol *et al.*).[147, 149]

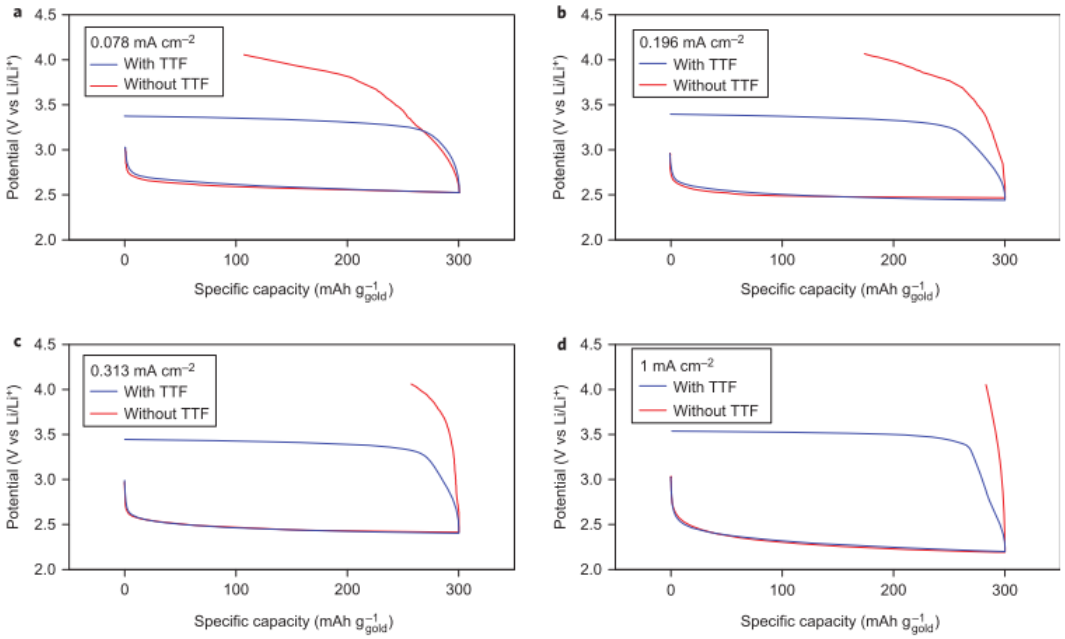

Fig. 1.9: First cycle of a nanoporous gold electrode with 10 mM and 1 M $LiClO_4$ in DMSO as the electrolyte at different rates. Reproduced with permission. Copyright 2013, Springer Nature.[147]

2,2,6,6-tetramethylpiperidnyloxyl (TEMPO) is a persistent nitroxyl radical, protected by four methyl groups. On charge, TEMPO is oxidised to $TEMPO^+$, which has been shown to oxidise Li_2O_2. Bergner *et al.* found that without TEMPO their cells achieved only 27 cycles, whereas with TEMPO over 55 cycles were possible (at 100 mA cm^{-2} on Ketjen black in 0.1 M LiTFSI/diglyme).[150] Use of TEMPO also resulted in a lower charge potential, with the redox potential of TEMPO at 3.74 V. Bergner *et al.* further identified another nitroxyl, 1-methyl-2-azaadamantane-*N*-oxyl (1-Me-AZADO), which can achieve a charging potential below 3.6 V (depending on the depth of discharge) and a greater cell capacity than TEMPO.[151] Further derivatives of TEMPO have since been demonstrated in Li-O_2 cells.[152, 153]

A large number of charge RMs contain nitrogen functionalities. Kundu *et al.* identified tris[4-(diethylamino)phenyl]amine (TDPA) as having a redox couple at 3.1 V, thus giving the cell a charging overpotential of only 140 mV, with more than 100 cycles achieved with a round trip efficiency of more than 80%.[154] Use of TDPA resulted in only a small amount of CO_2 release during charging as measured by OEMS, however this is likely due to the charging potential not increasing above 3.82 V until very close to the end of charge when TDPA is in use. *N*-methylphenothiazine (MPT) was found to have a large charge overpotential of 670 mV and a round trip efficiency of approximately 76%, when coupled with single walled nanotubes. [155] [156, 157] *N,N,N',N'*-tetramethyl-*p*-phenylenediamine (TMPD) has also found use in Li-O_2 cells and is used extensively in **Chapter 3**.[147, 149, 153]

Yao *et al.* investigated cobalt bis(terpyridine) (CBTP), which they found to have a charging onset potential of 3.2 V.[158] Here the redox couple was located on the cobalt centre, which passes between the +2 and +3 oxidation states. Despite CBTP having faster charging kinetics than TTF, OEMS measurements showed that the cycling efficiency of CBTP was poorer and more CO_2 was evolved, leading to the conclusion that CBTP is unsuitable for use as a RM. The transition metal-containing ferrocene and ruthenocene have also been tested in Li-O_2 cells.[149, 153, 159, 160]

Lim *et al.* combined a porous carbon nanotube cathode with LiI; the cathode was designed to maximise transport of the RM thereby leading to a higher catalytic activity.[161] The I^- is initially oxidised to I_3^- or I_2, both of which were suggested to react chemically with Li_2O_2 to produce O_2 and the initial I^- anion, with the I_3^- levels being

monitored using UV-visible spectroscopy.[162] The charge potential using I^- was found to be below 3.5 V, with reversible and stable cycling achieved for over 900 cycles.[161]

Li *et al.* reported that I_2 is the active oxidised state of I^-, rather than I_3^-.[163] This was confirmed by mixing known quantities of Li_2O_2 with I_3^- and Li^+, I_2, and I_2 with Li^+ (all in TEGDME), then comparing the quantities of O_2 evolved. Negligible quantities of O_2 were detected in the I_3^- with Li^+ solution, whereas in both solutions containing I_2 some O_2 was detected, with more O_2 observed when Li^+ was present.

That Li^+ has a positive effect on oxygen evolution led to the identification of the mechanism:

$$I_2 + Li_2O_2 \rightarrow 2Li^+ + 2I^- + O_2 \qquad \textbf{Eq. 1.13}$$

$$I^- + I_2 \rightarrow I_3^- \qquad \textbf{Eq. 1.14}$$

$$Li^+ + I^- \rightarrow LiI \qquad \textbf{Eq. 1.15}$$

As Li_2O_2 is chemically oxidised by I_2 rather than I_3^-, **Equation 1.14** results in the inactivation of the RM. To minimise this reaction, Li *et al.* reduced the dissociation of I^- into the electrolyte by using LiI(3-hydroypropionitrile)$_2$ (LiI(HPN)$_2$) rather than LiI.[163] In the Li(HPN)$_2$ complex I^- is bound more strongly compared to in LiI, meaning the I^- formed during Li_2O_2 oxidation by I_2 is quickly tied up to prevent the reaction in **Equation 1.14** from occurring. An additional issue with the use of LiI was highlighted by Kwak *et al.*; whilst low concentrations of LiI allow O_2 to be reduced to Li_2O_2, at high concentrations of LiI the RM promotes side reactions which form LiOH, reducing the capacity of the cell.[164]

When a polymer electrolyte was employed, it was found that a 50 mM LiI-mediated Li-O_2 cell could undergo 400 cycles in ambient air (making it a true Li-air cell).[165] The polymer was designed to be hydrophobic and was filled with an aprotic electrolyte, which reduced the passivation of the lithium counter electrode.

Kwak *et al.* turned their attention to LiBr, which they anticipated would operate in a similar manner to LiI.[166] Low concentrations of LiBr was found to improve cell performance, while also having fewer side reactions than when LiI is employed. The LiBr cell charging potential was approximately 3.5 V.

With many possible compounds having the potential to act as RMs, a logical method for identification with the desired characteristics of low charging potential and high cycling stability is required. Lim *et al.* provided a computational method of screening RMs whereby the energy of the highest occupied molecular orbital (HOMO) of a candidate RM was calculated in a TEGDME-like solvent, which can be translated into a redox potential.[167] Once a candidate molecule with an appropriate redox potential has been identified then experimental tests to determine its catalytic ability towards Li_2O_2 oxidation may be conducted. Through this method a number of potential RM candidates were selected and tested via cyclic voltammetry and reaction with Li_2O_2, with 5,10-dihydro-5,10-dimethylphenoxazine (DMPZ) found to have an Li_2O_2 oxidation potential of 3.29 V and an electron to O_2 ratio of 2.08. In addition, it was found that whilst the redox potentials of 1,5-naphthalenediamine, 4,*N*,*N*-trimethylaniline and 1-phenylpyrrolidine were below 4 V, none of these

compounds exhibited good stability during cyclic voltammetry or when added to Li_2O_2, and so were deemed unsuitable as RMs.

RMs are selected based on their ability to facilitate the oxidation of Li_2O_2 to O_2. However, as explored earlier there are numerous other by-products present within a Li-O_2 cell that require electrooxidation during charge. An investigation by Kim *et al.* showed that neither of the RMs tested (TEMPO and DMPZ) were capable of oxidising Li_2CO_3, and that their use prevented the cell potential from rising sufficiently positive to enable direct electrooxidation.[168] This will prove problematic over multiple cycles as these passivating products accumulate on the cathode, leading to rapid cell death. Only RMs with a very positive redox potential, such as phenoxathiin which operates at 4.275 V, have been observed to oxidise Li_2CO_3.[169]

1.4.1.2 Charge Redox Mediator Kinetics

The kinetics of the reaction between Li_2O_2 and RM^+ needs to be sufficiently fast to sustain the desired current density of Li-O_2 cells. Chen *et al.* undertook a study of the kinetics of a range of charge RMs, finding that there was no correlation between the standard heterogeneous rate constant for RM oxidation at the electrode surface and the rate of Li_2O_2 oxidation by RM^+, indicating that the reaction is not an outer sphere electron transfer reaction but rather inner sphere[f].[153] It was suggested that the presence

[f] When outer sphere electron transfer occurs, the redox active species remain separate and intact before, during and after the transfer of the electron. In contrast, during inner sphere electron transfer the two redox sites are connected by a covalent bridge.

of sterically bulky groups around the redox centre reduces the rate of Li_2O_2 oxidation, with the nature of the redox centre also being important in determining the rate. RRDE studies found that the observed current for a given RM's reaction with a Li_2O_2 suspension increases with redox potential.[170] This was explained through Butler-Volmer kinetics, whereby a greater overpotential leads to a lower activation energy and hence faster kinetics. **Chapter 4** explores the reaction kinetics of both established and novel RMs with Li_2O_2, providing new insight into the mechanism of operation.

1.4.1.3 Discharge Redox Mediators

Lacey *et al.* introduced the concept of using a RM to catalyse the ORR (indeed they introduced the concept of using redox shuttles within Li-O_2 cells) using ethyl viologen ditriflate in 1-butyl-3-methylpyrrolidinium TFSI (an ionic liquid), which is analogous to the methyl viologen paraquat found in biological systems that leads to superoxide formation.[171] However, at high concentrations of the viologen it was found that the shuttle decomposes upon reaction with superoxide.

2,5-di-tert-butyl-1,4-benzoquinone (DBBQ) was identified by Gao *et al.* as a discharge RM.[172] The mechanism of DBBQ is somewhat different from that of charge RMs; charging RMs act as an electron shuttle between the cathode and the Li_2O_2, whereas DBBQ does not. Nor does DBBQ act as a conventional electrocatalyst, to which the O_2 is bound both before and after reduction. Rather the reduced DBBQ molecule coordinates with Li^+ to form LiDDBQ, which then reacts with O_2 to form

the $LiDBBQO_2$ intermediate. $LiDBBQO_2$ can then either disproportionate or react with another LiDBBQ to form Li_2O_2 and regenerate the DBBQ.

In the absence of DBBQ, reduction of O_2 to Li_2O_2 proceeds via the LiO_2 intermediate. The potential of formation of LiO_2 is significantly more negative than the standard potential for Li_2O_2 formation, and it is the need to reach this potential that results in the large overpotential during discharge. The presence of DBBQ causes the O_2 reduction to occur at approximately the DBBQ reduction potential, as a result of the $LiDBBQO_2$ rather than LiO_2 being the intermediate. $LiDBBQO_2$ has a lower free energy than LiO_2, leading to a less negative potential required for cell discharge. **Figure 1.10** illustrates schematically cell discharge with DBBQ and the effect of DBBQ on the energy of the potential-determining determining step.

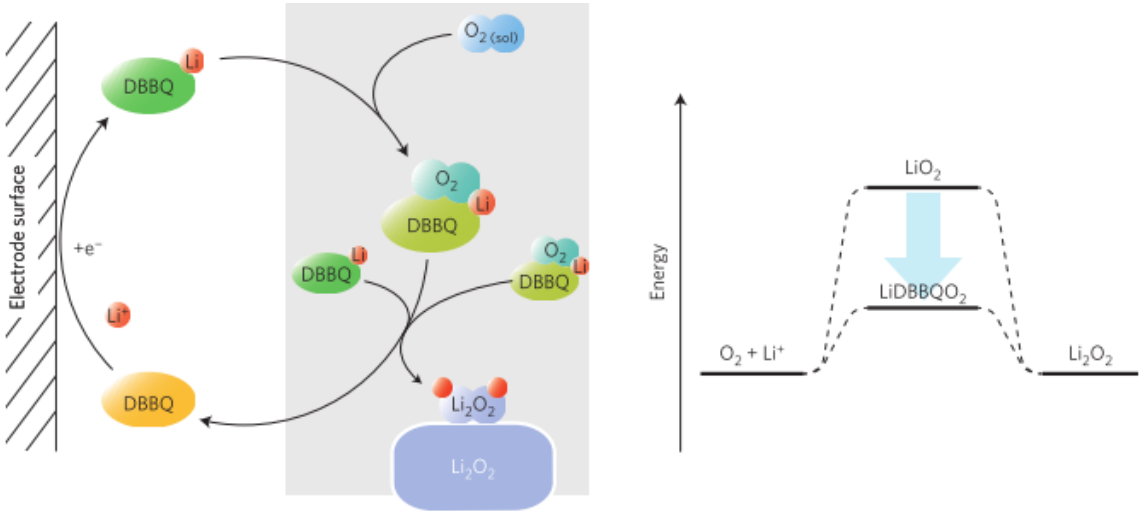

Fig. 1.10: a. Illustration of the proposed mechanism of DBBQ operation on discharge and **b.** the effect of DBBQ on the potential-determining step. Reproduced with permission. Copyright 2016, Springer Nature.[172]

DBBQ has the additional benefit of inducing solution-based formation of Li_2O_2.[173] By forming Li_2O_2 in solution as opposed to on the cathode surface, cell death by passivation is postponed and the discharge capacity is increased 80 to 100-fold. Solution-based growth can also occur without the need for high donor number solvents, as demonstrated by the use of DBBQ in TEGDME and DME by Gao *et al.*, allowing research efforts to be focused on very low DN (and therefore weakly LiO_2 solvating) yet stable solvents.[172]

Other quinones have been investigated for their ability to operate during Li-O_2 cell discharge, including benzo[1,2,-*b*4,5-*b*']dithiophene-4,8-dione, and anthraquinone.[174, 175] Dilithium quinone-1,4-dicarboxylate was found to behave as a charge RM.[176]

1.4.1.4 Dual and Bifunctional Redox Mediators

It is not possible to charge fully a Li-O_2 cell that contains DBBQ (or any discharge RM that facilitates solution-based growth) without also having a charge RM present. This is due to the solution-based growth causing the Li_2O_2 to be electrically isolated from the cathode, preventing direct oxidation through the cathode. Zhu *et al.*, using ethyl viologen and I^- as the discharge and charge RMs, respectively, demonstrated the idea of a dual RM system for Li_2O_2 cells in a redox flow cell.[177] Gao *et al.* subsequently used a combination of DBBQ and TEMPO, thereby decoupling entirely the electrochemical reactions at the cathode surface from the formation and decomposition

of Li_2O_2 in the solution.[178] By preventing the insoluble and insulating Li_2O_2 from forming on the cathode, the performance of the Li-O_2 cell is now limited primarily by the mass transport of O_2, an issue that can be solved with gas diffusion electrodes, with dual RMs showing less carbon cathode decomposition due to the Li_2O_2 no longer being in direct contact. A combination of DBBQ and LiI has also been found to improve the stability of ionic liquid electrolytes.[179]

While Gao *et al.* used two separate RMs, one to operate on discharge and the other on charge, Yu *et al.* found that 2,6-di-tert-butyl-hydroxytoluene (BHT) could facilitate both Li_2O_2 formation and decomposition (a bifunctional RM), with *in situ* XRD measurements revealing that the formation and oxidation of Li_2O_2 were the main cycling reactions.[180] BHT has a quasireversible redox couple (BHT/BHT^+) that operates at 3.0 V, with BHT^+ capable of oxidising Li_2O_2. Furthermore, the discharge potential is less negative in the presence of BHT, postulated as being due to a strong interaction between BHT and O_2 or O_2^- (due to the labile proton on the hydroxyl group on the BHT) which allow formation of the complex Li[BHT-O_2]. Disproportionation of this complex resulted in Li_2O_2 formation and recovery of BHT. In addition to being a bifuctional RM, BHT is also a cheap and environmentally friendly compound, widely used in the food, cosmetic and plastics industries.

Ryu *et al.* and Mu *et al.* studied the haem molecule as a bifucntional RM, capitalising on the Fe^{II}/Fe^{III} couple.[160, 181] During both discharge and charge the haem molecule acts as an electron shuttle between the cathode and the O_2 or Li_2O_2, forming a complex with superoxide. It was found that the choice of anion is important; $LiPF_6$

was found to both prevent electron transfer and inhibit superoxide coordination, whereas $LiClO_4$ did not. Haem has also been incorporated into MOF nanosheets, increasing the discharge capacity and facilitating 100 cycles.[181]

Additional advances in bifunctional RMs include MoCl, *N*-methyl-*N*-propyl pyrrolidine bromide, heptyl viologen dibromide and manganese selen-type complexes.[182-185]

1.4.1.5 Redox Mediators in other Metal-Oxygen Systems

RMs have found application in Na-O_2 cells, with ethyl viologen increasing the discharge capacity by approximately 50% and resulting in the formation of NaO_2 only.[186] At the time of writing, there have been no studies of RMs in K-O_2 cells.

1.4.1.6 Redox Mediator Shuttling and Counter Electrode Reaction

Besides any instability of the charge RM itself to the reactive oxygen species present in the cell, two main issues face their use.[g] Firstly, there is the potential for RM^+ to migrate across the cell and react at the counter electrode, either to reform RM or to form other side products. This "shuttling effect" means that the observed current and capacity is not due to Li_2O_2 oxidation. When shuttling occurs, there is an increased chance that some Li_2O_2 will be left unoxidised at the end of charge, leading to

[g] Similar issues are faced by discharge RMs, however this work focuses only on those RMs used to facilitate Li_2O_2 oxidation on charge.

passivation over multiple cycles. While RM shuttling is problematic in and of itself, a further potential ramification is that both the RM and lithium counter electrode are consumed in parasitic side reactions, again shortening the life expectancy of the cell.[187] Strategies to prevent the contact of RMs with the counter electrode are therefore required, with notable examples discussed in the following paragraphs.

Zhang *et al.* found that I_3^- can diffuse across the cell and react with the lithium counter electrode to form LiI, which only partially redissolved back into the electrolyte (remaining instead as a layer on the counter electrode surface) leading to loss of RM.[188] To circumvent this problem, InI_3 was used as a RM, with the In^{3+} sacrificially reacting with the lithium counter electrode to form a thin indium layer on the surface during charge. This prevents the I_3^- from being reduced, thereby maintaining the concentration of RM in solution. The indium layer was also found to suppress lithium dendrite formation. Similarly to In^{3+}, organic iodides were also found to produce a protective layer on the lithium counter electrode surface.[51] As with InI_3, $InBr_3$ was found to prevent lithium dendrite formation and suppress RM shuttling.[189]

CsI was found by Lee *et al.* to act as a multifunctional RM; while the I^- is involved in the oxidation of Li_2O_2, the Cs^+ acts to prevent the formation of lithium dendrites.[190] The prevention of dendrite growth is essential as dendrites can cause cells to short circuit, which leads to safety issues. Cs^+ (and Rb^+) can remain dissolved in solution at potentials where Li^+ would be reduced to lithium metal. On charge, the Cs^+ cations migrate towards the counter electrode and affix to the growing dendrites, impeding their growth. A comparison of SEM images of the counter electrode surface

after charge with and without CsI revealed a smooth lithium surface for the former, contrasted with the rough and porous surface of the latter.

The use of $LiNO_3$ has been shown to prevent reaction of MPT^+ with the lithium counter electrode (a reaction in which the MPT^+ degrades the SEI protection of the native lithium).[187] NO_3^- reacts with the lithium metal to form NO_2^-, which then acts as a scavenger of RM^+ thereby preventing the MPT^+ from degrading the SEI. $LiNO_3$ itself was also found to have a catalytic effect, lowering the charging overpotential.[191]

Besides the additives discussed above, physical barriers can also prevent RM migration and counter electrode degradation, with many examples of the successful use of Li^+-conducting ceramic electrolytes and functionalised membranes preventing the passage of RM^+ across the cell.[178, 192-195] The issue of lithium counter electrode stability is also pertinent to LIB research, with a solution for LIBs likely to also be applicable to Li-O_2 cells.

1.4.2 Protic Additives

Protons have been found to act as phase transfer catalysts within Li-O_2 cells. Gao *et al.* demonstrated that the addition of phenol to a cell leads to an approximately 33-fold increase in the discharge capacity, with Li_2O_2 observed as the major discharge product.[196] During discharge, the Li_2O_2 that is formed undergoes a cation exchange reaction, according to the scheme:

$$Li_2O_2 + HA \rightarrow LiOOH + LiA \qquad \textbf{Eq. 1.16}$$

with LiOOH being soluble in the ether electrolyte; as Li_2O_2 is formed it is removed from the cathode surface, preventing passivation. The conjugate base of HA then deprotonates the LiOOH to reform Li_2O_2 in solution, with particles of Li_2O_2 growing in solution via an Ostwald ripening process. In order for the protic additive to function as a phase transfer catalyst, the conjugate base must be sufficiently strong to deprotonate LiOOH; it was found that the conjugate base of perchloric acid had an insufficiently high *p*Ka to enable this reverse reaction. This is presented schematically in **Figure 1.11**.

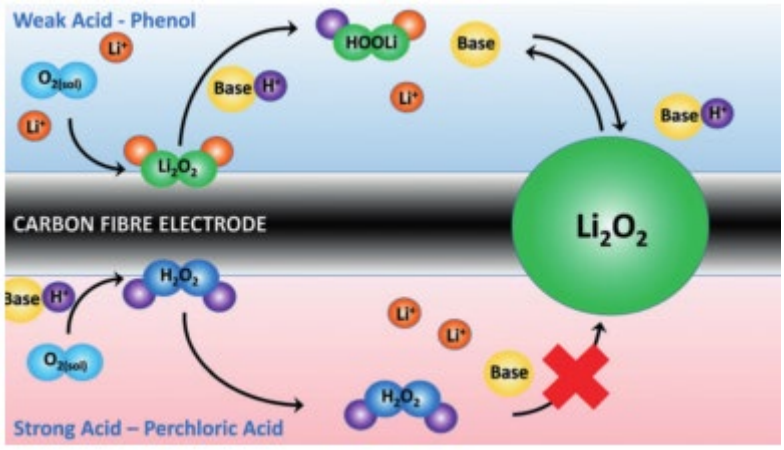

Fig. 1.11: Illustration of the action of phenol and perchloric acid during discharge of a Li-O_2 cell. Reproduced with permission. Copyright 2017, John Wiley and Sons.[196]

Xia *et al.* similarly found that the use of either water or acetic acid in Na-O_2 cells resulted in much greater discharge capacities due to a phase transfer catalysis effect, with NaO_2 as the main discharge product and the soluble species being HO_2.[197]

Unlike the work of Gao *et al.* where recharging the cell in the presence of phenol was impossible, here water was shown to not only allow recharge of the Na-O_2 cell, but also reduced the overpotential on charge.[196, 197]

The effect of protic additives on K-O_2 cell discharge capacity has yet to be investigated; **Chapter 5** of this work evaluates the effect of phenol on the K-O_2 discharge reaction.

1.5 Singlet Oxygen

1.5.1 Formation of Singlet Oxygen in Li-O_2 Cells

Generally, it has been assumed that the reactive oxygen species within a Li-O_2 cell was either superoxide or peroxide. However, in 2011 Hassoun *et al.* proposed the existence of singlet oxygen (term symbol $^1\Delta_g$ and hereinafter referred to as $^1O_2$), an electronically excited state of dioxygen, during cell cycling, with McCloskey *et al.* further postulating the presence of $^1O_2$.[34, 198, 199] Whilst the ground state triplet oxygen, $^3\Sigma_g^-$ (hereinafter referred to as $^3O_2$), has two unpaired electrons with the parallel spin in separate $1\pi_g$ molecular orbitals, in $^1O_2$ the two electrons are paired with opposite spins in the same $1\pi_g$ orbital. The molecular orbital energy level diagrams for $^3O_2$ and $^1O_2$ are given in **Figure 1.12**.

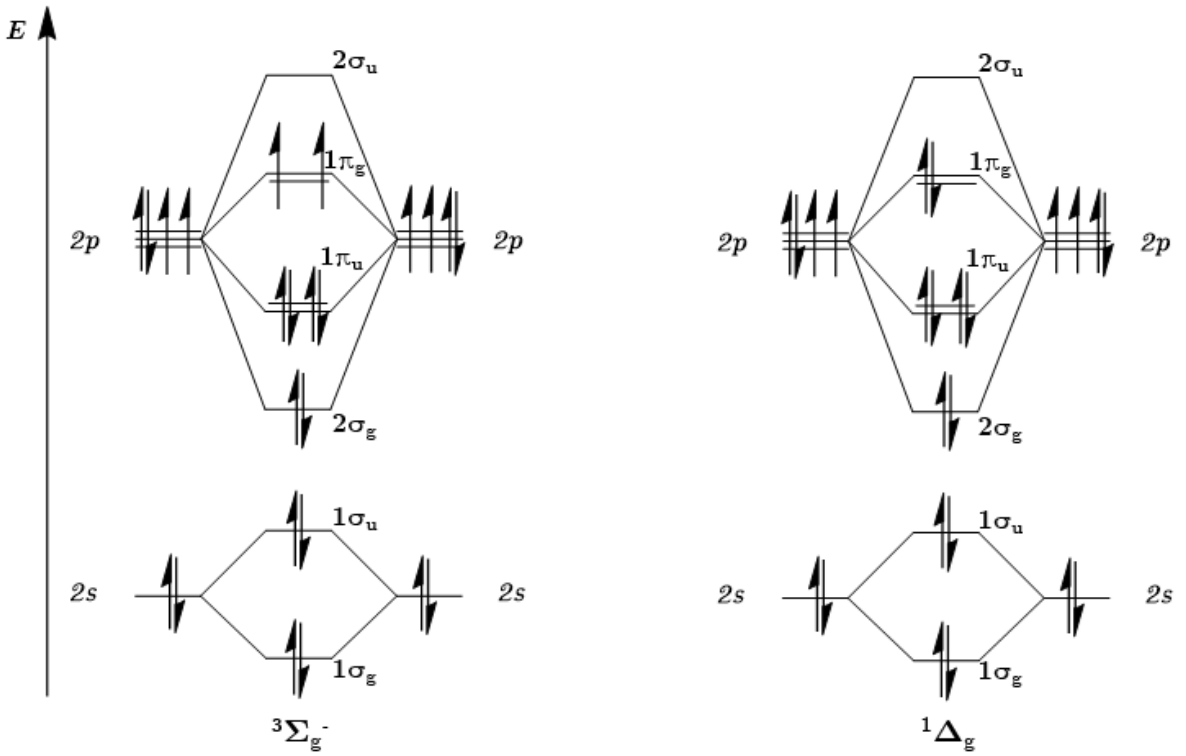

Fig. 1.12: Molecular orbital energy level diagram of $^3O_2$ (left) and $^1O_2$ (right). The 1s atomic orbitals and corresponding molecular orbitals have been omitted from the diagrams.

Wandt *et al.* proceeded to provide the first conclusive evidence of the presence of $^1O_2$ on charging through the use of electron paramagnetic resonance spectroscopy (EPR), whereby the $^1O_2$ would react with 4-oxo-TEMP within the cell to form 4-oxo-TEMPO, which is EPR active.[200] Formation of $^1O_2$ thus caused an EPR signal to be detected, but only above 3.5 V, with a lower limit of 0.5% of all evolved oxygen being in the singlet state. Wandt *et al.* suggested that $^1O_2$ was formed during the direct second oxidation step of LiO_2:

$$LiO_2 \rightarrow {}^1O_2 + Li^+ + e^- \qquad \textbf{Eq. 1.17}$$

Mahne *et al.* demonstrated the use of the $^1O_2$ trap 9,10-dimethylanthracene (DMA) to efficiently remove $^1O_2$ during cycling.[201] $^1O_2$ reacts irreversibly with DMA to form the endoperoxide DMA-O_2, according to the reaction:

$$DMA + {}^1O_2 \rightarrow DMA - O_2 \qquad \textbf{Eq. 1.18}$$

The quantity of $^1O_2$ present within the cell can be determined through fluorescence spectroscopy; DMA is a fluorescent species whereas DMA-O_2 is not, and so successful removal of $^1O_2$ from the system will lead to a corresponding decrease in the measured fluorescence intensity. In contrast to Wandt *et al.*, Mahne *et al.* suggest that $^1O_2$ is formed from the onset of charge (although the cells presented polarised rapidly to above the 3.5 V onset potential described by Wandt *et al.*). It is further suggested that $^1O_2$ is generated during discharge through the disproportionation of LiO_2:

$$2LiO_2 \rightarrow Li_2O_2 + {}^1O_2 \qquad \textbf{Eq. 1.19}$$

This route to $^1O_2$ was investigated further by Mourad *et al.*, who found that disproportionation of KO_2 through the addition of a lithium salt results in the formation of $^1O_2$, with strong Lewis acids stabilising superoxide over peroxide and so driving the disproportionation reaction.[41] Cordoba *et al.* further identified $^1O_2$ as arising from superoxide disproportionation in cells utilising a DMSO electrolyte.[202]

That $^1O_2$ arises from LiO_2 disproportionation is unfortunate, given that the desirable solution-based discharge to ensure high capacities is dependent upon this mechanism. Computational work by Houchins *et al.* demonstrates that disproportion of free superoxide (that is to say, superoxide that is not associated with an alkali metal

cation) results in the formation of $^1O_2$ according to Marcus kinetics (an explanation of Marcus kinetic theory is given in **Section 2.1.5** on page 83).[203] The rate constants for $^1O_2$ and $^3O_2$ production can be tuned by the donor and acceptor number of the solvent, which determines the degree of association of M^+ and O_2^-. The quantity of $^1O_2$ formed through disproportion of LiO_2 has also been shown to be sensitive to the cathode surface and any catalytic species present.[204]

The presence of water within the cell has been proposed as a route to $^1O_2$ formation, according to the equation:[201, 205]

$$2O_2^- + 2H^+ \rightarrow H_2O_2 + {}^1O_2 \qquad \textbf{Eq. 1.20}$$

This route to $^1O_2$ formation has been suggested as allowing $^1O_2$ formation below the thermodynamic potential and on discharge, however given that water is usually only a trace impurity within the cell it is difficult to reconcile the quantity of $^1O_2$ detected with the level of water present. Reaction of RMs with LiO_2 has also been shown to result in the formation of $^1O_2$ when the formal potential of the RM is greater than 3.5 V.[206]

The oxidation of Li_2CO_3 has long been shown to produce CO_2, however the fate of the third oxygen atom remained a mystery, given the lack of O_2 formation concurrent with CO_2 release. It has since been demonstrated through the use of singlet traps that oxidation of Li_2CO_3 yields stoichiometric quantities of $^1O_2$.[63] The lack of observation of this oxygen in mass spectrometry experiments indicates that $^1O_2$ is heavily involved in parasitic side reactions within the cell.

1.5.2 Strategies to Counteract Singlet Oxygen

Mahne *et al.* indicate that the presence of $^1O_2$ traps and quenchers within a cell results in a decrease in the quantity of Li_2CO_3 formed during discharge.[201] This provides evidence that $^1O_2$ is indeed involved in the decomposition reactions to form Li_2CO_3, and as such its presence is undesirable. While $^1O_2$ traps are beneficial within the cell, they are single-use only, as the reaction between trap and $^1O_2$ is irreversible. As such, the use of $^1O_2$ quenchers, which remove the excess energy of $^1O_2$ through a physical process, is much more desirable since they are not consumed during cell cycling. However, the quencher used by Mahne *et al.*, 1,4-diazabicyclo[2.2.2]octane (DABCO), is only stable up to approximately 3.5 V; given it is not uncommon for Li-O_2 cells to charge at higher potentials DABCO was found to be unsuitable for general applications.[201] With a subtle modification of DABCO through monoalkylation of one of the tertiary amine functionalities to form the quaternary amine salt (pentyl)DABCOnium TFSI, the stability window of the quencher was extended to 4.2 V.[207]

An alternative solution to finding new quenchers is to suppress the charging potential such that it always remains within the stability window of DABCO. This was achieved by Kwak *et al.* who utilised DABCO with high concentrations of DMPZ (200 mM) to keep the charge potential below 3.5 V, leading to greatly improved cyclability.[208] However, the study presents conflicting data, with the authors maintaining that the charging potential remains below approximately 3.5 V whilst also showing oxidation of carbonates, which is well established as occurring only above

3.82 V.[63] Furthermore, the high RM concentration along with poor O_2 yields on charge suggests that a significant proportion of the capacity is not due to Li_2O_2 oxidation. Other studies have, however, demonstrated the ability of RMs themselves to act as $^1O_2$ quenchers.[155, 209]

1.5.3 Parasitic Reactions of Singlet Oxygen

Kwak *et al.* demonstrated that $^1O_2$ reacts with the RMs TTF and DMPZ, which they suggest is the cause for the decreased catalytic effect of organic RMs over the course of successive cycles.[210, 211] Due to $^1O_2$ being an electrophile, it was found to react more readily with the neutral RMs rather than the oxidised forms, as observed using UV-vis spectroscopy. In contrast, TEMPO and other nitroxyl derivatives were found to be stable towards $^1O_2$, suggesting that despite their higher redox potential they may be most suited for use in Li-O_2 cells.[211]

Despite Mahne *et al.* demonstrating that the presence of $^1O_2$ results in the formation of Li_2CO_3, the mechanism for this reaction remains unclear. When considering the ether solvents, one possible route involves reaction at the methylene carbon, as demonstrated by Sagadevan *et al.*, where exposure of various ethers to $^1O_2$ at room temperature for between 8-12 hours resulted in the formation of lactones and hydroperoxides, with improved yields in the presence of Lewis acids, via the mechanism presented in **Figure 1.13**.[212] The reaction occurred selectively at the α-carbon position, with the presence of the $^1O_2$ quencher NaN_3 reducing the obtained yields. The

effect of superoxide was also investigated, however exposure of THF to KO_2 for 36 hours in the absence of light did not yield the products observed with $^1O_2$. As discussed in **Section 1.3.1** (page 16), Huang *et al.*, exposed their novel fully methylated cyclic ether to $^1O_2$ (and separately also to superoxide), however no decomposition of the solvent was observed.[75]

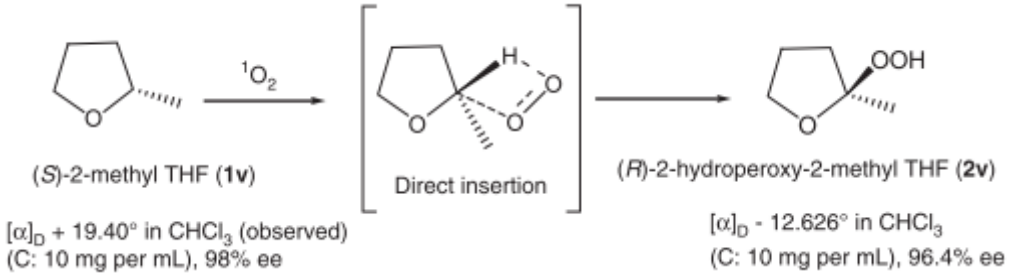

Fig. 1.13: Mechanism for attack of α-hydrogen on ethereal carbon by $^1O_2$. Reproduced with permission. Copyright 2017, Springer Nature.[212]

1.6 Potassium-Oxygen Cells

As discussed in **Section 1.1.2** (page 2), in contrast to Li-O_2 cells the primary discharge product in K-O_2 cells is KO_2, the product of a one-electron reduction of O_2 in the presence of K^+ ions.[15, 35] Further reduction to K_2O_2 is possible upon application of a more negative potential.[35] In comparison to LiO_2, KO_2 is the thermodynamically and kinetically stable product due to the interaction of a soft acid and soft base.[35] Despite the lower theoretical specific energy of K-O_2 compared to Li-O_2, the former has a much lower overpotential on charge (of only a few hundred millivolts) leading to a higher round trip efficiency.[15] A further advantage is that a greater surface route discharge

capacity is possible as KO_2 demonstrates some limited conductivity, unlike Li_2O_2.[17] Nonetheless, cathode passivation by KO_2 does eventually occur.

It was found that the majority of decomposition products arise from reaction of the potassium metal counter electrode with either the electrolyte (in studies utilising DME) or O_2 species.[213] To circumvent this issue and the issue of potassium dendrite formation, protective layers may be placed between the counter electrode and the liquid electrolyte or more stable alternative counter electrode materials such as K_3Sb may be used.[214-217] Reports also indicate that ether solvents are relatively stable towards KO_2, with HCOOK and KF being the main observed side products when LiPF6-DME was used.[40] Potassium bis(trifluoromethane)sulfonimide (KTFSI) was found to also be resistant to nucleophilic attack by KO_2.[218]

With K-O_2 cells displaying much greater stability and lower charge overpotentials, it presents a viable alternative to Li-O_2. There are also currently no reports of $^1O_2$ formation during charge of K-O_2 cells. Further discussion of K-O_2 cells occurs in **Chapter 5**, where the effects of a protic additive on the discharge reaction are considered.

1.7 Thesis Objectives

Despite metal-oxygen batteries having been established for a number of years and great strides having been made in attempting to solve the large number of issues facing their

commercialisation, there are three key questions that have yet to be fully addressed by the field:

1. Is singlet oxygen an inevitable consequence of charging a Li-O_2 cell or can strategies be developed to avoid its formation?
2. What factors determine the reaction kinetics between redox mediators and Li_2O_2?
3. Can the discharge capacity of a K-O_2 cell be increased through the use of protic additives (acting as phase transfer catalysts)?

In answering these questions this thesis will provide an insight into the underlying chemistry occurring within these systems, with the conclusions helping to direct future research of metal-oxygen batteries.

1.8 References

1. R. J. Brodd, in *Encyclopedia of Electrochemical Power Sources*, ed. J. Garche, Elsevier, 2009, pp. 254-261.
2. V. Etacheri, R. Marom, R. Elazari, G. Salitra and D. Aurbach, *Energy Environ. Sci.*, 2011, **4**, 3243-3262.
3. L.-X. Yuan, Z.-H. Wang, W.-X. Zhang, X.-L. Hu, J.-T. Chen, Y.-H. Huang and J. B. Goodenough, *Energy Environ. Sci.*, 2011, **4**, 269-284.
4. M. V. Reddy, A. Mauger, C. M. Julien, A. Paolella and K. Zaghib, *Materials (Basel)*, 2020, **13**, 8, 1884.
5. J. Park, J. Y. Hwang and W. J. Kwak, *J. Phys. Chem. Lett.*, 2020, **11**, 7849-7856.
6. T. Hosaka, K. Kubota, A. S. Hameed and S. Komaba, *Chem. Rev.*, 2020, **120**, 6358-6466.
7. E. Peled, D. Golodnitsky, R. Hadar, H. Mazor, M. Goor and L. Burstein, *J. Power Sources*, 2013, **244**, 771-776.

8. H. S. Hirsh, Y. Li, D. H. S. Tan, M. Zhang, E. Zhao and Y. S. Meng, *Adv. Energy Mater.*, 2020, **10**, 2001274.
9. L. Bravo Diaz, X. He, Z. Hu, F. Restuccia, M. Marinescu, J. V. Barreras, Y. Patel, G. Offer and G. Rein, *J. Electrochem. Soc.*, 2020, **167**, 090559.
10. W. J. Kwak, Rosy, D. Sharon, C. Xia, H. Kim, L. R. Johnson, P. G. Bruce, L. F. Nazar, Y. K. Sun, A. A. Frimer, M. Noked, S. A. Freunberger and D. Aurbach, *Chem. Rev.*, 2020, **120**, 14, 6626-6683.
11. T. Ogasawara, A. Debart, M. Holzapfel, P. Novak and P. G. Bruce, *J. Am. Chem. Soc.*, 2006, **128**, 1390-1393.
12. S. F. Tie and C. W. Tan, *Renew. Sustain. Energy Rev.*, 2013, **20**, 82-102.
13. J. A. Sanguesa, V. Torres-Sanz, P. Garrido, F. J. Martinez and J. M. Marquez-Barja, *Smart Cities*, 2021, **4**, 372-404.
14. P. G. Bruce, L. J. Hardwick and K. M. Abraham, *MRS Bull.*, 2011, **36**, 506-512.
15. X. Ren and Y. Wu, *J. Am. Chem. Soc.*, 2013, **135**, 2923-2926.
16. P. G. Bruce, S. A. Freunberger, L. J. Hardwick and J.-M. Tarascon, *Nat. Mater.*, 2012, **11**, 19-29.
17. Y. Chen, Z. P. Jovanov, X. Gao, J. Liu, C. Holc, L. R. Johnson and P. G. Bruce, *J. Electroanal. Chem.*, 2018, **819**, 542-546.
18. D. Capsoni, M. Bini, S. Ferrari, E. Quartarone and P. Mustarelli, *J. Power Sources*, 2012, **220**, 253-263.
19. Y. Wang, R. Ohnishi, E. Yoo, P. He, J. Kubota, K. Domen and H. Zhou, *J. Mater. Chem.*, 2012, **22**, 15549-15555.
20. E. M. Benbow, S. P. Kelly, L. Zhao, J. W. Reutenauer and S. L. Suib, *J. Phys. Chem. C*, 2011, **115**, 22009-22017.
21. P. He, Y. Wang and H. Zhou, *Chem. Commun.*, 2011, **47**, 10701-10703.
22. J. Suntivich, K. J. May, H. A. Gasteiger, J. B. Goodenough and Y. Shao-Horn, *Science*, 2011, **334**, 1383-1385.
23. J. Suntivich, H. A. Gasteiger, N. Yabuuchi and Y. Shao-Horn, *J. Electrochem. Soc.*, 2010, **157**, B1263-B1268.
24. Y. Wang, Y. Liu, X. Lu, Z. Li, H. Zhang, X. Cui, Y. Zhang, F. Shi and Y. Deng, *Electrochem. Commun.*, 2012, **20**, 171-174.
25. F. Cheng and J. Chen, *Chem. Soc. Rev.*, 2012, **41**, 2172-2192.
26. H. Kim, G. Jeong, Y. U. Kim, J. H. Kim, C. M. Park and H. J. Sohn, *Chem. Soc. Rev.*, 2013, **42**, 9011-9034.
27. T. Zhang and H. Zhou, *Nat. Commun.*, 2013, **4**, 1817.
28. H.-K. Lim, H.-D. Lim, K.-Y. Park, D.-H. Seo, H. Gwon, J. Hong, W. A. Goddard, H. Kim and K. Kang, *J. Am. Chem. Soc.*, 2013, **135**, 9733-9742.
29. G. Wang, L. Huang, S. Liu, J. Xie, S. Zhang, P. Zhu, G. Cao and X. Zhao, *ACS Appl. Mater. Interfaces*, 2015, **7**, 23876-23884.
30. L. Liu, H. Guo, L. Fu, S. Chou, S. Thiele, Y. Wu and J. Wang, *Small*, 2019, **17**, 1903854.
31. L. Qin, N. Xiao, S. Zhang, X. Chen and Y. Wu, *Angew.*, 2020, **59**, 10498-10501.

32. B. D. McCloskey, R. Scheffler, A. Speidel, G. Girishkumar and A. C. Luntz, *J. Phys. Chem. C*, 2012, **116**, 23897-23905.
33. I. Kowalczk, J. Read and M. Salomon, *Pure Appl. Chem.*, 2007, **79**, 851-860.
34. D. T. Sawyer and J. S. Valentine, *Acc. Chem. Res.*, 1981, **14**, 393-400.
35. C. O. Laoire, S. Mukerjee, K. M. Abraham, E. J. Plichta and M. A. Hendrickson, *J. Phys. Chem. C*, 2009, **113**, 20127-20134.
36. C. O. Laoire, S. Mukerjee, K. M. Abraham, E. J. Plichta and M. A. Hendrickson, *J. Phys. Chem. C*, 2010, **114**, 9178-9186.
37. R. G. Pearson, *J. Am. Chem. Soc.*, 1963, **85**, 22, 3533-3539.
38. L. Johnson, C. Li, Z. Liu, Y. Chen, S. A. Freunberger, P. C. Ashok, B. B. Praveen, K. Dholakia, J.-M. Tarascon and P. G. Bruce, *Nat. Chem.*, 2014, **6**, 1091-1099.
39. E. J. Calvo and N. Mozhzhukhina, *Electrochem. Commun.*, 2013, **31**, 56-58.
40. N. Xiao, R. T. Rooney, A. A. Gewirth and Y. Wu, *Angew.*, 2018, **57**, 1227-1231.
41. E. Mourad, Y. K. Petit, R. Spezia, A. Samojlov, F. F. Summa, C. Prehal, C. Leypold, N. Mahne, C. Slugovc, O. Fontaine, S. Brutti and S. A. Freunberger, *Energy Environ. Sci.*, 2019, **12**, 2559-2568.
42. A. I. Belova, D. G. Kwabi, L. V. Yashina, Y. Shao-Horn and D. M. Itkis, *J. Phys. Chem. C*, 2017, **121**, 1569-1577.
43. D. Zhai, H. H. Wang, J. Yang, K. C. Lau, K. Li, K. Amine and L. A. Curtiss, *J. Am. Chem. Soc.*, 2013, **135**, 15364-15372.
44. A. Dutta, K. Ito, A. Nomura and Y. Kubo, *Adv. Sci. (Weinh)*, 2020, **7**, 2001660.
45. B. D. McCloskey, A. Valery, A. C. Luntz, S. R. Gowda, G. M. Wallraff, J. M. Garcia, T. Mori and L. E. Krupp, *J. Phys. Chem. Lett.*, 2013, **4**, 2989-2993.
46. Y.-C. Lu and Y. Shao-Horn, *J. Phys. Chem. Lett.*, 2012, **4**, 93-99.
47. S. Ganapathy, B. D. Adams, G. Stenou, M. S. Anastasaki, K. Goubitz, X. F. Miao, L. F. Nazar and M. Wagemaker, *J. Am. Chem. Soc.*, 2014, **136**, 16335-16344.
48. Y. Wang, N.-C. Lai, Y.-R. Lu, Y. Zhou, C.-L. Dong and Y.-C. Lu, *Joule*, 2018, **2**, 2364-2380.
49. Y. Wang, Y.-R. Lu, C.-L. Dong and Y.-C. Lu, *ACS Energy Lett.*, 2020, **5**, 5, 1355-1363.
50. E. Yoo and H. Zhou, *ACS Appl. Mater. Interfaces*, 2020, **12**, 16, 18490-18495.
51. X. P. Zhang, Y. Y. Sun, Z. Sun, C. S. Yang and T. Zhang, *Nat. Commun.*, 2019, **10**, 3543.
52. J. Read, *J. Electrochem. Soc.*, 2002, **149**, A1190-A1195.
53. H. Cheng and K. Scott, *J. Power Sources*, 2013, **235**, 226-233.
54. S. A. Freunberger, Y. Chen, Z. Peng, J. M. Griffin, L. J. Hardwick, F. Barde, P. Novak and P. G. Bruce, *J. Am. Chem. Soc.*, 2011, **133**, 8040-8047.
55. W. Xu, V. V. Viswanathan, D. Wang, S. A. Towne, J. Xiao, Z. Nie, D. Hu and J.-G. Zhang, *J. Power Sources*, 2011, **196**, 3894-3899.

56. W. Xu, K. Xu, V. V. Viswanathan, S. A. Towne, J. S. Hardy, J. Xiao, Z. Nie, D. Hu, D. Wang and J.-G. Zhang, *J. Power Sources*, 2011, **196**, 9631-9639.
57. S. A. Freunberger, Y. Chen, N. E. Drewett, L. J. Hardwick, F. Barde and P. G. Bruce, *Angew.*, 2011, **50**, 8609-8613.
58. M. Marinaro, S. Theil, L. Jörissen and M. Wohlfahrt-Mehrens, *Electrochim. Acta*, 2013, **108**, 795-800.
59. G. Horwitz, E. J. Calvo, L. P. P. Méndez De Leo and E. de la Llave, *Phys. Chem. Chem. Phys.*, 2020, **22**, 16615-16623.
60. C. Laoire, S. Mukerjee, E. J. Plichta, M. A. Hendrickson and K. M. Abraham, *J. Electrochem. Soc.*, 2011, **158**, A302-A308.
61. H. Wang and K. Xie, *Electrochim. Acta*, 2012, **64**, 29-34.
62. H. G. Jung, J. Hassoun, J. B. Park, Y. K. Sun and B. Scrosati, *Nat. Chem.*, 2012, **4**, 579-585.
63. N. Mahne, S. E. Renfrew, B. D. McCloskey and S. A. Freunberger, *Angew.*, 2018, **57**, 19, 5529-5533.
64. V. S. Bryantsev and F. Faglioni, *J. Phys. Chem. A*, 2012, **116**, 7128-7138.
65. D. Zhu, L. Zhang, M. Song, X. Wang, J. Mei, L. M. Lau and Y. Chen, *J. Solid State Electrochem.*, 2013, **17**, 2865-2870.
66. K. R. Ryan, L. Trahey, B. J. Ingram and A. K. Burrell, *J. Phys. Chem. C*, 2012, **116**, 19724-19728.
67. J. M. García, H. W. Horn and J. E. Rice, *J. Phys. Chem. Lett.*, 2015, **6**, 1795-1799.
68. D. Sharon, V. Etacheri, A. Garsuch, M. Afri, A. A. Frimer and D. Aurbach, *J. Phys. Chem. Lett.*, 2012, **4**, 127-131.
69. L. A. Huff, J. L. Rapp, L. Zhu and A. A. Gewirth, *J. Power Sources*, 2013, **235**, 87-94.
70. V. S. Bryantsev, *Chem. Phys. Lett.*, 2013, **558**, 42-47.
71. L. Teodoro and C. Alessandro, *New J. Phys.*, 2013, **15**, 095009.
72. Q. Zhao, Y. Zhang, G. Sun, L. Cong, L. Sun, H. Xie and J. Liu, *ACS Appl. Mater. Interfaces*, 2018, **10**, 31, 26312-26319.
73. S. Lin, H. Hua, Z. Li and J. Zhao, *ACS Appl. Mater. Interfaces*, 2020, **12**, 30, 33710-33718.
74. B. D. Adams, R. Black, Z. Williams, R. Fernandes, M. Cuisinier, E. J. Berg, P. Novak, G. K. Murphy and L. F. Nazar, *Adv. Energy Mater.*, 2015, **5**, 1400867.
75. Z. Huang, H. Zeng, M. Xie, X. Lin, Z. Huang, Y. Shen and Y. Huang, *Angew.*, 2019, **58**, 2345-2349.
76. D. Xu, Z. Wang, J. Xu, L. Zhang and X. Zhang, *Chem. Commun.*, 2012, **48**, 6948-6950.
77. M. A. Schroeder, N. Kumar, A. J. Pearse, C. Liu, S. B. Lee, G. W. Rubloff, K. Leung and M. Noked, *ACS Appl. Mater. Interfaces*, 2015, **7**, 11402-11411.
78. N. Mozhzhukhina, L. P. Méndez De Leo and E. J. Calvo, *J. Phys. Chem. C*, 2013, **117**, 18375-18380.
79. R. Younesi, P. Norby and T. Vegge, *ECS Electrochem. Lett.*, 2014, **3**, A15-A18.

80. D. Sharon, M. Afri, M. Noked, A. Garsuch, A. A. Frimer and D. Aurbach, *J. Phys. Chem. Lett.*, 2013, **4**, 3115-3119.
81. Z. Peng, S. A. Freunberger, Y. Chen and P. G. Bruce, *Science*, 2012, **337**, 563-566.
82. M. J. Trahan, S. Mukerjee, E. J. Plichta, M. A. Hendrickson and K. M. Abraham, *J. Electrochem. Soc.*, 2013, **160**, A259-A267.
83. D. Xu, Z.-l. Wang, J.-j. Xu, L.-l. Zhang, L.-m. Wang and X.-b. Zhang, *Chem. Commun.*, 2012, **48**, 11674-11676.
84. F. Bardé, Y. Chen, L. Johnson, S. Schaltin, J. Fransaer and P. G. Bruce, *J. Phys. Chem. C*, 2014, **118**, 18892-18898.
85. V. S. Bryantsev, V. Giordani, W. Walker, M. Blanco, S. Zecevic, K. Sasaki, J. Uddin, D. Addison and G. V. Chase, *J. Phys. Chem. A*, 2011, **115**, 12399-12409.
86. Y. Chen, S. A. Freunberger, Z. Peng, F. Barde and P. G. Bruce, *J. Am. Chem. Soc.*, 2012, **134**, 7952-7957.
87. V. S. Bryantsev, V. Giordani, W. Walker, J. Uddin, I. Lee, A. C. T. van Duin, G. V. Chase and D. Addison, *J. Phys. Chem. C*, 2013, **117**, 11977-11988.
88. R. Liu, Y. Lei, W. Yu, H. Wang, L. Qin, D. Han, W. Yang, D. Zhou, Y. He, D. Zhai, B. Li and F. Kang, *ACS Energy Lett.*, 2017, **2**, 313-318.
89. D. Sharon, P. Sharon, D. Hirshberg, M. Salama, M. Afri, L. J. W. Shimon, W.-J. Kwak, Y.-K. Sun, A. A. Frimer and D. Aurbach, *J. Am. Chem. Soc.*, 2017, **139**, 11690.
90. F. De Giorgio, F. Soavi and M. Mastragostino, *Electrochem. Commun.*, 2011, **13**, 1090-1093.
91. C. J. Allen, J. Hwang, R. Kautz, S. Mukerjee, E. J. Plichta, M. A. Hendrickson and K. M. Abraham, *J. Phys. Chem. C*, 2012, **116**, 20755-20764.
92. T. Kuboki, T. Okuyama, T. Ohsaki and N. Takami, *J. Power Sources*, 2005, **146**, 766-769.
93. L. Cecchetto, M. Salomon, B. Scrosati and F. Croce, *J. Power Sources*, 2012, **213**, 233-238.
94. S. Monaco, A. M. Arangio, F. Soavi, M. Mastragostino, E. Paillard and S. Passerini, *Electrochim. Acta*, 2012, **83**, 94-104.
95. K. Cai, W. Pu, Y. Gao, J. Hou, C. Deng, C. Wang and Z. Mao, *Int. J. Hydrog. Energy*, 2013, **38**, 11023-11027.
96. S. Das, J. Højberg, K. B. Knudsen, R. Younesi, P. Johansson, P. Norby and T. Vegge, *J. Phys. Chem. C*, 2015, **119**, 18084-18090.
97. H. M. Kwon, M. L. Thomas, R. Tatara, Y. Oda, Y. Kobayashi, A. Nakanishi, K. Ueno, K. Dokko and M. Watanabe, *ACS Appl. Mater. Interfaces*, 2017, **9**, 6014-6021.
98. E. Knipping, C. Aucher, G. Guirado and L. Aubouy, *New J. Chem.*, 2018, **42**, 4693-4699.
99. A. Khetan, H. Pitsch and V. Viswanathan, *J. Phys. Chem. Lett.*, 2014, **5**, 8, 1318-1323.

100. A. Khetan, A. Luntz and V. Viswanathan, *J. Phys. Chem. Lett.*, 2015, **6**, 1254-1259.
101. M. M. Ottakam Thotiyl, S. A. Freunberger, Z. Peng and P. G. Bruce, *J. Am. Chem. Soc.*, 2013, **135**, 494-500.
102. B. D. McCloskey, A. Speidel, R. Scheffler, D. C. Miller, V. Viswanathan, J. S. Hummelshøj, J. K. Nørskov and A. C. Luntz, *J. Phys. Chem. Lett.*, 2012, **3**, 997-1001.
103. M. Leskes, N. E. Drewett, L. J. Hardwick, P. G. Bruce, G. R. Goward and C. P. Grey, *Angew.*, 2012, **51**, 8560-8563.
104. M. Leskes, A. J. Moore, G. R. Goward and C. P. Grey, *J. Phys. Chem. C*, 2013, **117**, 26909-26939.
105. D. M. Itkis, D. A. Semenenko, E. Y. Kataev, A. I. Belova, V. S. Neudachina, A. P. Sirotina, M. Havecker, D. Teschner, A. Knop-Gericke, P. Dudin, A. Barinov, E. A. Goodilin, Y. Shao-Horn and L. V. Yashina, *Nano Lett.*, 2013, **13**, 4697-4701.
106. J. Xiao, D. Wang, W. Xu, D. Wang, R. E. Williford, J. Liu and J.-G. Zhang, *J. Electrochem. Soc.*, 2010, **157**, A487-A492.
107. S. B. Ma, D. J. Lee, V. Roev, D. Im and S.-G. Doo, *J. Power Sources*, 2013, **244**, 494-498.
108. J. B. Park, J. Lee, C. S. Yoon and Y. K. Sun, *ACS Appl. Mater. Interfaces*, 2013, **5**, 13426-13431.
109. E. Yoo and H. Zhou, *ChemSusChem*, 2016, **9**, 1-7.
110. B. Sun, S. Chen, H. Liu and G. Wang, *Adv. Funct. Mater.*, 2015, **25**, 4436-4444.
111. D. Su, S. Dou and G. Wang, *NPG Asia Materials*, 2015, **7**, e155.
112. M. M. Ottakam Thotiyl, S. A. Freunberger, Z. Peng, Y. Chen, Z. Liu and P. G. Bruce, *Nat. Mater.*, 2013, **12**, 1050-1056.
113. A. C. Luntz and B. D. McCloskey, *Chem. Rev.*, 2014, **114**, 11721-11750.
114. D. Kundu, R. Black, B. Adams, K. Harrison, K. Zavadil and L. F. Nazar, *J. Phys. Chem. Lett.*, 2015, **6**, 2252-2258.
115. W. J. Kwak, K. C. Lau, C. D. Shin, K. Amine, L. Curtiss and Y. K. Sun, *ACS Nano*, 2015, **9**, 4129-4137.
116. X. Wang, S. Cai, D. Zhu and Y. Chen, *RSC Adv.*, 2015, **5**, 88485-88491.
117. L. J. Wang, J. Zhang, X. Zhao, L. L. Xu, Z. Y. Lyu, M. Lai and W. Chen, *RSC Adv.*, 2015, **5**, 73451-73456.
118. J. Xie, X. Yao, Q. Cheng, I. P. Madden, P. Dornath, C. C. Chang, W. Fan and D. Wang, *Angew.*, 2015, **54**, 4299-4303.
119. K. Liao, T. Zhang, Y. Wang, F. Li, Z. Jian, H. Yu and H. Zhou, *ChemSusChem*, 2015, **8**, 1429-1434.
120. M. A. Schroeder, A. J. Pearse, A. C. Kozen, X. Chen, K. Gregorczyk, X. Han, A. Cao, L. Hu, S. B. Lee, G. W. Rubloff and M. Noked, *Chem. Mater.*, 2015, **27**, 5305-5313.

121. F. Li, D. M. Tang, Y. Chen, D. Golberg, H. Kitaura, T. Zhang, A. Yamada and H. Zhou, *Nano Lett.*, 2013, **13**, 4702-4707.
122. F. Li, D. M. Tang, Z. Jian, D. Liu, D. Golberg, A. Yamada and H. Zhou, *Adv. Mater.*, 2014, **26**, 4659-4664.
123. F. Li, D.-M. Tang, T. Zhang, K. Liao, P. He, D. Golberg, A. Yamada and H. Zhou, *Adv. Energy Mater.*, 2015, **5**, 13, 1500294.
124. D. Oh, K. Virwani, L. Tadesse, M. Jurich, N. Aetukuri, L. E. Thompson, H.-C. Kim and D. S. Bethune, *J. Phys. Chem. C*, 2017, **121**, 1404-1411.
125. S. Ma, Y. Wu, J. Wang, Y. Zhang, Y. Zhang, X. Yan, Y. Wei, P. Liu, J. Wang, K. Jiang, S. Fan, Y. Xu and Z. Peng, *Nano Lett.*, 2015, **15**, 8084-8090.
126. G. Zhao, Z. Xu and K. Sun, *J. Mater. Chem. A*, 2013, **1**, 12862.
127. D. Wittmaier, N. A. Cañas, I. Biswas and K. A. Friedrich, *Adv. Energy Mater.*, 2015, **5**, 19, 1500763.
128. X. Yao, Q. Cheng, J. Xie, Q. Dong and D. Wang, *ACS Appl. Mater. Interfaces*, 2015, **7**, 21948-21955.
129. C. Shang, S. Dong, P. Hu, J. Guan, D. Xiao, X. Chen, L. Zhang, L. Gu, G. Cui and L. Chen, *Sci. Rep.*, 2015, **5**, 8335.
130. B. Wu, H. Zhang, W. Zhou, M. Wang, X. Li and H. Zhang, *ACS Appl. Mater. Interfaces*, 2015, **7**, 23182-23189.
131. C. Shang, X. Zhang, L. Shui, Z. Chen, H. Liao, M. Li, X. Wang and G. Zhou, *Appl. Surf. Sci.*, 2018, **457**, 804-808.
132. D. Kundu, R. Black, E. J. Berg and L. F. Nazar, *Energy Environ. Sci.*, 2015, **8**, 1292-1298.
133. K. P. Yao, Y. C. Lu, C. V. Amanchukwu, D. G. Kwabi, M. Risch, J. Zhou, A. Grimaud, P. T. Hammond, F. Barde and Y. Shao-Horn, *Phys. Chem. Chem. Phys.*, 2014, **16**, 2297-2304.
134. Z. Wang, Y. You, J. Yuan, Y. X. Yin, Y. T. Li, S. Xin and D. Zhang, *ACS Appl. Mater. Interfaces*, 2016, **8**, 6520-6528.
135. W. Yin, Y. Shen, F. Zou, X. Hu, B. Chi and Y. Huang, *ACS Appl. Mater. Interfaces*, 2015, **7**, 4947-4954.
136. J. K. Papp, J. D. Forster, C. M. Burke, H. W. Kim, A. C. Luntz, R. M. Shelby, J. J. Urban and B. D. McCloskey, *J. Phys. Chem. Lett.*, 2017, **8**, 1169-1174.
137. E. Nasybulin, W. Xu, M. H. Engelhard, Z. Nie, X. S. Li and J.-G. Zhang, *J. Power Sources*, 2013, **243**, 899-907.
138. R. Black, S. H. Oh, J. H. Lee, T. Yim, B. Adams and L. F. Nazar, *J. Am. Chem. Soc.*, 2012, **134**, 2902-2905.
139. C. Luo, J. Li, S. Tong, S. He, J. Li, X. Yang, X. Li, Y. Meng and M. Wu, *Chem. Commun.*, 2018, **54**, 2858-2861.
140. Q. C. Zhu, F. H. Du, S. M. Xu, Z. K. Wang, K. X. Wang and J. S. Chen, *ACS Appl. Mater. Interfaces*, 2016, **8**, 3868-3873.
141. S. Tong, M. Zheng, Y. Lu, Z. Lin, X. Zhang, P. He and H. Zhou, *Chem. Commun.*, 2015, **51**, 7302-7304.

142. S. Liu, Z. Wang, C. Yu, Z. Zhao, X. Fan, Z. Ling and J. Qiu, *J. Mater. Chem. A*, 2013, **1**, 12033.
143. X. Lin, X. Lu, T. Huang, Z. Liu and A. Yu, *J. Power Sources*, 2013, **242**, 855-859.
144. P. Du, J. Lu, K. C. Lau, X. Luo, J. Bareno, X. Zhang, Y. Ren, Z. Zhang, L. A. Curtiss, Y.-K. Sun and K. Amine, *Phys. Chem. Chem. Phys.*, 2013, **15**, 5572-5581.
145. D. Chalasani and B. L. Lucht, *ECS Electrochemistry Letters*, 2012, **1**, A38-A42.
146. E. Nasybulin, W. Xu, M. H. Engelhard, Z. Nie, S. D. Burton, L. Cosimbescu, M. E. Gross and J.-G. Zhang, *J. Phys. Chem. C*, 2013, **117**, 2635-2645.
147. Y. Chen, S. A. Freunberger, Z. Peng, O. Fontaine and P. G. Bruce, *Nat. Chem.*, 2013, **5**, 489–494.
148. G. V. Chase, S. Zecevic, T. Walker Wesley, J. Uddin, K. A. Sasaki, P. Giordani Vincent, V. Bryantsev, M. Blanco, D. D. Addison, 2012, *Soluble Oxygen Evolving Catalysts for Rechargable Metal-Air Batteries*, US20120028137A1.
149. P. P. Bawol, P. Reinsberg, C. J. Bondue, A. A. Abd-El-Latif, P. Konigshoven and H. Baltruschat, *Phys. Chem. Chem. Phys.*, 2018, **20**, 21447-21456.
150. B. J. Bergner, A. Schurmann, K. Peppler, A. Garsuch and J. Janek, *J. Am. Chem. Soc.*, 2014, **136**, 15054-15064.
151. B. J. Bergner, C. Hofmann, A. Schurmann, D. Schroder, K. Peppler, P. R. Schreiner and J. Janek, *Phys. Chem. Chem. Phys.*, 2015, **17**, 31769-31779.
152. Y. Hase, J. Seki, T. Shiga, F. Mizuno, H. Nishikoori, H. Iba and K. Takechi, *Chem. Commun.*, 2016, **52**, 12151-12154.
153. Y. Chen, X. Gao, L. R. Johnson and P. G. Bruce, *Nat. Commun.*, 2018, **9**, 767.
154. D. Kundu, R. Black, B. Adams and L. F. Nazar, *ACS Cent. Sci.*, 2015, **1**, 510-515.
155. Z. Liang, Q. Zou, J. Xie and Y.-C. Lu, *Energy Environ. Sci.*, 2020, **13**, 2870-2877.
156. N. Feng, X. Mu, X. Zhang, P. He and H. Zhou, *ACS Appl. Mater. Interfaces*, 2017, **9**, 3733-3739.
157. N. Feng, P. He and H. Zhou, *ChemSusChem*, 2015, **8**, 600-602.
158. K. P. C. Yao, J. T. Frith, S. Y. Sayed, F. Bardé, J. R. Owen, Y. Shao-Horn and N. Garcia-Araez, *J. Phys. Chem. C*, 2016, **120**, 16290-16297.
159. C. Zhu, Y. Wang, L. Shuai, Y. Tang, M. Qiu, J. Xie, J. Liu, W. Wen, H. Chen, S. Nan, M. Dou and Q. He, *Chin. Chem. Lett.*, 2019, **31**, 7, 1997-2002.
160. W. H. Ryu, F. S. Gittleson, J. M. Thomsen, J. Li, M. J. Schwab, G. W. Brudvig and A. D. Taylor, *Nat. Commun.*, 2016, **7**, 12925.
161. H. D. Lim, H. Song, J. Kim, H. Gwon, Y. Bae, K. Y. Park, J. Hong, H. Kim, T. Kim, Y. H. Kim, X. Lepro, R. Ovalle-Robles, R. H. Baughman and K. Kang, *Angew.*, 2014, **53**, 3926-3931.
162. I. Landa-Medrano, M. Olivares-Marín, R. Pinedo, I. Ruiz de Larramendi, T. Rojo and D. Tonti, *Electrochem. Commun.*, 2015, **59**, 24-27.
163. Y. Li, S. Dong, B. Chen, C. Lu, K. Liu, Z. Zhang, H. Du, X. Wang, X. Chen, X. Zhou and G. Cui, *J. Phys. Chem. Lett.*, 2017, **8**, 4218-4225.

164. W.-J. Kwak, D. Hirshberg, D. Sharon, H.-J. Shin, M. Afri, J.-B. Park, A. Garsuch, F. F. Chesneau, A. A. Frimer, D. Aurbach and Y.-K. Sun, *J. Mater. Chem. A*, 2015, **3**, 8855-8864.
165. Z. Guo, C. Li, J. Liu, Y. Wang and Y. Xia, *Angew.*, 2017, **56**, 7505-7509.
166. W.-J. Kwak, S.-J. Park, H.-G. Jung and Y.-K. Sun, *Adv. Energy Mater.*, 2017, **8**, 1702258.
167. H.-D. Lim, B. Lee, Y. Zheng, J. Hong, J. Kim, H. Gwon, Y. Ko, M. Lee, K. Cho and K. Kang, *Nat. Energy*, 2016, **1**, 16066.
168. H. Kim, W.-J. Kwak, H.-G. Jung and Y.-K. Sun, *J. Mater. Chem. A*, 2020, **8**, 5622-5628.
169. D. Cao, X. Liu, X. Yuan, F. Yu and Y. Chen, *ACS Appl. Mater. Interfaces*, 2021, **13**, 33, 39341-39346.
170. Y. Ko, H. Park, B. Lee, Y. Bae, S. K. Park and K. Kang, *J. Mater. Chem. A*, 2019, **7**, 6491-6498.
171. M. J. Lacey, J. T. Frith and J. R. Owen, *Electrochem. Commun.*, 2013, **26**, 74-76.
172. X. Gao, Y. Chen, L. Johnson and P. G. Bruce, *Nat. Mater.*, 2016, **15**, 882–888.
173. Z. Z. Shen, S. Y. Lang, Y. Shi, J. M. Ma, R. Wen and L. J. Wan, *J. Am. Chem. Soc.*, 2019, **141**, 6900-6905.
174. X. Liu, P. Zhang, L. Liu, J. Feng, X. He, X. Song, Q. Han, H. Wang, Z. Peng and Y. Zhao, *ACS Appl. Mater. Interfaces*, 2020, **12**, 10607-10615.
175. P. Zhang, L. Liu, X. He, X. Liu, H. Wang, J. He and Y. Zhao, *J. Am. Chem. Soc.*, 2019, **141**, 6263-6270.
176. J. Liu, S. Renault, D. Brandell, T. Gustafsson, K. Edström and J. Zhu, *ChemSusChem*, 2015, **8**, 2198-2203.
177. Y. G. Zhu, C. Jia, J. Yang, F. Pan, Q. Huang and Q. Wang, *Chem. Commun.*, 2015, **51**, 9451-9454.
178. X. Gao, Y. Chen, L. R. Johnson, Z. P. Jovanov and P. G. Bruce, *Nat. Energy*, 2017, **2**, 17118.
179. J. P. Vivek, T. Homewood and N. Garcia-Araez, *J. Phys. Chem. C*, 2019, **123**, 20241-20250.
180. W. Yu, W. Yang, R. Liu, L. Qin, Y. Lei, L. Liu, D. Zhai, B. Li and F. Kang, *Electrochem. Commun.*, 2017, **79**, 68-72.
181. X. Mu, Y. Liu, X. Zhang, H. Wei, P. He and H. Zhou, *Batteries & Supercaps*, 2020, **3**, 336-340.
182. X.-G. Wang, Z. Zhang, Q. Zhang, C. Wang, X. Zhang, Z. Xie and Z. Zhou, *J. Mater. Chem. A*, 2019, **7**, 14239-14243.
183. C. Zheng, W. Ding and C. Wang, *J. Mater. Chem. A*, 2019, **7**, 6180-6186.
184. S. Sakamoto, H. Minowa, M. Nohara, M. Iwata, M. Hayashi and T. Komatsu, *Electrochemistry*, 2019, **87**, 365-369.
185. H. Liu, M. Liu, L. Yang, Y. Song, X. Wang, K. Yang and F. Pan, *Chem. Commun.*, 2019, **55**, 6567-6570.

186. J. T. Frith, I. Landa-Medrano, I. Ruiz de Larramendi, T. Rojo, J. R. Owen and N. Garcia-Araez, *Chem. Commun.*, 2017, **53**, 12008-12011.
187. S. Ha, Y. Kim, D. Koo, K.-H. Ha, Y. W. Park, D.-M. Kim, S. Son, T. Yim and K. T. Lee, *J. Mater. Chem. A*, 2017, **5**, 10609-10621.
188. T. Zhang, K. Liao, P. He and H. Zhou, *Energy Environ. Sci.*, 2016, **9**, 1024-1030.
189. J. Liu, T. Wu, S. Zhang, D. Li, Y. Wang, H. Xie, J. Yang and G. Sun, *J. Power Sources*, 2019, **439**, 227095.
190. C. K. Lee and Y. J. Park, *ACS Appl. Mater. Interfaces*, 2016, **8**, 8561-8567.
191. Rosy, S. Akabayov, M. Leskes and M. Noked, *ACS Appl. Mater. Interfaces*, 2018, **10**, 29622-29629.
192. Z.-F. Chen, X. Lin, H. Xia, Y. Hong, X. Liu, S. Cai, J.-N. Duan, J. Yang, Z. Zhou, J.-K. Chang, M. Zheng and Q. Dong, *J. Mater. Chem. A*, 2019, **7**, 14260-14270.
193. S. H. Lee, J.-B. Park, H.-S. Lim and Y.-K. Sun, *Adv. Energy Mater.*, 2017, **7**, 18, 1602417.
194. L. Shi, Z. Li, Y. Li, G. Wang, M. Wu and Z. Wen, *ACS Appl. Mater. Interfaces*, 2021, **13**, 30766-30775.
195. D. Li, Z. Kang, H. Sun, Y. Wang, H. Xie, J. Liu and J. Zhu, *Chem. Eng. J.*, 2022, **428**, 131105.
196. X. Gao, Z. P. Jovanov, Y. Chen, L. R. Johnson and P. G. Bruce, *Angew.*, 2017, **56**, 6539-6543.
197. C. Xia, R. Black, R. Fernandes, B. Adams and L. F. Nazar, *Nat. Chem.*, 2015, **7**, 496-501.
198. J. Hassoun, F. Croce, M. Armand and B. Scrosati, *Angew.*, 2011, **50**, 2999-3002.
199. B. D. McCloskey, D. S. Bethune, R. M. Shelby, T. Mori, R. Scheffler, A. Speidel, M. Sherwood and A. C. Luntz, *J. Phys. Chem. Lett.*, 2012, **3**, 3043-3047.
200. J. Wandt, P. Jakes, J. Granwehr, H. A. Gasteiger and R.-A. Eichel, *Angew.*, 2016, **55**, 1-5.
201. N. Mahne, B. Schafzahl, C. Leypold, M. Leypold, S. Grumm, A. Leitgeb, Gernot A. Strohmeier, M. Wilkening, O. Fontaine, D. Kramer, C. Slugovc, Sergey M. Borisov and Stefan A. Freunberger, *Nat. Energy*, 2017, **2**, 17036.
202. D. Córdoba, H. B. Rodríguez and E. J. Calvo, *ChemistrySelect*, 2019, **4**, 12304-12307.
203. G. Houchins, V. Pande and V. Viswanathan, *ACS Energy Lett.*, 2020, **5**, 6, 1893-1899.
204. A. Samojlov, D. Schuster, J. Kahr and S. A. Freunberger, *Electrochim. Acta*, 2020, **362**, 137175.
205. L. Schafzahl, N. Mahne, B. Schafzahl, M. Wilkening, C. Slugovc, S. M. Borisov and S. A. Freunberger, *Angew.*, 2017, **56**, 15728-15732.
206. Y. K. Petit, E. Mourad, C. Prehal, C. Leypold, A. Windischbacher, D. Mijailovic, C. Slugovc, S. M. Borisov, E. Zojer, S. Brutti, O. Fontaine and S. A. Freunberger, *Nat. Chem.*, 2021, **13**, 465-471.

207. Y. K. Petit, C. Leypold, N. Mahne, E. Mourad, L. Schafzahl, C. Slugovc, S. M. Borisov and S. A. Freunberger, *Angew.*, 2019, **58**, 6535-6539.
208. W.-J. Kwak, S. A. Freunberger, H. Kim, J. Park, T. T. Nguyen, H.-G. Jung, H. R. Byon and Y.-K. Sun, *ACS Catal.*, 2019, **9**, 9914-9922.
209. P. L. Arrechea, K. B. Knudsen, J. W. Mullinax, J. B. Haskins, C. W. Bauschlicher, J. W. Lawson and B. D. McCloskey, *ACS Applied Energy Materials*, 2020, **3**, 8812-8821.
210. W. J. Kwak, H. Kim, Y. K. Petit, C. Leypold, T. T. Nguyen, N. Mahne, P. Redfern, L. A. Curtiss, H. G. Jung, S. M. Borisov, S. A. Freunberger and Y. K. Sun, *Nat. Commun.*, 2019, **10**, 1380.
211. W.-J. Kwak, J. Park, H. Kim, J. M. Joo, D. Aurbach, H. R. Byon and Y.-K. Sun, *ACS Energy Lett.*, 2020, **5**, 6, 2122-2129.
212. A. Sagadevan, K. C. Hwang and M. D. Su, *Nat. Commun.*, 2017, **8**, 1812.
213. X. Ren, K. C. Lau, M. Yu, X. Bi, E. Kreidler, L. A. Curtiss and Y. Wu, *ACS Appl. Mater. Interfaces*, 2014, **6**, 19299-19307.
214. W. D. McCulloch, X. Ren, M. Yu, Z. Huang and Y. Wu, *ACS Appl. Mater. Interfaces*, 2015, **7**, 26158-26166.
215. W. Yu, K. C. Lau, Y. Lei, R. Liu, L. Qin, W. Yang, B. Li, L. A. Curtiss, D. Zhai and F. Kang, *ACS Appl. Mater. Interfaces*, 2017, **9**, 31871-31878.
216. X. Ren, M. He, N. Xiao, W. D. McCulloch and Y. Wu, *Adv. Energy Mater.*, 2017, **7**, 1601080.
217. N. Xiao, J. Zheng, G. Gourdin, L. Schkeryantz and Y. Wu, *ACS Appl. Mater. Interfaces*, 2019, **11**, 16571-16577.
218. N. Xiao, G. Gourdin and Y. Wu, *Angew.*, 2018, **57**, 10864-10867.

Chapter 2

Experimental Techniques

Contents

This Chapter describes the theories behind the techniques used within this work. Details regarding specific experimental parameters may be found in the Experimental Sections of the relevant Results Chapters.

2.1 Electrochemical Techniques

2.1.1 Underlying Theory of Fundamental Electrochemistry

2.1.1.1 Reaction Kinetics at the Electrode Interface

All of the electrochemical processes in this work can be described as one or more simple one-electron transfer reactions:[1, 2]

$$O + ne^- \rightleftharpoons R \qquad \textbf{Eq. 2.1}$$

where O is a species that is reduced (that is to say, gains electrons) to form R. The standard Gibbs free energy, ΔG°, of an electrochemical cell is given by the equation:

$$\Delta G^\circ = -nFE^\circ_{cell} \qquad \textbf{Eq. 2.2}$$

where n is the number of electrons transferred, F is the Faraday Constant and E°_{cell} is the standard cell potential[1] for the redox couple O/R (although in practice the formal potential under a different set of conditions is usually measured). Given that ΔG° can also be expressed as a function of the equilibrium constant, K:

$$\Delta G^\circ = RT \ln K \qquad \textbf{Eq. 2.3}$$

and that the change in Gibbs free energy at non-standard conditions, ΔG, is given by **Equation 2.4**:

$$\Delta G = \Delta G^\circ + RT \ln K \qquad \textbf{Eq. 2.4}$$

then substitution of **Equation 2.2** into **Equation 2.4** will yield the E_{cell} at non-standard conditions, with the equation named the Nernst Equation:

$$E_{cell} = E^\circ_{cell} - \frac{RT}{nF} \ln K \qquad \textbf{Eq. 2.5}$$

[1] Standard conditions are 298.15 K, 10^5 Pa and species' activities of 1.

The overall current density for a reversible electron transfer reaction, j, is the sum of the anodic, j_a, and cathodic, j_c, current densities. At equilibrium there is no net passing of current, with the concentrations of O and R remaining unchanged as the oxidation of R and reduction of O will be occurring at the same rate. This is given by **Equation 2.6:**

$$j = j_a + j_c = 0 \qquad \textbf{Eq. 2.6}$$

With j_a positive and j_c negative, by convention. The exchange current density, j_0, is given by:

$$j_a = -j_c = j_0 \qquad \textbf{Eq. 2.7}$$

and is a measure of the electron transfer activity at equilibrium, according to the equation:

$$j_0 = nFk_s(c_O)^{\alpha_a}(c_R)^{\alpha_c} \qquad \textbf{Eq. 2.8}$$

Where c_O and c_R are the concentrations of O and R, respectively, k_s is the standard rate constant for both oxidation and reduction at the equilibrium potential, and α_a and α_c are the anodic and cathodic transfer coefficients, respectively. For a simple electron transfer reaction, both α_a and α_c have values which are close to 0.5, such that:

$$\alpha_a + \alpha_c = 1 \qquad \textbf{Eq. 2.9}$$

and are assumed to be constant in most calculations. However, the transfer coefficients do have some potential dependence, as demonstrated by **Equation 2.10**:

$$\alpha = \frac{1}{2} + \frac{nF\Delta\eta}{16°\Delta G^{\ddagger}} \qquad \textbf{Eq. 2.10}$$

where $^{\circ}\Delta G^{\ddagger}$ is the activation energy for reduction and oxidation at the equilibrium potential, E_e, and η is the overpotential, given by:

$$\eta = E - E_e \qquad \textbf{Eq. 2.11}$$

The rate of oxidation and reduction for the reaction in **Equation 2.1** would be expected to obey the following rate laws at the surface of an electrode:

$$Rate_O = k_a c_R \qquad \textbf{Eq. 2.12}$$

$$Rate_R = k_c c_O \qquad \textbf{Eq. 2.13}$$

However, experimentally it has been found that the rate constants follow the general form:

$$k_a = k_a^0 exp \frac{\alpha_a nFE}{RT} \qquad \textbf{Eq. 2.14}$$

$$k_c = k_c^0 exp - \frac{\alpha_c nFE}{RT} \qquad \textbf{Eq. 2.15}$$

Given the relationship described in **Equation 2.6**, and taking into account the sign convention assigned to each current density, the net current density at a given potential can be expressed as:

$$j = nFk_a^0 c_R exp \frac{\alpha_a nFE}{RT} - nFk_c^0 c_O exp - \frac{\alpha_c nFE}{RT} \qquad \textbf{Eq. 2.16}$$

Combining **Equations 2.11** and **2.16** and setting the conditions to those at equilibrium, where $\eta = 0$, results in **Equation 2.17**:

$$j_0 = nFk_a^0 c_R exp \frac{\alpha_a nFE_e}{RT} = -nFk_c^0 c_O exp - \frac{\alpha_c nFE_e}{RT} \qquad \textbf{Eq. 2.17}$$

which may be further combined with **Equation 2.11** and **2.16** to give:

$$j = j_0 \left(exp \frac{\alpha_a nF\eta}{RT} - exp - \frac{\alpha_c nF\eta}{RT} \right) \qquad \textbf{Eq. 2.18}$$

which is more commonly expressed in the form of the Butler-Volmer Equation:

$$j = j_0 \left(exp \frac{\alpha_a nF\eta}{RT} - exp - \frac{(1-\alpha_a)nF\eta}{RT} \right) \qquad \textbf{Eq. 2.19}$$

When the potential is more positive than the E_e the current density will be anodic, whereas more negative potentials lead to a cathodic current dominating. Given the opposite signs of the cathodic and anodic terms and their exponential dependence, even moderate overpotentials (where $\eta > 26$ mV) result in two limiting cases: for moderate positive overpotentials, **Equation 2.19** simplifies to:

$$j = j_0 \, exp \frac{\alpha_a nF\eta}{RT} \qquad \textbf{Eq. 2.20}$$

whilst at moderate negative overpotentials, **Equation 2.19** simplifies to:

$$j = j_0 \, exp - \frac{\alpha_c nF\eta}{RT} \qquad \textbf{Eq. 2.21}$$

When expressed in the form of their common logarithms, **Equation 2.20** and **2.21** are known as the Tafel Equations:

$$\log|j| = \log j_0 + \frac{\alpha_a nF}{2.3RT}\eta \qquad \textbf{Eq. 2.22}$$

$$\log|j| = \log j_0 - \frac{\alpha_c nF}{2.3RT}\eta \qquad \textbf{Eq. 2.23}$$

which, for reversible electron transfer reactions, yield linear plots for $\log|j|$ *vs* η.

2.1.1.2 Effect of Mass Transport

In order to sustain a given current a continuous supply of reactant and removal of product from the electrode surface must be ensured. This occurs through a process termed mass transport of which there are three forms:[1, 2]

1. Diffusion, defined as the movement of a species due to a gradient in concentration, where particles move from high concentration to low concentration until a uniform concentration is obtained. Diffusion occurs in all systems.
2. Convection, defined as the movement of a species due to external mechanical forces. This may be a deliberate process, through stirring, or natural due to random vibrations and local temperature gradients. The use of hydrodynamic techniques can be used to create a well-defined convection regime, which dominates mass transport and makes the contribution of diffusion negligible.
3. Migration, defined as the movement of charged species due to a potential field. As such, any neutral species, either reactant, product or solvent, are unaffected by this process. A high concentration of supporting electrolyte is generally used to minimise the effect of migration on electroactive species; a large excess of inert ions will carry the majority of charge through the solution, rather than the electroactive species.

In a M-O_2 cell the effects of migration are mitigated by the high concentration of supporting electrolyte, and the only convection will be that through natural processes (and so care to maintain a constant temperature is essential). Consequently, diffusion plays the greatest role in determining the flux of reactants, be it O_2, M^+ or RMs, to the cathode surface.

2.1.2 Cyclic Voltammetry

Cyclic voltammetry is an extremely powerful electrochemical tool, and more often than not the first experiment that an electrochemist will perform to gain insight into a new system. The potential of the working electrode is swept between two potential limits at a constant scan rate before the direction of scan is reversed. The current (or current density) response is recorded with changing potential, with changes in peak shape and position giving insight into the nature of the electroactive species under investigation. The reversal of the potential scan allows for identification of any stable electroactive species formed during the forward scan. **Figure 2.1** illustrates a representative cyclic voltammogram (CV), demonstrating the electrochemistry of potassium ferricyanide.

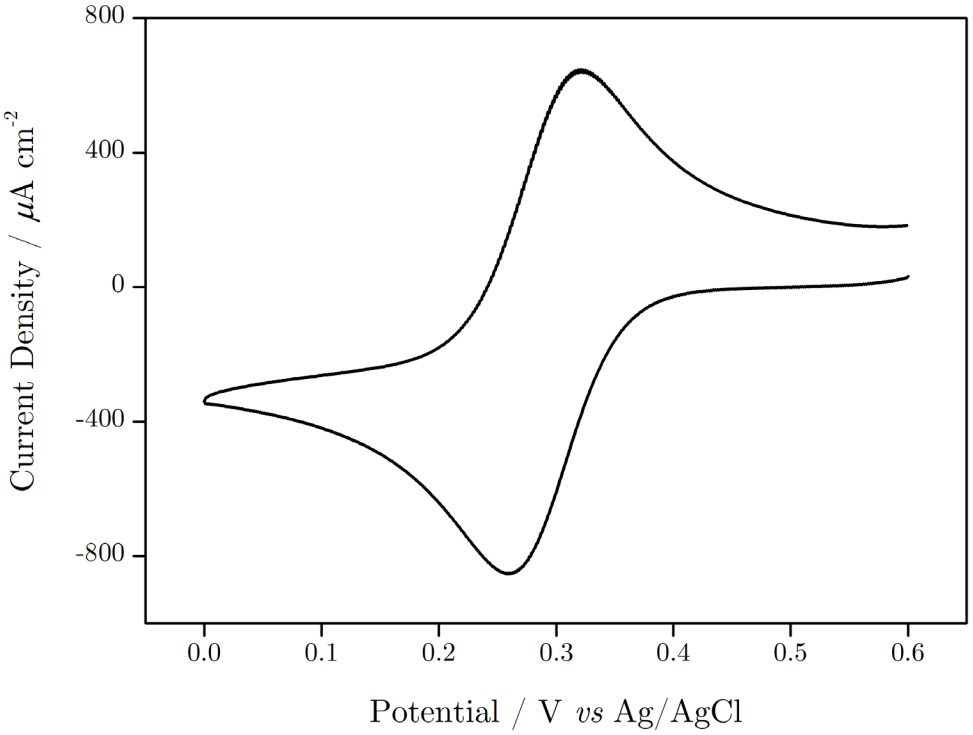

Fig. 2.1: Cyclic voltammetry of 4 mM $K_3[Fe(CN)_6]$ in 1 M $KOH_{(aq)}$, at a scan rate 100 mV s^{-1}. Reproduced from **Chapter 5**.

The peak shape of a typical CV is determined by the effect of the changing potential on the concentration of electroactive species at the electrode surface.[1, 2] The minimal current observed at distances far from the formal potential of the redox couple is due to non-faradaic processes, including double layer capacitance. With a solution that initially contains only the oxidised species, O, as the potential nears the formal potential a current begins to flow; this current is caused by the one-electron reduction:

$$O + e^- \rightarrow R \qquad \textbf{Eq. 2.24}$$

This leads to a corresponding decrease in the concentration of O at the electrode surface. As the potential is changed rapidly the concentration profile cannot reach a steady-state thickness, meaning that as the concentration of O at the electrode surface decreases, the concentration profile expands into the solution. The drop in concentration leads to an increase in the flux of O to the surface (observed as an increase in the current). When the surface concentration reaches zero a maximum current is reached, after which point the effects of depletion of the surface concentration are observed through a decrease in current.

When the potential scan direction is reversed, the concentration of O at the electrode remains zero until the potential approaches the formal potential for the couple O/R. From this point the surface concentration of O beings to increase, whilst the concentration of R decreases. The reverse peak current behaves in a similar manner to the reduction peak, eventually passing through a maximum when the surface concentration of R reaches zero.

The scan rate, ν, has an effect on the measured current, with a larger scan rate leading to a greater current. Qualitatively, this is because at higher scan rates the time to change the surface concentration is lower, and so the diffusion layer is thinner. Such dependence of the peak current density, j_p, on the scan rate is revealed in the Randles-Sevèik Equation:

$$j_p = 0.4463\left(\frac{F^3}{RT}\right)^{\frac{1}{2}} n^{\frac{3}{2}} D^{\frac{1}{2}} c\nu^{\frac{1}{2}} \qquad \textbf{Eq. 2.25}$$

With all cyclic voltammetry, the effect of double layer charging and iR (Ohmic) drop due to high resistance must be taken into account. Whilst a reversible one-electron redox couple has an ideal peak separation of 59 mV, increasing electrolyte resistance will cause this separation to increase. iR corrections may be applied to cyclic voltammetry measurements to compensate for this electrolyte resistance.

Some cyclic voltammograms in this work display sinusoidal noise at scan rates of 100 mV s^{-1} and above. This noise is attributed to an aliasing of the alternating current mains electricity against the sampling period at 100 mV s^{-1} and 200 mV s^{-1}.[3] This aliasing may be mitigated through use of a Faraday cage, however no Faraday cage was employed during the course of this work.

2.1.3 Rotating Ring Disc Electrode

A rotating ring disc electrode (RRDE) allows the study of electrode processes under a well-defined steady state convection regime, thereby removing the effects of diffusion. The RRDE consists of a polished disc electrode, commonly either gold, platinum or

glassy carbon, surrounded by a ring of electrode material, set within a sheath of insulating material of significantly larger diameter (**Figure 2.2a**). The disc and the ring are electrically isolated by a thin wall of the insulating material and may be controlled independently. The disc and the ring surfaces are flush with the surface of the sheath, and are polished to ensure both a clean electrode surface and no inadvertent ridges being present. The RRDE is rotated perpendicular to the surface of the disc, causing the electrode to act as a pump in drawing up fresh electrolyte solution to the electrode surface. Upon reaching the surface, the electrolyte is thrown outwards as the solid surface prevents its continued movement vertically. This provides a well-defined steady state mass transport regime that is dominated by convection and where the limiting current is a function of the square root of the rotation rate of the electrode, as given for a reversible electron transfer by the Levich Equation:

$$j_L = 0.62 \frac{nFD^{2/3}}{\upsilon^{1/6}} \omega^{1/2} \qquad \textbf{Eq. 2.26}$$

Where j_L is the mass transport limiting current density, D is the diffusion constant of the electroactive species, υ is the viscosity of the electrolyte and ω is the rotation rate. Given that this equation is not directly employed in this work, its derivation here has been omitted, although a full explanation may be found in other works.[1] The effect of the RRDE on the motion of the solution is demonstrated in **Figure 2.2b**.

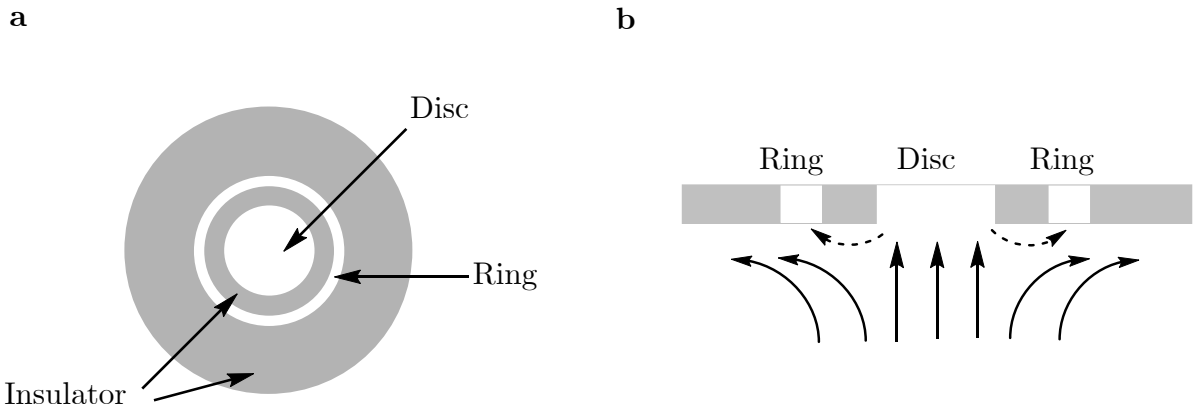

Fig. 2.2: a. Plan of a RRDE and **b.** solution flow pattern due to forced convection when RRDE is rotated.

Due to the positioning of the disc and ring electrodes and the movement of the electrolyte across the surface of the RRDE, the ring is downstream of the disc. Consequently, any species generated at the disc may be detected at the ring. The fraction of said species reaching the ring will, however, be dependent upon characteristic factors of the RRDE, such as the radius of the disc and inner and outer radii of the ring, and the stability of the electro-generated species in the electrolyte, along with the rotation rate. The fraction of a completely stable species formed at the disc that is detected at the ring is termed the collection efficiency, N, and may be calculated theoretically. However, in practice it is much simpler and more accurate, given the variable effect of polishing on electrode surface, to calculate the collection efficiency empirically using the equation:

$$N_{empirical} = \left|\left(\frac{i_{ring}}{i_{disc}}\right)\left(\frac{n_{disc}}{n_{ring}}\right)\right| \qquad \textbf{Eq. 2.27}$$

Experimental calculation of the collection efficiency also removes the issue of uncertainties in the dimensions of the machined electrode parts. To calculate the collection efficiency of an RRDE an electroactive species with stable oxidised and reduced forms is used (such as ferricyanide and ferrocyanide); the species is reduced at the disc then oxidised at the ring (or *vice versa*).

2.1.4 Scanning Electrochemical Microscopy

2.1.4.1 Microelectrode Theory

Scanning Electrochemical Microscopy (SECM) experiments use microelectrodes, defined as electrodes with a disc radii of between 0.1 and 100 μm.[1] Due to the small size of the electrodes, at steady state the main diffusional mass transport is at right angles to the edge of the disc, resulting in a hemispherical diffusion field, as illustrated in **Figure 2.3b**.[1] This contrasts with a macroelectrode, where such perimeter diffusion contribution is negligible (**Figure 2.3a**).

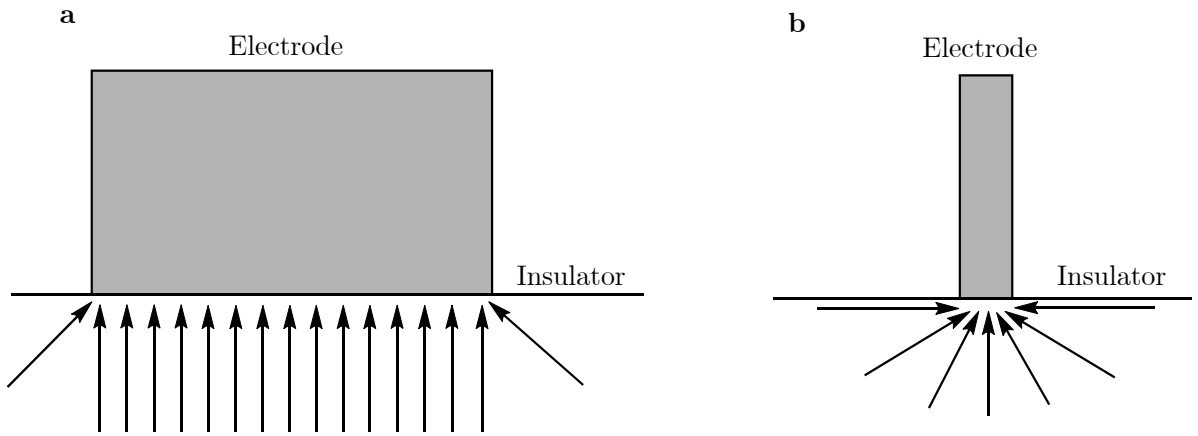

Fig. 2.3: Schematic illustrating the diffusion of an electroactive species to the surface of an **a.** macroelectrode and **b.** microelectrode.

The current density response of a microelectrode to a potential step where the reaction is diffusion controlled is given by:

$$j = \frac{nFD^{\frac{1}{2}}c}{\pi^{\frac{1}{2}}t^{\frac{1}{2}}} + \frac{4nFDc}{\pi a} \qquad \textbf{Eq. 2.28}$$

where the first term gives the current density under conditions of linear diffusion to a planar electrode and the second term is the hemispherical diffusion. For a microelectrode, the former term dominates at short times, whereas the latter dominates at steady state. This means that the limiting current at steady state, $i_{L\infty}$, is given by:

$$i_{L\infty} = 4nFDac \qquad \textbf{Eq. 2.29}$$

where c is the bulk concentration of said species and a is the radius of the microelectrode. **Figure 2.4** demonstrates the diffusion to the microelectrode surface at different times.

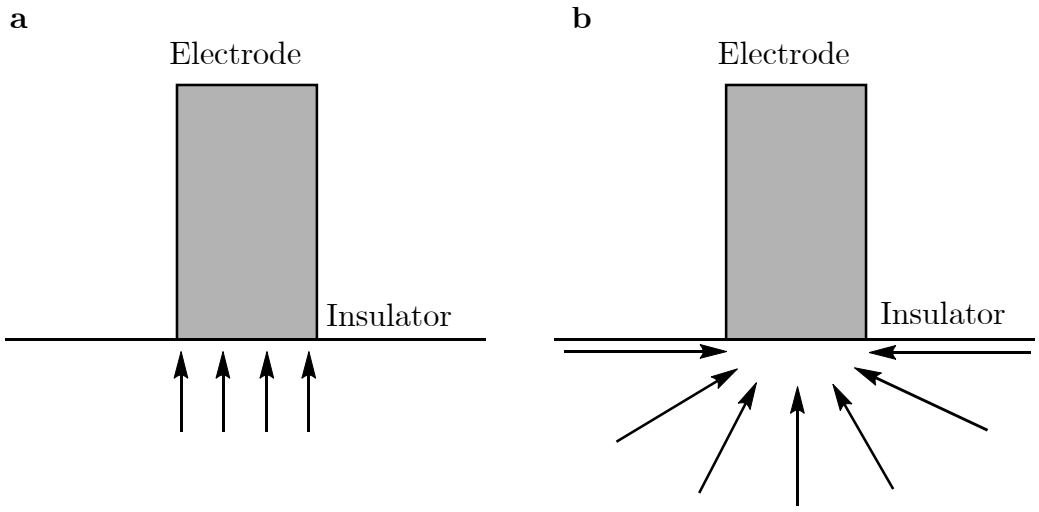

Fig. 2.4: Diffusion to a microdisc electrode at **a.** short times and **b.** at steady state.

The radius of the insulator, r_{glass}, surrounding the microelectrode has a profound effect on the measured current. It has been shown that microdisc electrodes with small, finite insulator radius to electrode radius, R_g, as given by **Equation 2.30**:

$$R_g = \frac{r_{glass}}{a} \qquad \textbf{Eq. 2.30}$$

demonstrate an enhanced diffusion limited current, as expressed by the approximated equation:[4-6]

$$i_L = 4nFDac\beta \qquad \textbf{Eq. 2.31}$$

where β is given by:[7]

$$\beta = 1 + \frac{0.23}{(R_g^3 - 0.81)^{0.36}} \qquad \textbf{Eq. 2.32}$$

β is obtained experimentally by considering the ratio between the limiting current of a microelectrode with small R_g, i_{Ls}, compared to that with a large R_g, i_{Ll}:

$$\beta = \frac{i_{Ls}}{i_{Ll}} \qquad \textbf{Eq. 2.33}$$

There are several expressions that approximate β with all giving solutions with relative errors of less than 0.3%; **Equation 2.32** was selected on the basis of being the mathematically simplest to compute.[7]

2.1.4.2 Scanning Electrochemical Microscopy Theory

A typical SECM experiment involves a three-electrode cell, with the working electrode being moved slowly towards a substrate by an electric motor. The substrate may or may not also act as an electrode; in this work the substrate was a pellet of Li_2O_2 produced using a die press (further experimental details are given in **Section 4.2.11**

on page 176). A representative schematic of a SECM cell configuration is given in **Figure 2.5**.

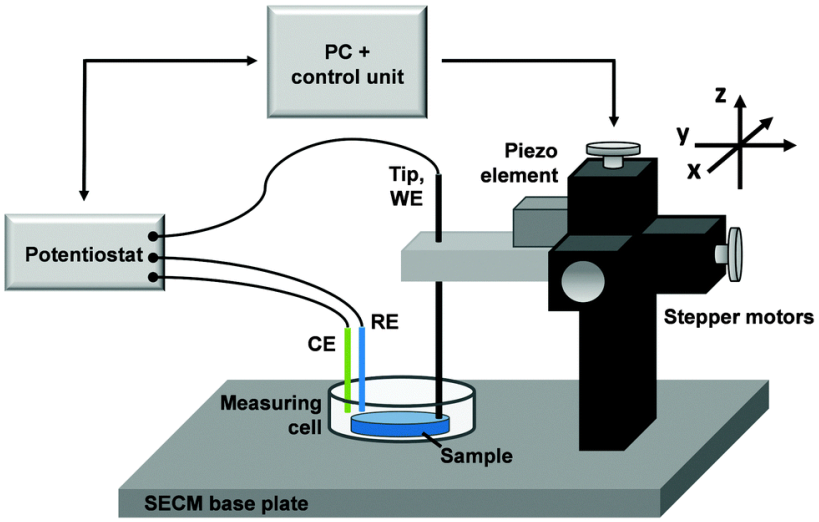

Fig. 2.5: Schematic of a SECM cell, where WE, CE and RE are the working, counter, and reference electrodes, respectively. In this work, the "sample" was a pellet of Li_2O_2. Reproduced with permission. Copyright 2015, Royal Society of Chemistry.[8]

As the tip moves closer to the substrate, the diffusion of reactant species to the surface of the working electrode is impeded, leading to a decrease in measured current, $i_{L\infty} > i$, if the substrate is an insulator. However, if the substrate is conductive and able to regenerate the reactants from the products, then an increase in current at the working electrode is observed, $i_{L\infty} < i$. This results in a feedback loop, where the measured current is dependent upon the distance, d, of the working electrode from the substrate surface. This is presented schematically in **Figure 2.6**.

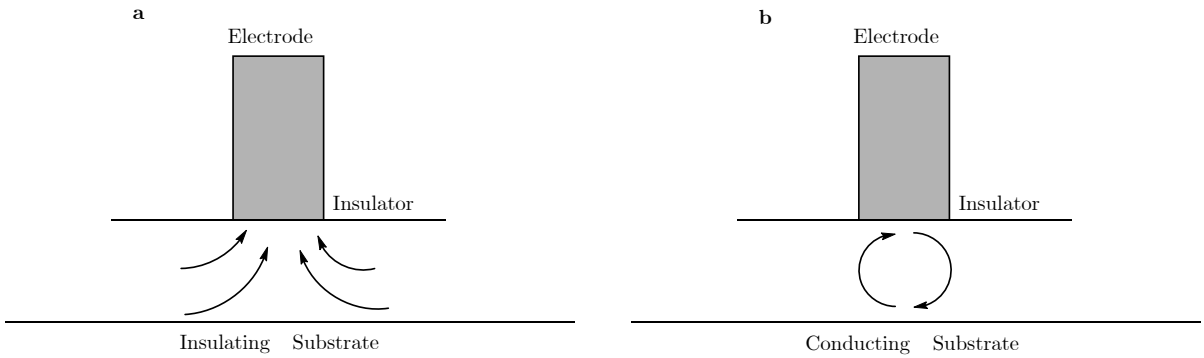

Fig. 2.6: Diffusion to a SECM electrode tip when the substrate is **a.** an insulator and **b.** a conductor.

Invariably, SECM data is reported as the tip current normalised against the limiting current at infinite distance from the substrate, Ni:

$$Ni = \frac{i}{i_{L\infty}} \qquad \textbf{Eq. 2.34}$$

as a function of a dimensionless distance, L, given by:

$$L = \frac{d}{a} \qquad \textbf{Eq. 2.35}$$

The resultant dimensionless plots are termed approach curves. The current of the feedback loops can be determined using equations developed by Lefrou, Cornut and Griveau; these equations are discussed in greater detail in **Chapter 4**.[7, 9-11] By using these equations to model the experimental current response, the apparent rate constant for the reaction of RM^+ with Li_2O_2, k_{app}, may be determined.

2.1.5 Marcus Theory

The transfer of an electron is very fast relative to molecular vibrations (10^{-15}-10^{-16} s and 10^{-13} s, respectively), such that a molecule can be considered to be stationary when electron transfer occurs.[12] The Franck-Condon principle states that for electron

transfer to occur, the reactants and the products must have the same nuclear geometry at the moment of electron transfer.[12, 13] This is demonstrated in **Figure 2.7**, where electron transfer can only take place once the thermal fluctuations bring the geometry of the reactant, O, to the coordinate where the energy parabolas of O and R intersect.

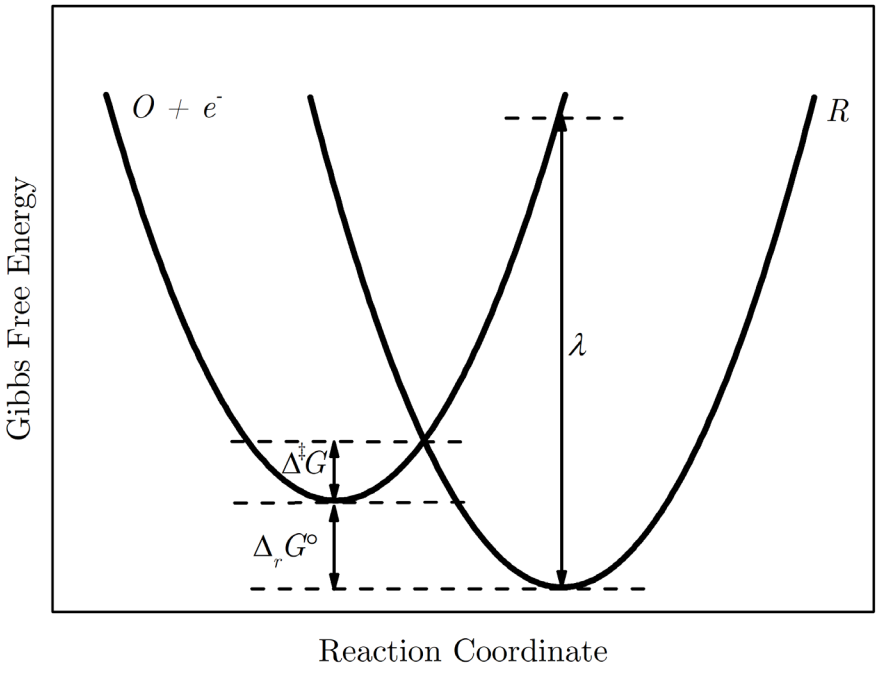

Fig. 2.7: Gibbs free energy surfaces for the electron transfer process between species O and R. The energy of the species is such that net reduction is occurring.

The rate constant for the electron transfer is therefore dependent upon the Gibbs energy of activation, $\Delta^{\ddagger}G$, according to **Equation 2.36**:

$$k = KZ \exp -\frac{\Delta^{\ddagger}G}{RT} \qquad \textbf{Eq. 2.36}$$

where K is the transmission coefficient and Z is given by:[1]

$$Z = \frac{\delta k_B T}{h} \qquad \textbf{Eq. 2.37}$$

with δ a reaction length of the order of a molecular diameter. The transmission coefficient gives the probability of an electron tunnelling event occurring, and is given by the equation:

$$K = K_t^{\circ} \exp -\beta x \qquad \textbf{Eq. 2.38}$$

where K_t° is a proportionality constant, β is a constant determined by the energy barrier and the medium between the states, and x is the distance between the redox centre and the electrode.

It was noted by Marcus that $\Delta^{\ddagger}G$ is dependent upon the reorganisation of the reactant and the solvent surrounding it, as given by **Equation 2.39**:

$$\Delta^{\ddagger}G = \frac{(\Delta_r G^{\circ} + \lambda)^2}{4\lambda} \qquad \textbf{Eq. 2.39}$$

where λ is the total reorganisation energy, that is to say the sum of the inner and outer sphere reorganisation energies needed for the reactants and solvent to rearrange in order to obtain the equilibrium geometry of the product.[14, 15] As such, $\Delta^{\ddagger}G = 0$ when:

$$\Delta_r G^{\circ} = -\lambda \qquad \textbf{Eq. 2.40}$$

Combining **Equations 2.36** and **2.39** results in **Equation 2.41**:

$$k = KZ \exp\left(-\frac{1}{RT}\frac{(\Delta_r G^{\circ} + \lambda)^2}{4\lambda}\right) \qquad \textbf{Eq. 2.41}$$

the natural logarithm of which gives:

$$\ln k = \ln(KZ) - \frac{1}{RT}\frac{(\Delta_r G^\circ + \lambda)^2}{4\lambda} \qquad \textbf{Eq. 2.42}$$

This yields a downward sloping parabola, with the rate increasing as $\Delta_r G^\circ$ increases until a maximum rate is reached when **Equation 2.40** is satisfied. Beyond this maximum the rate of electron transfer decreases as $\Delta_r G^\circ$ continues to increase. This is known as the inverted region, illustrated schematically in **Figure 2.8**.

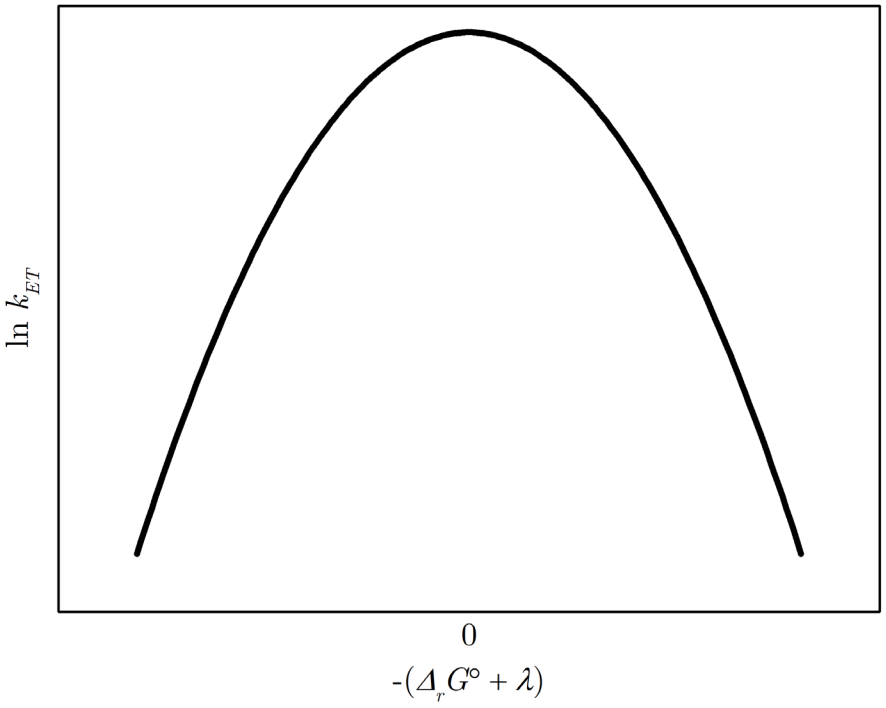

Fig. 2.8: Marcus plot demonstrating the inverse parabolic relationship between ln k and $\Delta_r G^\circ$, with the maximum rate found where $\Delta_r G^\circ = -\lambda$.

2.1.6 Cell Cycling

2.1.6.1 Preparation of Cell Components

In this work two key cell components were constructed in-house: the lithium iron phosphate ($LiFePO_4$) counter/reference electrodes and $^{12/13}C$ cathodes. $LiFePO_4$ was

used as a counter and reference electrode material due to its chemical stability towards the electrolyte and O_2, compared to lithium metal, along with its stable redox potential of 3.45 V *vs* Li^+/Li. The $LiFePO_4$ counter/reference electrodes were constructed from a slurry of $LiFePO_4$ (99.5%, TCI), PTFE (60wt% in H_2O, Sigma Aldrich) and carbon black (Super P, 99%, TIMCAL) in a ratio of 8:1:1, using isopropanol (99.9%, Sigma Aldrich) as the solvent. The PTFE was included as a binder to hold the structure together, while the carbon was included to improve the electrical conductivity of the counter/reference electrodes. The $LiFePO_4$ was then dried in an oven at 70°C overnight to remove the residual isopropanol.

The stable, well-defined redox potential of $LiFePO_4$ comes from a lithium-deficient phase. To achieve partial delithiation, the $LiFePO_4$ counter/reference electrodes were placed in a solution of glacial acetic acid (1.5 mL, >99%, Sigma Aldrich) and hydrogen peroxide (3.6 mL, 30%, Sigma Aldrich) in deionised water (250 mL) for 15 minutes. The counter/reference electrodes were then washed successively with deionised water and ethanol, before being dried at 120°C under vacuum for 24 hours.

Carbon cathodes were constructed out of a slurry of carbon black or isotopically labelled ^{13}C carbon (99 atom%, Sigma Aldrich) with PTFE and isopropanol in an 8:1:1 ratio, pasted onto a stainless steel mesh (100 mesh) to give a mass loading of 4 mg per cathode. Again, the PTFE acted as a binder to hold the cathode together. The cathodes were then dried at 70°C under vacuum for 24 hours prior to use.

Glass fibre separators (Whatman) were ubiquitous in all Swagelok-type cells, used to avoid direct physical contact between the counter/reference electrode and cathode. They were dried at 300°C under vacuum for 24 hours prior to use.

The solvent used in the majority of experiments was TEGDME (>99%, Sigma Aldrich), which was distilled under vacuum and dried over 4Å molecular sieves and stored in an Ar glovebox prior to use. DME (99.5%, Sigma Aldrich) when used was distilled under Ar then dried over molecular sieves and stored similarly to TEGDME. During distillation of both TEGDME and DME, sodium (1.5 g per 500 mL solvent, 99.9%, Sigma Aldrich) and benzophenone (9.0 g per 500 mL solvent, >99%, Sigma Aldrich) were added to the reaction vessel to quench any explosive peroxides formed during the distillation process.

The lithium salt used for the electrolyte was LiTFSI (99.95%, Sigma Aldrich), which was dried under vacuum at 150°C for 24 hours prior to use. When used, KTFSI (97%, Sigma Aldrich), was similarly dried under vacuum at 150°C for 24 hours prior to use. The KTFSI used contained insoluble K_2CO_3 as an impurity, and so when KTFSI was dissolved in TEGDME the precipitate was allowed to settle before the clear solution was decanted.

2.1.6.2 Swagelok-type Cell Assembly

The majority of cells in the work were constructed from Swagelok components. These homemade cells typically feature a stainless steel anodic current collector upon which a counter/reference electrode pellet, glass fibre separators and/or solid-state electrolyte

and a cathode material are stacked sequentially, housed within an insulated tubular casing. The cathodic current collector is generally a hollow steel tube, allowing it to double as an O_2 reservoir, with two valves allowing the cell to be purged with O_2 prior to cycling. To ensure the cell is airtight, compression ferrules were used at all connections. **Figure 2.9** illustrates a cross-section of a typical Swagelok cell. Before use the cell casings were dried under vacuum at 70°C for at least 6 hours.

Cells were constructed within an Ar glovebox. The casings were pre-assembled, with the exception of the cathode current collector. The components were placed in the casing in the following order: counter/reference electrode, two separators, cathode. If a solid electrolyte were used, this would sit between the counter/reference electrode and the cathode, with both an o-ring to form a seal and glass fibre separators to contain any liquid electrolyte present on either side. The cells were then purged with O_2 for 2 minutes, before being allowed to equilibrate for an hour before cycling.

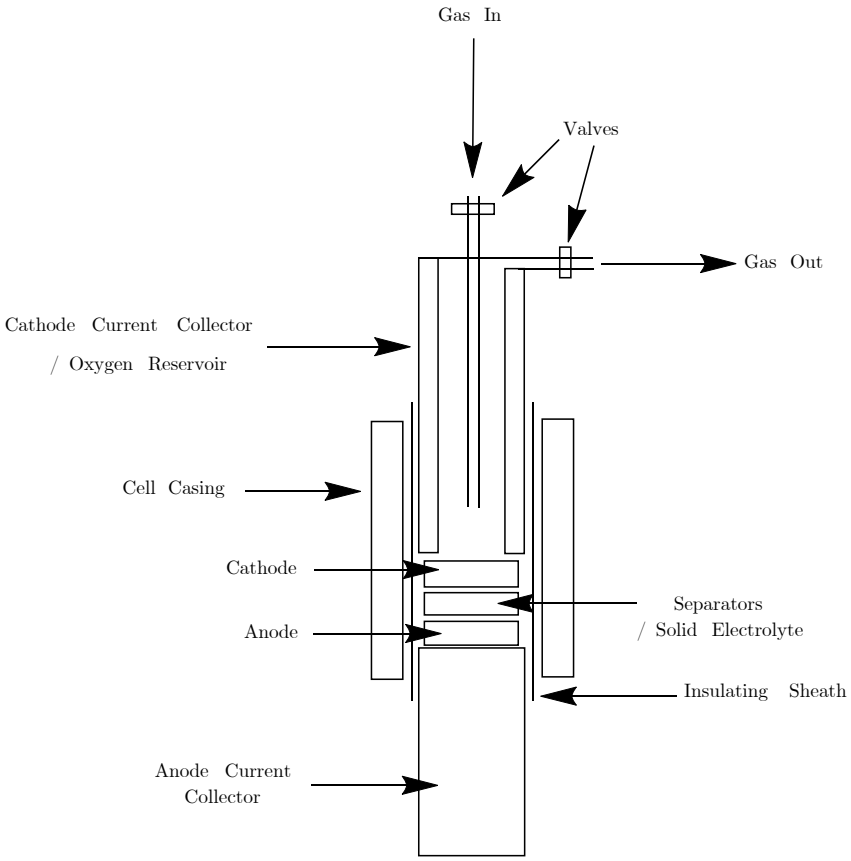

Fig. 2.9: Cross-section of a Swagelok-type M-O_2 cell.

2.1.6.3 Cycling Experiments

The cycling of cells is an essential aspect of any work pertaining to battery science. Cells are typically cycled galvanostatically, meaning they are both discharged and charged at a constant rate. This rate is generally normalised to either the mass or the geometric surface area of the cathode material. The potential is then measured as a function of the capacity passed, with the cell being cycled between two predetermined potential cut-off points. Potentiostatic cycling is also possible, where the potential is fixed and the current response measured. Here the current can be seen to decay over the course of the experiment, as the surface concentration of reactants decreases. The

experiments are controlled using potentiostats, with the VMP3 and SP-300 from Biologic used in this work.

Chapter 3 and **4** heavily utilise RMs. It is important to note that for any given concentration of RM there will be an associated capacity due to its oxidation observed during charge, given in **Equation 2.43** as:

$$Q = \frac{[RM]vF}{3.6} \qquad \textbf{Eq. 2.43}$$

where [RM] is the concentration of RM, v is the volume of electrolyte, F is the Faraday Constant, and Q is the charge in mAh. Some studies use RM concentrations that provide a capacity close to that of the total cell capacity; in such cases care must be taken to ensure that improvements to cell operation are not simply due to oxidation/reduction of the RM.[16]

2.2 Mass Spectrometry

2.2.1 Principles of Mass Spectrometry

Mass spectrometry operates on the principle that when charged particles are accelerated in a vacuum, a magnetic field will separate them by an amount proportional to their mass. There are a number of methods of sample injection, two of which will be discussed in greater detail in later Sections. In most cases, samples enter the instrument in the gas phase, and so must be sufficiently volatile such that with a moderate amount of heating they will vaporise. All measurements are conducted under high vacuum to minimise undesired collisions between species, with typical pressures

of 10^{-6} to 10^{-7} Pa required.[17, 18] Generally speaking, only a small fraction of the sample will leak into the ionisation chamber, with the vast majority simply bypassing through an exhaust valve.

All mass spectrometry in this work utilises electron impact (EI) as the ion generation method, although other methods including positive and negative chemical ionisation and electrospray are possible.[17] Within the ion source using EI, the incoming stream of sample atoms/molecules intersects an electron beam passing between a filament (cathode), invariably composed of thorium dioxide, and a counter/reference electrode.[19] The voltage between the cathode and the counter/reference electrode can be varied between 0 and 300 V to generate electrons of differing energies, although usually electrons of 70 eV are desired. Collision of the neutral sample molecules and the electrons results in the loss of an electron from the former, giving:

$$\mathrm{M} + \mathrm{e}^- \rightarrow \mathrm{M}^+ + 2\mathrm{e}^- \qquad \textbf{Eq. 2.44}$$

Occasionally a neutral molecule may lose two electrons to give M^{2+}. The generated ions are then accelerated by applying a potential to the source, with the ions reaching full speed at the exit slit, which permits only the central homogenous region of the ion beam to enter the mass analyser. The velocity, ν, of the ions is given by:[17]

$$\nu = \sqrt{\frac{2zU}{m}} \qquad \textbf{Eq. 2.45}$$

where z is the ionic charge, m is the ion mass and U is the acceleration potential. Any non-ionised molecules are removed from the system via the high vacuum pumps.

The analyser separates the ions according to their masses using a magnetic field, usually of approximately 1 T, with lighter ions deflected more than heavier ones, when they possess the same charge. The radius of deflection, r, may be expressed as:

$$r = \frac{mv}{zB} \qquad \textbf{Eq. 2.46}$$

where B is the magnetic field strength. Rearrangement of **Equation 2.45** and combination with **Equation 2.46** gives the mass-to-charge ratio, m/z, that is generally reported in mass spectrometry:

$$\frac{m}{z} = \frac{r^2 B^2}{2U} \qquad \textbf{Eq. 2.47}$$

If the acceleration potential and magnetic field strength are kept constant, m/z is directly proportional to the square of the radius of deflection; for this type of spectrometer, a large number of individual detectors is required. However, if the acceleration potential and the radius of deflection are constant, then m/z is proportional to the square of the magnetic field strength. The field strength may then be varied and one detector used.

The ions may be detected using either a Faraday or an electron multiplier detector. A Faraday detector is a conductive metal cup that gains a small charge when the ions collide with it. The metal can then be discharged to measure the small current, which is directly proportional to the number of ions that collided, according to the equation:

$$\frac{N}{t} = \frac{i}{e} \qquad \textbf{Eq. 2.48}$$

Where N/t is the number of ions observed per given time, i is the current and e is the elementary charge.

With an electron multiplier detector, incoming ions strike a material that releases electrons in a secondary emission process. A potential is applied between said plate and another, causing the emitted electrons to accelerate towards the latter and undergo a further secondary emission. This process may be repeated many times, with each collision resulting in an increase in the total number of electrons. When the electrons finally hit the detector, the signal intensity is much greater than if the initial incident ion struck it directly, as occurs in a Faraday detector. If, however, the sample concentration is sufficiently high then a simple Faraday detector is adequate for precise analysis.

The spectrometer can be configured to perform either a continuous scan, where the magnetic field strength is varied to reveal all m/z ratios present in a sample, or single ion monitoring, where one or several particular m/z ratios are monitored.

2.2.2 *Operando* Electrochemical Mass Spectrometry

The *operando* mass spectrometry (OEMS) employed extensively in this work operates in the same manner as described above, with individual m/z values ($m/z = 32$, 44 and 45 in particular) monitored using a Faraday detector. A carrier gas of known composition at a constant flow rate carries the sample gases directly into the mass spectrometer. This method relies on all components being in the gas phase at room

temperature and pressure, with a solvent trap in-line to prevent ingress of liquid material from cells.

2.2.3 Gas Chromatography Mass Spectrometry

Gas chromatography mass spectrometry (GCMS) allows for the separation of components from a mixture based on their affinity with a solid phase column prior to their admission into a mass spectrometer.[20] A sample dissolved in a solvent is injected into a heated port where it is vaporised. The sample vapour passes onto a cool chromatography column, located in an oven, where it condenses. The oven temperature is slowly increased; when the temperature reaches the boiling point of a sample component, said component vaporises and passes along the column and into the mass spectrometer. The speed at which a component travels along the column is based on its affinity to the solid stationary phase, with a greater affinity leading to a slower rate of movement along the column. Different columns may be substituted in to provide different stationary phases, depending on the nature of the sample components to be separated.

A carrier gas, typically helium, facilitates the movement of a sample through the column. The point at which the column enters the mass spectrometer is kept at high temperature to ensure none of the sample condenses prior to ionisation. The mass spectrometer operates as described in **Section 2.2.1** (page 91).[18]

2.3 Electronic Spectroscopy

2.3.1 Ultraviolet-Visible Absorption Spectroscopy

The electrons in atoms and molecules can undergo excitation by incoming photons, if said photons are of sufficient energy.[17] The energies required for such a process are to the order of several electronvolts, meaning the light required is in the visible and ultraviolet regions of the electromagnetic spectrum.

Upon absorption of a photon of sufficient energy, an electron is excited from a ground electronic state to a higher electronic state, as represented schematically in **Figure 2.10**. Vibrational transitions can accompany an electronic transition, however these are rarely seen in liquid or solid samples, being resolved only for gaseous samples. Whether an electronic transition is possible or not is determined by selection rules, the origin of which is the conservation of angular momentum during the transition.[13]

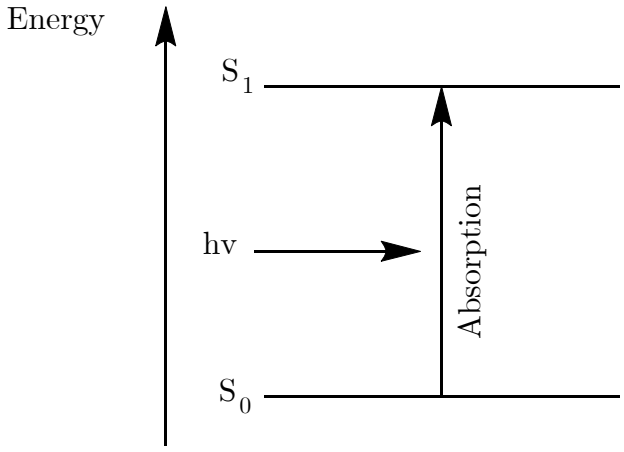

Fig. 2.10: Illustration of the electronic transition on absorption of UV light.

The transmitted intensity of light, I, is linked empirically to the concentration of the sample, c, through the Beer-Lambert law:[19]

$$I = I_0 10^{-\varepsilon c l} \qquad \textbf{Eq. 2.49}$$

Where I_0 is the incident light intensity, ε is the molar absorption coefficient (also known as the extinction coefficient) and l is the path length of the light through the sample (typically the cuvette used will give a path length of 1 cm). The molar absorption coefficient is a measure of how strongly a given species attenuates the incidental light, with ε_{max} indicating the intensity of the electronic transition.

The transmittance, T, of a sample is the ratio of incident light that passes through the sample to the detector, given by:

$$T = \frac{I}{I_0} \qquad \textbf{Eq. 2.50}$$

from which the absorbance, A, of the sample, may be determined:

$$A = \log \frac{I_0}{I} \qquad \textbf{Eq. 2.52}$$

This allows for the more familiar version of the Beer-Lambert law:

$$A = \varepsilon c l \qquad \textbf{Eq. 2.53}$$

It should be noted that the linearity of the Beer-Lambert law only holds at relatively low concentrations; at high concentrations significant deviations from linearity may be observed due to saturation of absorbance bands. On a practical level, calibration curves using standard solutions of known concentration of the analyte should always be constructed.

2.3.2 Fluorescence Spectroscopy

Once a species has been excited to a higher electronic state, it needs to lose its excess energy. This may occur through both radiative and nonradiative decay mechanisms.[13, 17] Most energy is lost through nonradiative decay, where the excess energy is converted into the vibrational energy of surrounding molecules, meaning it is "lost as heat". There are two radiative decay processes, fluorescence and phosphorescence, with the observational distinction being the timescale over which they occur; fluorescence is a spontaneous emission that occurs within a few nanoseconds following excitation, whereas the emission in phosphorescence occurs over several seconds to hours.

Upon initial promotion of an electron by a photon into an excited electronic state, identical to the process described in **Section 2.3.1** on page 96 regarding UV-vis absorption spectroscopy, the molecule drops down the vibrational energy levels to the lowest vibrational level of the excited state through non-radiated decay. If surrounding molecules are unable to accept the large remaining energy quanta, then the molecule may emit the energy as a photon. The electronic transition proceeds according to the Franck-Condon principle, meaning the larger the overlap of two vibrational wave functions the more likely the vertical transition is to occur. Since some energy is lost through nonradiative decay, the radiative emission is usually of higher wavelength than the absorbed photon (the exception being the 0-0 absorption and fluorescence peaks, which overlap since here no non-radiative decay occurs). Surrounding molecules with widely spaced vibrational levels, such as water, are capable of absorbing all the

electronic excitation energy, and so are seen to quench the fluorescence.[19] The Jablonski diagram in **Figure 2.11** displays schematically the process of fluorescence.

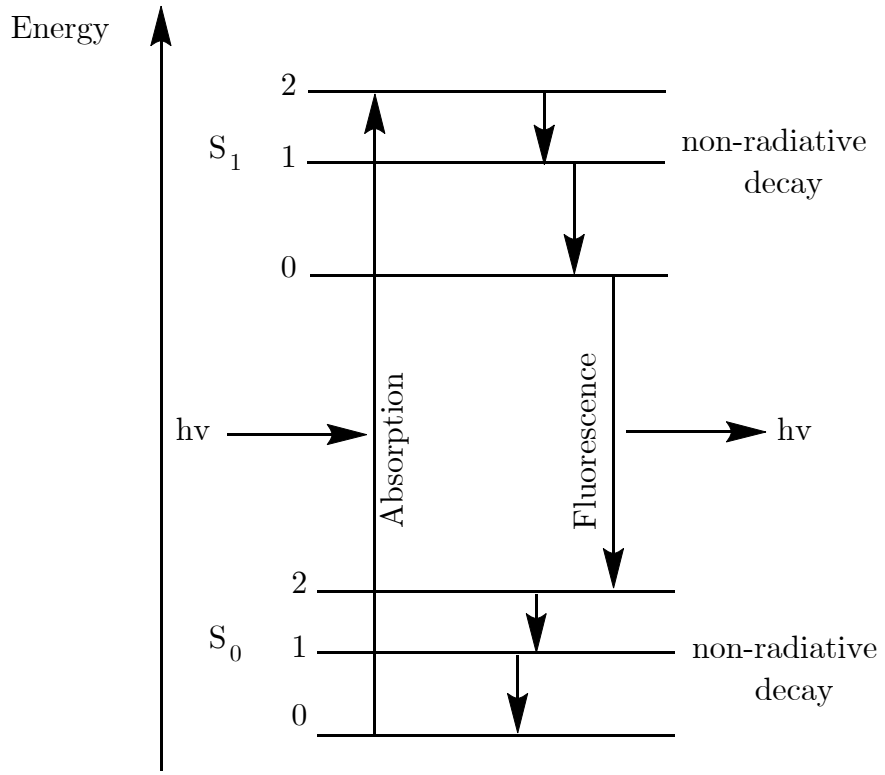

Fig. 2.11: Jablonski diagram for the absorption and fluorescence emission of an idealised fluorophore between the ground state singlet (S_0) and an excited singlet state (S_1).

Phosphorescence does not feature in this work, although for completeness a brief explanation is warranted. The initial excitation and nonradiative decay steps are similar to those found in fluorescence, although the presence of an excited triplet state results in an additional mechanism for energy loss (**Figure 2.12**). At the point where the potential energy curves of the singlet and triplet excited states intersect, the two excited states possess the same geometry, which allows an unpairing of electrons, termed intersystem crossing (ISC). ISC is a nonradiative decay process, and once it has occurred the excited triplet state continues to lose energy by moving down the

vibrational energy levels. The molecule finds it difficult to make the final electronic transition because moving from the triplet back to the singlet state is spin-forbidden. As such, this electronic transition is slow resulting in a weak emission that can last several hours.[11, 19]

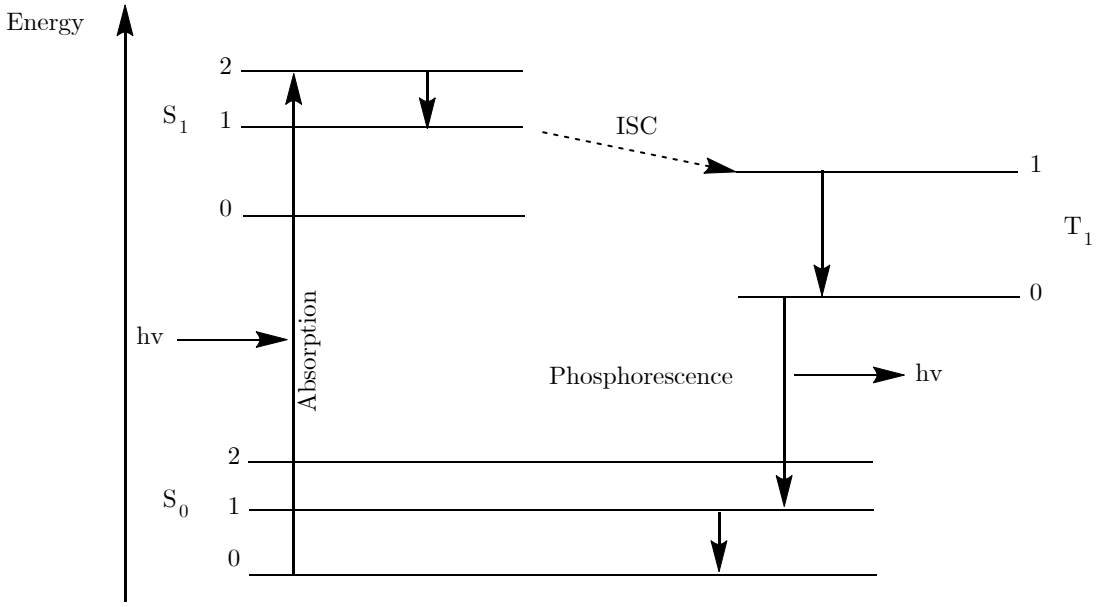

Fig. 2.12: Jablonski diagram for the absorption and phosphorescence emission of an idealised phosphor (*ISC* = intersystem crossing) between the ground state singlet (S_0), an excited singlet state (S_1) and an excited triplet state (T_1).

In a fluorescence spectroscopy experiment, the excitation light is generally monochromatic so as to excite a single electronic transition. Furthermore, the incident light is at right angles to the detector to minimise the interference of stray light with the fluorescence emission. There is a linear relationship between the fluorescence emission, I_f, and fluorophore concentration, according to the equation:[21]

$$I_f = kI_0\varepsilon lc\Phi \qquad \textbf{Eq. 2.54}$$

where k is a proportionality constant associated with the instrument and Φ is the fluorescence quantum yield. However, this linear relation only holds for low concentrations, with high concentrations leading to the emitted photons being reabsorbed by the fluorophore. Other species present may also absorb emitted photons, leading to a decrease in the fluorescence emission intensity measured, termed the inner filter effect. Photobleaching, whereby the fluorophore is permanently inactivated by the excitation light, is a further issue minimised by only exposing the sample to light for short excitation periods.

2.4 Fourier Transform Infrared Spectroscopy

Molecules can absorb photons that have insufficient energy to cause electronic excitation, but which can lead to a change in the vibrational and rotational energy levels of the species. If the two atoms of a chemical bond are modelled as point masses connected by a spring, then the amount of force, K, required to move the atoms from their equilibrium potions, Δr, is given by Hooke's law:[13, 17, 19]

$$K = -k\Delta r \qquad \textbf{Eq. 2.55}$$

where the force constant, k, is a measure of the strength of the bond between the atoms. The vibration frequency, ν, of the bond may be approximated by a harmonic oscillator:

$$\nu = \frac{1}{2\pi}\sqrt{\frac{k}{\mu}} \qquad \textbf{Eq. 2.56}$$

where the reduced mass, μ, of the atoms is given by:

$$\mu = \frac{m_1 m_2}{m_1 + m_2} \qquad \textbf{Eq. 2.57}$$

From this we can see that the stronger the bond, as given by a larger force constant, the greater the vibrational frequency. Furthermore, the heavier the atoms are the lower the vibrational frequency.

It should be noted that an anharmonic oscillator gives a better description of vibrational energy than the harmonic oscillator, particularly the observation of the presence of a dissociation energy. Additionally, not all bonds absorb in the infrared; absorption only occurs when there is a change in the bond's dipole moment. This makes infrared spectroscopy a complementary technique to Raman spectroscopy, in which a change in the polarisability of the molecule must be possible for a signal to be observed.[11]

It is common in modern instrumentation that the data at all frequencies is collected simultaneously through the use of the Fourier Transform, rather than the instrument scanning sequentially through all frequencies. This allows for a more rapid data collection, improves the signal to noise ratio, and increases the precision of the wavenumbers (in units of cm^{-1}) reported.[11]

2.5 X-Ray Diffraction

Crystalline solids are constructed of repeating unit cells, whose lengths are described by the lattice parameters *a*, *b* and *c* with the angles between them denoted α, β and γ.[22] Unit cells may be classified into one of seven crystal systems according to rotational

symmetry, from which fourteen Bravais lattices can be described. The planes of the lattice points are described by Miller indices, *hkl*, which are the reciprocals of the intersectional distances between the axis. The separation of parallel planes, d_{hkl}, (all having the same *hkl*) in a lattice is given by:

$$\frac{1}{d_{hkl}^2} = \frac{h^2}{a^2} + \frac{k^2}{b^2} + \frac{l^2}{c^2} \qquad \textbf{Eq. 2.58}$$

The incident x-rays are scattered by the electrons in the atoms, such that the incoming and outgoing waves may interfere either constructively or destructively. Whether constructive or destructive interference occurs is dependent on the path length difference of the incoming and outgoing waves which itself is determined by the glancing angle, θ, with a reflection observed only when the number of wavelengths, n, is an integer. If the glancing angle satisfies Bragg's law:[23]

$$n\lambda = 2d_{hkl}\, sin\, \theta \qquad \textbf{Eq. 2.59}$$

then a reflection will be observed. Some crystal structures give characteristic reflection patterns, with some systematic absences occurring.[11, 20]

X-ray diffraction may be conducted either on a single crystal or, in the case of this work, powder samples. The x-rays are generated by firing electrons at a copper (or other metal such as molybdenum or silver) target, with filters applied to ensure that only the K_α radiation is diffracted by the sample. Given that a powder sample contains randomly orientated crystallites, rotation of the sample reveals all of the available diffraction angles. The resultant diffraction pattern may then be qualitatively compared to known samples or computational modelling to achieve identification, or fitted to model data through Reitveld refinement (a least squares fitting) to provide

quantification of the lattice parameters of the sample.[24] Further information on crystallite size may be extracted from the peak width.[25, 26]

2.6 Nuclear Magnetic Resonance

Nuclear magnetic resonance (NMR) spectroscopy is a highly sensitive, non-destructive technique that allows for element-specific probing of the chemical environments within a species. Application of an external magnetic field to a nucleus results in the splitting of the nuclear spin energy levels. The energy of nuclear spin in a magnetic field, E_m, is given by:[13]

$$E_m = -\gamma \hbar B_0 m_l \qquad \textbf{Eq. 2.60}$$

Where γ is the gyromagnetic ratio of the specific nucleus, B_0 is the strength of the magnetic field, m_l is the nuclear spin quantum number, and ħ is the quantisation of angular momentum involving Plank's constant, h:

$$\hbar = \frac{h}{2\pi} \qquad \textbf{Eq. 2.61}$$

When the sample is exposed to radiation of frequency ν, resonance between said frequency and the energy separation occurs when the resonance condition is satisfied:

$$h\nu = \gamma \hbar B_0 \qquad \textbf{Eq. 2.62}$$

The frequencies required for nuclei are in the radio frequency of the electromagnetic spectrum (around 500 MHz).

In this work ^{1}H and ^{13}C NMR is utilised, with both nuclei having spin = ½ and natural abundances of 99.985% and 1.10%, respectively.[17] In order to minimise the

intensity of ^{1}H peaks from the solvent in the acquired spectra, deuterated solvents were used; ^{2}H (and ^{12}C) has a nuclear spin quantum number of 0, and so is NMR silent.[11, 15]

2.7 Density Functional Theory

Density functional theory (DFT) is a computational methodology that allows the ground state electron probability density for a polyatomic species to be determined. **Equation 2.63** gives the Schrödinger Equation for when N electrons are interacting with multiple nuclei:

$$\left[-\frac{\hbar^2}{2m}\sum_{i=1}^{N}\nabla_i^2+\sum_{i=1}^{N}V(\boldsymbol{r}_i)+\sum_{i=1}^{N}\sum_{j<i}U(\boldsymbol{r}_i,\boldsymbol{r}_j)\right]\Psi=E\Psi \qquad \textbf{Eq. 2.63}$$

where m is the mass of an electron and the terms in the square brackets give, from left to right, the kinetic energy of each electron, the interaction energy between each electron and the collection of atomic nuclei, and the interaction energy between different electrons.[27] Ψ is a function of the spatial coordinates of the N electrons.

DFT calculates the electron probability density for a particular spatial position, $\rho(\boldsymbol{r})$, given by the equation:

$$\rho(\boldsymbol{r})=\sum_{i}|\Psi_i(\boldsymbol{r})|^2 \qquad \textbf{Eq. 2.64}$$

through solving iteratively and self-consistently the Kohn-Sham Equations:

$$\left[-\frac{\hbar^2}{2m}\nabla^2+V(\boldsymbol{r})+V_H(\boldsymbol{r})+V_{XC}(\boldsymbol{r})\right]\Psi_i(\boldsymbol{r})=\varepsilon_i\Psi_i(\boldsymbol{r}) \qquad \textbf{Eq. 2.65}$$

where $V(\boldsymbol{r})$ defines the interaction between an electron and the atomic nuclei, $V_H(\boldsymbol{r})$ is the Hartree potential, given by:

$$V_H(\boldsymbol{r}) = e^2 \int \frac{n(\boldsymbol{r}')}{|\boldsymbol{r} - \boldsymbol{r}'|} d^3r' \qquad \textbf{Eq. 2.66}$$

and $V_{XC}(\boldsymbol{r})$ is the exchange correlation potential, which acts as a corrective term. First, an initial guess of the electron density is made, followed by solving of the Kohn-Sham equations. The electron density is then calculated from the solution of the Kohn-Sham equations; this process is repeated until the calculated electron density agrees with that used to initially solve the equation. This is the ground state electron density.[13, 27]

This work utilised Gaussian16 to run the DFT calculations, using the University of Oxford Advanced Research Computing facilities. The theory level used, that is to say the approximations used to describe electron-electron interactions for the $V_{XC}(\boldsymbol{r})$, was Becke-Lee-Yang-Parr (B3LYP). The basis set, which is a set of functions the sum of which are used to describe the overall wave function, was triple-zeta valence polarisation (TZVP). Increasing the size of the basis set can improve the accuracy of the calculations, however computing requirements are also increased.[11, 25]

2.8 References

1. D. Pletcher, *A First Course in Electrode Processes*, The Royal Society of Chemistry Cambridge, 2nd edn., 2009.
2. A. J. Bard and L. R. Faulkner, *Electrochemical Methods. Fundamentals and Applications*, Wiley, 2 edn., 2000.
3. A. W. Colburn, K. J. Levey, D. O'Hare and J. V. Macpherson, *Phys. Chem. Chem. Phys.*, 2021, **23**, 8100-8117.

4. D. Shoup and A. Szabo, *J. Electroanal. Chem.*, 1984, **160**, 27-31.
5. Y. Feng and J. Leddy, *Anal. Chem.*, 1995, **67**, 1259-1270.
6. G. Zhao, D. M. Giolando and J. R. Kirchhoff, *Anal. Chem.*, 1995, **67**, 2592-2598.
7. C. Lefrou and R. Cornut, *ChemPhysChem*, 2010, **11**, 547-556.
8. E. Ventosa and W. Schuhmann, *Phys. Chem. Chem. Phys.*, 2015, **17**, 28441-28450.
9. C. Lefrou, *J. Electroanal. Chem.*, 2006, **592**, 103-112.
10. R. Cornut and C. Lefrou, *J. Electroanal. Chem.*, 2007, **608**, 59-66.
11. R. Cornut, S. Griveau and C. Lefrou, *J. Electroanal. Chem.*, 2010, **650**, 55-61.
12. A. C. Fisher, *Electrode Dynamics*, Oxford University Press, 2009.
13. P. Atkins and J. De Paula, *Atkins' Physical Chemistry*, Oxford University Press, 9th edn., 2010.
14. R. A. Marcus, *J. Chem. Phys.*, 1965, **43**, 679-701.
15. C. Costentin, D. H. Evans, M. Robert, J.-M. Saveant and P. S. Singh, *J. Am. Chem. Soc.*, 2005, **127**, 12490-12491.
16. W.-J. Kwak, S. A. Freunberger, H. Kim, J. Park, T. T. Nguyen, H.-G. Jung, H. R. Byon and Y.-K. Sun, *ACS Catal.*, 2019, **9**, 9914-9922.
17. M. Hesse, H. Meier and B. Zeeh, *Spectroscopic Methods in Organic Chemistry*, Thieme, 2nd edn., 2008.
18. A. L. Rockwood, M. M. Kushnir and N. J. Clarke, in *Principles and Applications of Clinical Mass Spectrometry*, eds. N. Rifai, A. R. Horvath and C. T. Wittwer, Elsevier, 2018, ch. 2, pp. 33-65.
19. P. Atkins, T. Overton, J. Rourke, M. Weller and F. Armstrong, *Shriver and Atkins' Inorganic Chemistry*, Oxford University Press, 5th edn., 2010.
20. D. S. Hage, in *Principles and Applications of Clinical Mass Spectrometry*, eds. N. Rifai, A. R. Horvath and C. T. Wittwer, Elsevier, 2018, ch. 1, pp. 1-32.
21. *An Introduction to Fluorescence Spectroscopy*, Perkin Elmer Ltd., 2000.
22. L. E. Smart and E. A. Moore, *Solid State Chemistry: An Introduction*, CRC Press, Taylor & Francis Group, 4th edn., 2012.
23. W. H. Bragg and W. L. Bragg, *Proc. R. Soc. London, A*, 1913, **88**, 428-438.
24. H. M. Rietveld, *J. Appl. Cryst.*, 1969, **2**, 65-71.
25. P. Scherrer, *Gottinger Nachrichten*, 1918, 98-100.
26. A. L. Patterson, *Phys. Rev.*, 1939, **56**, 978-982.
27. D. S. Sholl and J. A. Steckel, *Density Functional Theory - A Practical Introduction*, Wiley, 2009.

Chapter 3

Avoiding Singlet Oxygen by Using Low Potential Redox Mediators to Suppress the Charging Potential in Lithium-Oxygen Batteries

Contents

3.1 Introduction

One of the key barriers to a commercially viable Li-O_2 cell is the high level of decomposition of both the carbon cathode and ethereal electrolyte on charge.[1-3] Not only does this decomposition consume the cell components, it also causes passivation of the cathode leading to early cell death.[2] Whilst a number of different candidate solvents and cathode materials have been investigated, most suffer some degree of decomposition or, if displaying increased stability, in many cases lead to a decrease in the specific energy due to their increased mass.[1, 4-7] Carbon and ethers consequently remain the preferred species for the cathode and electrolyte solvent, respectively.[8]

As discussed in **Chapter 1** (**Section 1.5**, page 49), singlet oxygen ($^1O_2$) has been found to be a significant cause of decomposition within Li-O_2 cells, particularly on charge.[9-14] There are a number of routes to $^1O_2$, including direct electrooxidation of LiO_2 and Li_2CO_3 and disproportion of LiO_2, with both the solvent and cathode material

affecting the ratio of $^1O_2$ to $^3O_2$ formed.[11, 12, 14-17] For long-term cyclability to be achieved, methods of mitigating or avoiding decomposition due to $^1O_2$ must be developed, with $^1O_2$ traps and quenchers having been shown to be promising in this regard.[11, 18, 19]

This Chapter demonstrates that there is a window of charge between 2.96 V and 3.31 V where, due to thermodynamic considerations, electrooxidation of Li_2O_2 does not result in the formation of $^1O_2$. Furthermore, it is revealed that due to the competing kinetics of direct electrooxidation and disproportionation of LiO_2, which result in different proportions of $^1O_2$, formation of Li_2CO_3 can be minimised provided the charging potential remains below 3.45 V. This is demonstrated using low potential RMs, use of which results in a decrease in Li_2CO_3 formation on charge of approximately 75% compared to unmediated cells. The reactivity of Li_2O_2 with the carbon cathode and ethereal electrolyte is also considered.

3.2 Experimental

3.2.1 Cyclic Voltammetry

Cyclic voltammograms were obtained using a Biologic SP-300 potentiostat and were conducted inside a N_2 glovebox. 10 mM RM (2,2,6,6-tetramethyl-1-piperidinyloxy (TEMPO, 98%, Sigma Aldrich) or *N,N,N',N'*-tetramethyl-*p*-phenylenediamine (TMPD, 99%, Sigma Aldrich)) (30 mM 5,10-dihydro-5,10-dimethylphenazine (DMPZ, 99%, TCI) was used for the cyclic voltammetry in **Appendix 3.5.1** on page 159), along with 30 mM 9,10-dimethylanthracene (DMA, 99%, Sigma Aldrich) when

applicable, was dissolved in dried and distilled TEGDME (>99%, Sigma Aldrich) with 1 M LiTFSI (99.95%, Sigma Aldrich) as supporting electrolyte, which was degassed using N_2 prior to use. The RMs and DMA were used as received, whilst the TEGDME and LiTFSI were prepared as described in **Section 2.1.6.1** on page 86.

The working electrode was a planar gold disc (3 mm diameter), polished using a slurry of 0.05 μm alumina on a fine abrasive pad followed by electrochemical cleaning by cycling in a 0.1 M $HClO_4$ (Sigma Aldrich) solution. The counter electrode was a platinum wire and the reference electrode was partially delithiated $LiFePO_4$ in TEGDME with 1 M LiTFSI supporting electrolyte behind a Vycor® glass frit (3.45 V *vs* Li^+/Li). The current density response at a scan rate of 100 mV s^{-1} was measured, with the solution being stirred between scans. iR (Ohmic drop) corrections of 85% were applied to the measurements. The formal potential, E^0, was taken as the midpoint potential between the anodic and cathodic peaks. The theory of cyclic voltammetry is discussed in **Section 2.1.2** on page 74.

3.2.2 Cell Component Preparation

The $LiFePO_4$ counter electrodes (which also served as the reference electrodes) were constructed from a slurry of $LiFePO_4$ (99.5%, TCI), PTFE (60wt% in H_2O, Sigma Aldrich) and carbon black (Super P, 99+%, TIMCAL) in a ratio of 8:1:1. Lithium metal (99.9%, Sigma Aldrich) counter/reference electrodes were cut from ribbon inside an Ar glove box. Carbon cathodes were constructed out of a slurry of either Carbon-13 (99 atom%, Sigma Aldrich) or carbon black, PTFE and isopropanol (99.9%, Sigma

Aldrich) in an 8:1:1 ratio pasted onto a stainless steel mesh (100 mesh). Glass fibre (Whatman) separators were used. When required, a Li^+-conducting solid electrolyte (Ohara Inc.) was prepared by polishing on damp 2000 grit sandpaper then drying at 70°C under vacuum overnight. Rubber o-rings were used to provide a water-tight seal between compartments. Full details regarding cell component preparation is described in **Section 2.1.6.1** (page 86).

3.2.3 Cell Cycling

3.2.3.1 Galvanostatic Cell Cycling

Cells were cycled using a Biologic VMP3 potentiostat in an Ar glovebox. Cells were assembled with either a $LiFePO_4$ or Li metal counter/reference electrode (depending on whether the redox potential of the RM is at or below that of $LiFePO_4$ (3.45 V *vs* Li^+/Li)), two glass fibre separators and a carbon cathode on stainless steel mesh. 1 M LiTFSI in TEGDME (300 μL) served as the electrolyte with 10 mM RM and 30 mM DMA added where required. Use of a solid electrolyte required DME (99.5%, Sigma Aldrich) with 1 M LiTFSI as the catholyte (containing 20 mM DMPZ) and TEGDME with 1 M LiTFSI as the anolyte.[20] The RMs were used as received. The cells were purged with dried O_2 (99.999%, BOC) for 2 minutes then allowed to equilibrate for 1 hour before cycling at a current density of 100 μA cm^{-2} (or 10 μA cm^{-2} for the solid electrolyte cells) at 20°C.

3.2.3.2 Potentiostatic Cell Cycling

Cells were constructed as detailed in **Section 3.2.3.1** (page 112) and discharged at a constant current density of 100 μA cm^{-2} to a capacity of 900 μAh cm^{-2}. Charging was conducted at a constant potential of 3.60 V to a fixed capacity of 600 μAh cm^{-2}.

3.2.4 Acid Treatment of Cells

Cells were stopped at various points of charge, disassembled and the cathode and separators washed with acetonitrile, then dried under vacuum for at least 1 hr. The cathode and separators were placed in a dried glass vial sealed with a rubber septum (SubaSeal) and magnetic stirrer bar, then attached to the mass spectrometer (Thermo Scientific PrimaBT benchtop gas analyser) with Ar as the carrier gas. Following the equilibration of the baseline, 1 M phosphoric acid (1.00 mL, Sigma Aldrich) was injected into the vial. The evolved $^{12}CO_2$ and $^{13}CO_2$ was measured by monitoring *m/z* 44 and 45 respectively, following industry-standard one-point calibration of the instrument using 0.1% O_2, 1000 ppm $^{12}CO_2$ and 500 ppm $^{13}CO_2$ made up to 100% with Ar (BOC).

3.2.5 *Operando* Electrochemical Mass Spectrometry

Cells were constructed as described in **Section 3.2.3.1** (page 112). The cells were connected to a Thermo Scientific PrimaBT benchtop gas analyser and cycled at 100 μA cm^{-2} to a fixed capacity of 1000 μAh cm^{-2}. The cells were continually purged using a carrier gas of 20% O_2 in Ar that was set to a flow rate of 1.00 mL min^{-1}. $^{16}O_2$

and $^{12}CO_2$ evolution was measured by monitoring the m/z 32 and 44 signals respectively. The instrument was calibrated as described is **Section 3.2.4** (page 113).

3.2.6 Li_2O_2 Quantification at the End of Discharge

Discharged cells were disassembled in an Ar glovebox and transferred into a vial, to which 1.00 mL H_2O was added. 2.00 mL of 2% $TiOSO_4$ (Sigma Aldrich) solution was added to the vial to produce the yellow $[Ti(O_2)]^{2+}$ complex (λ_{max} = 405 nm). The concentration of $[Ti(O_2)]^{2+}$ and hence Li_2O_2 was determined using a Thermo Evolution 200 UV-vis spectrometer and a calibration curve prepared using commercial Li_2O_2 (technical grade, Sigma Aldrich).

3.2.7 Fluorescence Spectroscopy

A cuvette with path length 1.00 cm was used, along with an electrolyte of 32 μM DMA and 1 M LiTFSI dissolved in distilled TEGDME. The solution was irradiated with light of wavelength 378 nm, with the intensity of the fluorescence peak at 437.9 nm monitored using an Ocean Optics DH-2000 fluorescence spectrometer. Partially delithiated $LiFePO_4$ with carbon black and PTFE was used as the counter electrode and reference electrodes. A cathode constructed from ^{13}C and PTFE slurry pasted onto a stainless-steel mesh then predischarged to 50 μAh was charged at a constant current density of 20 μA. The electrolyte was continually purged with O_2 throughout measurement, since O_2 concentration can affect DMA fluorescence through quenching.

3.3 Results and Discussion

3.3.1 Lithium Carbonate as a Proxy for Overall Cell Decomposition

The carbon cathode and ethereal electrolytes are known to decompose during both the discharge and charge of Li-O_2 cells, forming species including lithium acetate, lithium formate and lithium carbonate (Li_2CO_3).[21, 22] Whilst the accumulation of any decomposition products due to parasitic side reactions is unfavourable in Li-O_2 cells, the build-up of Li_2CO_3 is particularly problematic; as an insoluble and insulating solid, the formation of a Li_2CO_3 layer on the surface of the cathode during discharge and charge results in cell passivation and early cell death. Furthermore, Li_2CO_3 is oxidised only at potentials above 3.82 V, necessitating a higher charging overpotential for complete removal and thereby lowering the round-trip efficiency of the cell.[12]

In this work, Li_2CO_3 is used as proxy for total decomposition in a Li-O_2 cell due to its facile quantification via acid treatment of cell components; all further discussion of decomposition in this Chapter is with reference to the Li_2CO_3 quantities present. To distinguish between cathode and electrolyte decomposition, the cathode was constructed from isotopically labelled carbon (99 atom% ^{13}C), decomposition of which leads to $Li_2{}^{13}CO_3$ compared to ethereal electrolyte decomposition which leads to $Li_2{}^{12}CO_3$ formation (an explanation of the method of Li_2CO_3 analysis through treatment of the cathode and separators with acid may be found in **Section 3.2.4** (page 113).

3.3.2 Cyclic Voltammetry of TEMPO and TMPD

Given its ubiquitous use within the Li-O_2 field, 2,2,6,6-tetramethyl-1-piperidinyloxy, (TEMPO) was selected as one of the charge RMs for this study.[20, 23-25] TEMPO is a stable oxy-radical that is characterised by a highly reversible one-electron redox couple at 3.70 V, presented in **Scheme 3.1** and demonstrated through cyclic voltammetry in **Figure 3.1**.

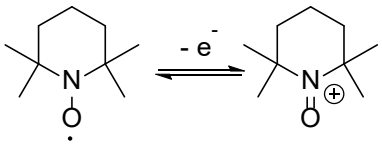

Scheme 3.1: TEMPO/TEMPO$^+$ redox couple.

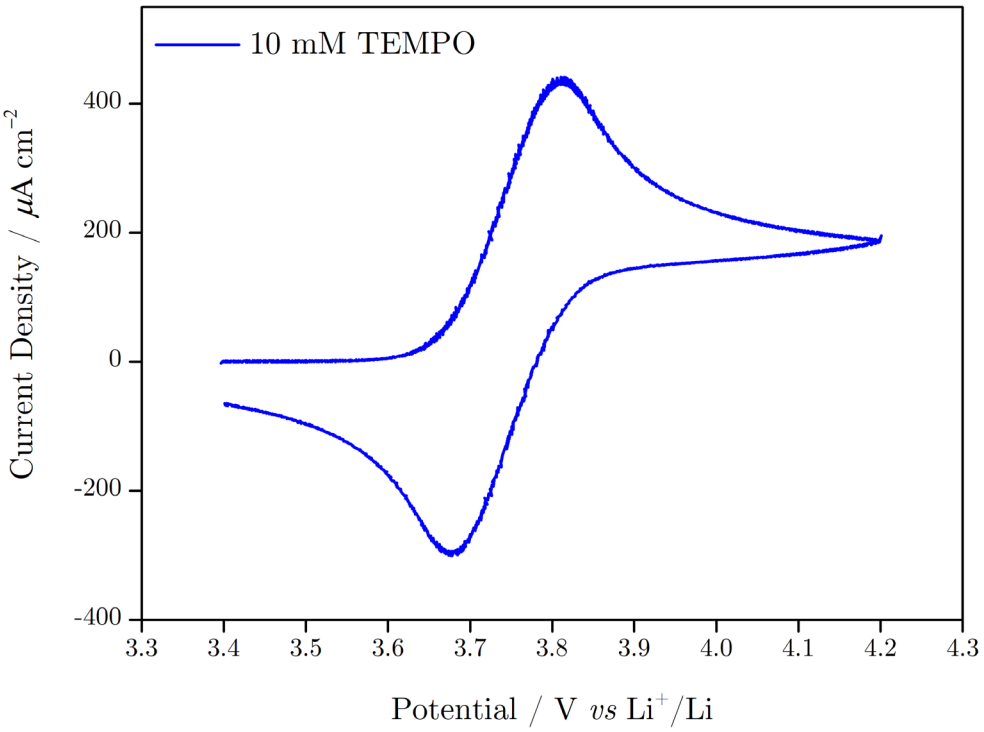

Fig. 3.1: Cyclic voltammogram of 10 mM TEMPO with 30 mM DMA in TEGDME with 1 M LiTFSI at a scan rate of 100 mV s^{-1}, with experimental conditions as described in **Section 3.2.1** (page 110).

N,N,N',N'-tetramethyl-*p*-phenylenediamine (TMPD), commonly known as Wurster's Blue, was also selected as a charge RM following recent studies demonstrating the ability of its first oxidation state to oxidise Li_2O_2.[25-27] The cyclic voltammetry of TMPD presented in **Figure 3.2a** shows a highly reversible first oxidation at 3.20 V, followed by a second oxidation at 3.75 V which yields a di-cation that, as evidenced by the lack of corresponding cathodic peak, is observed to be involved in an *ec* reaction. The cathodic shoulder at 3.35 V is suspected to arise from formation of a σ-dimer between two $TMPD^{2+}$ species, as observed in similar compounds[a] and evidenced by the lack of such shoulder when the potential range is truncated before the onset of $TMPD^{2+}$ formation (**Figure 3.2b**).[28] A representation of the successive oxidation of TMPD is presented in **Scheme 3.2**. Given that in this work the charging potential of cells containing TMPD used for Li_2CO_3 quantity analysis did not reach the potential required for the second oxidation of TMPD, this lack of stability is not considered to be problematic.

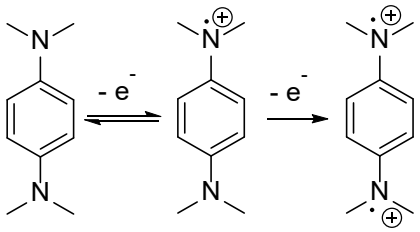

Scheme 3.2: TMPD/$TMPD^+$ and $TMPD^+$/$TMPD^{2+}$ redox couples.

[a] The cyclic voltammogram of 5,10-dihydro-5,10-dimethylphenazine (DMPZ) displays a similar cathodic peak which is absent when the anodic scan potential is limited to 3.45 V, as illustrated in **Appendix 3.5.1** (page 159). The novel RM DMHQ presented in **Chapter 4** is also suspected of undergoing a similar dimerisation reaction.

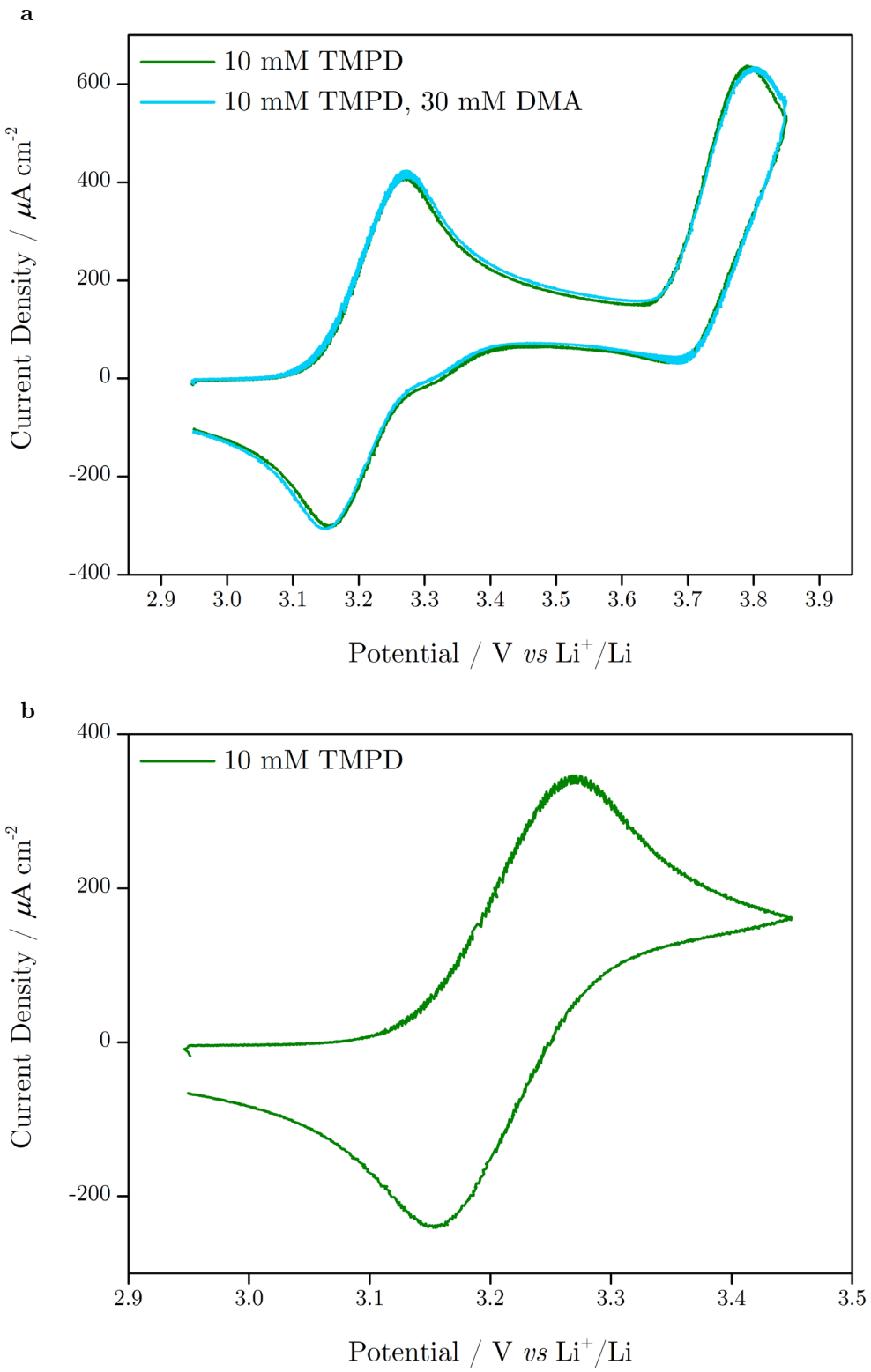

Fig. 3.2: a. Cyclic voltammograms of 10 mM TMPD with (cyan) and without (green) 30 mM DMA and **b.** cyclic voltammogram of 10 mM TMPD with the anodic scan limited to 3.45 V. TEGDME with 1 M LiTFSI served as the electrolyte, with a scan rate of 100 mV s^{-1}. Experimental conditions as described in **Section 3.2.1** (page 110).

3.3.3 Effect of RMs on Cathode and Electrolyte Decomposition

The effect of charging at a constant current density on the decomposition of the cathode and electrolyte was investigated, both when RMs were included and in their absence. Cells were constructed and cycled as described in **Section 3.2.3.1** (page 112), followed by acid treatment of the cathode and separators to determine the quantity of $Li_2{}^{13}CO_3$ and $Li_2{}^{12}CO_3$ present. The materials and conditions of cell cycling within this work are well established and known to produce Li_2O_2 on discharge and to evolve O_2 on charge.[20, 27, 29, 30] The yield of Li_2O_2 on discharge was found to be 68.9±9.9%, using UV-vis spectroscopy according to the method detailed in **Section 3.2.6** (page 114). This value is in line with other studies using similar cell conditions, although it is likely to be an underestimation of the true Li_2O_2 yield[b].[31-33]

Considering first the charging profiles of cells with and without TEMPO (**Figure 3.3a**), it can be seen that there is no difference between the two cell systems until the potential has reached approximately 3.50 V, at which point the TEMPO/TEMPO$^+$ redox couple becomes active. Whilst TEMPO-containing cells display a voltage plateau at approximately 3.50 V, cells without TEMPO continue to rapidly polarise to above 4.00 V.

[b] Schafzahl *et al.* demonstrated that the H_2O_2 produced upon addition of H_2O to the cathode and separators (according to the method detailed in **Section 3.2.6**, page 114) can decompose in the presence of carbon (and indeed without). This means that less H_2O_2 is available for reaction with the $TiOSO_4$, leading to an underestimation of the quantity of Li_2O_2 present at the end of discharge. L. Schafzahl, N. Mahne, B. Schafzahl, M. Wilkening, C. Slugovc, S. M. Borisov, S. A. Freunberger, *Angew.*, 2017, **56**, 15728-32.

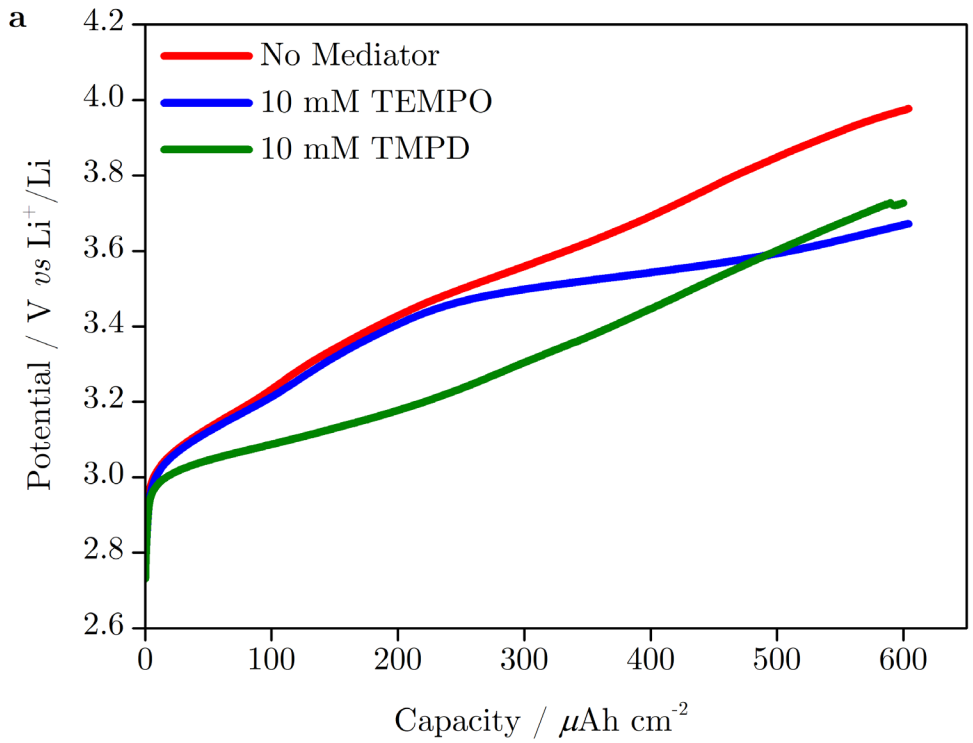
a
No Mediator
10 mM TEMPO
10 mM TMPD
Potential / V vs Li+/Li
Capacity / μAh cm-2
4.2
4.0
3.8
3.6
3.4
3.2
3.0
2.8
2.6
0
100
200
300
400
500
600

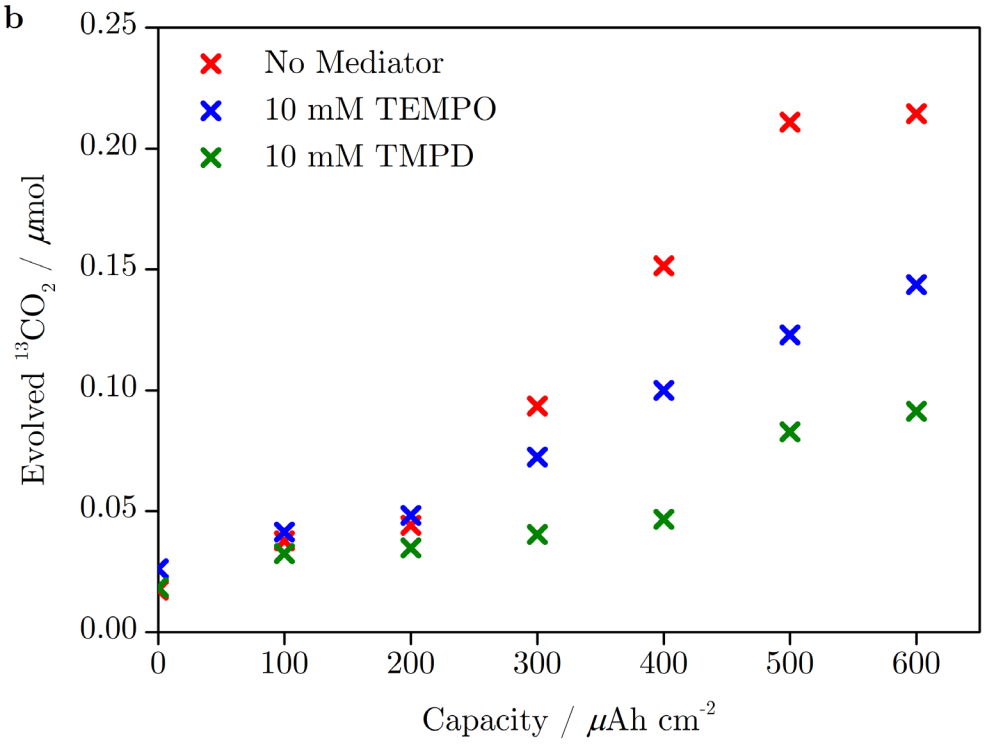
b
No Mediator
10 mM TEMPO
10 mM TMPD
Evolved 13CO2 / μmol
Capacity / μAh cm-2
0.25
0.20
0.15
0.10
0.05
0.00
0
100
200
300
400
500
600

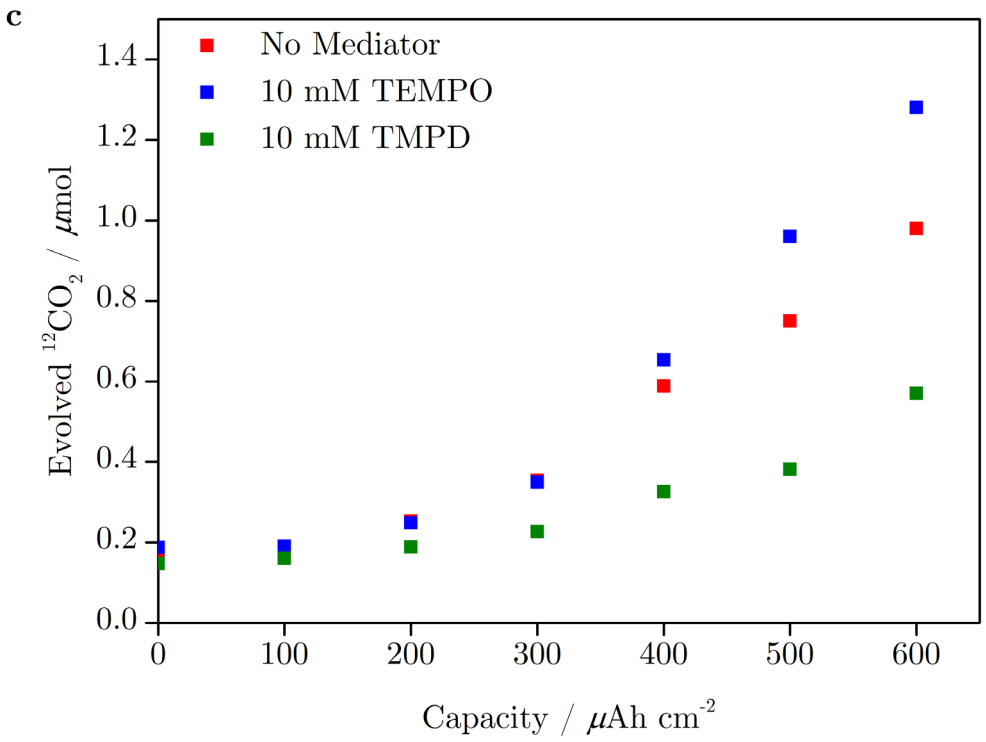

Fig. 3.3: Cell potential and Li_2CO_3 quantity at various points of charge without RMs, with 10 mM TEMPO and 10 mM TMPD**. a.** (previous page) Charging potential profiles at various points of charge, **b.** (previous page) evolved $^{13}CO_2$ originating from $Li_2{}^{13}CO_3$ from ^{13}C cathode decomposition, and **c.** evolved $^{12}CO_2$ originating from $Li_2{}^{12}CO_3$ from electrolyte decomposition. Electrolyte solution was 1.0 M LiTFSI in TEGDME under 1 atm O_2. Current density 100 μA cm^{-2}. Further experimental conditions for cell assembly and acid treatment to liberate CO_2 may be found in **Sections 3.2.3.1** (page 112) and **3.2.4** (page 113), respectively.

The similarities and differences observed in the charge profiles of cells with and without TEMPO are mirrored in the rate of Li_2CO_3 formation. Prior to the TEMPO/TEMPO$^+$ redox couple becoming active there is no difference between the two systems. However, upon the activation of the TEMPO/TEMPO$^+$ redox couple a clear distinction between the two systems becomes apparent, with the presence of the

oxidised RM being essential to the differences. As shown in **Figure 3.3b**, the presence of $TEMPO^+$ results in a lower rate of $Li_2{}^{13}CO_3$ formation compared to cells without the RM, demonstrating a reduced level of cathode decomposition. This is in stark contrast to the trend in the $Li_2{}^{12}CO_3$ quantity, presented in **Figure 3.3c**, where $TEMPO^+$ has the opposite effect, instead leading to an increase in electrolyte decomposition compared to cells without RMs.

This observation appears counter intuitive at first glance, as one might expect that if $TEMPO^+$ results in less cathode decomposition then it should also protect the electrolyte. However, consideration of the mechanism of RM operation provides an explanation for this result; $TEMPO^+$ is generated at the cathode surface and, as a discrete and stable molecule, is free to diffuse into the bulk electrolyte. This $TEMPO^+$ proceeds to react with Li_2O_2 interfacing with the electrolyte, rather than the Li_2O_2 in contact with the cathode surface. As such, the processes leading to cell decomposition that arise from Li_2O_2 oxidation now occur away from the cathode, thereby protecting the cathode at the expense of the electrolyte, which suffers increased levels of decomposition. This is further demonstrated in **Figure 3.4**, where unmediated cells and cells containing 10 mM TEMPO were charged at a constant potential of 3.60 V to a fixed capacity of 600 μAh cm^{-2}; cells containing TEMPO show lower levels of carbon cathode decomposition but higher levels of electrolyte decomposition than cells without TEMPO. Given the charging potential is the same in each system, the differences in cathode and electrolyte decomposition in **Figure 3.4** is attributed to the action of TEMPO in changing the location of Li_2O_2 oxidation.

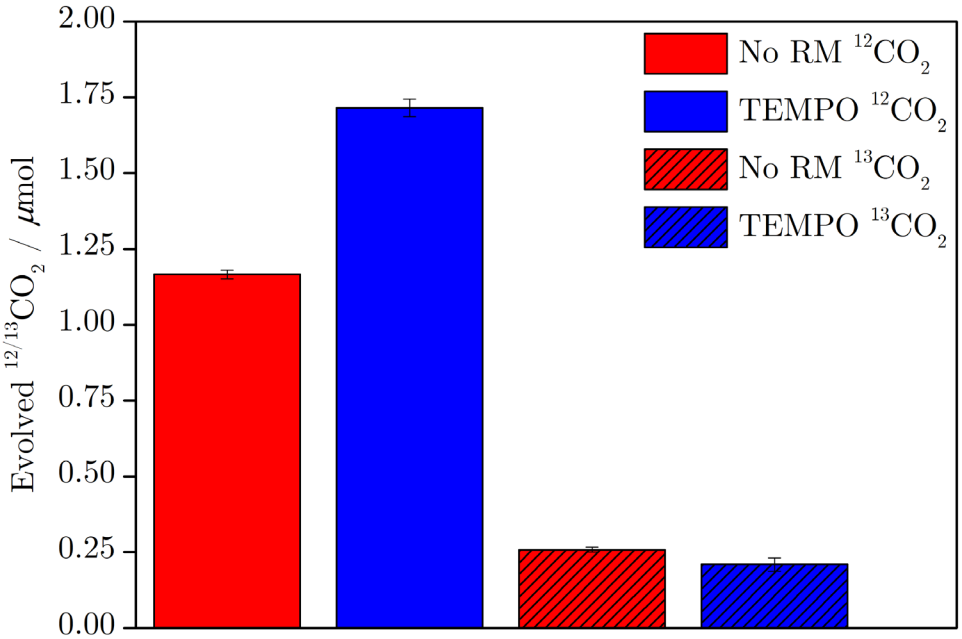

Fig. 3.4: Evolved CO_2 arising from the electrolyte (solid bars) and cathode (striped bars) in cells charged at a constant potential of 3.60 V to a fixed capacity of 600 μAh cm^{-2} with (blue) and without (red) 10 mM TEMPO in TEGDME with 1 M LiTFSI. Error bars illustrate standard deviation from at least three repeats. Further experimental details regarding cell cycling and acid treatment to liberate CO_2 may be found in **Sections 3.2.3.2** and **3.2.4**, respectively (both Sections on page 113).

The action of charge RMs in changing the location of Li_2O_2 oxidation, along with the expected effect of including a discharge RM, is illustrated in **Figure 3.5** (the main cause of parasitic side reactions, $^1O_2$, has been included in the diagram for completeness and will be discussed at length later in this Chapter). The protective benefits of moving the oxidation of Li_2O_2 away from the cathode surface has been previously demonstrated by *Gao et al.* and Liang *et al.*, however neither study acknowledged the deleterious effect this has on the electrolyte on cell charge.[20, 34]

A brief comment should be made about the data point at 600 μAh cm^{-2} for the system without RMs in **Figure 3.3b**, where there appears to be a plateau in the level of cathode decomposition at approximately 0.21 μmol $^{13}CO_2$ despite continuing cell charge. This plateau is an artefact resulting from the high cell potential at this point; Li_2CO_3 undergoes direct electrochemical oxidation above 3.82 V, resulting in a suppression in the level of Li_2CO_3 quantified.[12] **Figure 3.6** demonstrates that, when moving into the final third of charge, the potential for cells with and without $TEMPO^+$ increases above 3.82 V leading to a decrease in Li_2CO_3 quantity obtained through the method used in this work. As such, no definitive conclusions regarding cell decomposition may be drawn from the Li_2CO_3 quantity in this final part of the charge cycle, with this work instead focussing only on the first two thirds of charge. However, it may be assumed that, were Li_2CO_3 stable to a much higher potential, the level of Li_2CO_3 would continue to increase across the entirety of the charge profile, extending the trends identified here.

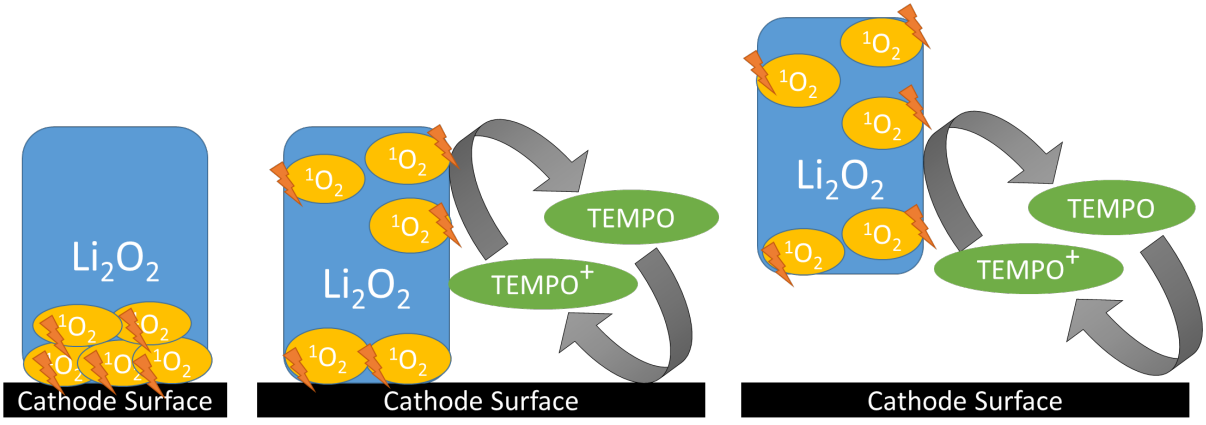

Fig. 3.5: Schematic illustrating the location of $^1O_2$ generation (yellow circles) in cells without RMs (left), with TEMPO (centre) and with both DBBQ and TEMPO (right). The yellow circles represent the location of Li_2O_2 oxidation, and hence $^1O_2$ formation, on charge.

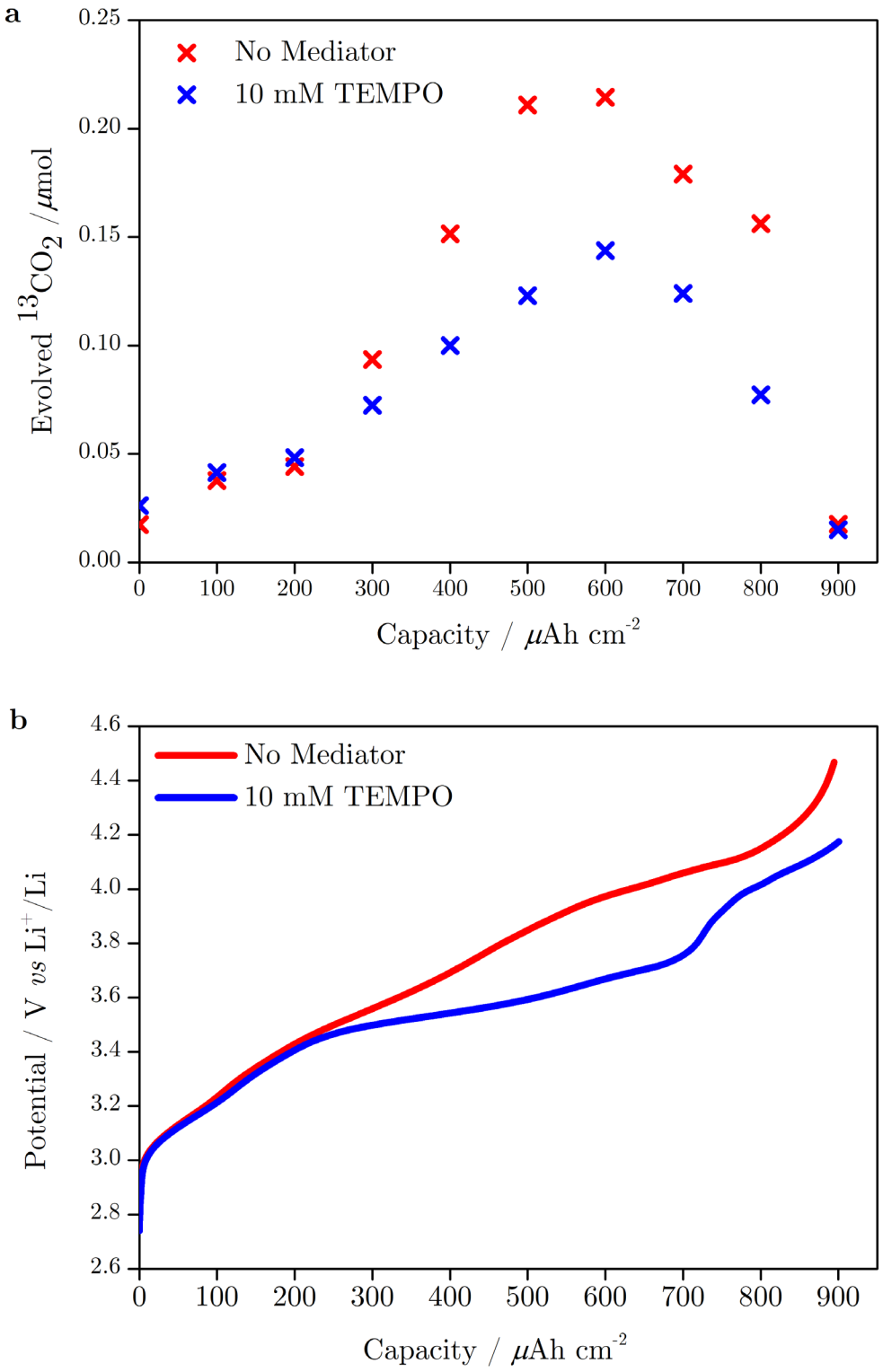

Fig. 3.6: a. Cathode decomposition over the full charge cycle in cells with (blue) and without (red) 10 mM TEMPO and **b.** corresponding charge profiles at a current density of 100 μA cm^{-2}. Electrolyte solution was 1.0 M LiTFSI in TEGDME under 1 atm O_2. Further experimental details (including CO_2 quantification) may be found in Sections **3.2.3.1** (page 112) and **3.2.4** (page 113), respectively.

It would be expected, given the explanation regarding its operation, that TEMPO may be substituted for any charge RM and that the same trend of cathode protection at the expense of the electrolyte, varying perhaps only in magnitude, would be observed. However, use of TMPD as the RM results in a lower level of $Li_2{}^{13}CO_3$ arising from the cathode (**Figure 3.3b**) than either TEMPO or in unmediated cells, with no significant increase until towards the end of the charging period. Even more strikingly, $TMPD^+$ leads to lower levels of electrolyte decomposition relative to unmediated cells, in contrast to $TEMPO^+$ where more electrolyte decomposition than the unmediated system is observed (**Figure 3.3c**). $TMPD^+$ is thus protecting both the cathode and electrolyte, whereas $TEMPO^+$ sacrifices the latter to save the former.

It is a well-established assumption that RMs behave in a very similar manner within Li-O_2 cells, with no unique mechanism provided for each RM, and so it is reasonable to assume here that $TMPD^+$ also promotes oxidation of Li_2O_2 in contact with the electrolyte over that directly at the cathode surface.[35] However, this is clearly an incomplete picture.

A key difference between the operation of TEMPO and TMPD is their charging potentials. **Figure 3.3a** shows that $TMPD^+$ has a lower charging plateau than cells with and without $TEMPO^+$, with slight polarisation towards the end of the charge period, indeed ending at a more positive potential than TEMPO. The exact relationship between the charging potential and Li_2CO_3 formation was determined by combining **Figure 3.3a** with each of **3.3b** and **3.3c** to produce **Figures 3.7a** and **3.7b**, respectively. It is clear that in all systems there is a slight linear increase in both

cathode and electrolyte decomposition from the onset of charge (above 2.96 V), followed by a greater increase in the rate of decomposition once the charging potential has reached approximately 3.45 V. This suggests that at this threshold potential a new process initiates leading to increased decomposition. Given that cells containing $TMPD^+$ charge at a potential below this range for a greater period of charge explains why, despite operating in otherwise the same way as $TEMPO^+$, $TMPD^+$ reduces the level of electrolyte decomposition whilst $TEMPO^+$ increases it, relative to cells unmediated cells. The factors that result in the trends observed are discussed in **Section 3.3.7** (page 139).

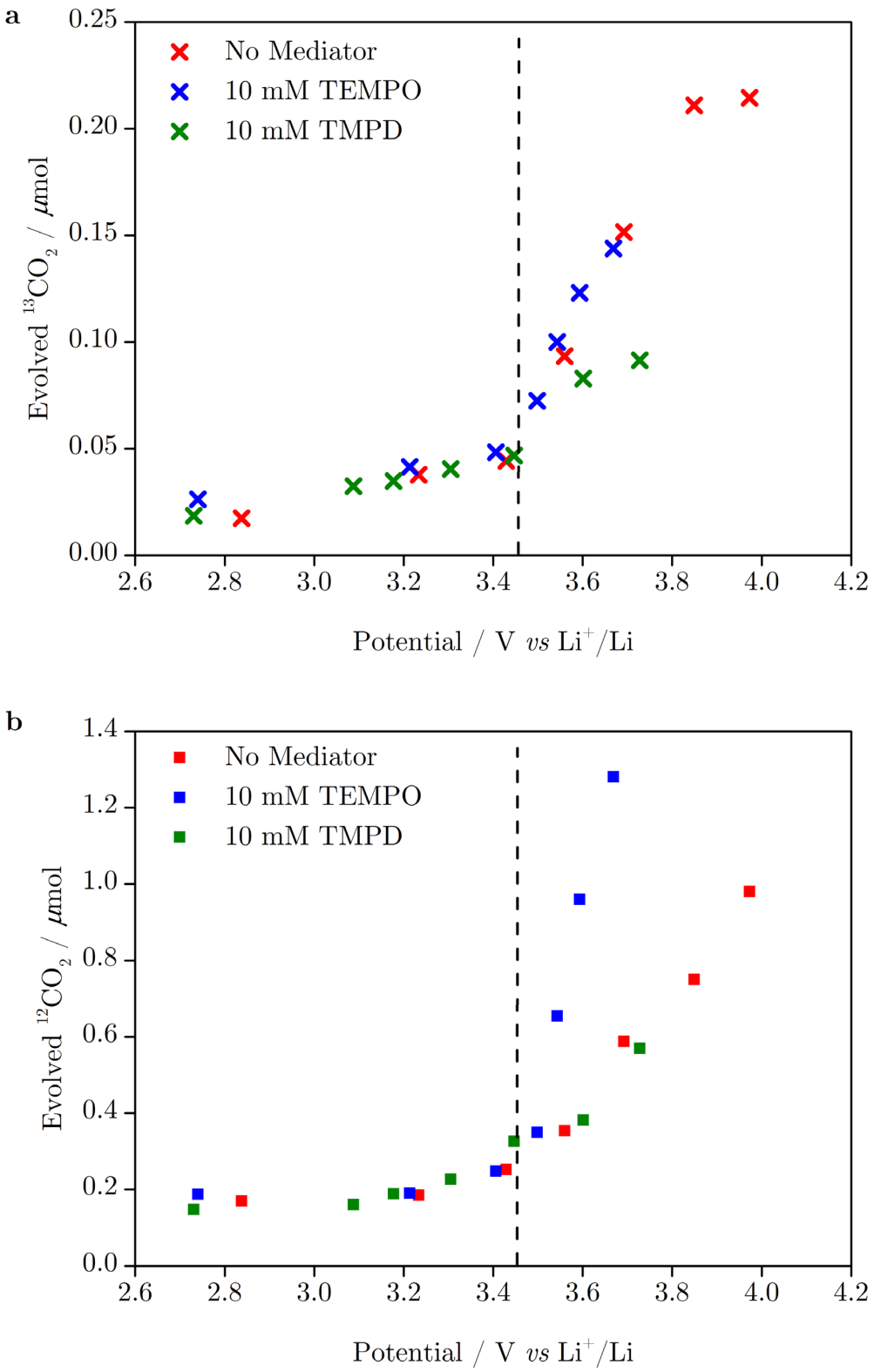

Fig. 3.7: Evolved CO_2 at various potentials during charge arising from **a.** cathode and **b.** electrolyte. Data extracted from **Fig. 3.3**.

3.3.4 Percentage Conversion of Capacity into Li_2CO_3

Whilst the discussion thus far has focussed on the decomposition during cell charge, it should be noted that some Li_2CO_3 formation occurs during discharge, accounting for approximately 1.1% of the total discharge capacity (1.0% originating from electrolyte decomposition and 0.1% from cathode decomposition[c]). It should be noted that the presence of charge RMs has negligible effect on the level of Li_2CO_3 at the end of discharge; this is to be expected given the RMs' inactivity at the more negative discharge potentials. Taking into account this baseline level of decomposition arising during discharge, it can be seen that the total amount of Li_2CO_3 generated during charge in cells without RMs accounts for approximately 9.1% (7.3% from electrolyte and 1.8% from cathode decomposition) of the charging capacity up to 600 μAh cm^{-2}. This represents a lower end fraction of charge capacity consumed by Li_2CO_3 formation; Li_2CO_3 is likely to still be produced above 3.82 V, although the rate of its electrooxidation will be far greater than the rate of its formation. The percentages calculated here are greater than those estimated by McCloskey *et al.*, who placed Li_2CO_3 quantities at between 5-7% of charge passed.[2] It is suggested that the greater values obtained in this work stems from the fact that here all Li_2CO_3 is liberated as CO_2 by the acid, whereas in McCloskey's work only the Li_2CO_3 in direct electrical contact with the cathode is oxidised (with the evolved CO_2 being measured via OEMS).

[c] The percentage of the capacity resulting in the formation of Li_2CO_3 was determined from the number of moles of Li_2CO_3 present and the moles of electrons transferred.

Charging with TEMPO results in only a slight variation in the total amount of Li_2CO_3 generated during charge compared to cells without a RM, at 10.8%. Use of TMPD, however, decreases this value to only 4.4% of the charge capacity, demonstrating the benefit of maintaining the charge potential below 3.45 V.

Whilst the level of decomposition on discharge is minimal relative to that on charge, its occurrence highlights one of the inherent issues surrounding Li-O_2 cells, namely their instability at all points of the cycle.

3.3.5 OEMS: Determining the Electron to Oxygen Ratio on Charge

The observation that Li_2CO_3 production increases at a markedly higher rate above approximately 3.45 V, regardless of whether RMs are included or not, is mirrored by the OEMS data presented in **Figure 3.8**. For unmediated cells and those containing TEMPO, there is an initial O_2 generation peak flux of 0.19 μmol min^{-1} at the start of charge, with the flux decreasing once the charge potential has reached 3.45 V.[d] A similar decrease in evolved O_2 at 3.45 V also occurs in cells containing TMPD and 5,10-dihydro-5,10-dimethylphenazine (DMPZ) (the cyclic voltammetry and OEMS data for DMPZ may be found in **Appendices 3.5.1** (page 159) and **3.5.2** (page 161), respectively), despite an absence of high peak flux. Indeed, this decrease in evolved O_2 above 3.45 V can be observed in the OEMS featured in numerous other studies.[10, 36-38] Notably, O_2 is generated from the start of charge in all cases (once the short delay

[d] The carrier gas was not changed from 20% O_2 in Ar between cell discharge and charge. To determine the O_2 evolved from Li_2O_2 oxidation, the cells were held at open circuit potential for several hours prior to charge to ensure a flat O_2 carrier gas baseline.

between O_2 evolution and instrumental detection has been accounted for), with CO_2 being evolved towards the end of charge once the potential has polarised sufficiently to electrooxidise any Li_2CO_3 present.

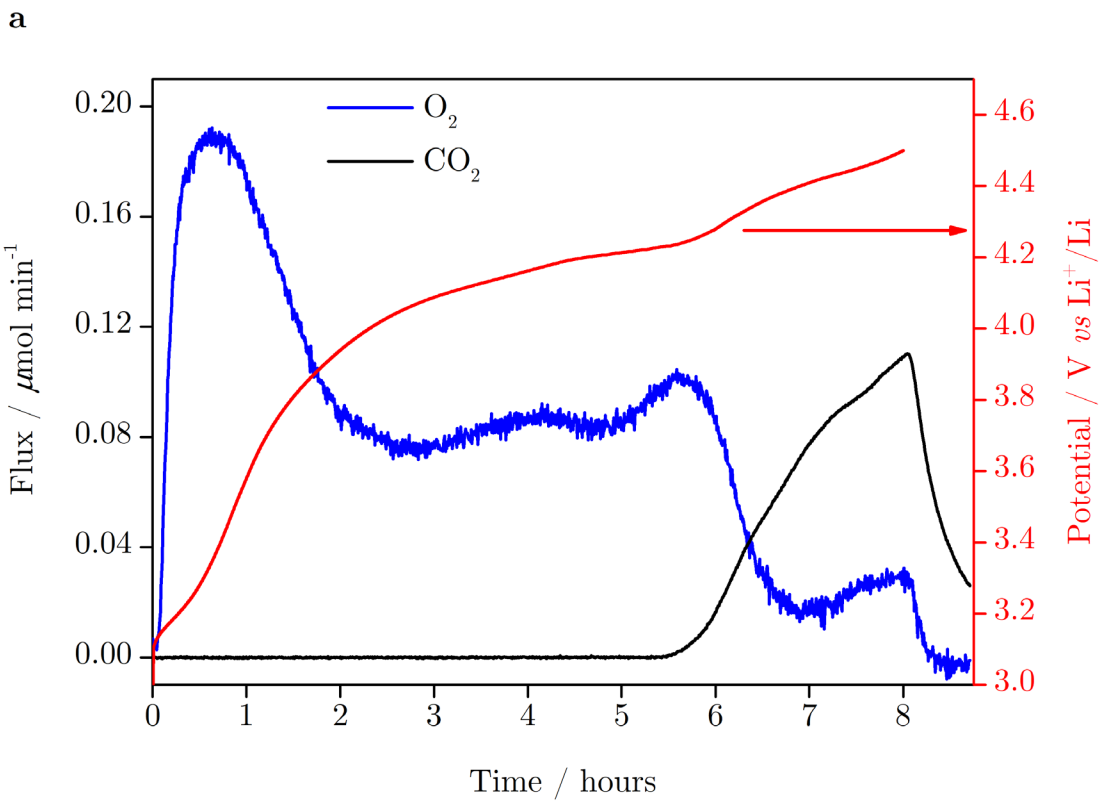

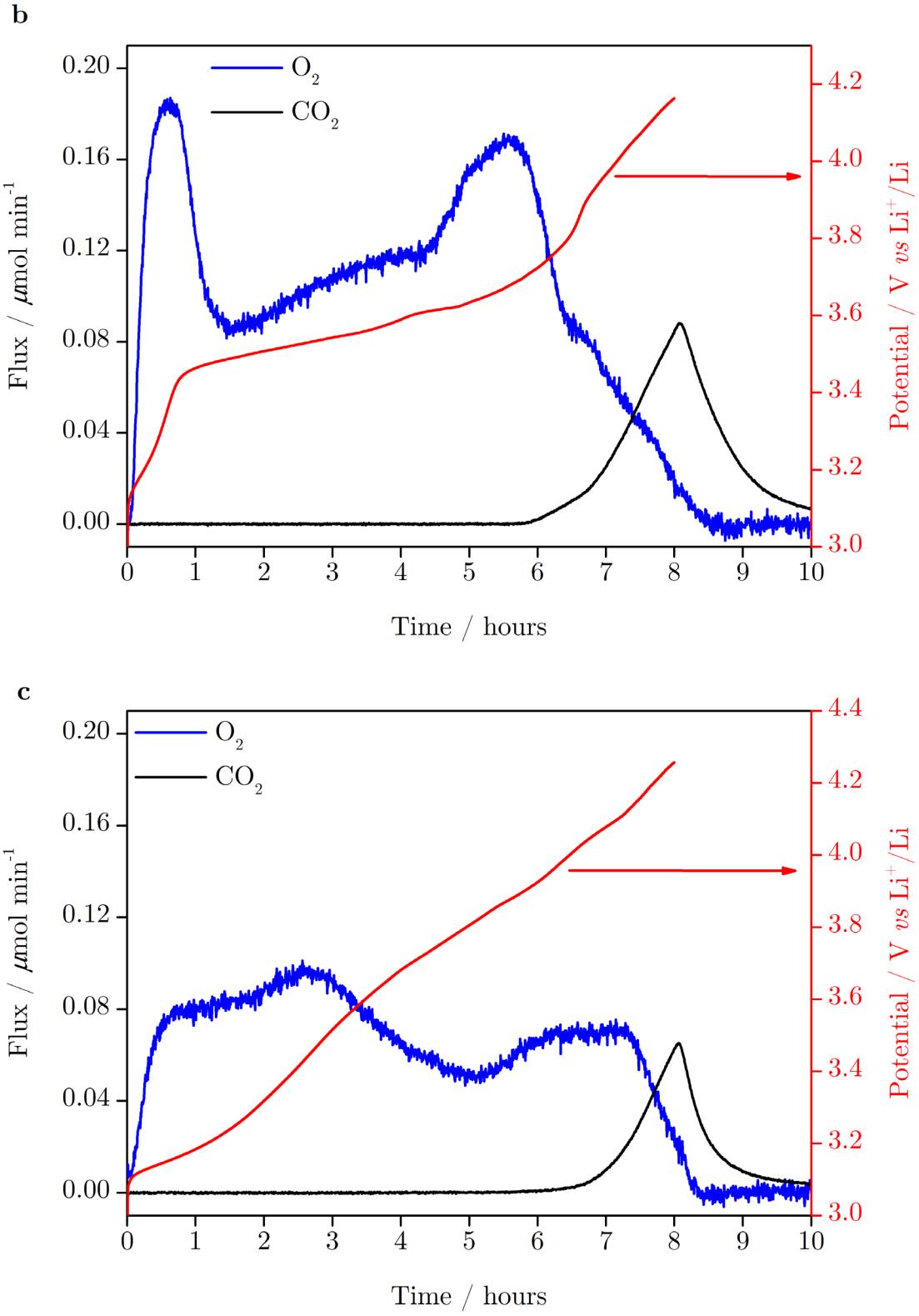

Fig 3.8: OEMS of charging cells **a.** (previous page) without RMs, **b.** with 10 mM TEMPO and **c.** with 10 mM TMPD in 1.0 M LiTFSI in TEGDME with a carrier gas of *circa* 20% O_2 in Ar (1.0 mL min^{-1} flow rate). Current density 100 μA cm^{-2}. Experimental details in **Section 3.2.5** (page 113).

From the quantity of O_2 evolved it was calculated that unmediated cells have an electron to O_2 ratio of 2.94, meaning that one molecule of O_2 was evolved for every 2.94 electrons passed. A value greater than the theoretical ratio of 2.00 for the oxidation of Li_2O_2 indicates that there are some parasitic side reactions occurring.[39] TEMPO has an improved ratio of 2.34, as expected from previous reports.[23] TMPD was found to have a poorer ratio than unmediated cells, at 3.88, demonstrating that while its inclusion results in less Li_2CO_3 being formed, as determined in **Section 3.3.3** (page 119), TMPD is heavily involved in side reactions that result in the passing of current without the evolution of O_2 (such as cycloaddition reactions with $^1O_2$).[40] As a further comparison, cells cycled with DMPZ were found to have an electron to O_2 ratio of 3.13; it is interesting to note that both RMs with a low redox potential have poor electron to O_2 yields.

Despite being worse than the unmediated cells, it should be noted that the electron to O_2 ratio obtained here for DMPZ is much closer to 2.00 than the values obtained by Lim *et al.* and Kwak *et al.*, who noted ratios of 5.76 and 8.52 (reduced to 6.03 when the $^1O_2$ quencher DABCO was included), respectively, even with the use of a solid electrolyte to prevent RM shuttling in the latter work.[18, 30] While the poor O_2 yield for cells containing low potential RMs may be attributed to the poor reaction kinetics of TMPD and DMPZ with Li_2O_2, which would likely lead to increased RM shuttling[e] to the counter electrode, given that the work conducted here has a higher O_2 yield for DMPZ without the use of a solid electrolyte compared to the

[e] A detailed explanation of RM shuttling is given in **Section 1.4.1.6** (page 45).

aforementioned studies, it is suggested that TMPD and DMPZ shuttling levels are quite low.[25, 35] This is further validated by TEMPO's improved electron to O_2 ratio compared to the unmediated system, which would not be expected if high levels of shuttling were taking place. It is therefore suggested that both TMPD and DMPZ are involved in other electrochemical processes that lead to the passing of current without a corresponding release of O_2, and hence the unfavourable electron to O_2 ratios.

It should be noted that, while the differences in electron to O_2 ratio between cell systems may mask the absolute level of Li_2CO_3 forming in Li-O_2 cells, it will not affect the observation that there is a marked increase in Li_2CO_3 formation at 3.45 V. With OEMS revealing that Li_2O_2 is oxidised below this threshold potential, it is clear that once 3.45 V is reached a new electrochemical process is initiated which forms a reactive species leading to Li_2CO_3.

3.3.6 Identifying the Reactive Intermediate Generated Above 3.45 V

Against the backdrop of the large number of recent publications focusing on the presence and effect of $^1O_2$ in Li-O_2 cells, in particular demonstrating its reactivity towards cell components, it was postulated that $^1O_2$ may be the cause for the significant increase in Li_2CO_3 observed at 3.45 V.[10-13, 16, 18, 39-42] In order to detect the presence of $^1O_2$ in charging cells, the $^1O_2$ trap 9,10-dimethylanthracene (DMA) was utilised.[11] $^1O_2$ combines with DMA in an irreversible equimolar reaction to form the endoperoxide 9,10-dimethylendoperoxianthracene (DMA-O_2), according to **Scheme 3.3**.

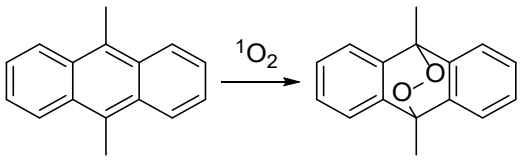

Scheme 3.3: Reaction of $^1O_2$ with DMA.

DMA reacts selectively with $^1O_2$, with $^3O_2$ having insufficient energy to undergo the required Diels Alder cycloaddition reaction, and is inert towards superoxide.[11, 43] DMA and its endoperoxide have been shown to be stable within the potential window that Li-O_2 cells operate, however no previous work has considered the implications of the presence of RMs in the electrolyte on DMA operation.[11] The cyclic voltammetry detailed in **Figures 3.1 and 3.2a** demonstrates that DMA is stable to both $TEMPO^+$ and $TMPD^+$, respectively, with the presence of DMA leading to no additional processes occurring beyond those attributed to the RM as evidenced by the lack of change in either the anodic or cathodic peak current densities. It should be noted that not all of the $^1O_2$ will react with DMA, as a proportion will react with cell components or will be quenched via another route.[11] As such, this work references what is the lower limit of $^1O_2$ concentration; indeed the true $^1O_2$ concentration may be higher.

DMA was added to unmediated cells and those containing either TEMPO or TMPD, with the results presented in **Figure 3.9**. In all cases, when DMA was present the total quantity of Li_2CO_3 from both the cathode and electrolyte at the end of charge was less than in cells without DMA. However, the presence of DMA only had an effect on the formation of Li_2CO_3 once the charging potential had reached 3.45 V, coinciding with the threshold potential for increased Li_2CO_3 formation as elucidated from **Figure**

3.7. This demonstrates that $^1O_2$ is present in all three systems on cell charging, with a mechanism for the formation of $^1O_2$ becoming active at 3.45 V. Importantly, the presence of DMA has a negligible effect on the charge profile; a comparison of the charge profiles of cells with and without DMA may be found in **Appendix 3.5.3**.

Despite lowering the quantity of Li_2CO_3 produced in all cell systems, DMA has the greatest effect in unmediated cells. It has previously been suggested that RMs may act as $^1O_2$ quenchers, and so in cells containing TEMPO and TMPD some of the $^1O_2$ may be expected to be quenched even without DMA present.[14, 44, 45] The addition of DMA will therefore be of less benefit in RM-containing cells than in unmediated cells.

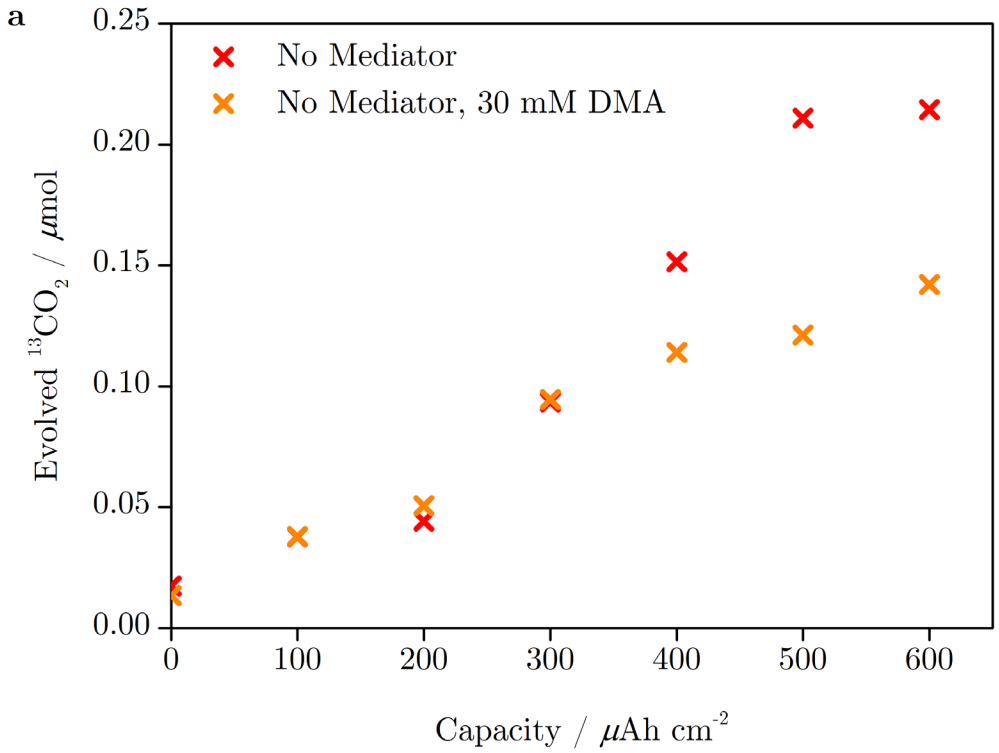

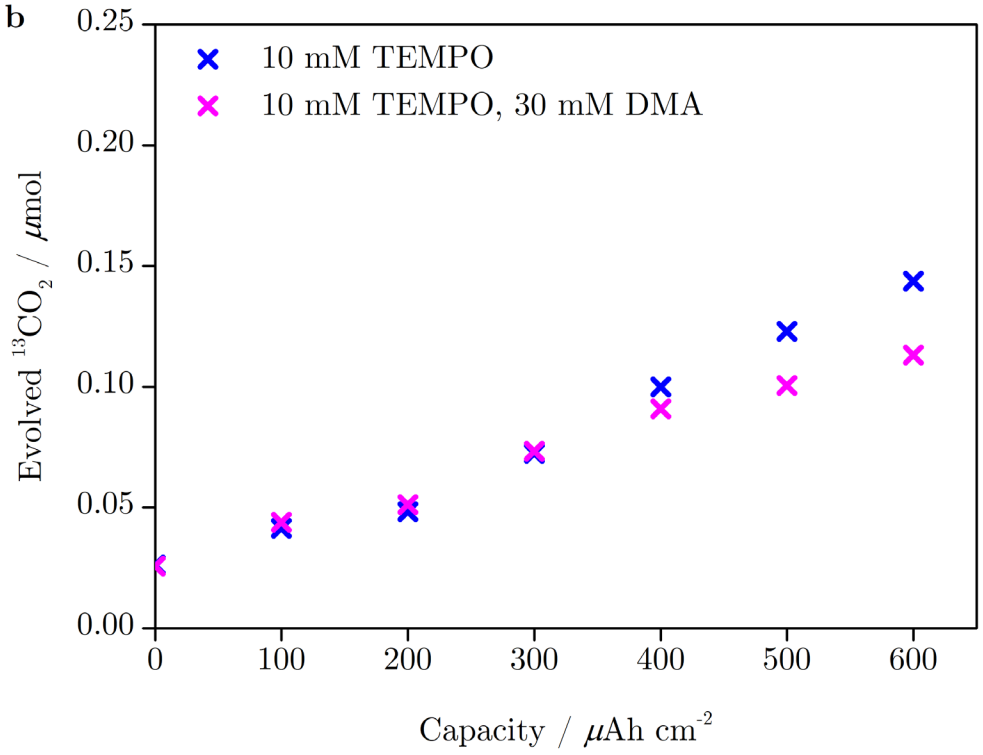
b
10 mM TEMPO
10 mM TEMPO, 30 mM DMA
Evolved $^{13}CO_2$ / μmol
Capacity / μAh cm^{-2}
0.00
0.05
0.10
0.15
0.20
0.25
0
100
200
300
400
500
600

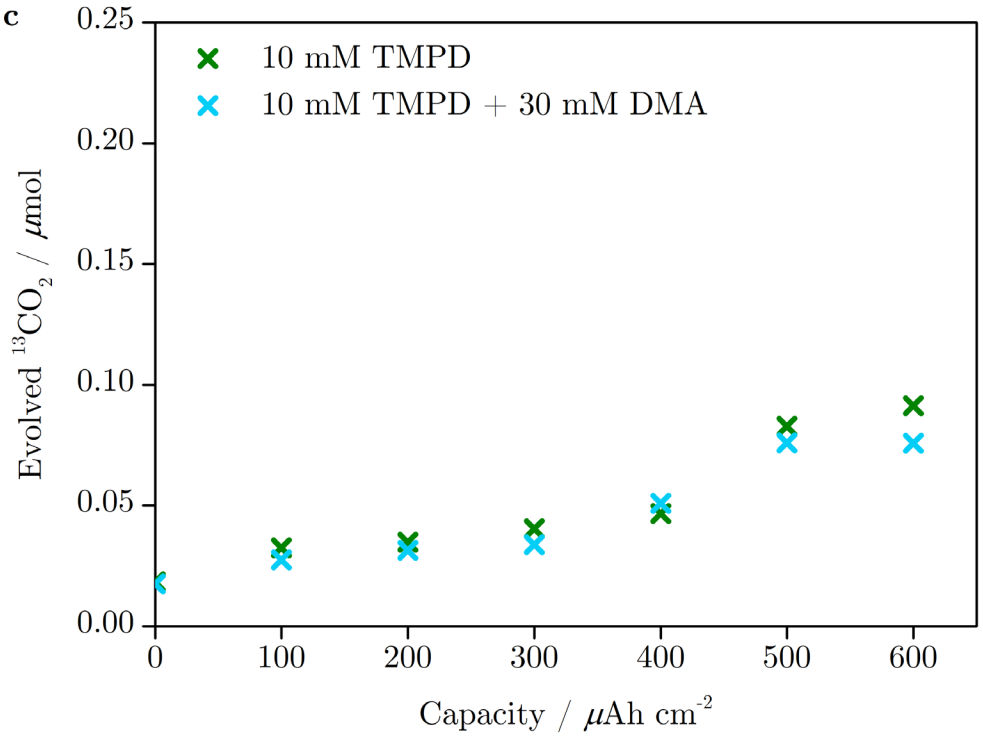
c
10 mM TMPD
10 mM TMPD + 30 mM DMA
Evolved $^{13}CO_2$ / μmol
Capacity / μAh cm^{-2}
0.00
0.05
0.10
0.15
0.20
0.25
0
100
200
300
400
500
600

d

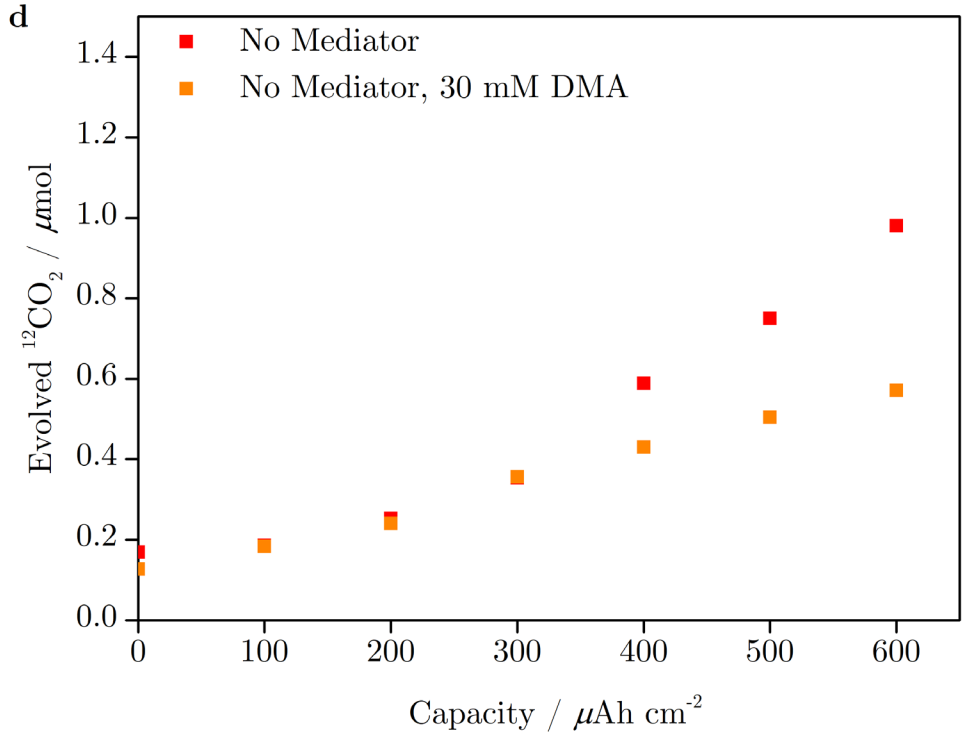
No Mediator
No Mediator, 30 mM DMA
Evolved $^{12}CO_2$ / μmol
Capacity / μAh cm^{-2}
0.0
0.2
0.4
0.6
0.8
1.0
1.2
1.4
0
100
200
300
400
500
600

e

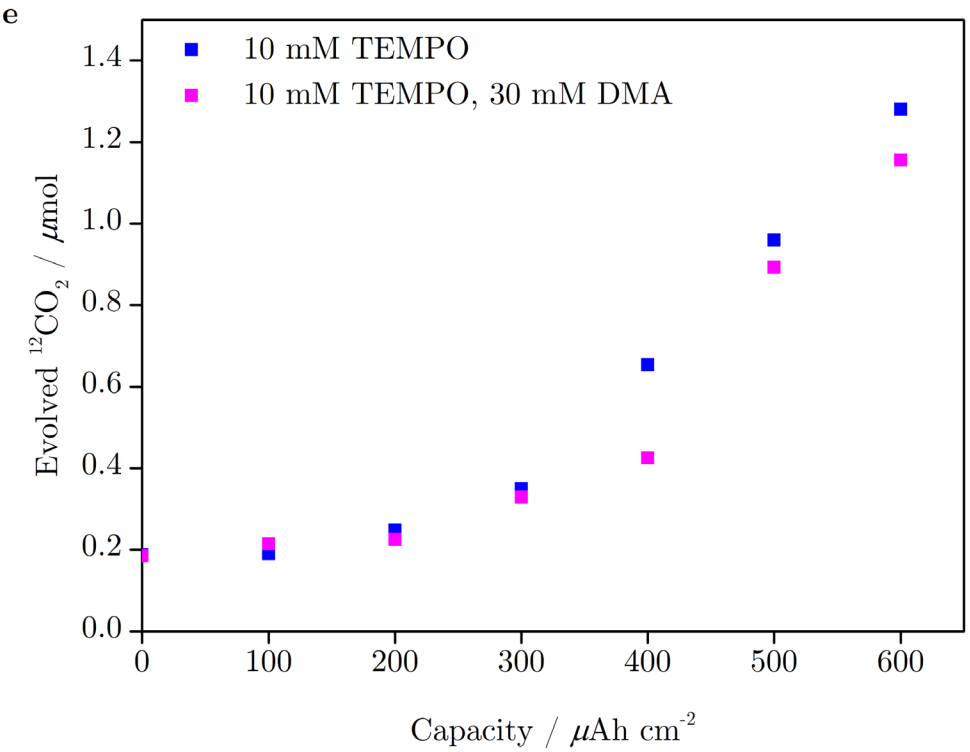
10 mM TEMPO
10 mM TEMPO, 30 mM DMA
Evolved $^{12}CO_2$ / μmol
Capacity / μAh cm^{-2}
0.0
0.2
0.4
0.6
0.8
1.0
1.2
1.4
0
100
200
300
400
500
600

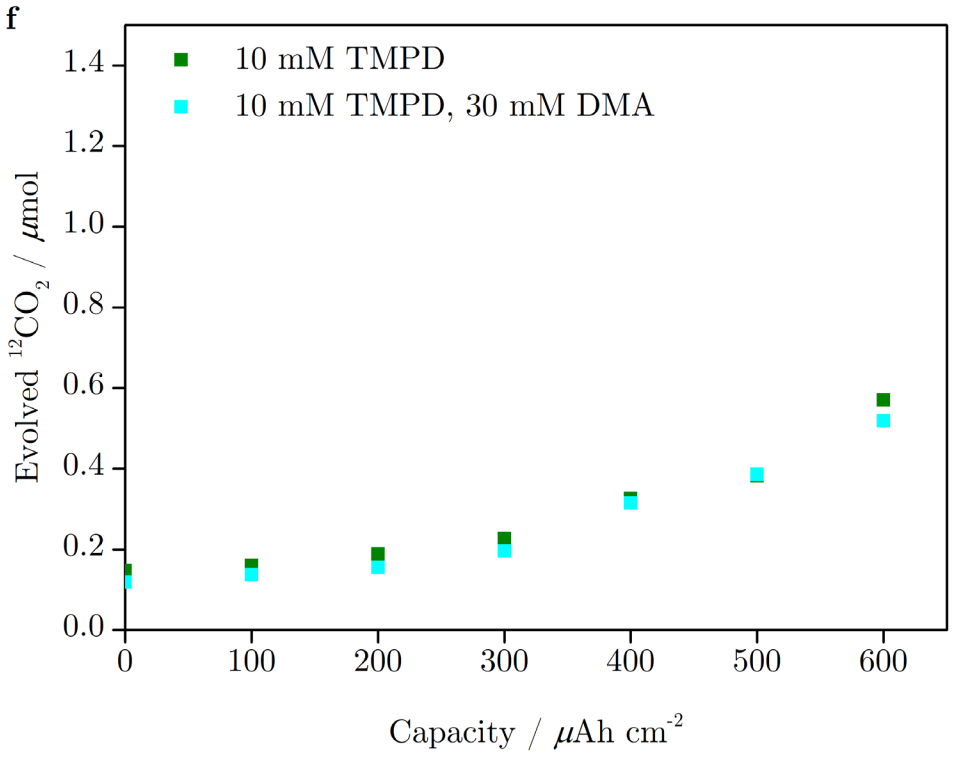

Fig. 3.9: Li_2CO_3 quantity at various points of charge in unmediated cells and those containing 10 mM TEMPO and 10 mM TMPD, with and without 30 mM DMA. **a-c.** $Li_2{}^{13}CO_3$ arising from the cathode and **e-f.** $Li_2{}^{12}CO_3$ arising from the electrolyte. Electrolyte solution was 1.0 M LiTFSI in TEGDME under 1 atm O_2. Current density 100 μA cm^{-2}. Further experimental details regarding cell cycling and acid treatment may be found in **Sections 3.2.3.1** (page 112) and **3.2.4** (page 113), respectively.

3.3.7 Fluorescence Spectroscopy to Elucidate the $^1O_2$ Onset Potential

To elucidate the exact potential at which $^1O_2$ forms, the fluorescence properties of DMA were exploited. As can be seen in **Figure 3.10**, DMA exhibits four fluorescence peaks, with the wavelengths of the peaks recorded in **Appendix 3.5.4** (page 163). An explanation for the physical process of fluorescence is given in **Section 2.3.2** (page 98).

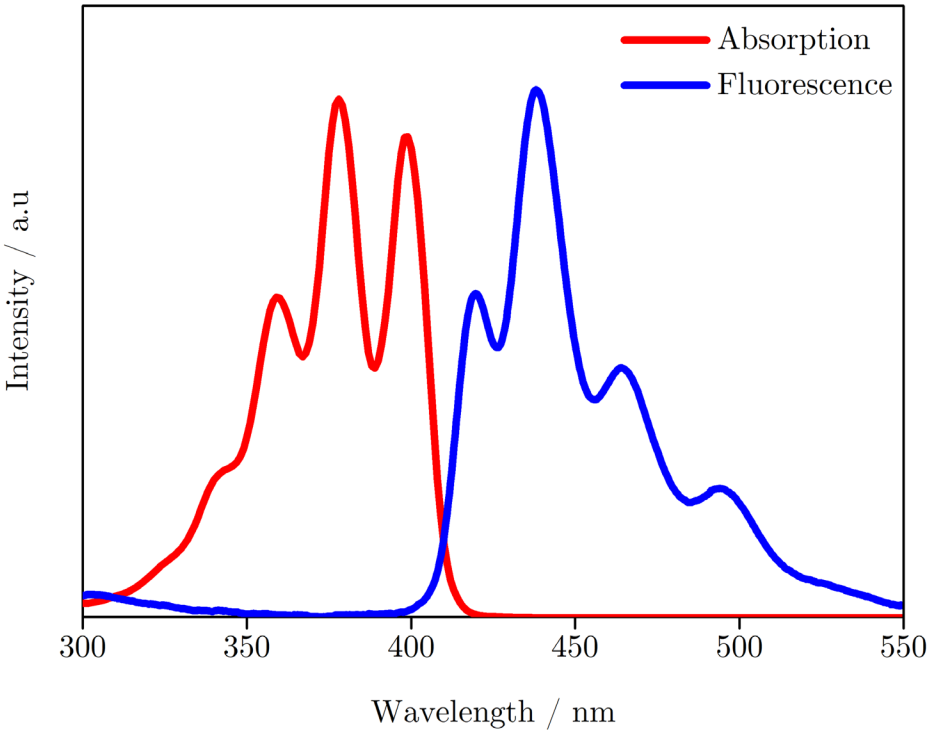

Fig. 3.10: Absorbance and fluorescence spectra of 32 μM DMA in TEGDME with 1 M LiTFSI. The fluorescence peak at 437.9 nm was monitored during cell charging. Experimental conditions as described in **Section 3.2.7** (page 114).

In contrast, the endoperoxide of DMA does not display fluorescence. As such, reaction of DMA with $^1O_2$ leading to a decrease in the former's concentration is reflected by a decrease in measured fluorescence intensity. To probe the exact potential at which $^1O_2$ begins to form in a charging Li-O_2 cell, an unmediated cell containing DMA was charged as described in **Section 3.2.7** (page 114), with the fluorescence emission at 437.9 nm monitored. It can be seen in **Figure 3.11** that there is no change in DMA concentration until the charging potential has reached 3.31 V, at which point the concentration of the $^1O_2$ trap begins to decrease. The OEMS of unmediated cells

in **Figure 3.8** shows that O_2 is indeed evolved below 3.31 V, verifying that the lack of $^1O_2$ below 3.31 V as observed through fluorescence spectroscopy is not simply due to no O_2 being evolved.

The decrease in DMA concentration is not constant, with the gradual linear decrease observed between 3.31 – 3.45 V followed by a much greater rate of DMA consumption above 3.45 V (the change in rate was determined from the first derivative of the DMA concentration). Further subsequent changes in the rate of DMA consumption above 3.80 V indicates there are a number of different processes occurring during charge that lead to different rates of $^1O_2$ evolution.

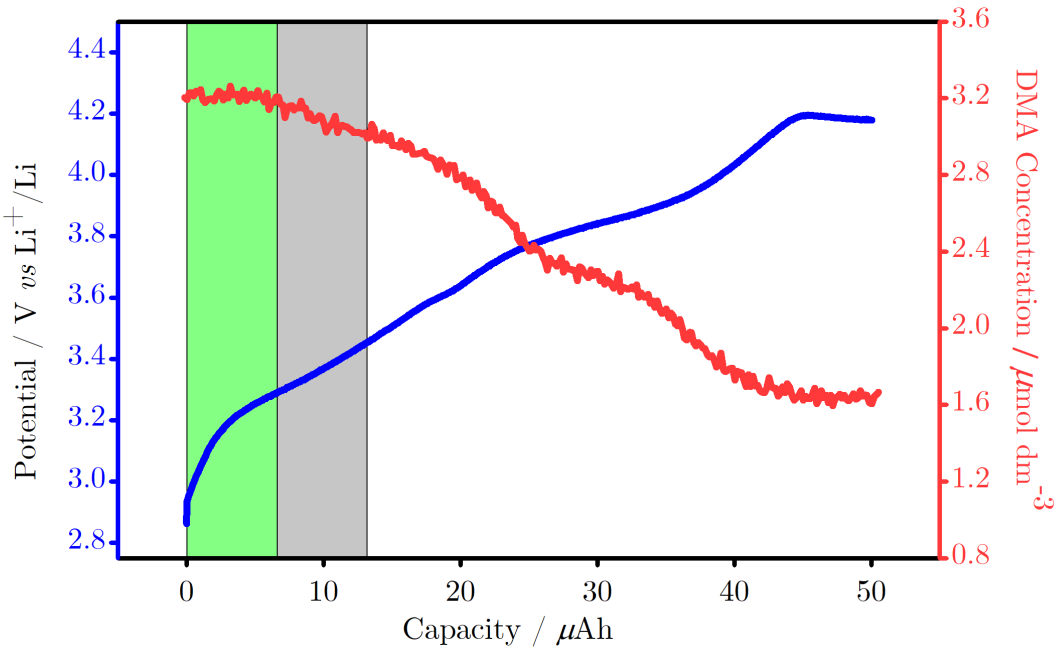

Fig. 3.11: *Operando* Fluorescence Spectroscopy during charge of Li-O_2 cell containing 32 μM DMA, with change in DMA concentration (red) and charge potential (blue) as a function of charge capacity. The region of the charge profile where the potential is below 3.31 V is shaded green, whilst the 3.31 – 3.45 V region is shaded grey. Electrolyte solution was TEGDME with 1.0 M LiTFSI under 1 atm O_2. Further experimental details may be found in **Section 3.2.7** (page 114), with data collected by Dr S. Yang.

The discrepancy between the onset potential of $^1O_2$ formation as determined through Li_2CO_3 quantification and that determined through fluorescence spectroscopy, with the latter revealing $^1O_2$ to form at a more negative potential, can be satisfactorily resolved through the thermodynamic and kinetic arguments presented in **Section 3.3.8** (page 142).

3.3.8 Theoretical Rationalisation of Experimental Observations

From the experimental data presented in this work thus far, it is clear that there are two key potential regions on charge where different routes to $^1O_2$ dominate: below and above 3.45 V. In addition, discussion of the selectivity of $^1O_2$ relative to $^3O_2$ and rationalisation of the absence of $^1O_2$ below 3.31 V is essential.

3.3.8.1 Charging Above 3.45 V: Direct Electrooxidation of LiO_2

For an O_2 molecule to be excited from the triplet to the singlet state, according to the transition:

$$^1\Delta_g \leftarrow {}^3\Sigma_g^- \qquad \textbf{Eq. 3. 1}$$

an input of energy is required. The commonly quoted energy for this transition is in the gas phase, corresponding to 0.97 eV, which for a single electron transition is equal to 0.97 V.[17, 46] Consideration must now be given to the energies of the oxygen-containing species produced during charge, with LiO_2 having been predicted and observed on charge in numerous studies, including within the solid structure of off-

stoichiometric $Li_{2-x}O_2$.[47-57] In work by Bender *et al.* the potential for the formation of $^3O_2$ from LiO_2, according to the reaction:

$$LiO_2 \rightarrow {}^3O_2 + Li^+ + e^- \qquad \textbf{Eq. 3.2}$$

was given as 2.46 V, while Mourad *et al.* and *Petit et al.* utilised a value of approximately 2.57 V.[14, 16, 58] As such, the equivalent reaction to yield $^1O_2$:

$$LiO_2 \rightarrow {}^1O_2 + Li^+ + e^- \qquad \textbf{Eq. 3.3}$$

would be ($E_0^{O_2/LiO_2}$ + ($^1\Delta_g \leftarrow {}^3\Sigma_g^-$)) V, giving a thermodynamic $^1O_2$ onset potential between 3.43 – 3.54 V. Given that the potential for the reaction:

$$Li_2O_2 \rightarrow LiO_2 + Li^+ + e^- \qquad \textbf{Eq. 3.4}$$

is 2.96 V, this computational range suggests that it is possible to charge a Li-O_2 cell without generating $^1O_2$ from direct LiO_2 electrooxidation, since there is a threshold potential that must be reached before $^1O_2$ evolution occurs.[59]

This theoretical onset potential of the formation of $^1O_2$ is confirmed by both the Li_2CO_3 and fluorescence data presented earlier in this Chapter. Once the charging potential has reached 3.45 V, there is a substantial increase in the rate of both Li_2CO_3 formation (**Figure 3.7**) and DMA consumption (**Figure 3.11**). Furthermore, DMA can be seen in **Figure 3.9** to minimise the quantity of Li_2CO_3 formed once the charging potential has reached 3.45 V, indicating that $^1O_2$ is being produced from this potential. The calculated onset potential range is further supported by the work of Wandt *et al.*, who reported an experimental $^1O_2$ onset potential of approximately 3.55 V using a spin trap.[10]

3.3.8.2 Rationalising $^{1/3}O_2$ Selectivity from Direct LiO_2 Electrooxidation

Although it becomes thermodynamically feasible for $^1O_2$ to be formed above the thermodynamic threshold of 3.43 – 3.54 V, it is clear that not all O_2 is evolved in the singlet state. It was previously suggested by Houchins *et al.* that there is no kinetic reason for the selectivity of $^1O_2$ over $^3O_2$.[17] However, the linear nature of the increase in Li_2CO_3 above 3.45 V and the decrease in DMA concentration with increasing charge demonstrates that this is not the case. The selectivity for $^1O_2$ and $^3O_2$ may be explained through consideration of the Butler-Volmer kinetics of the reactions present in **Equations 3.2** and **3.3**.

The Butler-Volmer Equation (**Equation 3.5**) gives the relationship between the current density and the applied overpotential for a reversible one-electron process:

$$j = j_0\left(exp\frac{\alpha_a nF\eta}{RT} - exp - \frac{(1-\alpha_a)nF\eta}{RT}\right) \qquad \textbf{Eq. 3.5}$$

which, for moderate positive overpotentials (where $\eta > 26$ mV), simplifies to the Tafel Equation:[60, 61]

$$j = j_0\left(exp\frac{\alpha_a nF\eta}{RT}\right) \qquad \textbf{Eq. 3.6}$$

This demonstrates that for an anodic process (where the potential is more positive than the equilibrium potential) an increase in overpotential leads to an increase in current density (a full explanation of the Butler-Volmer and Tafel equations and their terms, along with their derivation and the reasoning for the relationship they predict, may be found in **Section 2.1.1.1** (page 69)).

The total current density, j_{total}, for the direct electrooxidation of LiO_2 will be the sum of the current density for the oxidation of LiO_2 to $^3O_2$, j_{triplet}, and the current density arising from the oxidation of LiO_2 to $^1O_2$, j_{singlet}:[61]

$$j_{total} = j_{triplet} + j_{singlet} \qquad \textbf{Eq. 3.7}$$

It therefore holds that the relative contributions of LiO_2 oxidation to $^1O_2$ and $^3O_2$ to j_{total} will be given by:

$$j_{total} = j_{0\,triplet}\left(exp\frac{\alpha_{triplet}nF\eta_{triplet}}{RT}\right) + j_{0\,singlet}\left(exp\frac{\alpha_{singlet}nF\eta_{singlet}}{RT}\right) \qquad \textbf{Eq. 3.8}$$

The ratio of the current densities resulting from $^1O_2$ and $^3O_2$ generation (and thus the selectivity for $^1O_2$) is dependent upon the transfer coefficients, α, of each pathway, and the standard rate constant, k_s, of each electrochemical reaction, which may be extracted from the exchange current density, j_o:

$$j_0 = nFk_s(c_O)^{\alpha_a}(c_R)^{\alpha_c} \qquad \textbf{Eq. 3.9}$$

The selectivity for $^1O_2$, σ, is therefore given by **Equation 3.10**:[62]

$$\sigma = \frac{j_{singlet}}{j_{triplet}} = \left(\frac{j_{0\,singlet}}{j_{0\,triplet}}\right)\exp\left(\frac{nF(\alpha_{singlet}\eta_{singlet} - \alpha_{triplet}\eta_{triplet})}{RT}\right) \qquad \textbf{Eq. 3.10}$$

where $(\alpha_{singlet}\eta_{singlet} - \alpha_{triplet}\eta_{triplet})$ is a constant at all potentials above the onset potential for $^1O_2$ formation, with $\alpha_{singlet} = \alpha_{triplet} = 0.5$.

Assuming that all the terms in **Equation 3.10** are constants[f], then it is clear that the selectivity for $^1O_2$ will be independent of potential (once the potential is sufficiently positive to initiate formation of $^1O_2$) and so $^1O_2$ will be generated through

[f] The transfer coefficient is generally assumed to be a constant, but it is in fact potential dependent, as illustrated in **Section 2.1.1.1** (page 69). Slight deviation from linearity for the ratio of $^1O_2$ produced may therefore be attributed to variations in transfer coefficient.

direct electrooxidation of LiO_2 at a constant rate. This explains the approximately linear increase in Li_2CO_3 (observed in **Figures 3.3** and **3.7)** and the approximately linear decrease in DMA concentration (observed in **Figure 3.12)** above the 3.45 V threshold potential. The linear nature of DMA consumption can also be seen in other publications, but until now had yet to be given a detailed theoretical explanation.[11, 41] Should both k_s and α be known then it would be possible to predict the rate at which $^1O_2$ would be generated through direct electrooxidation of LiO_2. The results of the model described here are illustrated graphically in **Appendix 3.5.5** (page 160).

The transient deviation from linearity in the fluorescence spectroscopy at approximately 3.80 V coincides with the onset of Li_2CO_3 electrooxidation, however electrooxidation of Li_2CO_3 would be expected to increase the rate of $^1O_2$ formation, rather than decrease it.[12] Since Li_2CO_3 is being consumed at this point, comparison of the Li_2CO_3 quantity and the fluorescence data cannot be made. Further investigation using alternative techniques is required to fully explain this deviation from linearity.

3.3.8.3 Charging Below 3.45 V: Disproportionation of LiO_2

The thermodynamic calculations in the previous Section explain the presence of $^1O_2$ above 3.45 V, however they do not explain the small linear decrease in DMA fluorescence or slight increase in Li_2CO_3 below this potential. Whilst the direct electrochemical route to $^1O_2$ only occurs at a potential above 3.45 V, $^1O_2$ may still be formed through the disproportionation of LiO_2 at all potentials during both discharge and charge, as demonstrated by Mahne *et al.* and Mourad *et al.*:[11, 16]

$$2LiO_2 \rightarrow Li_2O_2 + {}^1O_2 \qquad \textbf{Eq. 3.11}$$

Beyond the requirement of an applied potential to generate the initial LiO_2 (unless the LiO_2 forms from addition of KO_2 to a lithium salt), this reaction is potential independent. The $^1O_2$ from LiO_2 disproportionation may also react with DMA present in the cell, providing an explanation for the decrease in DMA fluorescence intensity (**Figure 3.11),** and with the cathode and electrolyte, explaining the increase in Li_2CO_3 (**Figure 3.7**) below 3.45 V.

From the gradients of the DMA decrease and Li_2CO_3 increase below 3.45 V in **Figures 3.11** and **3.7**, respectively, it can be seen that the rate of $^1O_2$ formation through LiO_2 disproportionation is slower than that formed through direct electrochemical oxidation of LiO_2. This slower rate of $^1O_2$ formation through disproportionation can be explained through a comparison of the kinetics of the two processes, with the rate of LiO_2 disproportionation governed by the following rate equation:[63]

$$rate = k[LiO_2]^2 \qquad \textbf{Eq. 3.12}$$

Since the rate of LiO_2 disproportionation is second order with respect to LiO_2, it is essential that two LiO_2 moieties are able to come together. However, given that there has been no reported observation of soluble superoxide on charge in acetonitrile through SERS or in TEGDME (as used in the work) through RRDE (both of which are low donor number solvents), the diffusion of LiO_2 within the cell is considered unlikely and so the local concentration of LiO_2 will remain low.[51, 64] It is therefore assumed that the direct electrochemical oxidation of LiO_2 will have faster kinetics than

disproportionation, given that direct electrochemical oxidation of LiO_2 is possible even if the LiO_2 is on the outer edge of the Li_2O_2 particle and away from the cathode surface.[65] Indeed, it has been shown that the rate of $^1O_2$ formation via disproportionation in Na-O_2 cells with a TEGDME electrolyte is slower than direct electrochemical oxidation of NaO_2.[41]

Provided there is electrical contact of the Li_2O_2 with the cathode, direct electrooxidation of LiO_2 will dominate in a TEGDME electrolyte, however in higher donor number solvents such as DMSO this may not be the case, as LiO_2 becomes more soluble and the rate of disproportionation increases.[17, 51, 66] Furthermore, the exact ratio of $^1O_2$ to $^3O_2$ produced through disproportionation has been shown to vary depending on the donor number of the solvent, with a greater proportion of $^1O_2$ formed in high donor number solvents due to the Marcus kinetic behaviour of LiO_2 disproportionation (where the solvent reorganisation energy affects the rate of reaction).[17]

With the fluorescence spectroscopy showing that $^1O_2$ is formed at potentials above 3.31 V, it is interesting to note that the presence of DMA in charging cells has no discernible effect on Li_2CO_3 formation between 3.31 – 3.45 V, despite $^1O_2$ still being produced through disproportionation of LiO_2. However, given the low rate of $^1O_2$ formation through disproportionation and that Li_2CO_3 may be but one of a number of decomposition products arising from the reactions of $^1O_2$, it is suggested that the Li_2CO_3 quantification method is simply insufficiently sensitive to discern the change in Li_2CO_3 quantity due to the presence of DMA in the electrolyte below 3.45 V. Other

reactions may also be contributing to the formation of Li_2CO_3, which will be discussed in **Sections 3.3.9** and **3.3.10** (pages 152 and 156, respectively).

3.3.8.4 Absence of $^1O_2$ below 3.31 V

The absence of $^1O_2$ in the fluorescence spectroscopy below 3.31 V suggests that LiO_2 disproportionation does not occur below this potential. Since O_2 is observed to evolve from cells charging below this potential (**Figure 3.8 and Figure 3.17**) this suggests that there is an initial charging mechanism for the electrooxidation of Li_2O_2 where any generated LiO_2 is quickly consumed through direct electrooxidation to produce $^3O_2$ (**Equation 3.4** followed by **Equation 3.2**)[g]. This is supported by Houchins *et al.*, who suggested that an oxygen-rich Li_2O_2 surface termination is required for LiO_2 disproportionation to be favoured during charge.[17] Given that the calculated potential for the formation of the (0001) oxygen-rich terrace by Viswanathan *et al.* of 3.36 V is in approximate agreement with the experimentally determined $^1O_2$ onset potential of 3.31 V in this work, it is suggested that the lack of $^1O_2$ below 3.31 V is due to negligible LiO_2 disproportionation occurring below this potential.[54, 55, 67, 68] Instead, the generated LiO_2 will be quickly consumed via direct electrooxidation (which has a high overpotential at the start of charge) to form $^3O_2$.[54]

[g] The electrooxidation of LiO_2 to $^3O_2$, as given by **Equation 3.2**, has a potential of 2.46 – 2.57 V, and so is able to occur at all charging potentials (2.96 V and above).

3.3.8.5 Further Considerations: $^1O_2$ Quenching and Mediated Formation

In the discussions of $^1O_2$ formation and reaction, minimal reference has so far been made to possible $^1O_2$ quenching mechanisms that may be occurring (involving the electrolyte, the cathode or O_2^{-}). Given that it is a chemical process, the rate of quenching is expected to be independent of potential. RMs may also act as $^1O_2$ quenchers, with the quenching rate dependent upon a number of factors including number of atoms and the atomic mass of the heaviest atom.[14, 44, 45] As such, more quenching of $^1O_2$ is likely to occur in TEMPO-, TMPD- and DMPZ-containing cells, potentially leading to less decomposition through reaction of $^1O_2$ with either the electrolyte or cathode.

A further pathway of LiO_2 oxidation to yield $^1O_2$ exists involving reaction with RM^+, according to **Equation 3.13**:

$$LiO_2 + RM^+ \rightarrow {}^1O_2 + RM + Li^+ \qquad \textbf{Eq. 3.13}$$

However, given the low local concentration of RM^+ in a charging cell, it is unlikely that RM^+ will come into contact with LiO_2 before direct electrooxidation or disproportionation of LiO_2 occurs, and so this route is considered unlikely to contribute significantly to the oxidation of LiO_2. Of course, should a discharge RM be included in the cell to facilitate complete solution-based growth of Li_2O_2 on discharge, then indeed this pathway, along with LiO_2 disproportionation, would become more significant, as demonstrated by Petit *et al.*[14] It should be noted that in the work of Petit *et al.* both TMPD and DMPZ were shown to not form $^1O_2$ through chemical reaction with either

Li_2O_2 or KO_2 (which was used as a substitute for LiO_2), whereas TEMPO did form some $^1O_2$.[14]

3.3.8.6 Implications for Li-O_2 Cells

Through monitoring Li_2CO_3 formation, DMA consumption through fluorescence spectroscopy, and O_2 evolution through OEMS, this work has established that there is a potential region below 3.45 V (in a TEGDME electrolyte) in which a Li-O_2 cell may be charged with minimal quantities of $^1O_2$ being formed (and indeed with no $^1O_2$ detected below 3.31 V). Thermodynamic considerations provide an explanation for the sudden increase in Li_2CO_3 formation observed at 3.45 V (resulting from the onset of $^1O_2$ formation through direct electrooxidation of LiO_2), and novel application of Butler-Volmer kinetics has provided justification for the constant rate of decomposition stemming from the reaction of $^1O_2$ to form Li_2CO_3. The slower rate of $^1O_2$ formation through disproportionation compared to direct LiO_2 electrooxidation has been explained, and the absence of LiO_2 disproportionation below 3.31 V has also been justified. A visual summary of the different processes occurring during charge is presented in **Figure 3.12**.

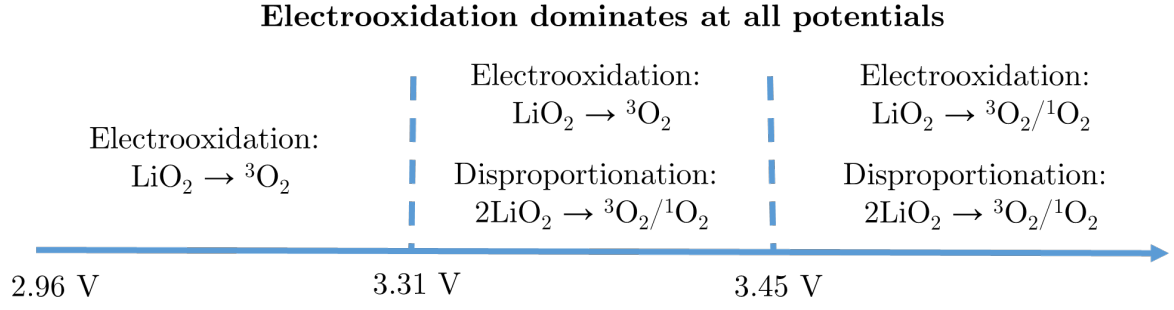

Fig. 3.12: Schematic summarising the reactions occurring in the different potential windows on charge.

The conclusions thus far provide an exciting opportunity for the Li-O_2 field; provided that the charging potential in TEGDME is restricted within the 2.96 – 3.45 V window, decomposition of the electrolyte and carbon cathode may be minimised. However, if the potential can be maintained below 3.31 V, then $^1O_2$, which is responsible for a significant proportion of decomposition in a charging Li-O_2 cell, may be avoided entirely.[11]

3.3.9 Minimising Decomposition through Low Charging Potential

Following the conclusions of the previous Section, it would be expected that cells in which the charge potential was maintained below 3.31 V (to ensure that no $^1O_2$ is generated) would have suppressed levels of Li_2CO_3 formation. To provide a further example of a low potential RM suppressing decomposition, DMPZ was used in place of TMPD. A direct comparison of the charge profile of DMPZ with TMPD, and the quantity of CO_2 evolved after charging to 600 μAh cm^{-2} can be seen in **Figure 3.13**, with there being negligible difference between the performance of the two RMs.

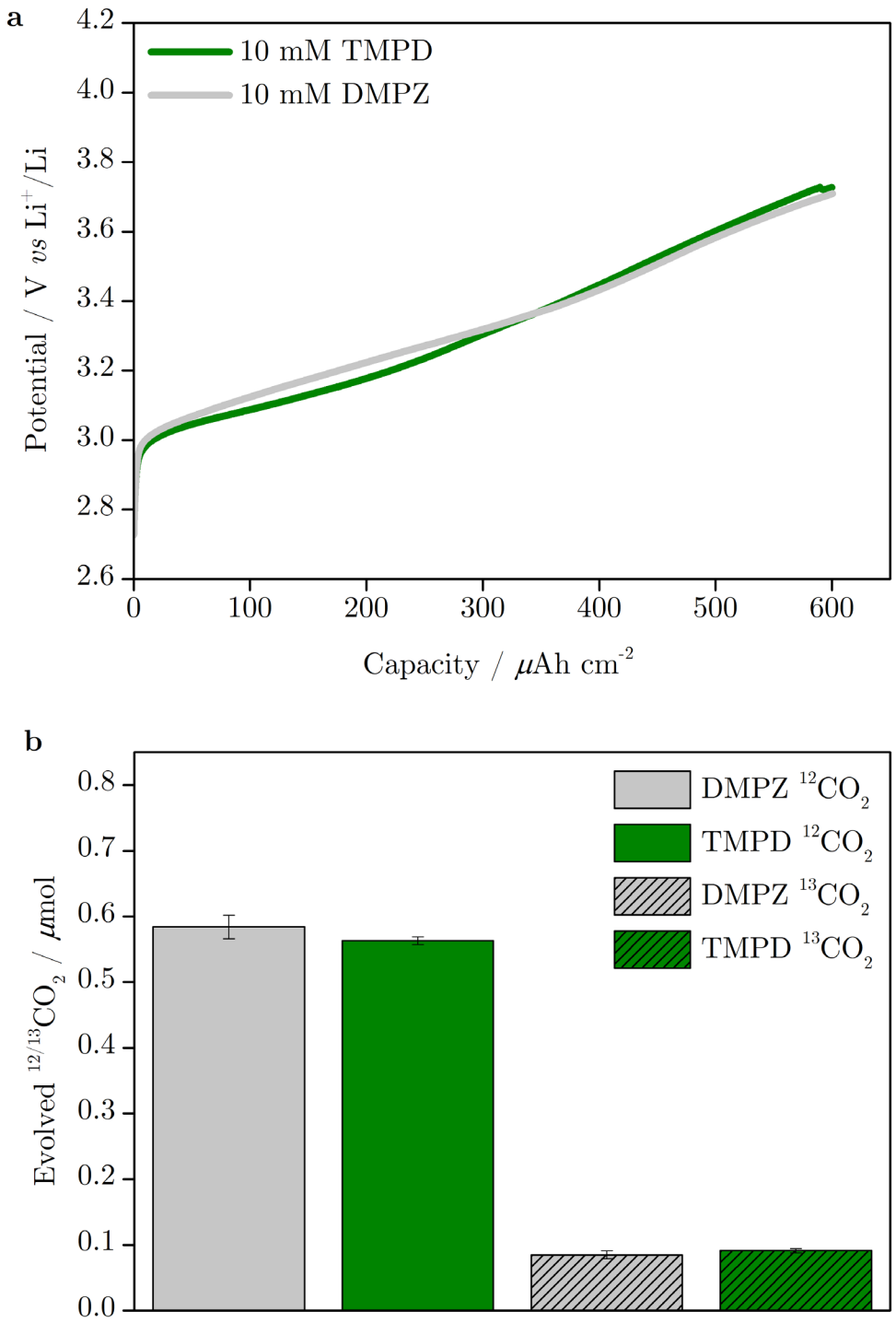

Fig. 3.13: a. Charge profile and **b.** CO_2 arising from electrolyte (solid bars) and cathode (striped bars) decomposition at a charge capacity of 600 μAh cm^{-2} in cells with 10 mM DMPZ (grey) and 10 mM TMPD (green). Electrolyte solution was TEGDME with 1.0 M LiTFSI under 1 atm O_2 at a current density 100 μA cm^{-2}. Error bars illustrate standard deviation from at least three repeats. Further experimental details may be found in **Sections 3.2.3.1** (page 112) and **3.2.4** (page 113), respectively.

To assist the cell in maintaining a charge potential below 3.31 V, the charge rate was reduced to 10 μA cm^{-2}, rather than the 100 μA cm^{-2} used in the earlier experiments. In addition, the cell was constructed with a Li^+-conducting solid electrolyte, which acted as a physical barrier preventing the passage of the 20 mM $DMPZ^+$ used from the cathode to the counter electrode, thus ensuring that RM^+ shuttling could not contribute to the charge capacity. These modified parameters led to suppressed decomposition of the electrolyte and carbon cathode, with no sudden increase in the rate of Li_2CO_3 formation caused by the onset of $^1O_2$ formation through direct electrooxidation of LiO_2 (**Figure 3.14**).

The total quantity of $Li_2{}^{12}CO_3$ present in the cell after charging to a capacity of 600 μAh cm^{-2} was 0.445 μmol, while the $Li_2{}^{13}CO_3$ quantity at the same point of charge was 0.058 μmol, as illustrated in **Figure 3.14**. This means that only 2.3% of the charge capacity results in Li_2CO_3 formation, compared to the 9.1% in unmediated which are permitted to polarise above 3.31 V (**Figure 3.3**), representing an overall decrease in total Li_2CO_3 of approximately 75%. This represents the first reported use in a Li-O_2 cell of low potential RMs to successfully suppress Li_2CO_3 formation without the need for a $^1O_2$ trap or quencher.

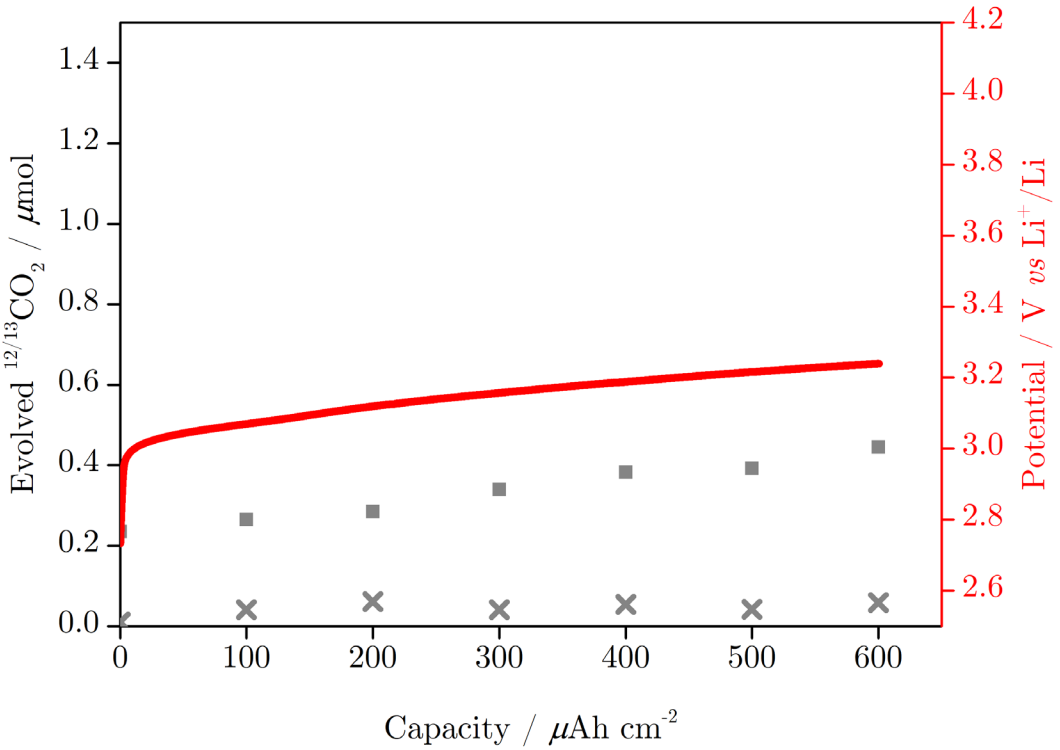

Fig. 3.14: Charge profile and evolved CO_2 from electrolyte (square) and cathode (cross) decomposition in cells containing 20 mM DMPZ in a DME with 1 M LiTFSI catholyte with a Li^+-conducting solid electrolyte, at a current density of 10 μA cm^{-2}. Further experimental details for cell cycling and acid treatment may be found in **Sections 3.2.3.1** (page 112) and **3.2.4** (page 113)**,** respectively.

Despite the significant improvement in electrolyte and cathode stability, there was still a small linear increase in Li_2CO_3, indicating that a residual level of decomposition is occurring even with the potential kept below 3.31 V. With low potential RMs suppressing the charging potential below 3.82 V, this residual low level of Li_2CO_3 formation remains problematic. Ordinarily, Li_2CO_3 is electrooxidised at potentials above 3.82 V and so is removed from the cathode surface. However, remaining below this potential will result in its accumulation and so lead to eventual

passivation of the cathode surface.[69] Furthermore, it has been shown that RMs are incapable of oxidising carbonates, with only one soluble redox-active species, binuclear cobalt phthalocyanine, being suggested to decompose Li_2CO_3 (and only then at a high potential of 3.74 V).[70, 71] Complete elimination of Li_2CO_3 formation is therefore essential if use of low potential RMs is to be a viable answer to the suppression of $^1O_2$.

3.3.10 Investigation of Whether Li_2O_2 Causes Decomposition

With the observation that there remains a low level of Li_2CO_3 formation even when the charge potential was maintained below 3.31 V, and observing that the rate of Li_2CO_3 increase is constant, attention was turned towards identifying the species responsible. A number of reports have suggested that Li_2O_2 in contact with both the carbon cathode and the ethereal electrolyte may result in the formation of carbonate species.[2, 72] Cells were therefore discharged to a fixed capacity and then either charged (in the presence of TEMPO) or left at open circuit potential[h] for an equivalent length of time. It was found that when the discharged cells were left at open circuit potential (OCV), there was no discernible increase in the quantity of Li_2CO_3 originating from either decomposition of the cathode or the electrolyte (**Figure 3.15**). In contrast and as already extensively highlighted, those cells in which a current was passed saw a substantial increase in Li_2CO_3 levels, particularly above 3.45 V.

[h] Open circuit potential is the potential between the working and reference electrodes when the two electrodes are electrically disconnected, meaning that no current can flow (equivalent to infinite resistance). Here the OCV was 2.74 V following discharge.

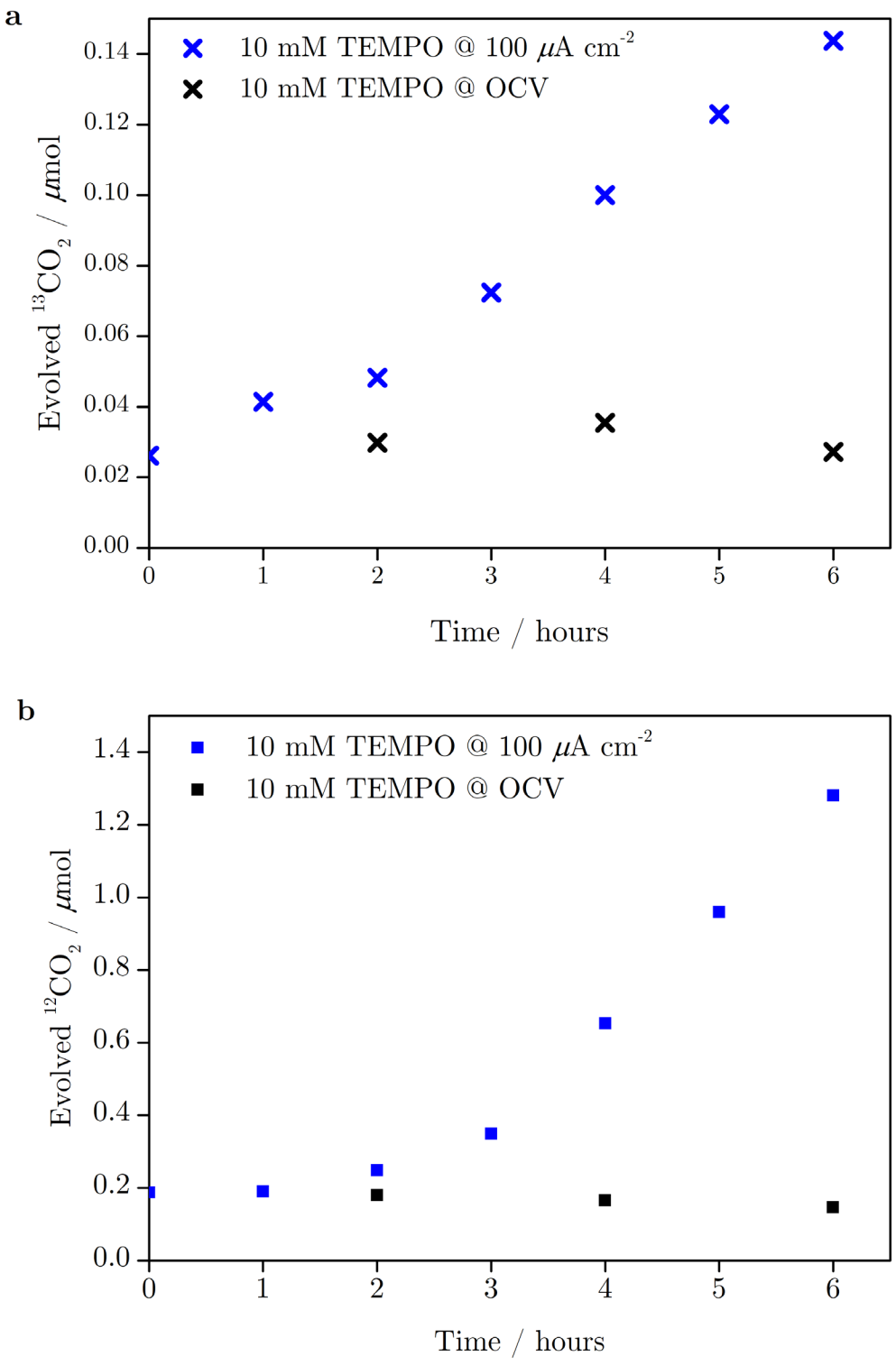

Fig. 3.15: Comparison of decomposition arising from **a.** the cathode and **b.** electrolyte when cells containing 10 mM TEMPO are discharged to 900 μAh cm^{-2} then either charged (blue, 100 μA cm^{-2}) or left at OCV (black) for equivalent time periods. Electrolyte was TEGDME with 1 M LiTFSI. Experimental details may be found in **Sections 3.2.3.1** and **3.2.4** (pages 112 and 113, respectively).

The lack of increase in Li_2CO_3 in the cells at open circuit suggests that both the carbon cathode and electrolyte are stable towards Li_2O_2 (over the period of time investigated), although it is still possible that Li_2O_2 is involved in side reactions to form species other than Li_2CO_3 (such as lithium formate and acetate). Regardless, this provides clear evidence that the residual Li_2CO_3 observed in **Figure 3.14**, which is not attributed to the electrochemical generation of $^1O_2$, only forms with the passing of current, indicating that such decomposition is due to another electrochemically generated intermediate (perhaps O_2^- or lithium-deficient $Li_{2-x}O_2$).[1, 49, 50, 73, 74]

3.4 Conclusions

The work in this Chapter has demonstrated that the electrochemical generation of $^1O_2$ is not an inevitable consequence of charging a Li-O_2 cell, but rather occurs at detectable levels only when the charging potential has increased above 3.31 V. Even then, the rate of $^1O_2$ formation remains low (and so Li_2CO_3 levels remain low) until the potential is above 3.45 V, at which point $^1O_2$ may be produced through direct electrooxidation of LiO_2. The use of low potential RMs such as TMPD and DMPZ can maintain the charging potential below this potential threshold, minimising the formation of $^1O_2$ and so reducing the degree of carbon cathode and ethereal electrolyte decomposition. However, keeping the charging potential below 3.82 V means that any Li_2CO_3 produced via alternative routes will build up during cycling, leading to cathode passivation. As such, tandem strategies to close down all routes to Li_2CO_3 are necessary.

3.5 Appendices

3.5.1 Cyclic Voltammetry of DMPZ

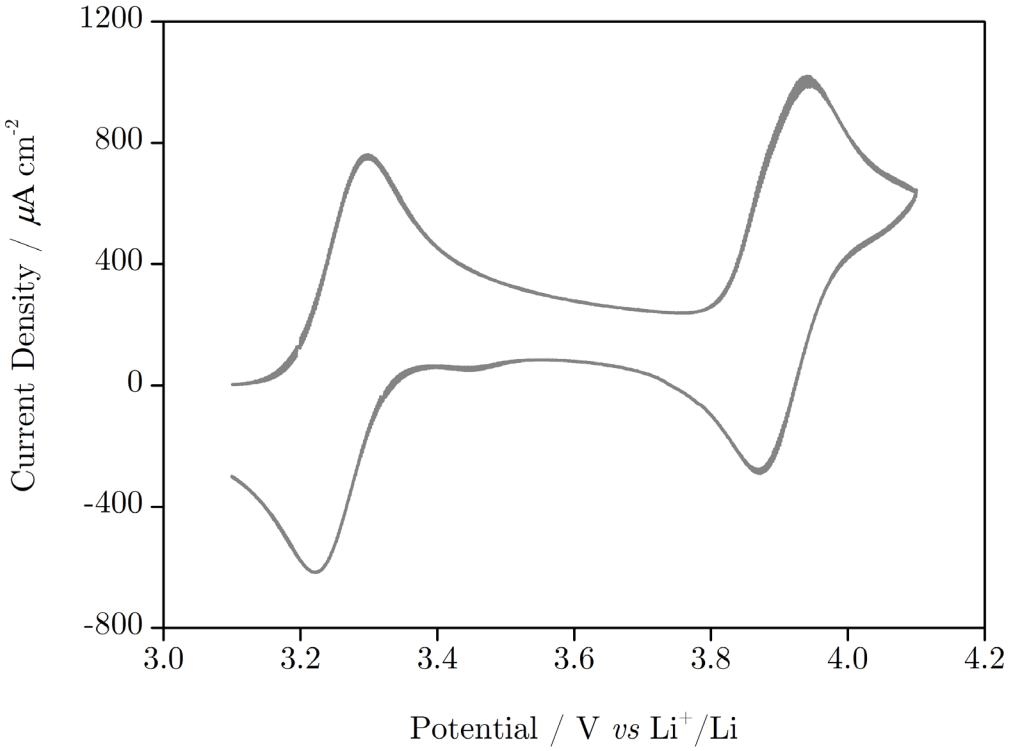

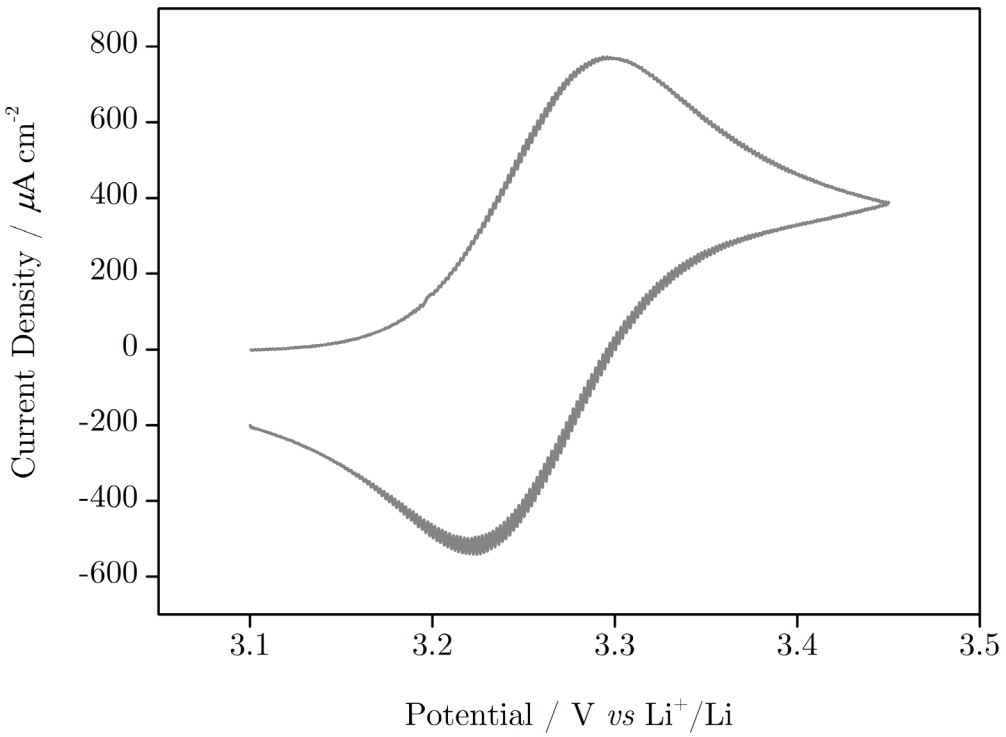

Fig. 3.16: a. (previous page) Cyclic voltammogram of 30 mM DMPZ in TEGDME with 1 M LiTFSI at a scan rate of 100 mV s^{-1} and **b.** cyclic voltammetry of the same with anodic scan limited to 3.45 V. Experimental conditions as described in **Section 3.2.1** (page 110).

3.5.2 OEMS of DMPZ

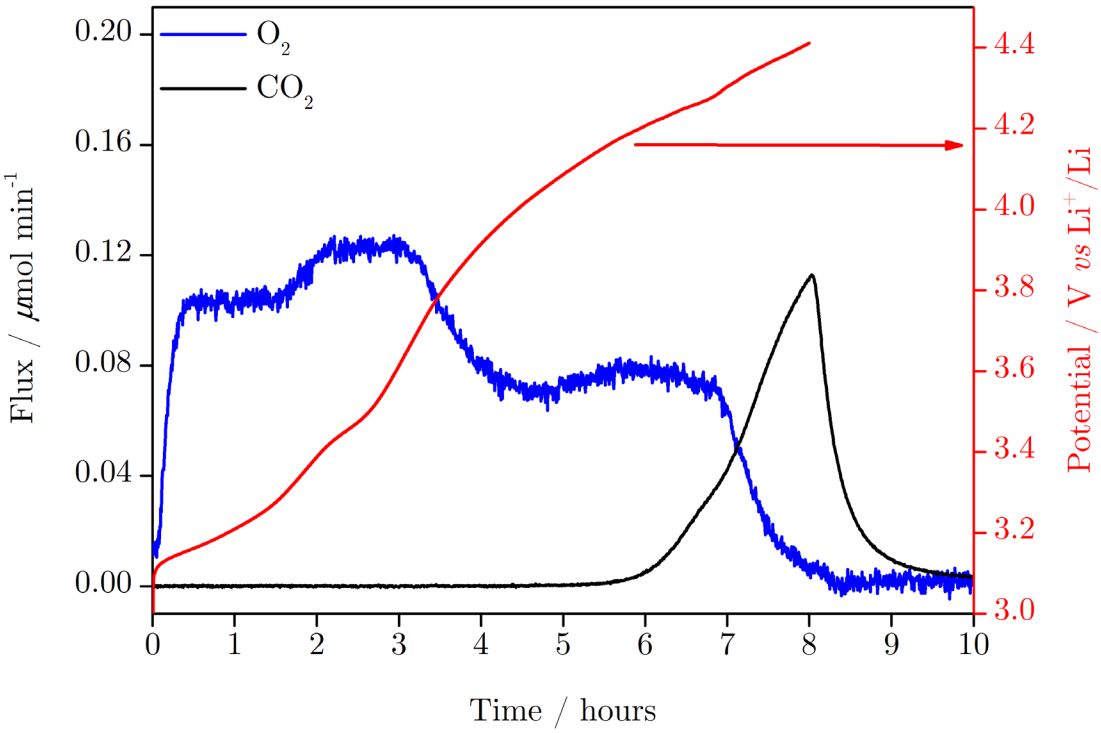

Fig 3.17: OEMS of charging cell with 10 mM DMPZ. O_2 recorded as percentage of total gas composition. Electrolyte solution was 1.0 M LiTFSI in TEGDME with a carrier gas of approximately 20% O_2 with Ar as the balance taking evolved gases to the mass spectrometer, at room temperature. Current density 100 μA cm^{-2} with a gas flow rate of 1.00 mL min^{-1}. Further experimental details may be found in **Section 3.2.5** (page 113).

3.5.3 Effect of Presence of DMA on Charge Profile

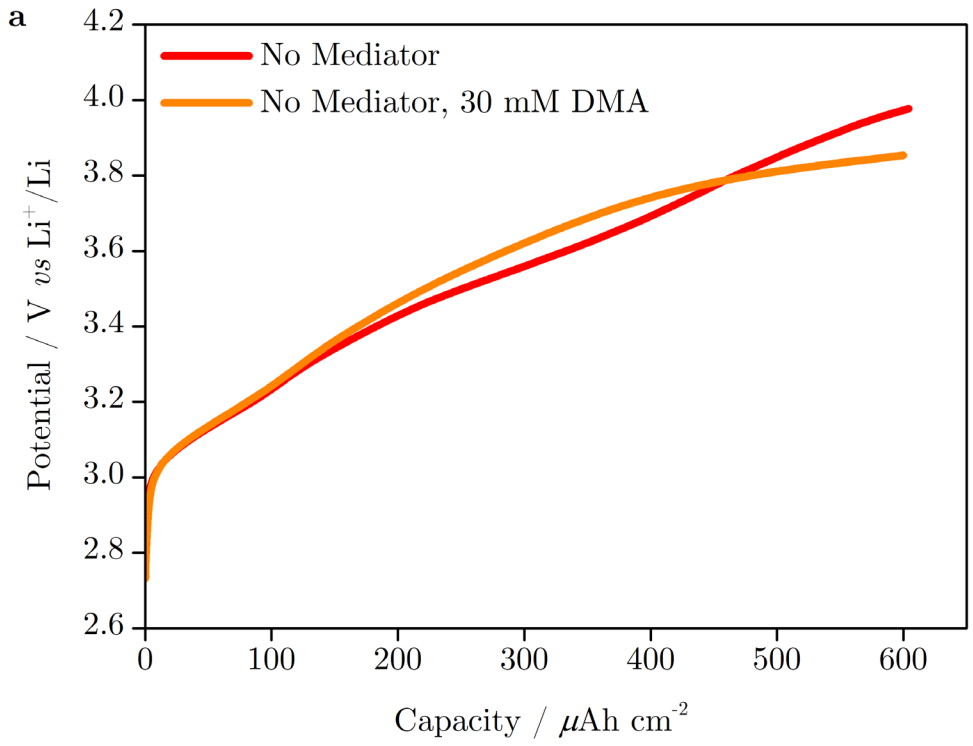

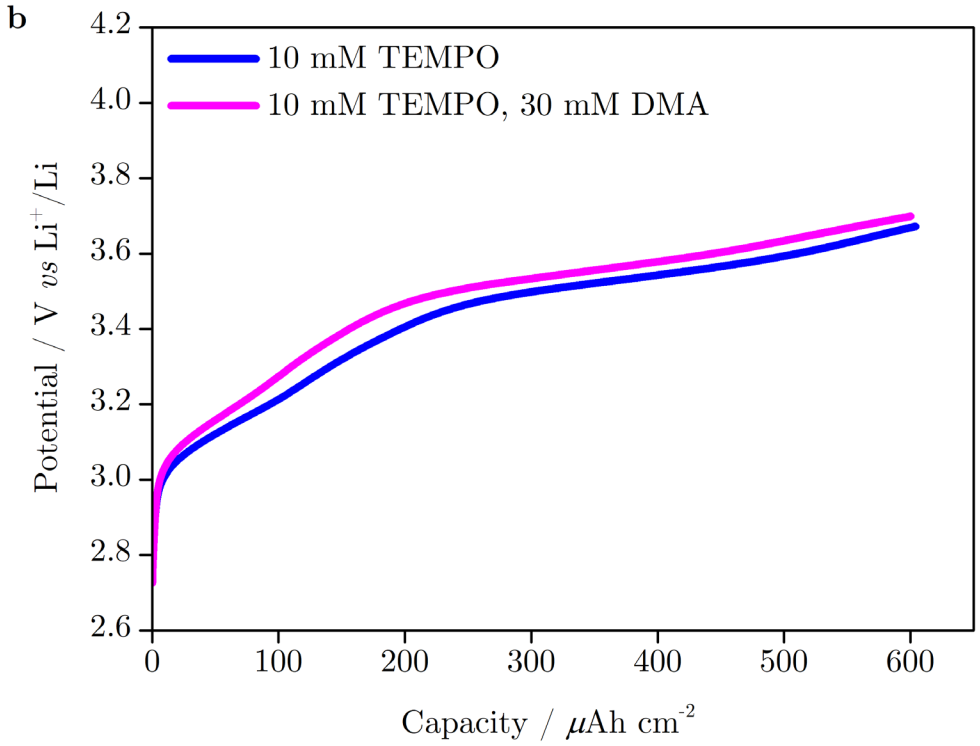

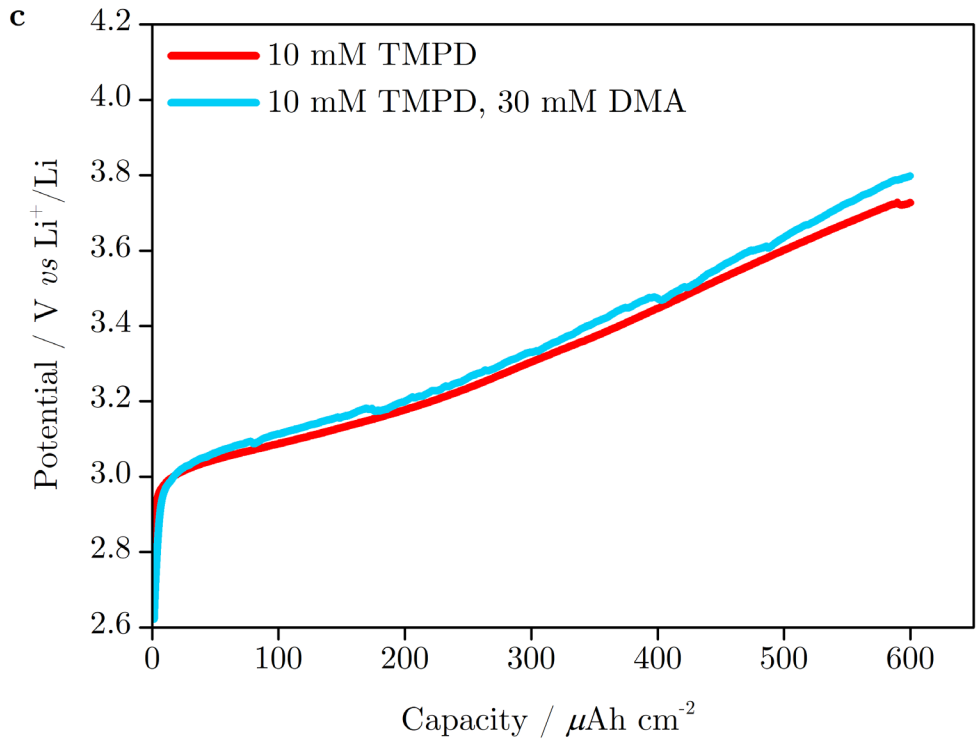

Fig. 3.18: Comparison cell charge profiles of **a.** no RM (previous page), **b.** 10 mM TEMPO (previous page) and **c.** 10 mM TMPD with and without 30 mM DMA in an electrolyte of TEGDME and 1 M LiTFSI. Current density of 100 μAh cm^{-2}. Further experimental details may be found in **Section 3.2.3.1** (page 112).

3.5.4 DMA Fluorescence Spectra Maxima

Emission Wavelength / nm				
419.8	437.9	464.0	494.1	520.7

Table 3.1: Peak fluorescence wavelengths for 32 μM DMA in TEGDME with 1 M LiTFSI. Sample was irradiated with monochromatic light scanned from 300 – 550 nm.

3.5.5 Selectivity for $^1O_2$ from Direct LiO_2 Electrooxidation Above 4.45 V

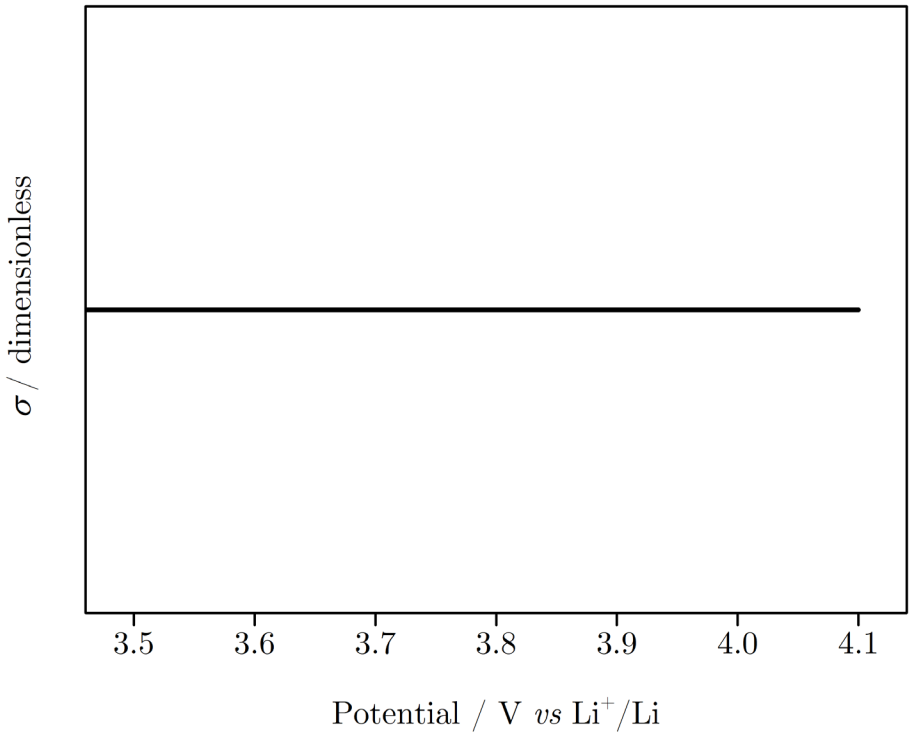

Fig. 3.19: Graphical result of the model for $^1O_2$ selectivity from direct electrooxidation of LiO_2 at increasing positive potential as described in **Section 3.3.8.2** (page 144). Arbitrary (yet constant) values for all variables were assigned, with the transfer coefficients of the reactions in **Equations 3.2** and **3.3** both set to 0.5.

3.6 References

1. B. D. Adams, R. Black, Z. Williams, R. Fernandes, M. Cuisinier, E. J. Berg, P. Novak, G. K. Murphy and L. F. Nazar, *Adv. Energy Mater.*, 2015, **5**, 1400867.
2. B. D. McCloskey, A. Speidel, R. Scheffler, D. C. Miller, V. Viswanathan, J. S. Hummelshøj, J. K. Nørskov and A. C. Luntz, *J. Phys. Chem. Lett.*, 2012, **3**, 997-1001.
3. B. D. McCloskey, D. S. Bethune, R. M. Shelby, G. Girishkumar and A. C. Luntz, *J. Phys. Chem. Lett.*, 2011, **2**, 1161-1166.
4. Z. Ma, X. Yuan, L. Li, Z.-F. Ma, D. P. Wilkinson, L. Zhang and J. Zhang, *Energy Environ. Sci.*, 2015, **8**, 2144-2198.

5. M. Balaish, A. Kraytsberg and Y. Ein-Eli, *Phys. Chem. Chem. Phys.*, 2014, **16**, 2801-2822.
6. Z. Huang, H. Zeng, M. Xie, X. Lin, Z. Huang, Y. Shen and Y. Huang, *Angew.,* 2019, **58**, 2345-2349.
7. D. Sharon, P. Sharon, D. Hirshberg, M. Salama, M. Afri, L. J. W. Shimon, W.-J. Kwak, Y.-K. Sun, A. A. Frimer and D. Aurbach, *J. Am. Chem. Soc.*, 2017, **139**, 34, 11690-11693.
8. W.-J. Kwak, Rosy, D. Sharon, C. Xia, H. Kim, L. R. Johnson, P. G. Bruce, L. F. Nazar, Y. K. Sun, A. A. Frimer, M. Noked, S. A. Freunberger and D. Aurbach, *Chem. Rev.*, 2020, **120**, 14, 6626-6683.
9. J. Hassoun, F. Croce, M. Armand and B. Scrosati, *Angew.*, 2011, **50**, 2999-3002.
10. J. Wandt, P. Jakes, J. Granwehr, H. A. Gasteiger and R.-A. Eichel, *Angew.*, 2016, **55**, 1-5.
11. N. Mahne, B. Schafzahl, C. Leypold, M. Leypold, S. Grumm, A. Leitgeb, Gernot A. Strohmeier, M. Wilkening, O. Fontaine, D. Kramer, C. Slugovc, Sergey M. Borisov and Stefan A. Freunberger, *Nat. Energy*, 2017, **2**, 17036.
12. N. Mahne, S. E. Renfrew, B. D. McCloskey and S. A. Freunberger, *Angew.*, 2018, **57**, 5529-5533.
13. D. Córdoba, H. B. Rodríguez and E. J. Calvo, *ChemistrySelect*, 2019, **4**, 12304-12307.
14. Y. K. Petit, E. Mourad, C. Prehal, C. Leypold, A. Windischbacher, D. Mijailovic, C. Slugovc, S. M. Borisov, E. Zojer, S. Brutti, O. Fontaine and S. A. Freunberger, *Nat. Chem.*, 2021, **13**, 465-471.
15. A. Samojlov, D. Schuster, J. Kahr and S. A. Freunberger, *Electrochim. Acta*, 2020, **362**, 137175.
16. E. Mourad, Y. K. Petit, R. Spezia, A. Samojlov, F. F. Summa, C. Prehal, C. Leypold, N. Mahne, C. Slugovc, O. Fontaine, S. Brutti and S. A. Freunberger, *Energy Environ. Sci.*, 2019, **12**, 2559-2568.
17. G. Houchins, V. Pande and V. Viswanathan, *ACS Energy Lett.*, 2020, **5**, 6, 1893-1899.
18. W.-J. Kwak, S. A. Freunberger, H. Kim, J. Park, T. T. Nguyen, H.-G. Jung, H. R. Byon and Y.-K. Sun, *ACS Catal.*, 2019, **9**, 9914-9922.
19. Y. K. Petit, C. Leypold, N. Mahne, E. Mourad, L. Schafzahl, C. Slugovc, S. M. Borisov and S. A. Freunberger, *Angew.*, 2019, **58**, 6535-6539.
20. X. Gao, Y. Chen, L. R. Johnson, Z. P. Jovanov and P. G. Bruce, *Nat. Energy*, 2017, **2**, 17118.
21. M. M. Ottakam Thotiyl, S. A. Freunberger, Z. Peng and P. G. Bruce, *J. Am. Chem. Soc.*, 2013, **135**, 494-500.
22. S. A. Freunberger, Y. Chen, N. E. Drewett, L. J. Hardwick, F. Barde and P. G. Bruce, *Angew.*, 2011, **50**, 8609-8613.
23. B. J. Bergner, A. Schurmann, K. Peppler, A. Garsuch and J. Janek, *J. Am. Chem. Soc.*, 2014, **136**, 15054-15064.

24. B. J. Bergner, C. Hofmann, A. Schurmann, D. Schroder, K. Peppler, P. R. Schreiner and J. Janek, *Phys. Chem. Chem. Phys.*, 2015, **17**, 31769-31779.
25. Y. Chen, X. Gao, L. R. Johnson and P. G. Bruce, *Nat. Commun.*, 2018, **9**, 767.
26. P. P. Bawol, P. Reinsberg, C. J. Bondue, A. A. Abd-El-Latif, P. Konigshoven and H. Baltruschat, *Phys. Chem. Chem. Phys.*, 2018, **20**, 21447-21456.
27. Y. Chen, S. A. Freunberger, Z. Peng, O. Fontaine and P. G. Bruce, *Nat. Chem.*, 2013, **5**, 489–494.
28. O. Yurchenko, D. Freytag, L. zur Borg, R. Zentel, J. Heinze and S. Ludwigs, *J. Phys. Chem. B*, 2012, **116**, 30-39.
29. X. Gao, Y. Chen, L. Johnson and P. G. Bruce, *Nat. Mater.*, 2016, **15**, 882–888.
30. H.-D. Lim, B. Lee, Y. Zheng, J. Hong, J. Kim, H. Gwon, Y. Ko, M. Lee, K. Cho and K. Kang, *Nat. Energy*, 2016, **1**, 16066.
31. B. D. McCloskey, A. Valery, A. C. Luntz, S. R. Gowda, G. M. Wallraff, J. M. Garcia, T. Mori and L. E. Krupp, *J. Phys. Chem. Lett.*, 2013, **4**, 2989-2993.
32. R. A. Wong, A. Dutta, C. Yang, K. Yamanaka, T. Ohta, A. Nakao, K. Waki and H. R. Byon, *Chem. Mater.*, 2016, **28**, 8006-8015.
33. B. Schafzahl, E. Mourad, L. Schafzahl, Y. K. Petit, A. R. Raju, M. O. Thotiyl, M. Wilkening, C. Slugovc and S. A. Freunberger, *ACS Energy Lett.*, 2017, **3**, 170-176.
34. Z. Liang, Y. Zhou and Y.-C. Lu, *Energy Environ. Sci.*, 2018, **11**, 3500-3510.
35. Y. Ko, H. Park, B. Lee, Y. Bae, S. K. Park and K. Kang, *J. Mater. Chem. A*, 2019, **7**, 6491-6498.
36. Z. Liang and Y. C. Lu, *J. Am. Chem. Soc.*, 2016, **138**, 7574-7583.
37. Y. Dou, R. Lian, G. Chen, Y. Wei and Z. Peng, *Energy Storage Materials*, 2020, **25**, 795-800.
38. B. J. Bergner, M. R. Busche, R. Pinedo, B. B. Berkes, D. Schroder and J. Janek, *ACS Appl. Mater. Interfaces*, 2016, **8**, 7756-7765.
39. B. D. McCloskey, D. S. Bethune, R. M. Shelby, T. Mori, R. Scheffler, A. Speidel, M. Sherwood and A. C. Luntz, *J. Phys. Chem. Lett.*, 2012, **3**, 3043-3047.
40. W. J. Kwak, H. Kim, Y. K. Petit, C. Leypold, T. T. Nguyen, N. Mahne, P. Redfern, L. A. Curtiss, H. G. Jung, S. M. Borisov, S. A. Freunberger and Y. K. Sun, *Nat. Commun.*, 2019, **10**, 1380.
41. L. Schafzahl, N. Mahne, B. Schafzahl, M. Wilkening, C. Slugovc, S. M. Borisov and S. A. Freunberger, *Angew.*, 2017, **56**, 15728-15732.
42. A. Sagadevan, K. C. Hwang and M. D. Su, *Nat. Commun.*, 2017, **8**, 1812.
43. A. Gomes, E. Fernandes and J. L. Lima, *J. Biochem. Biophys. Methods*, 2005, **65**, 45-80.
44. Z. Liang, Q. Zou, J. Xie and Y.-C. Lu, *Energy Environ. Sci.*, 2020, **13**, 2870-2877.

45. P. L. Arrechea, K. B. Knudsen, J. W. Mullinax, J. B. Haskins, C. W. Bauschlicher, J. W. Lawson and B. D. McCloskey, *ACS Applied Energy Materials*, 2020, **3**, 8812-8821.
46. S. Claude and R. Schmidt, *Chem. Rev.*, 2003, **103**, 1685−1757.
47. Z. Zhu, A. Kushima, Z. Yin, L. Qi, K. Amine, J. Lu and J. Li, *Nat. Energy*, 2016, **1**, 16111.
48. L. Luo, B. Liu, S. Song, W. Xu, J. G. Zhang and C. Wang, *Nat. Nanotechnol.*, 2017, **12**, 535-539.
49. S. Ganapathy, B. D. Adams, G. Stenou, M. S. Anastasaki, K. Goubitz, X. F. Miao, L. F. Nazar and M. Wagemaker, *J. Am. Chem. Soc.*, 2014, **136**, 16335-16344.
50. Y.-C. Lu and Y. Shao-Horn, *J. Phys. Chem. Lett.*, 2012, **4**, 93-99.
51. Y. Wang, N.-C. Lai, Y.-R. Lu, Y. Zhou, C.-L. Dong and Y.-C. Lu, *Joule*, 2018, **2**, 2364-2380.
52. Y. Wang, Y.-R. Lu, C.-L. Dong and Y.-C. Lu, *ACS Energy Lett.*, 2020, **5**, 5, 1355-1363.
53. B. M. Gallant, D. G. Kwabi, R. R. Mitchell, J. Zhou, C. V. Thompson and Y. Shao-Horn, *Energy Environ. Sci.*, 2013, **6**, 2518.
54. S. Kang, Y. Mo, S. P. Ong and G. Ceder, *Chem. Mater.*, 2013, **25**, 3328-3336.
55. J. S. Hummelshoj, A. C. Luntz and J. K. Norskov, *J. Chem. Phys.*, 2013, **138**, 034703.
56. B. Lee, J. Kim, G. Yoon, H.-D. Lim, I.-S. Choi and K. Kang, *Chem. Mater.*, 2015, **27**, 8406-8413.
57. T. Dabrowski and L. C. Ciacchi, *J. Phys. Chem. C*, 2015, **119**, 25807-25817.
58. C. L. Bender, P. Hartmann, M. Vračar, P. Adelhelm and J. Janek, *Adv. Energy Mater.*, 2014, **4**, 12, 1301863.
59. Y.-C. Lu, H. A. Gasteiger, M. C. Parent, V. Chiloyan and Y. Shao-Horn, *Electrochem. Solid-State Lett.*, 2010, **13**, A69-A72.
60. D. Pletcher, *A First Course in Electrode Processes*, The Royal Society of Chemistry Cambridge, 2nd edn., 2009.
61. V. Viswanathan, J. K. Nørskov, A. Speidel, R. Scheffler, S. Gowda and A. C. Luntz, *J. Phys. Chem. Lett.*, 2013, **4**, 556-560.
62. G. P. Sakellaropoulos and G. A. Francis, *J. Electrochem. Soc.*, 1979, **126**, 1928-1937.
63. V. S. Bryantsev, M. Blanco and F. Faglioni, *J. Phys. Chem. A*, 2010, **114**, 8165-8169.
64. Z. Peng, S. A. Freunberger, L. J. Hardwick, Y. Chen, V. Giordani, F. Barde, P. Novak, D. Graham, J. M. Tarascon and P. G. Bruce, *Angew.*, 2011, **50**, 6351-6355.
65. Y. Wang and Y. C. Lu, *Angew.*, 2019, **58**, 6962-6966.
66. L. Johnson, C. Li, Z. Liu, Y. Chen, S. A. Freunberger, P. C. Ashok, B. B. Praveen, K. Dholakia, J.-M. Tarascon and P. G. Bruce, *Nat. Chem.*, 2014, **6**, 1091-1099.

67. M. D. Radin, J. F. Rodriguez, F. Tian and D. J. Siegel, *J. Am. Chem. Soc.*, 2011, **134**, 1093-1103.
68. N. Mahne, O. Fontaine, M. O. Thotiyl, M. Wilkening and S. A. Freunberger, *Chem. Sci.*, 2017, **8**, 6716-6729.
69. H. D. Lim, H. Song, J. Kim, H. Gwon, Y. Bae, K. Y. Park, J. Hong, H. Kim, T. Kim, Y. H. Kim, X. Lepro, R. Ovalle-Robles, R. H. Baughman and K. Kang, *Angew.*, 2014, **53**, 3926-3931.
70. H. Kim, W.-J. Kwak, H.-G. Jung and Y.-K. Sun, *J. Mater. Chem. A*, 2020, **8**, 5622-5628.
71. Z. Liu, Y. Zhang, C. Jia, H. Wan, Z. Peng, Y. Bi, Y. Liu, Z. Peng, Q. Wang, H. Li, D. Wang and J.-G. Zhang, *Nano Energy*, 2017, **36**, 390-397.
72. K. R. Ryan, L. Trahey, B. J. Ingram and A. K. Burrell, *J. Phys. Chem. C*, 2012, **116**, 19724-19728.
73. R. Black, S. H. Oh, J. H. Lee, T. Yim, B. Adams and L. F. Nazar, *J. Am. Chem. Soc.*, 2012, **134**, 2902-2905.
74. D. Sharon, V. Etacheri, A. Garsuch, M. Afri, A. A. Frimer and D. Aurbach, *J. Phys. Chem. Lett.*, 2012, **4**, 127-131.

Chapter 4

Novel Redox Mediators for Use During Lithium-Oxygen Cell Charge and Investigation of Redox Mediator Reaction Kinetics with Lithium Peroxide

Contents

4.1 Introduction

The use of RMs on charge within the Li-O_2 cell brings with it three key benefits. Firstly, the overpotential on charge is reduced, leading to a greater round-trip efficiency for the cell.[1, 2] Secondly, all Li_2O_2 is able to be oxidised, even if it has become electrically disconnected from the cathode during the course of cycling (whilst the electrical disconnect of some Li_2O_2 occurs during regular cell cycling, use of discharge RMs to facilitate solution-based growth of Li_2O_2 results in almost complete absence of Li_2O_2 in direct contact with the cathode).[3, 4] Thirdly, if a RM of sufficiently low potential is utilised then decomposition of the electrolyte and the carbon cathode due to $^1O_2$ may be suppressed, as demonstrated in **Chapter 3**. However, it is important to note that not all RMs are created equal. While it is clearly evident that each RM

possesses its own potential at which it operates, work by Chen *et al.* further reveal differences in the heterogeneous reaction kinetics between RMs and Li_2O_2.[5] There is evidence that the presence of sterically bulky groups surrounding the redox centre reduces the rate of Li_2O_2 oxidation and that the nature of the redox centre itself is important in determining the rate, with the order of increasing rate being amines < thiols < nitroxyl functional groups.[5, 6]

Given the broad range of kinetics between RMs and Li_2O_2 as observed by Chen *et al.* it is clear that selection of the optimum RM is not simply a case of tuning for the desired potential. With low potential RMs such as TMPD and DMPZ exhibiting the slowest kinetics, it appears that there is a trade-off to be made between fast oxidation of Li_2O_2 by RM and minimising component degradation through low charging potentials.[5, 7] There is therefore a need to find new RMs that exhibit both a low redox potential and reaction kinetics with Li_2O_2 that are sufficiently fast to sustain cell charging without substantial polarisation at high rates.

This Chapter utilises Density Functional Theory (DFT) to screen a range of molecules to find those with oxidation potentials appropriate for their use within a Li-O_2 cell. From this a collection of novel candidate RMs is selected and, where necessary, synthesised based on their structural similarities and differences to known RMs. Following structural and electrochemical characterisation, including evaluation of the novel RMs' suitability for use within Li-O_2 cells, a detailed study of how the structure of RMs affects the kinetics of reaction with Li_2O_2 takes place. This involves comparison of the novel RMs with those already established in literature and

application of Marcus kinetic theory to rationalise trends in reaction rate constants measured by scanning electrochemical microscopy.

4.2 Experimental

4.2.1 Density Functional Theory Calculations

Geometry optimisation and energy evaluation were conducted using DFT calculation software Gaussian16 quantum chemistry package. For all the calculations, spin-unrestricted DFT was performed based on the Becke-Lee-Yang-Parr (B3LYP) hybrid exchange-correlation functional and triple-zeta valance polarisation (TZVP) basis set. The dielectric constant of tetraethylene glycol dimethyl ether (TEGDME) (7.78) was used to model the electrolyte environment.[8]

4.2.2 Synthesis of 1,4-Dimethyl-1,2,3,4-tetrahydroquinoxaline

1,2-Diiodobenzene (98%, 1.65 g, 5.00 mmol, Sigma Aldrich), 1,8-Diazabicyclo[5.4.0]undec-7-ene (DBU, 99.0%, 1.52 g, 10.00 mmol, Sigma Aldrich), *N*,*N*'-dimethylethylenediamine (DMEA, 98%, 0.88 g, 10.00 mmol, Sigma Aldrich) and CuI (99.999%, 0.02 g, 0.1 mmol, 1.00 mol%, Sigma Aldrich) were added to an oven dried flask, which resulted in the formation of a clear green solution. The solution was stirred at 110°C for 24 hours, resulting in a solution colour change to brown. The progress of the reaction was monitored via GCMS.

The resultant solution was filtered to remove the copper salt and washed with distilled H_2O followed by ethyl acetate (99.8%, Sigma Aldrich), the latter of which was

removed under reduced pressure. The product, 1,4-Dimethyl-1,2,3,4-tetrahydroquinoxaline (DMHQ), was purified via a silica column (hexane (>99%, Sigma Aldrich)/ethyl acetate 90:10 v%) to yield the product as a viscous yellow oil.

δ_H (400 MHz; DMSO-d_6) 6.56-6.41 (4H, m, aromatics), 3.26 (4H, s, -CH_2), 2.77 (6H, s, -CH_3). Impurities: 3.33 (2H, s, H_2O), 2.52-2.50 (6H, q, DMSO) - originating from DMSO-d_6, *m/z* 162.14 (M^+) calc. 162.12, ν_{max}/cm^{-1} 3056w (C-H), 2942-2813s (-CH_2-), 1594m (C=C), 1506s (C=C), 726s (Ar-H). FTIR and NMR data may be found in **Appendices 4.5.2a** (page 227) and **4.5.3a** (page 228), respectively.

4.2.3 Synthesis of 10-Methyl-10*H*-phenoxazine

Phenoxazine (98%, 1.00 g, 5.46 mmol, Sigma Aldrich) was dissolved in DMSO (20 mL, Sigma Aldrich) forming a clear, colourless solution. KOH (99.95%, 1.84 g, 5.46 mmol, Sigma Aldrich) was added to the solution and stirred at room temperature for 10 minutes, resulting in a colour change to dark green. MeI (99.5%, 0.77 g, 5.46 mmol, Sigma Aldrich) was added and the solution was stirred for 24 hours at room temperature.

The resultant solution was filtered to remove the KOH and washed with distilled H_2O followed by ethyl acetate, the latter of which was removed under reduced pressure. The product, 10-Methyl-10*H*-phenoxazine (MPO), was purified via a silica column (hexane/ethyl acetate 90:10 v%) to yield the product as a viscous yellow oil.

δ_H (400 MHz; DMSO-d_6) 6.92-6.72 (8H, m, aromatics), 3.04 (3H, s, -CH_3), *m/z* 197.08 (M^+) calc. 197.08, ν_{max}/cm^{-1} 3062w (C-H), 1478s (C=C), 1262s (C-O), 730s (Ar-H). FTIR and ^1H NMR data may be found in **Appendices 4.5.2b** (page 227) and **4.5.3b** (page 228), respectively.

4.2.4 X-Ray Diffraction

Powder XRD data was obtained using a Rigaku Miniflex with Cu K_α radiation in a N_2 atmosphere. At the end of discharge/charge cells were disassembled and the cathode washed with dimethoxyethane (DME, Sigma Aldrich) and dried under vacuum to remove excess electrolyte. The cathodes were affixed to a stainless steel sample holder using vacuum grease as an adhesive, and measurements were taken in the range of $10° < 2\Theta < 90°$ at a scan rate of 0.9° min^{-1}. All samples were rotated during the measurements.

4.2.5 Fourier Transform Infrared Spectroscopy

FTIR data was collected using a Nicolet iS 10 FTIR Spectrometer in attenuated total reflection mode under a N_2 atmosphere, with a small aliquot of the RM deposited on the crystal.

4.2.6 ^1H Nuclear Magnetic Resonance Spectroscopy

^1H NMR was collected using a Bruker AVIIIHD 400 MHz NMR spectrometer. DMSO-d_6 (Sigma Aldrich) was used as the solvent.

4.2.7 Gas Chromatography Mass Spectrometry

GCMS data was collected using a Thermo Scientific ISQ 7000 using helium as the carrier gas. The sample was dissolved in diethyl ether (Sigma Aldrich) then injected directly onto the column, which was heated from 25 - 220°C at a rate of 8°C min^{-1}. Electron impact ionisation was utilised.

.

4.2.8 Cyclic Voltammetry

Cyclic voltammetry was conducted inside a N_2 glovebox using a Biologic SP-300 potentiostat. The candidate RMs (oxanthrene (99%, Sigma Aldrich), thianthrene (97%, Sigma Aldrich) tetramethyltetraselenafulvalene (97%, Sigma Aldrich) and synthesised species) (10 mM) were dissolved in dried and distilled TEGDME (>99%, Sigma Aldrich) with 1 M LiTFSI (99.95%, Sigma Aldrich) as supporting electrolyte, and were used as received. The working electrode was a planar gold disc (3 mm diameter) (except for the cyclic voltammetry in **Figure 4.7b**, where a platinum electrode of 2 mm diameter was used), polished using a slurry of 0.05 μm alumina on a fine abrasive pad, followed by electrochemical cleaning in 0.1 M $HClO_4$ (Sigma Aldrich) with potential cycling. The counter electrode was a platinum wire and the reference electrode was partially delithiated $LiFePO_4$ (TCI) in TEGDME with 1 M LiTFSI electrolyte behind a Vycor® glass frit (3.45 V *vs* Li^+/Li). The current density response at scan rates of 10, 20, 50, 100, and 200 mV s^{-1} was measured, with the solution being stirred between scans. *iR* (Ohmic drop) corrections of 85% were applied to the measurements. E^0 was taken as the midpoint potential between the

anodic and cathodic peaks, and the onset potential was defined as the potential at which a current density of 14.15 μA cm^{-2} was recorded on the anodic scan.

4.2.9 Galvanostatic Cell Cycling

Cells were cycled using a Biologic VMP3 potentiostat in an Ar glovebox. Cells were assembled with either a $LiFePO_4$ (for MPO) or Li metal (for DMHQ) counter electrode. The $LiFePO_4$ counter electrodes were constructed from a slurry of $LiFePO_4$, PTFE (60wt% in H_2O, Sigma Aldrich) and carbon black (Super P, 99+%, TIMCAL) in a ratio of 8:1:1. Carbon cathodes were constructed out of a slurry of carbon black, PTFE and isopropanol (99.9%, Sigma Aldrich) in an 8:1:1 ratio pasted onto a stainless steel mesh (100 mesh). Glass fibre (Whatman) separators were used. Full details regarding cell component preparation is described in **Section 2.1.6.1** (page 86)**.**

30 mM RM with 1 M LiTFSI in TEGDME (300 μL) served as the electrolyte, with the RMs used as received. The cells were purged with dried O_2 (99.999%, BOC) for 2 minutes then allowed to equilibrate for 1 hour before cycling at a current density of 100 μA cm^{-2} to a fixed capacity of 1,000 μAh cm^{-2} (unless otherwise stated). The one-electron oxidation of the 30 mM of RM added to the electrolyte equated to a maximum of 241.2 μAh cm^{-2} of the charge capacity, assuming no reaction of the RM with Li_2O_2.

4.2.10 *Operando* Electrochemical Mass Spectrometry

Cells were constructed as described in **Section 4.2.9** (page 176). The cells were connected to a Thermo Scientific PrimaBT benchtop gas analyser and cycled at 100 µA cm^{-2} to a fixed capacity of 1000 μAh cm^{-2}. The cells were continually purged using a carrier gas of 20% O_2 in Ar (BOC) that was set to a flow rate of 1.0 mL min^{-1}. $^{16}O_2$ and $^{12}CO_2$ evolution was measured by monitoring the m/z 32 and 44 signals respectively, following industry-standard one-point calibration of the instrument using 0.1% O_2, 1000 ppm $^{12}CO_2$ and 500 ppm $^{13}CO_2$ made up to 100% with Ar (BOC).

4.2.11 Scanning Electrochemical Microscopy

SECM was performed using a 920D (CH Instruments) in a glovebox under a N_2 atmosphere with <1 ppm H_2O and O_2. A platinum microdisc (12.5 μm diameter) was used as the working electrode, which was polished using alumina (0.05 μm), sonicated in isopropanol, and dried under vacuum at 50°C prior to use. Partially delithiated $LiFePO_4$ in TEGDME with 1 M LiTFSI behind a Vycor® glass frit was used as the reference, and a platinum wire was used as the counter. The electrolyte was 0.1 M LiTFSI in TEGDME. To obtain the approach curves, the working electrode was held at constant potential (3.65 V for DMHQ and 4.00 V for MPO) as it was moved towards the substrate at a rate of 0.1 μm s^{-1}.

Li_2O_2 pellets of diameter 6 mm were used as the substrate, formed from a fine powder using a die press under 1 tonne pressure. The Li_2O_2 powder was synthesised in-house by Dr S. Ahn according to an established procedure, and was found via XRD

and $KMnO_4$ titration to be of >99% purity, compared to the 94% purity of commercially available Li_2O_2 powder (technical grade, Sigma Aldrich).[9]

Cyclic voltammetry was performed using a platinum microdisc electrode (12.5 μm diameter, similarly prepared to all other microdisc electrodes) to obtain the diffusion coefficient, with a scan rate of 100 mV s^{-1}. The chronoamperometry experiments were performed using platinum microdisc electrodes (12.5 μm diameter) with differing R_g values at constant potentials (3.65 V for DMHQ and 4.00 V for MPO). Partially delithiated $LiFePO_4$ in TEGDME with 1 M LiTFSI behind a Vycor® glass frit and a platinum wire were used as the reference and counter electrodes, respectively, in both the cyclic voltammetry and chronoamperometry, with 0.1 M LiTFSI in TEGDME serving as the electrolyte.

4.3 Discussion

4.3.1 Selecting Redox Mediator Candidates Using DFT

Taking inspiration from the work of Lim *et al.*, through which the charge RM 5,10-dihydro-5,10-dimthylphenazine (DMPZ) was identified, DFT calculations as described in **Section 4.2.1** (page 172) were conducted.[2] The molecules' orbital energies, including that of the highest occupied molecular orbital, or HOMO, ε, were extracted from the calculation output files.

Koopmans' theorem states that the first ionisation energy of a molecular system, I, is equal to the negative of the orbital energy of the HOMO, as given by **Equation 4.1**:[10]

$$I = -\varepsilon \qquad \textbf{Eq. 4. 1}$$

The output of the DFT calculations provide the energy of the HOMO in units of Hartrees; using the relationship of 1 Hartree = 27.2113961 eV, it is possible to obtain absolute electrode potentials[a].[11]

With the standard hydrogen electrode (SHE) having a potential of -4.44 V *vs* the absolute potential scale and with the Li^+/Li redox couple being equal to -3.0401 V *vs* SHE, it was determined that the Li^+/Li couple is at -1.69 V *vs* the absolute potential scale. It should be noted that the standard potential of Li^+/Li varies depending on the solvent used, given that the value of -3.0401 V *vs* SHE is derived in an aqueous environment.[12] The computational values obtained here make use of the aqueous value, rather than that obtained in an organic solvent such as TEGDME. However, it is estimated that the resultant difference is less than 0.2 V and that, given its use in other published works, use of the aqueous value was deemed appropriate here.[2] A detailed discussion of the theory behind the DFT calculations conducted here is given in **Section 2.7** (page 105), with a discussion of the validity of the computational model provided in **Section 4.3.7** (page 207).

Candidate species were selected for DFT analysis based on their structural similarities to known RMs, whilst also taking into account factors that may affect the redox potential (such as the degree of stabilisation afforded to the redox active site) and reaction kinetics (such as steric bulk).[6] The calculated redox potentials of all the

[a] The absolute electrode potential is defined as the potential of a half-cell *vs* an electron in a vacuum at rest. S. Trasatti, *J. Electroanal. Chem.*, 1986, **209**, 417-428.

RM structures trialled may be found in **Appendix 4.5.1** (page 226), whilst a comparison of the calculated and experimental redox potentials of the RMs selected for further study may be found in **Table 4.1**, along with several established RMs for reference.

A significant number of established RMs feature a tertiary amine functionality which acts as the redox-active site, such as DMPZ (**Figure 4.1a**), MPT (**Figure 4.1b**) and TMPD (**Scheme 3.2**), with an additional heteroatom located at the para position.[2, 13-16] 10-methyl-10*H*-phenoxazine (MPO, **Figure 4.1c**) was selected for study due to being the oxygen analogue of both DMPZ and MPT, with comparison of the three providing insight into the importance of the role of the non-redox active heteroatom in determining the reaction kinetics. Thianthrene and oxanthrene (**Figure 4.1e** and **4.1f**, respectively) were selected for further experimental study due to their replacement of the redox-active tertiary amine functionality with either an additional sulfur (thianthrene) or oxygen (oxanthrene) atom.[1, 16] This would allow a comparison of how the nature of the redox-active site affects the rate of Li_2O_2 oxidation.

1,4-dimethyl-1,2,3,4-tetrahydroquinoxaline (DMHQ, **Figure 4.1d**), which differs from DMPZ through the replacement of a bridging 1,2-substituted phenyl ring by an ethylene bridge, was selected for further study to investigate the effect of decreasing the steric bulk surrounding the redox-active site on the reactions kinetics.

Due to the success of tetrathiafulvalene (TTF, **Figure 4.1g**)) as a RM, its selenium analogue tetramethyltetraselenafulvalene (TSF, **Figure 4.1h**) was also

selected for further investigation, again to give insight into the role of the heteroatoms in determining RM kinetics.[14]

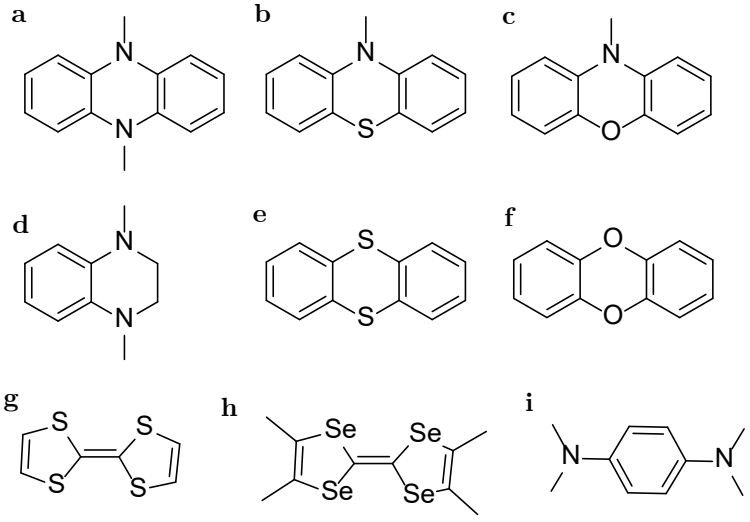

Fig. 4.1: Structures of RMs considered in this work: **a.** DMPZ, **b.** MPT, **c.** MPO, **d.** DMHQ, **e.** thianthrene, **f.** oxanthrene, **g.** TTF, **h.** TSF, and **i.** TMPD.

RM	Thianthrene‖	Oxanthrene‖	TSF‖	DMHQ‖†	MPO‖†	DMPZ	MPT	TMPD
Computational E^0 / **V**	4.10	4.40	3.38	3.48	3.65	3.11	3.62	3.35
Experimental E^0 / **V**	4.34	4.51	3.53	3.38	3.73	3.15	3.67[16]	3.20

Table 4.1: Calculated and experimental redox potential values for RMs tested in this study, along with previously published RMs DMPZ, TMPD and MPT for comparison. Computational details may be found in **Section 4.2.1** (page 172) and the experimental conditions may be found **in Section 4.2.8** (page 175). ‖Novel RM. †Synthesised in-house.

4.3.2 Cyclic Voltammetry of Thianthrene

As can be seen from the cyclic voltammetry presented in **Figure 4.2**, thianthrene has an E^0 of 4.37 V, in broad agreement with the calculated value of 4.10 V, and an onset potential of 4.15 V (a discussion of the validity of the computational model and a comparison with the experimentally determined values may be found in **Section 4.3.7** on page 207).

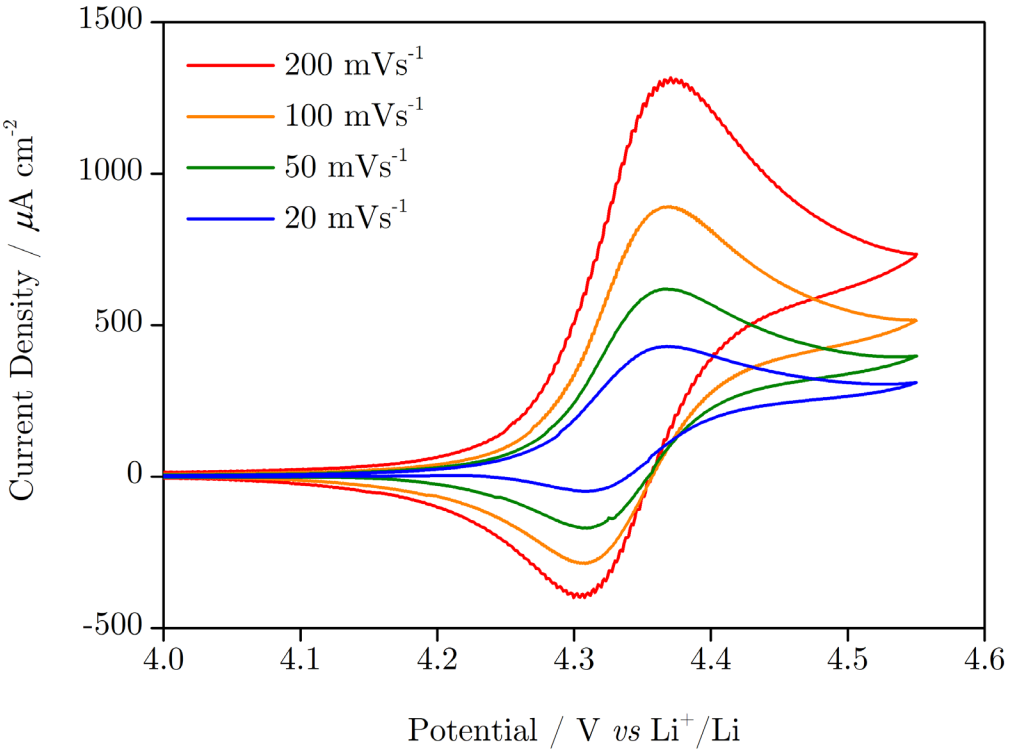

Fig. 4.2: Cyclic voltammetry of 10 mM thianthrene at multiple scan rates, with experimental conditions as described in **Section 4.2.8** (page 175).

Whilst thianthrene exhibits a strong anodic peak, the reverse cathodic peak has a much smaller current density. As the scan rate decreases (and as such the timeframe of the experiment increases) the magnitude of the reverse peak also decreases; even at

a high scan rate of 200 mV s^{-1} the cathodic peak is significantly smaller than the anodic peak. This is indicative of a coupled homogenous chemical (*ec*) reaction occurring between the thianthrene^{+} and another species present in the electrolyte, making thianthrene unsuitable for use as a RM.[17]

Despite the instabilities of thianthrene observed through cyclic voltammetry leading to no further investigation in this work, Arrechea *et al.* subsequently examined thianthrene as a possible RM and found that while its oxidised form is capable of oxidising Li_2O_2 to O_2, it is unstable and forms thianthrene sulfoxide.[18] Their investigation further revealed that whilst thianthrene derivatives are not well suited as RMs, they might find use as $^1O_2$ quenchers. A similar theory was proposed by Liang *et al.*, who also suggested that RMs could act as $^1O_2$ quenchers (discussion of RMs' abilities to quench $^1O_2$ was discussed in the **Chapters 1** and **3**, and is beyond the scope of the work presented in this Chapter).[19]

4.3.3 Cyclic Voltammetry of Oxanthrene

Oxanthrene was found to be similarly unstable like thianthrene, despite having a redox potential of E^0 of 4.51 V and an onset potential of 4.20 V, which both lie within the computational and experimental stability window of TEGDME[b].[2] Similarly to thianthrene, oxanthrene also undergoes an *ec* reaction, however the rate constant for

[b] In the absence of O_2 and Li_2O_2, TEGDME was found to be stable to above 4.75 V (**Figure 4.30** in **Section 4.5.4** on page 228). This is supported by Freunberger *et al.*, who similarly found TEGDME to be electrochemically stable up to a potential of 4.75 V. S. Freunberger, Y. Chen, N. E. Drewett, L. J. Hardwick, F. Barde, P. G. Bruce, *Angew.*, 2011, **50**, 8609-13.

the chemical step is much greater than that for the reaction involving thianthrene; the chemical reaction involving oxanthrene$^+$ is sufficiently fast that there is no observable cathodic peak for CVs obtained at scan rates of 10 mV s^{-1} and 20 mV s^{-1} (observed in **Figure 4.3**). Given the highly reactive nature of oxanthrene$^+$ with the electrolyte, further investigations involving this species were not conducted.

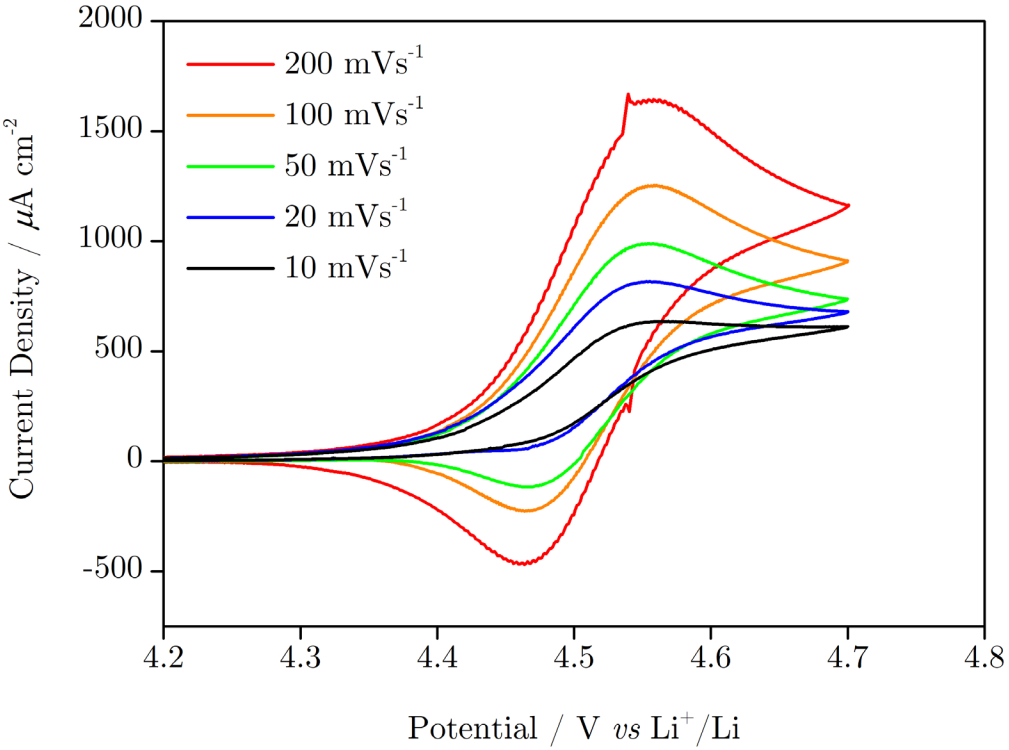

Fig. 4.3: Cyclic voltammetry of 10 mM oxanthrene at multiple scan rates, with experimental conditions as described in **Section 4.2.8** (page 175). It should be noted that the data incontinuities occurring during the 200 mV s^{-1} scan at 4.55 V in the cyclic voltammetry of oxanthrene are artefacts arising from changes in the current density range recorded by the potentiostat, rather than a consequence of further electrochemical process occurring.

4.3.4 Cyclic Voltammetry of Tetramethyltetraselenofulvalene

TSF has two oxidations at $E^0_1 = 3.53$ V and $E^0_2 = 3.73$ V, similar to TTF, however unlike TTF the second oxidation of TSF leads to an *ec* reaction (**Figure 4.4**). The potential of the first oxidation is in relatively close agreement with the computational value of 3.38 V. Despite the reversible nature of the first oxidation making TSF a promising species to use in the kinetics investigation, TSF was found to have poor solubility in TEGDME, with an estimated maximum concentration of 4 mM achieved. A RM concentration this low would likely have difficulty in sustaining the desired low potential plateau in a working cell, with a minimum RM concentration of 10 mM typically employed in the literature.[2, 4, 13, 14, 16, 20, 21] As such, no further study of TSF was carried out. For completeness, Ryu *et al.* provided one rare example of the use of a RM concentration of less than 10 mM, utilising a haem biomolecule which has a solubility limit of 2.3 mM in TEGDME.[22] It should also be noted that TSF may have greater solubility in other solvents that have traditionally been used in Li-O_2 cells, however the performance of RMs in non-ether solvents is beyond the scope of this work.

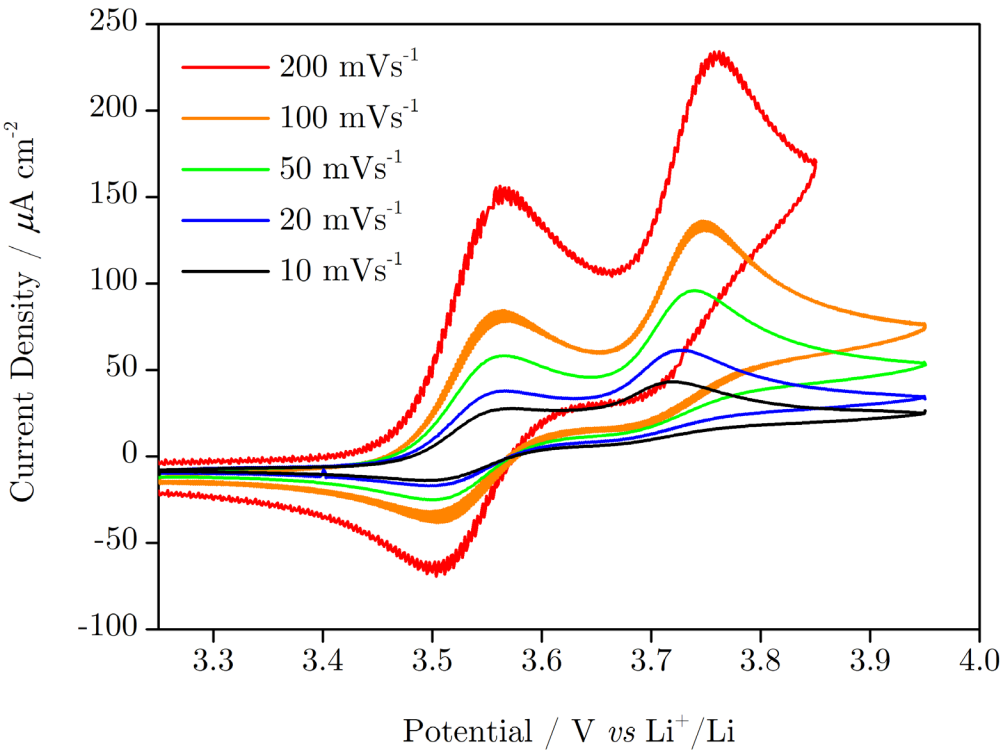

Fig. 4.4: Cyclic voltammetry of 4 mM TSF at multiple scan rates, with experimental conditions as described in **Section 4.2.8** (page 175).

4.3.5 DMHQ Analysis

4.3.5.1 Synthesis of DMHQ

Synthesis of DMHQ proceeded via a copper-catalysed cross-coupling reaction as demonstrated by Shen *et al.*, according to **Scheme 4.1**:[23]

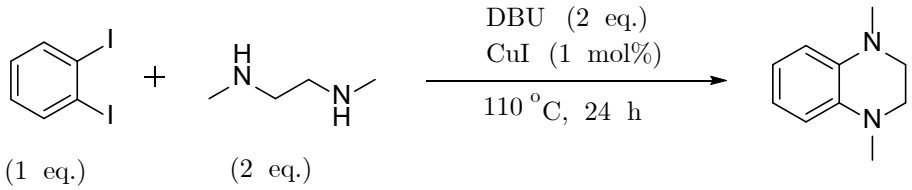

Scheme 4.1: Synthesis of DMHQ. Experimental details may be found in **Section 4.2.2** (page 172).

In this reaction, the DMEA has the triple function of reagent, ligand for the copper, and solvent. Whilst the exact mechanism for this reaction is not fully understood, with a number of different routes proposed depending on the nature of the ligands, it is highly likely that an oxidative addition, reductive elimination catalytic pathway is followed, as presented in **Figure 4.5**. The aryl iodide binds to the copper through a η^6-coordinated intermediate, with electrons donated by the copper causing the Ar-I bond to break due to back donation into the Ar-I σ* antibonding orbital. The aryl and iodide are thus coordinated to the copper in a *cis* configuration relative to each other, with the copper having undergone oxidation from Cu(I) to Cu(III). The iodide is then substituted by an incoming DMEA ligand, which is subsequently deprotonated by DBU (a non-nucleophilic base), before forming a σ-bond with the aryl moiety through a reductive elimination step (whereupon the Cu(III) reverts to Cu(I)).

DMHQ was successfully synthesised using the described method, with structure and purity assessed via GCMS, FTIR and ^{1}H NMR, the latter two detailed in **Appendices 4.5.2a** (page 227) and **4.5.3a** (page 228), respectively. Whilst the obtained yield of 3.31% was lower than that reported in the literature, with significant product loss attributed to the purification process, sufficient material was produced to allow full characterisation and electrochemical analysis.[23]

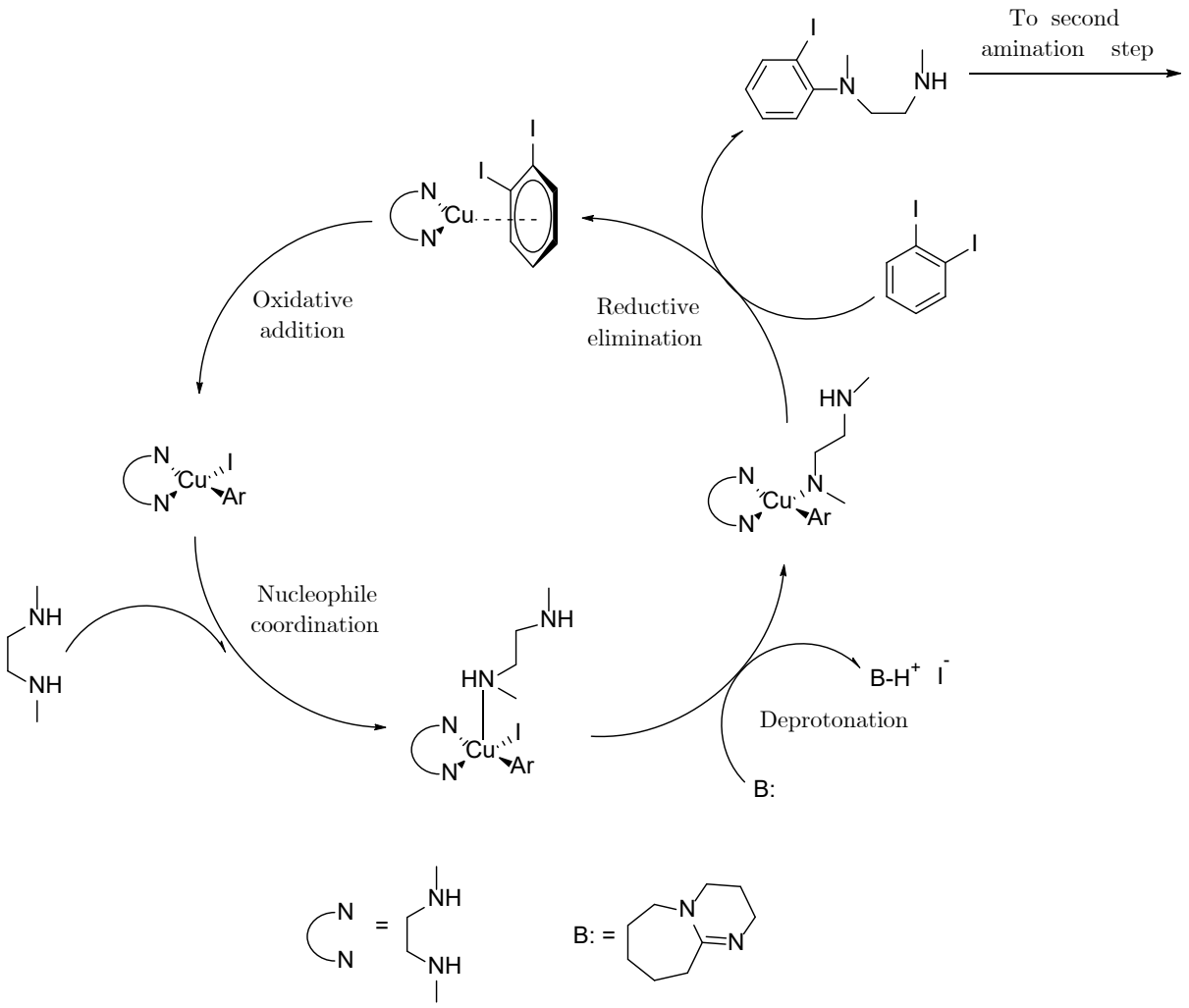

Fig. 4.5: Catalytic cycle for the cross-coupling reaction leading to the formation of DMHQ. Oxidative addition and subsequent reductive elimination steps lead to the regeneration of the Cu(I) catalyst.

Given the bifunctional nature of both diiodobenzene and DMEA, oligomerisation of the reagents is theoretically possible, leading to species based on the molecules presented in **Figure 4.6**. However, the crude reaction mixture showed minimal quantities of other products besides DMHQ. This selectivity for DMHQ can be rationalised through an entropic argument; a ring closure reaction between the DMEA 'arm' and the aryl functionality is more favourable than further oligomerisation as, with the former, two molecules are formed from the one starting molecule (DMHQ

and HI are formed from the ring closure reaction of one DMEA-iodobenzene intermediate).[c]

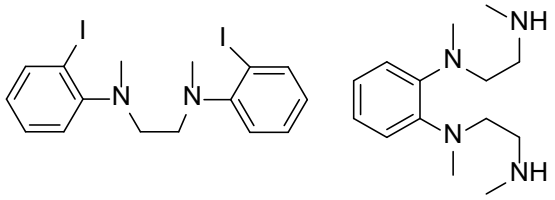

Fig. 4.6: Suggested structures of DMEA-diiodobenzene dimers.

4.3.5.2 Cyclic Voltammetry of DMHQ

Through the cyclic voltammetry experiments presented in **Figure 4.7**, DMHQ was found to have a reversible one-electron oxidation at $E^0 = 3.38$ V, along with a second oxidation at 3.99 V, with the resultant cations displayed in **Scheme 4.2**. Given that the second oxidation is at an undesirably high potential and exhibits *ec* behaviour, only the first oxidation of DMHQ was studied further in this work. The first oxidation potential of DMHQ is in relatively good agreement with the computational value of 3.48 V. The onset potential of DMHQ oxidation is 3.25 V.

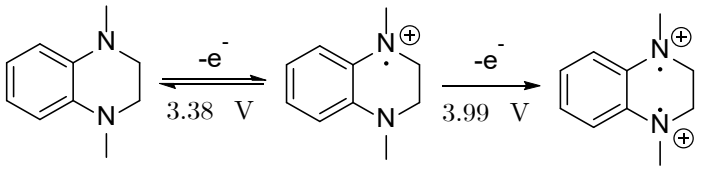

Scheme 4.2: Resultant structures as a result of successive one-electron oxidations of DMHQ.

[c] In many other circumstances there would be a kinetic argument as to why the ring closure is favoured over oligomerisation, as the DMEA substituent of the intermediate is in close proximity to the copper centre upon the bonding of the aryl ring to the copper. However, in this particular reaction the copper centre is complexed to multiple DMEA ligands, leading to no obvious kinetic preference for the pre-bonded DMEA moiety over the other available ligand.

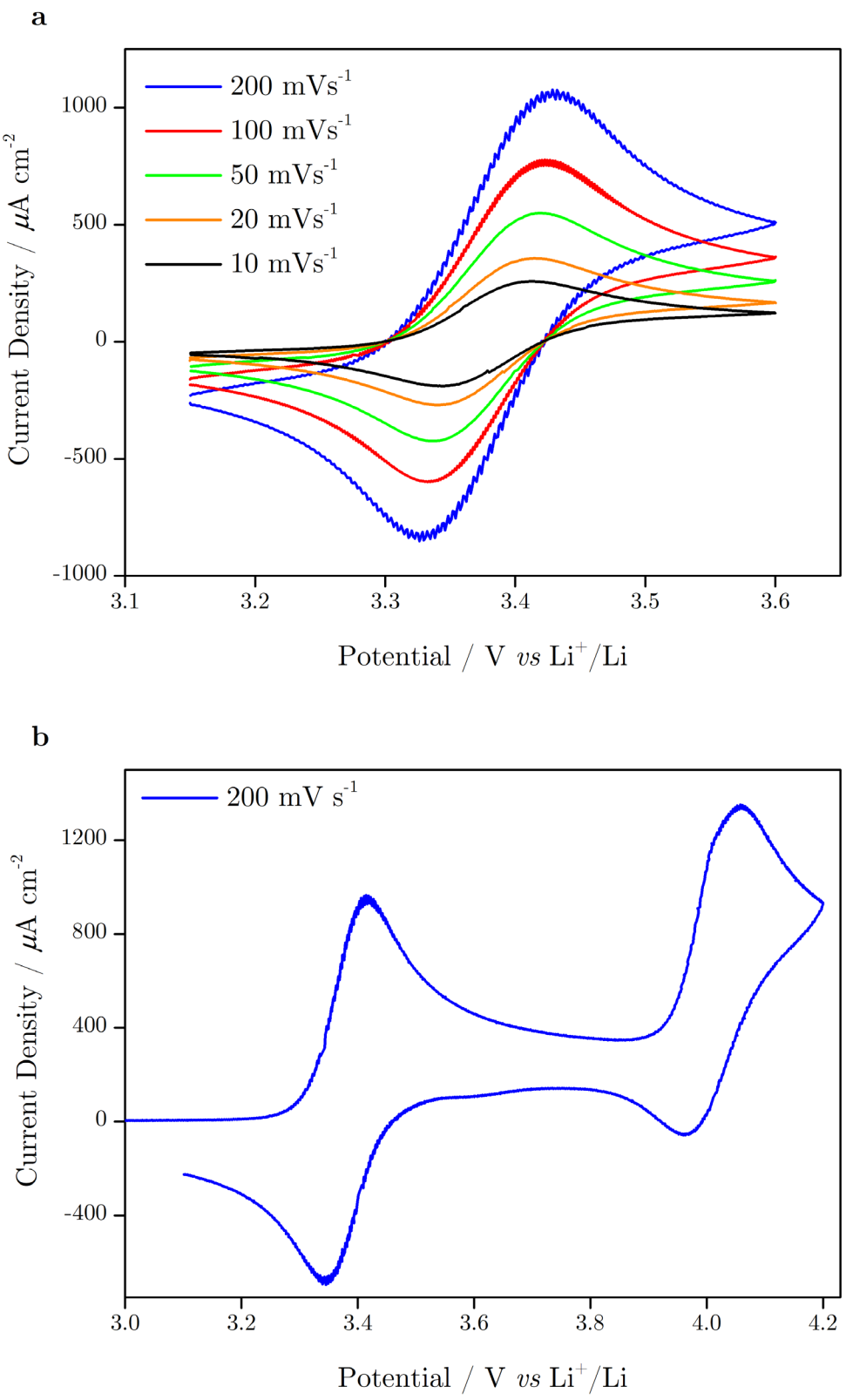

Fig. 4.7: Cyclic voltammetry of 10 mM DMHQ at **a.** multiple scan rates, and **b.** at 200 mV s^{-1} with a wider anodic window, displaying the second oxidation to $DMHQ^{2+}$. Experimental conditions as described in **Section 4.2.8** (page 175), with the cyclic voltammogram in **b.** obtained using a Pt electrode.

4.3.5.3 Cell Cycling with DMHQ

Addition of 30 mM DMHQ to a Li-O_2 cell resulted in the suppression of the charging potential relative to a cell without RMs. As can be seen in **Figure 4.8**, use of DMHQ resulted in a charging plateau at approximately 3.30 V which remained relatively stable for the first two thirds of charge, representing a decrease in charge overpotential of approximately 0.90 V compared to cells without RMs.[d] Towards the end of charge the cell potential begins to polarise towards 4.00 V as a result of carbonates being present in the cell; RMs are unable to electrooxidise carbonates unless the RM operates above 3.82 V.[24-27]

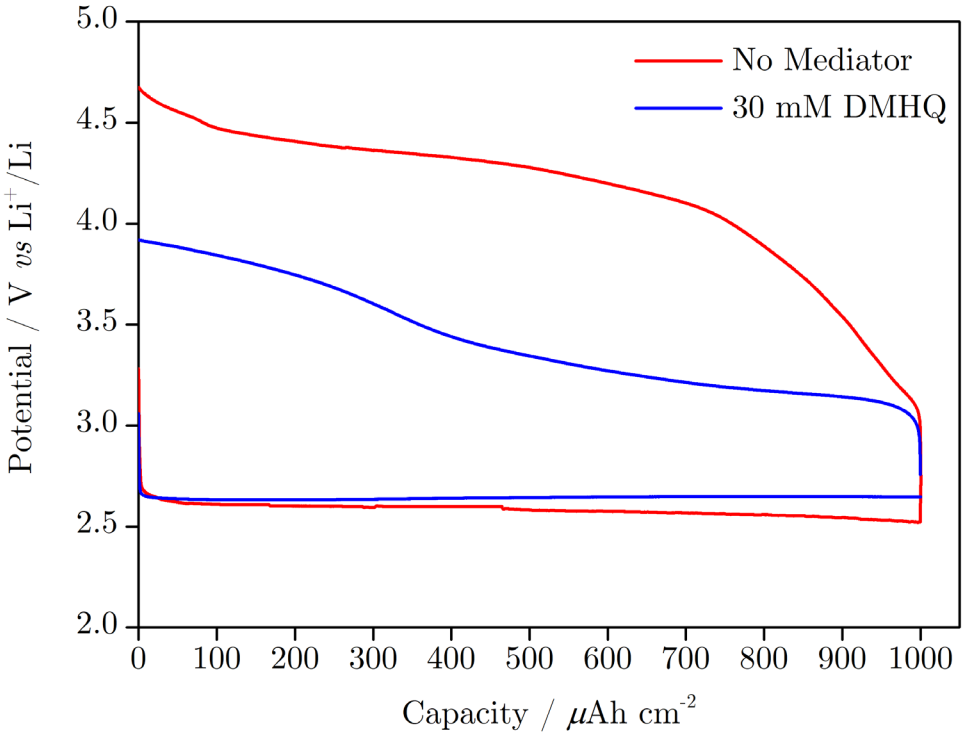

Fig. 4.8: First galvanic discharge and charge cycle of a cell containing 30 mM DMHQ (blue) and a cell containing no RM (red), with the discharge capacity limited to 1000 μAh cm^{-2}. Experimental conditions as detailed in **Section 4.2.9** (page 176).

[d] Variations in the discharge potentials observed in **Figs. 4.8** and **4.15** arise from natural variations between cells rather than the action of charge RMs, which have no effect on cell discharge.

4.3.5.4 DMHQ Performance Over Multiple Cycles

Cells containing 30 mM DMHQ were able to achieve 21 cycles to a fixed capacity of 1000 μAh cm^{-2} at 100 μA cm^{-2}, compared to cells without DMHQ which were only able to achieve 11 cycles before capacity fade was observed (**Figure 4.9**). This represents a 90% increase in cyclability when DMHQ was used in the cell.

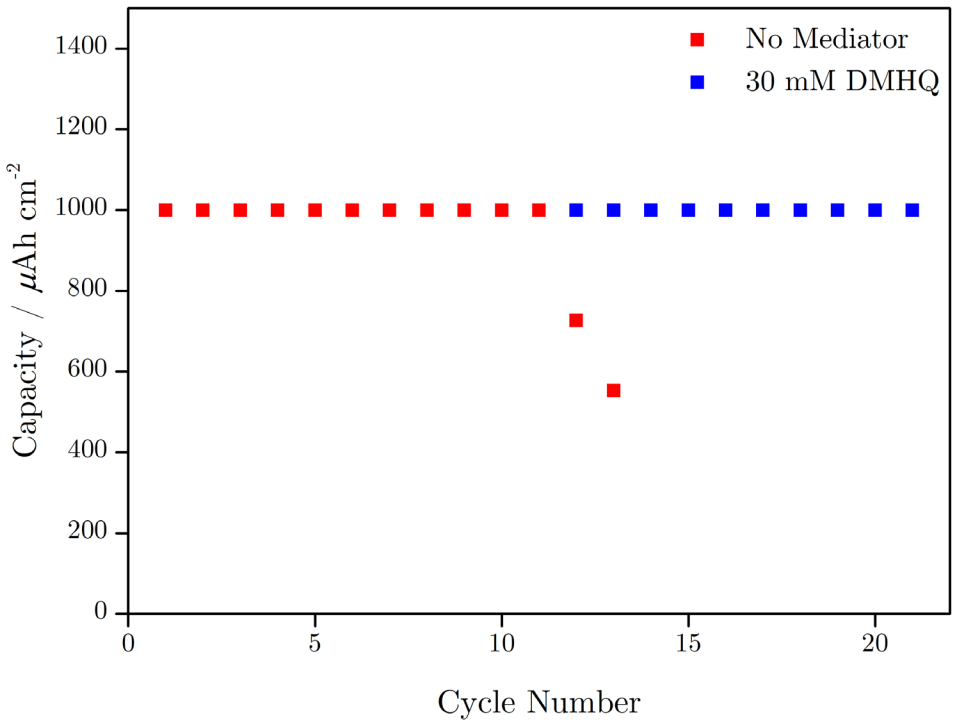

Fig. 4.9: Cyclability of cells containing without (red) and with (blue) 30 mM DMHQ with the discharge capacity limited to 1000 μAh cm^{-2} and with a discharge potential limit of 2.20 V. Experimental conditions as described in **Section 4.2.9** (page 176).

A key question when discussing RM operation is whether the RM is capable of sustaining the same charging potential plateau as observed on the first charge. Of the reports that provide charge data over multiple cycles, all demonstrate a tendency for

the charging overpotential to increase over the course of successive cycles.[2, 13, 20, 22, 28-30] DMHQ is no different; despite exhibiting a low potential on the first charge, on subsequent cycles the charge potential reached 4.40 V at an increasingly early point during charge, as seen in **Figure 4.10**. The decreased overpotential on discharge after the third cycle is interesting to note, and may be attributed to material (likely Li_2O_2) being present on the cathode surface that has not been removed during the previous charge cycle. This material provides a nucleation point for the more facile deposition of Li_2O_2 on the subsequent discharge, leading to a smaller discharge overpotential.[17, 31, 32]

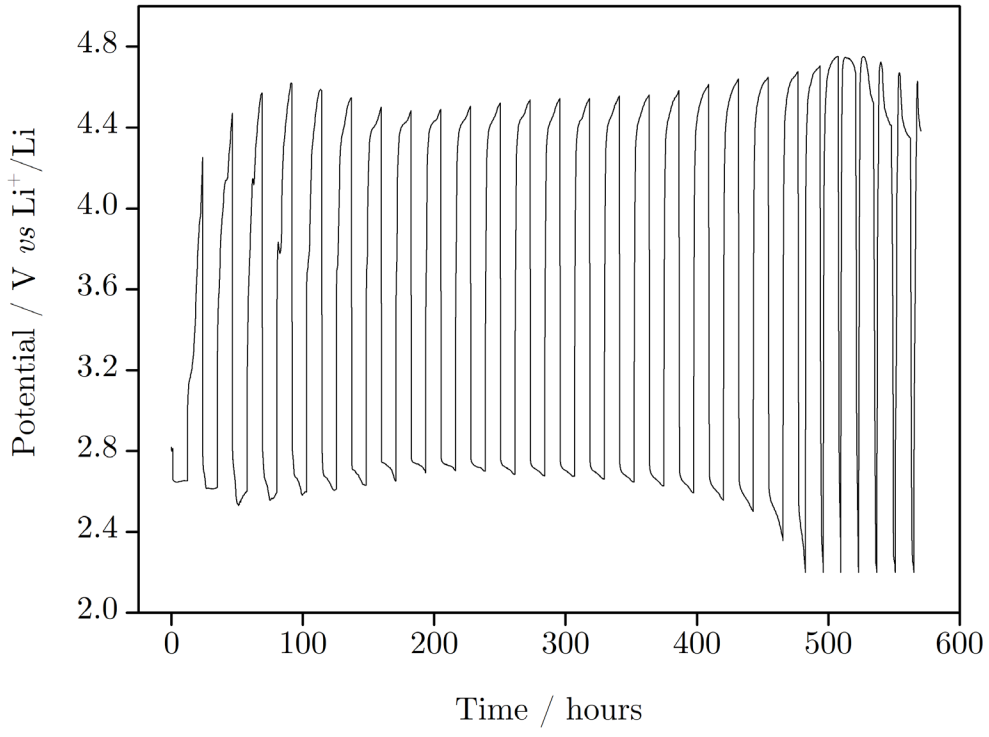

Fig. 4.10: Potential profiles of cells containing 30 mM DMHQ on repeated cycling at 100 μA cm^{-2}, with the discharge capacity limited to 1000 μAh cm^{-2} and a discharge potential limit of 2.20 V. Experimental conditions are as described in **Section 4.2.9** (page 176).

4.3.5.5 XRD: Formation and Removal of Li_2O_2 in the Presence of DMHQ

To ensure that Li_2O_2 is indeed formed and oxidised within the cell during cycling with DMHQ, XRD analysis of the pristine, discharged and charged cathodes was performed (**Figure 4.11**). The XRD patterns of the discharge cathodes clearly show the three Li_2O_2 peaks of greatest intensity (at $2\Theta = 32.85°$, $34.85°$ and $58.66°$) which correspond to the (010), (011) and (110) lattice planes, respectively.[33] Charged cathodes do not exhibit these peaks, indicating that oxidation of Li_2O_2 has occurred. Discharged and charged cells also contain the most intense Li_2CO_3 peak at $2\Theta = 31.68°$, indicating that decomposition of cell components is occurring within the cell and that not all of the Li_2CO_3 is being electrooxidised on charge.

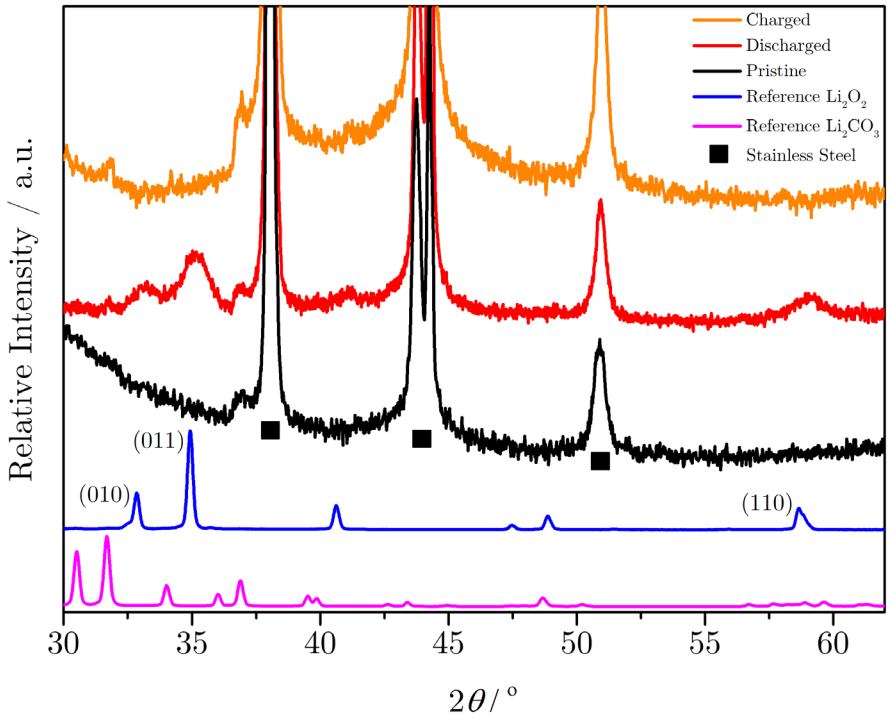

Fig. 4.11: XRD data for a pristine cathode (black) and those discharged (red) and charged (orange) in the presence of 30 mM DMHQ. Experimental conditions for cell cycling are given in **Section 4.2.9** and those for the XRD are given in **Section 4.2.4** (pages 176 and 174, respectively).

4.3.5.6 OEMS: O_2 Formation on Charge with DMHQ

The use of OEMS as presented in **Figure 4.12** demonstrated that addition of 30 mM of DMHQ to the cell resulted in an electron to O_2 ratio of 3.62, compared to a value of 2.94 for identical cells without DMHQ present (the OEMS data for cells without RMs may be found in **Figure 3.8a** within **Chapter 3**). This indicates that the presence of DMHQ results in Faradaic process(es) that lead to the passing of current without the concurrent evolution of O_2 gas. This may be through the shuttling effect of DMHQ to the counter electrode or through other reactions involving DMHQ but not leading to O_2 liberation. The observation of CO_2 evolution above 3.82 V is indicative of Li_2CO_3 electrooxidation, which demonstrates that decomposition has taken place within the cell. The peak flux of O_2 generation for DMHQ was lower than in the no RM system, at approximately 0.08 μmol min^{-1} with no sharp initial peak in O_2 evolution (this peak is also absent in the OEMS of other low potential RMs, such as TMPD and DMPZ, the nature of which is discussed in **Section 3.3.5** (page 130)).

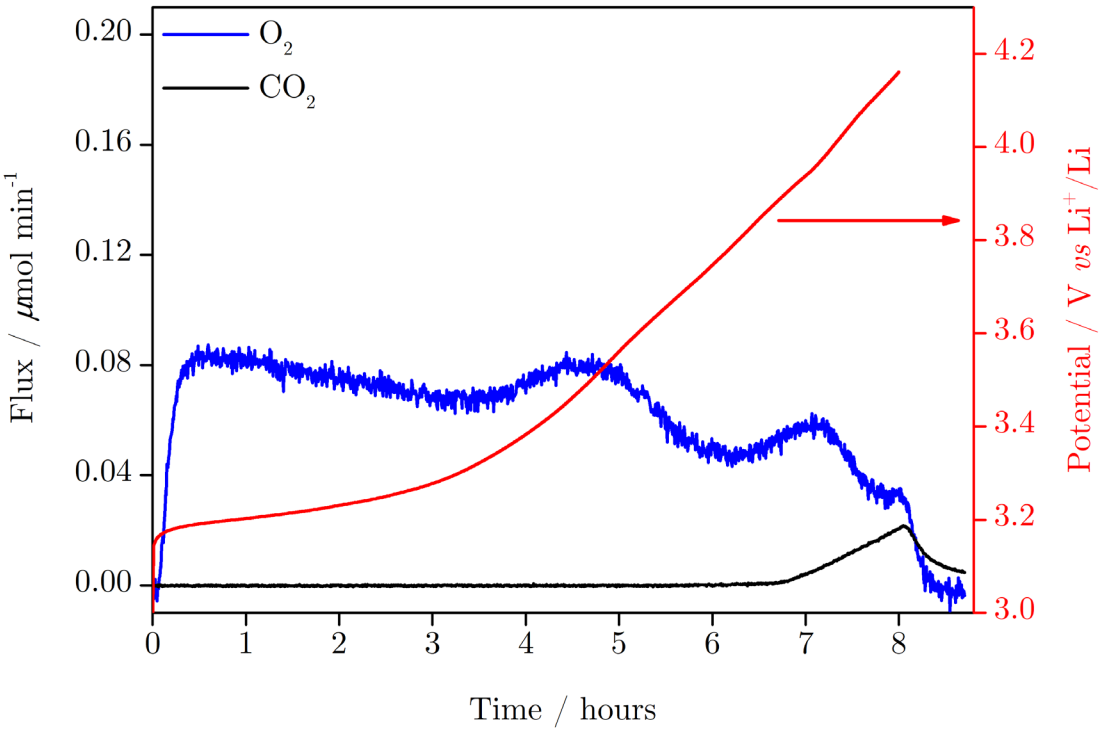

Fig. 4.12: OEMS (O_2 in blue and CO_2 in black) and charge profile (red) for a cell containing 30 mM DMHQ, charging at a constant current density of 100 μA cm^{-2}. Experimental conditions detailed in **Section 4.2.10** (page 177).

4.3.5.7 Evaluation of DMHQ as a Charge Redox Mediator

It is apparent that despite being able to provide a low charging potential on the first cycle, DMHQ lacks the ability to sustain a low potential over multiple cycles. This, in addition to a relatively poor electron to O_2 ratio of 3.62, strongly suggests that DMHQ is involved in side reactions during cell operation. However, this electron to O_2 ratio is comparable to that of both TMPD and DMPZ (3.88 and 3.18, respectively) as found in **Section 3.3.5** (page 130). Given the structural similarities of DMHQ to DMPZ, it is anticipated that DMHQ will react with $^1O_2$ leading to the former's deactivation as a redox-active species within the potential window under investigation.[34] It is also

possible that $DMHQ^{2+}$ undergoes a similar reaction to both $TMPD^{2+}$ and $DMPZ^{2+}$ to form a σ-dimer, evidenced by a small cathodic peak in **Figure 4.7b** at approximately 3.60 V.[35] As such, use of DMHQ as a RM in a commercial setting is unlikely.

4.3.6 MPO Analysis

4.3.6.1 Synthesis of MPO

Synthesis of MPO proceeded via a base-catalysed alkylation reaction as described in **Section 4.2.3** (page 173) and as presented in **Scheme 4.3**:

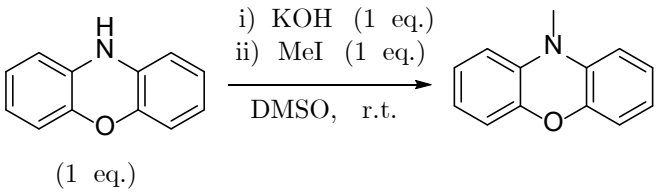

Scheme 4.3: Synthesis of MPO. Experimental procedure may be found in **Section 4.2.3** (page 173).

where potassium hydroxide acts as a base by deprotonating the phenoxazine which, in its anionic form, proceeds to attack the methyl iodide in a S_N2 substitution reaction. The mechanism for the reaction is presented in **Figure 4.13**.

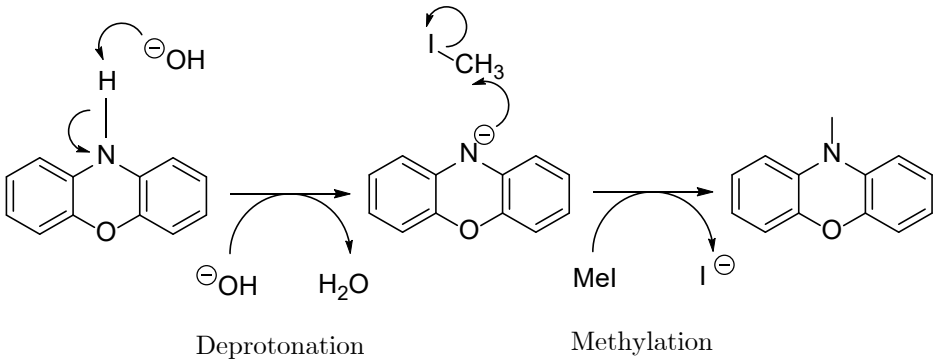

Fig. 4.13: Reaction mechanism for the formation of MPO.

The methylation can be said with confidence to proceed via a S_N2 rather than a S_N1 mechanism due to methyl iodide being sterically open to attack by a nucleophile and iodide being an excellent leaving group.[36]

MPO was successfully synthesised using the described method, with structure and purity assessed via GCMS, FTIR, ^{1}H NMR, with the latter two detailed in **Appendices 4.5.2b** (page 227) and **4.5.3b** (page 228), respectively. The yield of MPO was 21.38%.

4.3.6.2 Cyclic Voltammetry of MPO

MPO was found to have a reversible one-electron oxidation at $E^0 = 3.73$ V, in close agreement with the value of 3.65 V predicted by DFT (**Figure 4.14**), with an onset potential of 3.65 V. There was no loss of anodic peak at slow scan rates, indicating that there were no *ec* reactions occurring involving the MPO. The structure of MPO^+ is given in **Scheme 4.4**.

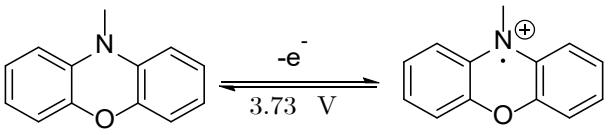

Scheme 4.4: One-electron oxidation of MPO to MPO^+.

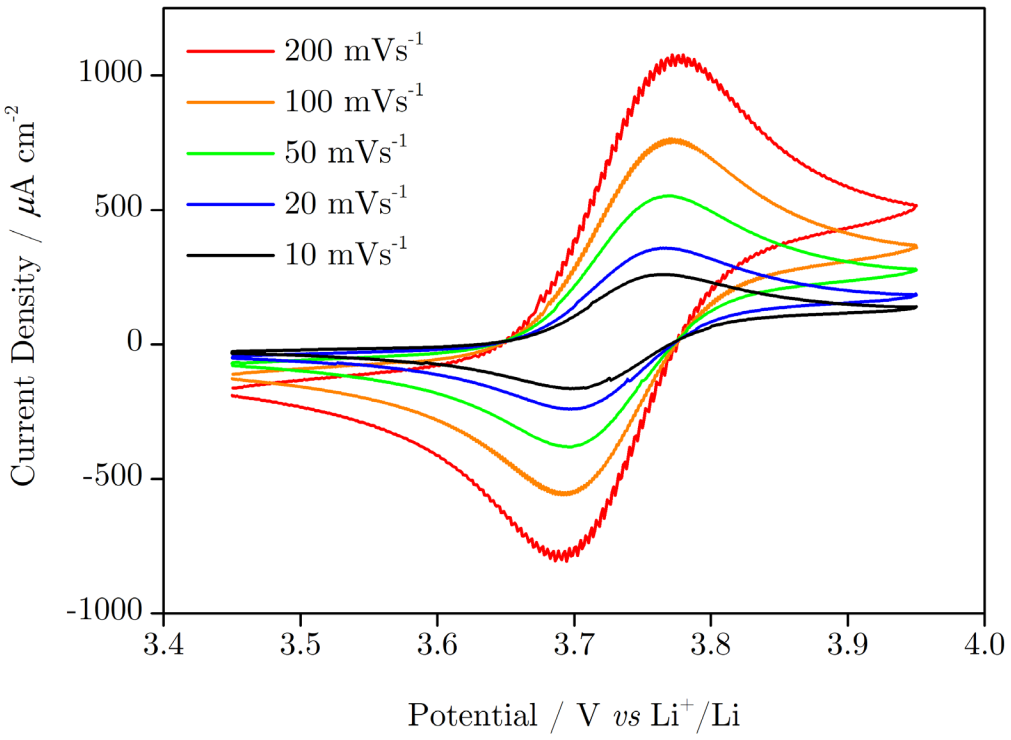

Fig. 4.14: Cyclic voltammetry of 10 mM MPO at multiple scan rates, with experimental conditions as described in **Section 4.2.8** (page 175).

4.3.6.3 Cell Cycling with MPO

Cells containing 30 mM MPO display a relatively flat charging plateau of approximately 3.50 V, reducing the overpotential of the cell by 0.85 V compared to a cell without MPO present (**Figure 4.15**). Towards the end of charge, cells containing MPO display a rise in potential indicating that some Li_2CO_3 is present in the cells (formed through parasitic side reactions).

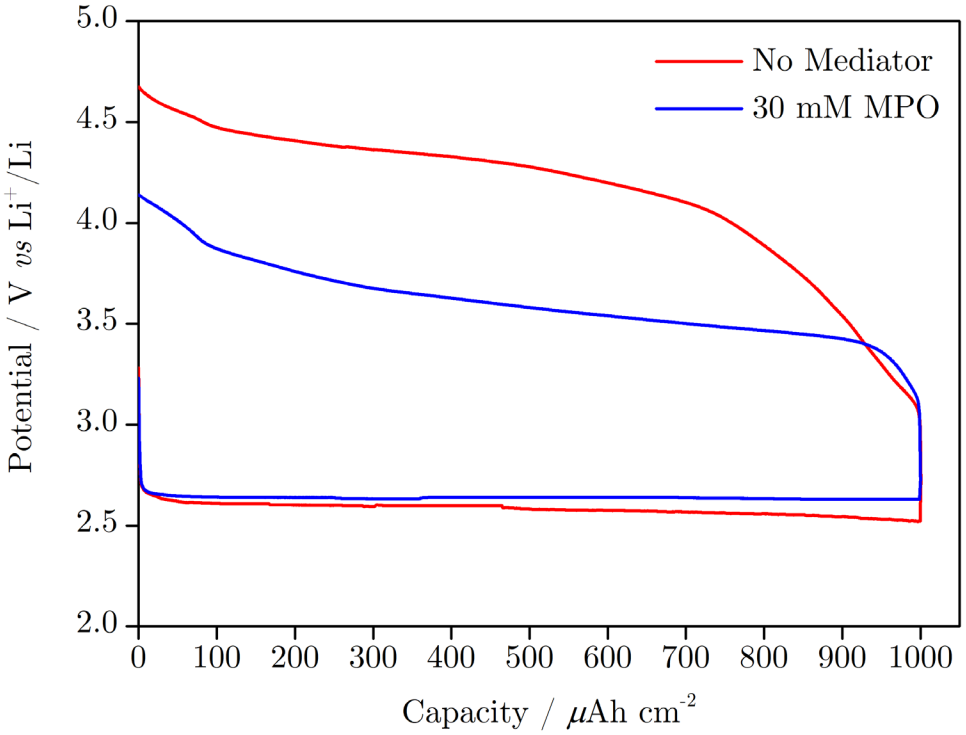

Fig. 4.15: First galvanic discharge and charge cycle of a cell containing 30 mM MPO (blue) and a cell containing no RM (red), with the discharge capacity limited to 1000 μAh cm^{-2}. Experimental conditions as detailed in **Section 4.2.9** (page 176).

4.3.6.4 MPO Performance Over Multiple Cycles

Cells containing MPO demonstrate greater levels of cyclability, achieving 29 cycles when limited to a capacity of 1000 μAh cm^{-2} at 100 μA cm^{-2} before capacity fade begins compared to 22 cycles without MPO (**Figure 4.16**). This represents an increase in cyclability of 32% when MPO is utilised.

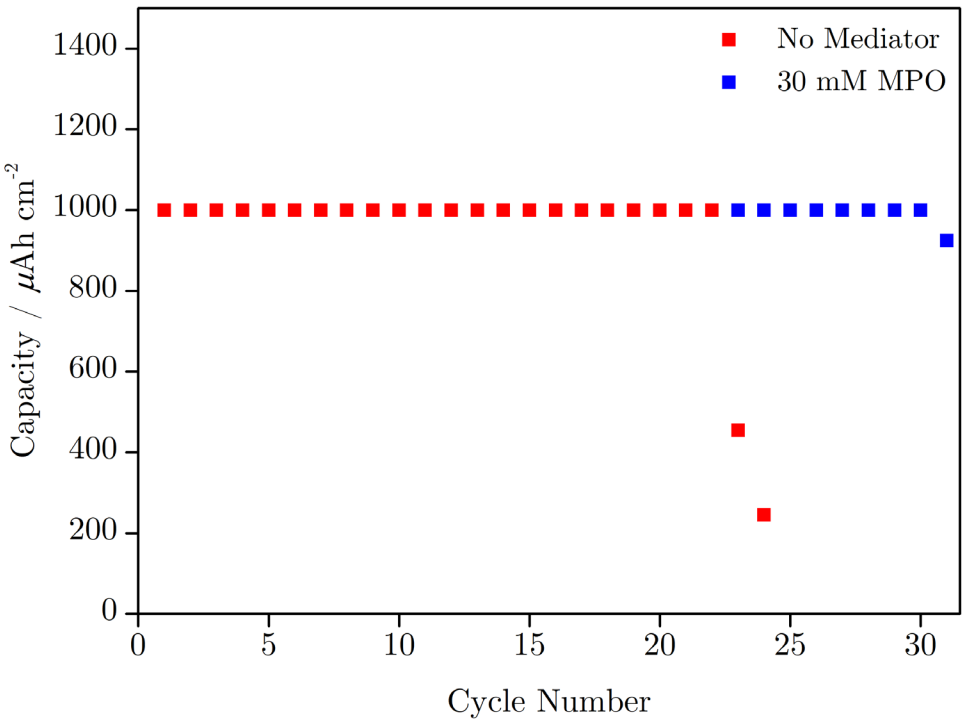

Fig. 4.16: Cyclability of cells containing without (red) and with (blue) 30 mM MPO with the discharge capacity limited to 1000 μAh cm^{-2} and with a discharge potential limit of 2.20 V. Experimental conditions as described in **Section 4.2.9** (page 176).

Whilst the charge potential increased with each cycle, cells containing MPO were able to keep the charge plateau below 4.4 V for a greater proportion of charge for a larger number of cycles compared to DMHQ, seen in **Figure 4.17**. Similarly to DMHQ, after the first cycle the discharge plateau of MPO-containing cells shifts to a more positive potential for a number of cycles until shortly before capacity fade begins.

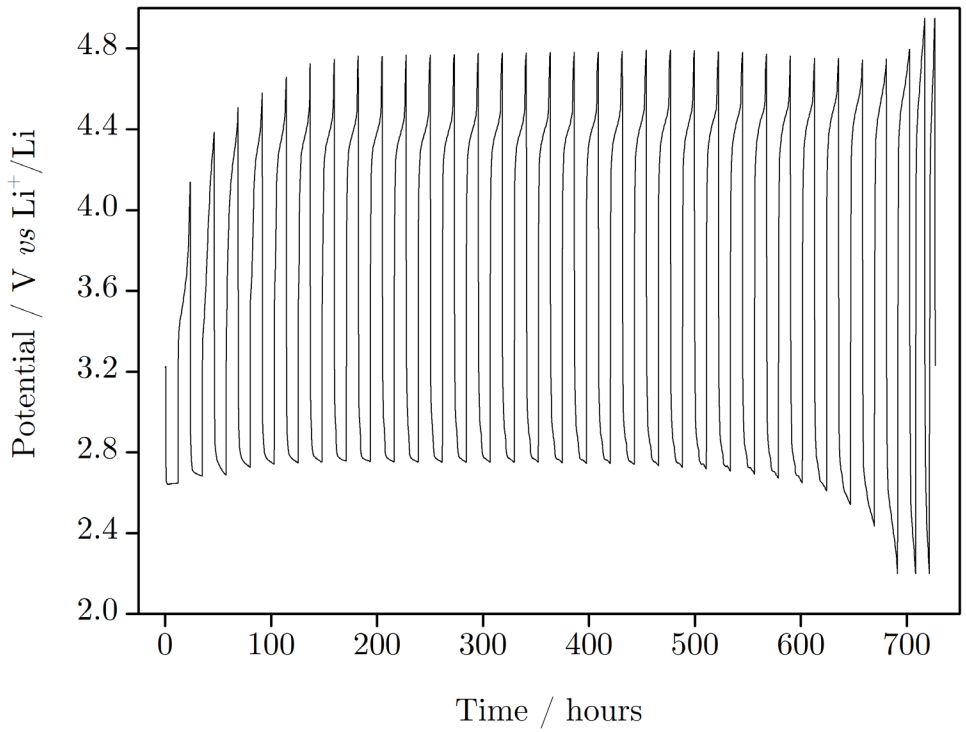

Fig. 4.17: Potential profiles of cells containing 30 mM MPO on repeated cycling at 100 μA cm^{-2}, with the discharge capacity limited to 1000 μAh cm^{-2} and a discharge potential limit of 2.20 V. Experimental conditions are as described in **Section 4.2.9** (page 176).

4.3.6.5 XRD: Formation and Removal of Li_2O_2 in the Presence of MPO

To ensure that Li_2O_2 is indeed formed and oxidised within the cell during cycling with MPO, XRD analysis of the pristine, discharged and charged cathodes was performed (**Figure 4.18**). The XRD patterns of the discharged cathodes clearly show the three Li_2O_2 peaks of greatest intensity for the (010), (011) and (110) lattice planes. Charged cathodes do not exhibit these peaks, indicating oxidation of Li_2O_2 has occurred. Whilst discharged cells also contain the most intense Li_2CO_3 peak at $2\Theta = 31.68°$, unlike DMHQ cells, MPO-containing cells do not contain traces of Li_2CO_3 in the charged

cathodes. This may be due to MPO-containing cells reaching a higher potential towards the end of charge than DMHQ, allowing for complete oxidation of the Li_2CO_3 present.

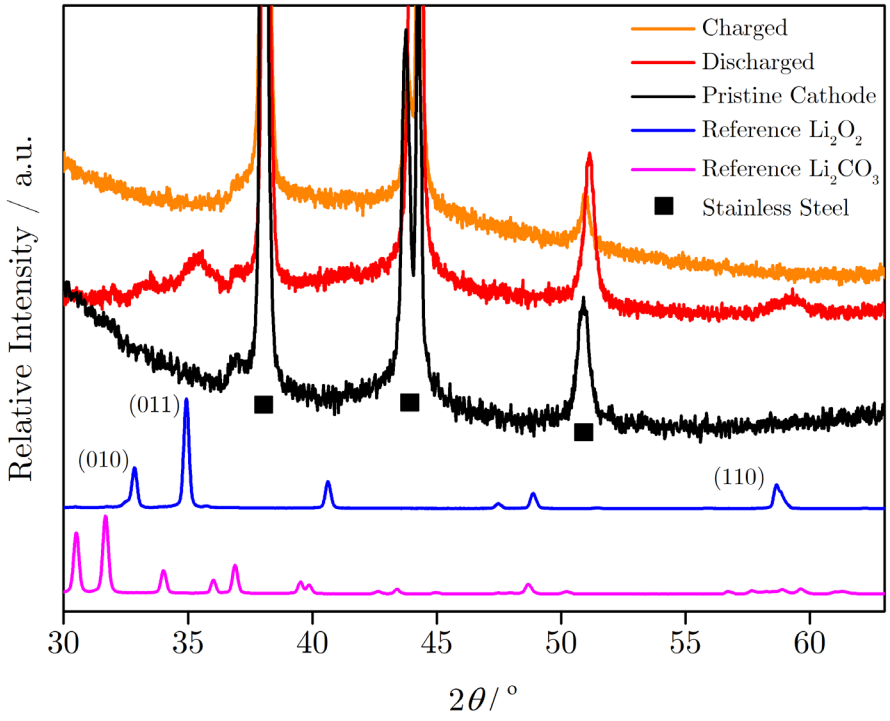

Fig. 4.18: XRD data for pristine cathode and those discharged (red) and charged (orange) in the presence of 30 mM MPO, as described in **Section 4.2.9** (page 176). Experimental conditions for XRD are given in **Section 4.2.4** (page 174).

4.3.6.6 OEMS: O_2 Formation on Charge with MPO

Addition of MPO to cells led to an improvement in the electron to O_2 ratio on charge, with 30 mM MPO giving a ratio of 2.69 in contrast to the value of 2.94 obtained without MPO (**Figure 4.19** presents the OEMS data for MPO, while **Figure 3.8a** provides that for cells without RMs). Furthermore, use of MPO led to a peak O_2 flux of approximately 0.19 μmol min^{-1}, which is comparable both with cells containing

TEMPO (**Appendix 4.5.5** (page 230)) and cells without any RM. As with most cells, CO_2 is liberated towards the end of charge once the potential exceeds 3.82 V.

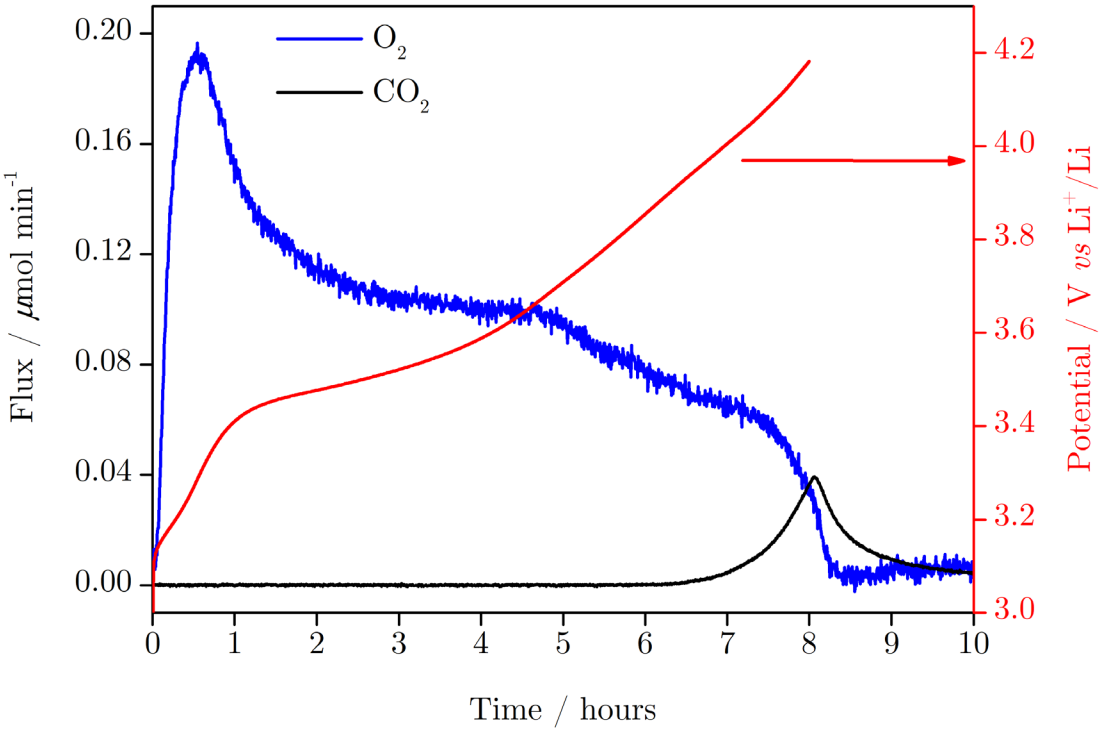

Fig. 4.19: OEMS (O_2 in blue and CO_2 in black) and charge profile (red) for a cell containing 30 mM MPO, charging at a constant current density of 100 μA cm^{-2}. Experimental conditions detailed in **Section 4.2.10** (page 177).

The ability of MPO to operate at a higher current density of 200 μA cm^{-2} was investigated. It was found that whilst MPO was able to sustain its lower charge plateau at the higher current density, the electron to O_2 ratio increased marginally to 3.03; this suggests that as the current density increases, so too does the degree of MPO shuttling between the cathode and the counter electrode (**Figure 4.20**). Despite this, the broad trend for the gas flux over charge is similar for MPO-containing cells at both

100 μA cm^{-2} and 200 μA cm^{-2}, with a small amount of CO_2 liberated towards the end of charge.

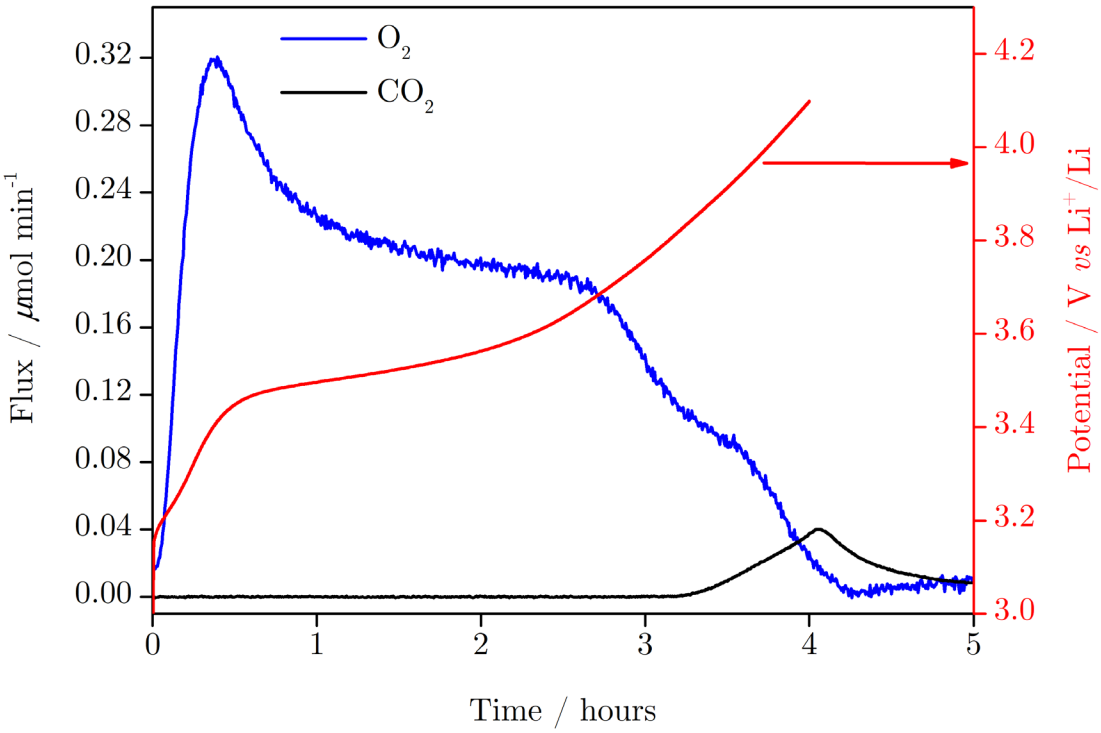

Fig. 4.20: OEMS (O_2 in blue and CO_2 in black) and charge profile (red trace) for a cell containing 30 mM MPO, charging at a constant current density of 200 μA cm^{-2}. Experimental conditions detailed in **Section 4.2.10** (page 177).

4.3.6.7 Evaluation of MPO as a Charge Redox Mediator

Use of MPO improves the cyclability of the cell, increasing the number of achievable cycles from 22 to 29 before capacity fade is observed. When compared to cells without RMs, on the first cycle the use of MPO leads to both a lower charging potential and an electron to O_2 ratio with a value closer to the theoretical value of 2.00 expected for the oxidation of Li_2O_2. Furthermore, XRD data reveals that all Li_2O_2 has been oxidised

by the end of charge. Of all RMs used either here or in **Chapter 3**, only TEMPO has a superior electron to O_2 ratio, at 2.29 for a concentration of 30 mM TEMPO at 100 μA cm^{-2} (**Appendix 4.5.5** (page 230)). As such, MPO is a promising candidate for use as a RM in a commercial Li-O_2 cell.

4.3.7 Discussion of the Validity of the Computational Model

Comparison of the computational oxidation potential values obtained through the DFT calculations with the experimental values obtained through cyclic voltammetry is essential to confirm the validity of the chosen computational parameters. The values obtained both computationally and experimentally are in relatively good agreement, despite the errors that are intrinsic to DFT calculations, with the values for MPO having a difference of only 0.08 V and those for DMHQ being within 0.10 V of each other.[37] Deviation of the experimental values from the calculated values may also be attributed to the lack of ions (such as Li^+, $TFSI^-$ and O_2^-) in the DFT experiments, which may affect the stability (and hence the redox potential) of the oxidised RM.[2]

The values of the DFT calculations are in closer agreement to the (less positive) onset potentials of the RMs, rather than their formal potentials. This suggests that the DFT calculations may provide, in some cases, a good indication of the potential at which the cell will operate; in a working Li-O_2 cell containing a RM the charging plateau is generally below the formal potential of the RM.[28] A comparison of all calculated and experimental oxidation potentials for RMs used in this work can be seen within **Table 4.1** (page 182).

4.3.8 Investigation of Novel RM Reaction Kinetics with Li_2O_2

4.3.8.1 SECM Constant Current

To investigate the reaction kinetics of DMHQ and MPO with Li_2O_2 the apparent rate constant, k_{app}, was extracted using SECM (a full and detailed explanation of the theory behind SECM is provided in **Section 2.1.4** (page 79)). The k_{app} represents the rate constant for the rate-determining step in the mechanism of RM^+ reaction with Li_2O_2. The precise identity of the rate-limiting reaction step is as-yet unknown.

In contrast to the cyclic voltammetry performed earlier in this Chapter where macroelectrodes were used, SECM is performed using microelectrodes[e] (specifically microdisc electrodes) which produce a diffusion-limited current response, $i_{L\infty}$, defined according to **Equation 4.2**:

$$i_{L\infty} = 4nFDac \qquad \textbf{Eq. 4.2}$$

where n is the number of electrons transferred, F is the Faraday constant, D is the diffusion coefficient of the electroactive species, c is the bulk concentration of said species, and a is the radius of the microelectrode. Due to the significant contribution of edge diffusion when using microdisc electrodes (discussed in **Section 2.1.4.1** (page 79)), the effect of the size of the insulating sheath surrounding the electrode proper must be taken into account though the following modification of **Equation 4.2**:

$$i_L = 4nFDac\beta \qquad \textbf{Eq. 4.3}$$

[e] The classification of an electrode as macro or micro is determined by its radius; microelectrodes have radii within the range 0.1 – 100 μm, with the radius most commonly used being 5 – 25 μm. Macroelectrodes encompass any electrodes greater than 100 μm and microelectrodes with a radius of less than 25 μm may further be classified as ultramicroelectrodes. D. Pletcher, *A First Course in Electrode Processes*, The Royal Society of Chemistry Cambridge, 2nd edn., 2009.

where β is given by **Equation 4.4**:

$$\beta = 1 + \frac{0.23}{(R_g^3 - 0.81)^{0.36}} \qquad \textbf{Eq. 4. 4}$$

Rearrangement of **Equation 4.4** allows for evaluation of the dimensionless constant R_g, which is given by **Equation 4.5**:

$$R_g = \frac{r_{glass}}{a} \qquad \textbf{Eq. 4. 5}$$

with β obtained experimentally from the ratio between the limiting current of a microelectrode with small R_g, i_L, and that of a microelectrode with a large R_g, $i_{L\infty}$:

$$\beta = \frac{i_L}{i_{L\infty}} \qquad \textbf{Eq. 4. 6}$$

From the chronoamperometric data presented in **Figure 4.21** it was possible to determine the values of β for the microdisc reactions involving DMHQ and MPO, given in **Table 4.2**. It should be noted that the microdisc experiments are very susceptible to vibrations, which cause the fluctuations in the chronoamperometric data observed in **Figure 4.21**.

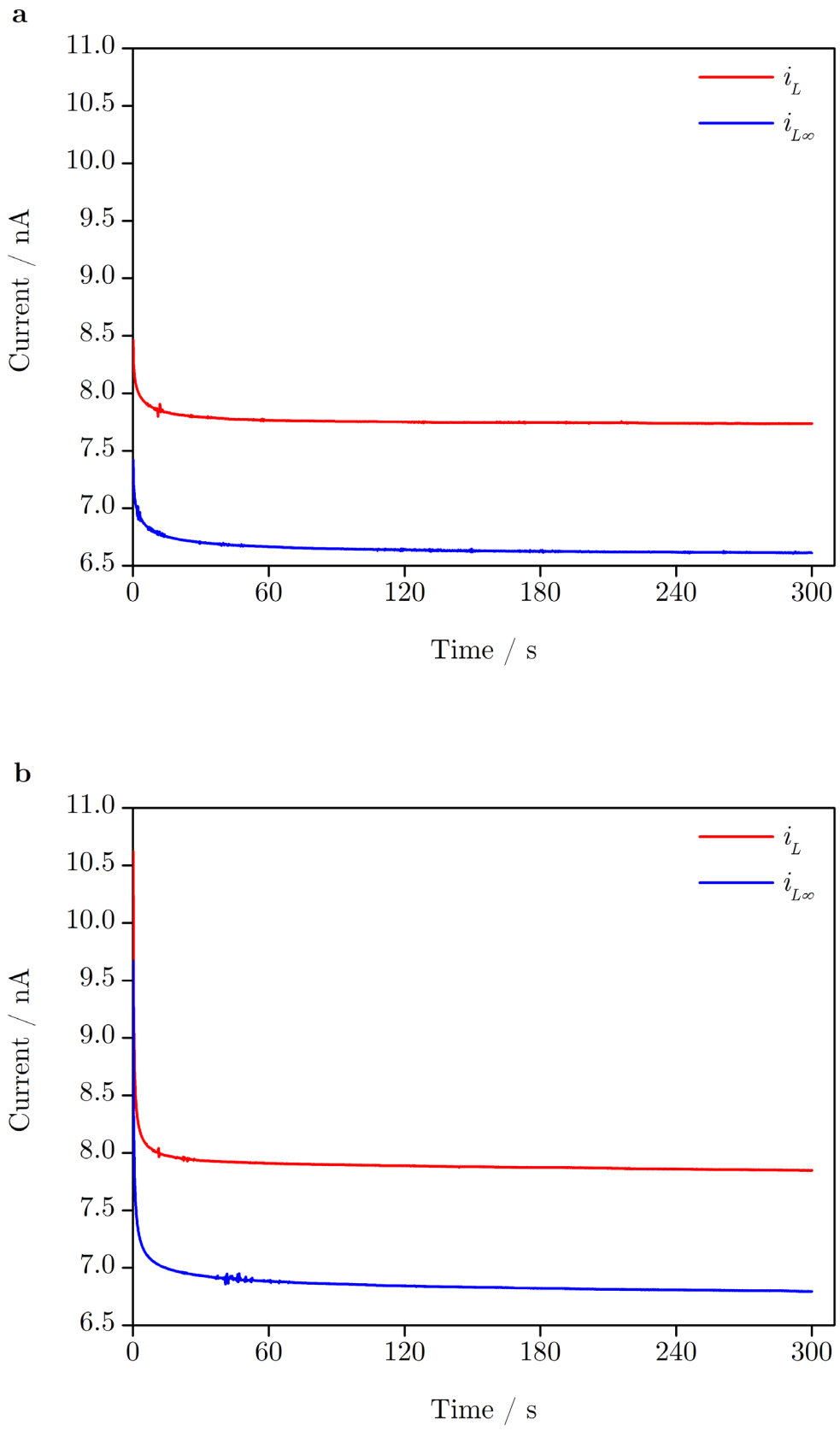

Fig. 4.21: Chronoamperometry of **a.** DMHQ and **b.** MPO at Pt microelectrodes with small (red) and large (blue) R_g values, as described in **Section 4.2.11** (page 177).

4.3.8.2 Calculation of k_{app}

Using SECM as described in **Section 4.2.11** (page 177), the approach curves of DMHQ and MPO were obtained. As can be seen in **Figure 4.22**, both DMHQ and MPO exhibit approach curves typical of the negative feedback associated with the substrate being an insulator. However, it is clear that, of the two RMs, MPO displays the faster kinetics, which may be inferred from the slight rise in current immediately prior to the exponential decrease as the normalised distance of the electrode tip from the substrate surface, L, tends towards zero.[5, 38]

In order to determine the k_{app} for each RM, the experimental SECM data was fitted to an approximate analytical expression that defines the feedback curve at a microdisc electrode, developed by Lefrou *et al.*[38-40] This analytical expression is valid for any value of $R_g < 20$ and any $\varkappa$ when $L > 0.1$, where $\varkappa$ is the dimensionless rate constant.[41] The expression for the current resulting from positive feedback, Ni_T^{cond}, where bringing the electrode tip closer to the substrate surface leads to an increase in current, is given by **Equation 4.6**:

$$Ni_T^{cond} \approx \alpha(R_g) + \frac{1}{\beta(R_g)}\frac{\pi}{4ArcTanL} + \left(1 - \alpha(R_g) - \frac{1}{2\beta(R_g)}\right)\frac{2}{\pi}ArcTanL \qquad \textbf{Eq. 4.6}$$

where β is given by **Equation 4.4** and α is given by **Equation 4.7**:

$$\alpha = ln2 + ln2\left(1 - \frac{2}{\pi}ArcCos\frac{1}{R_g}\right) - ln2\left(1 - \left(\frac{2}{\pi}ArcCos\frac{1}{R_g}\right)^2\right) \qquad \textbf{Eq. 4.7}$$

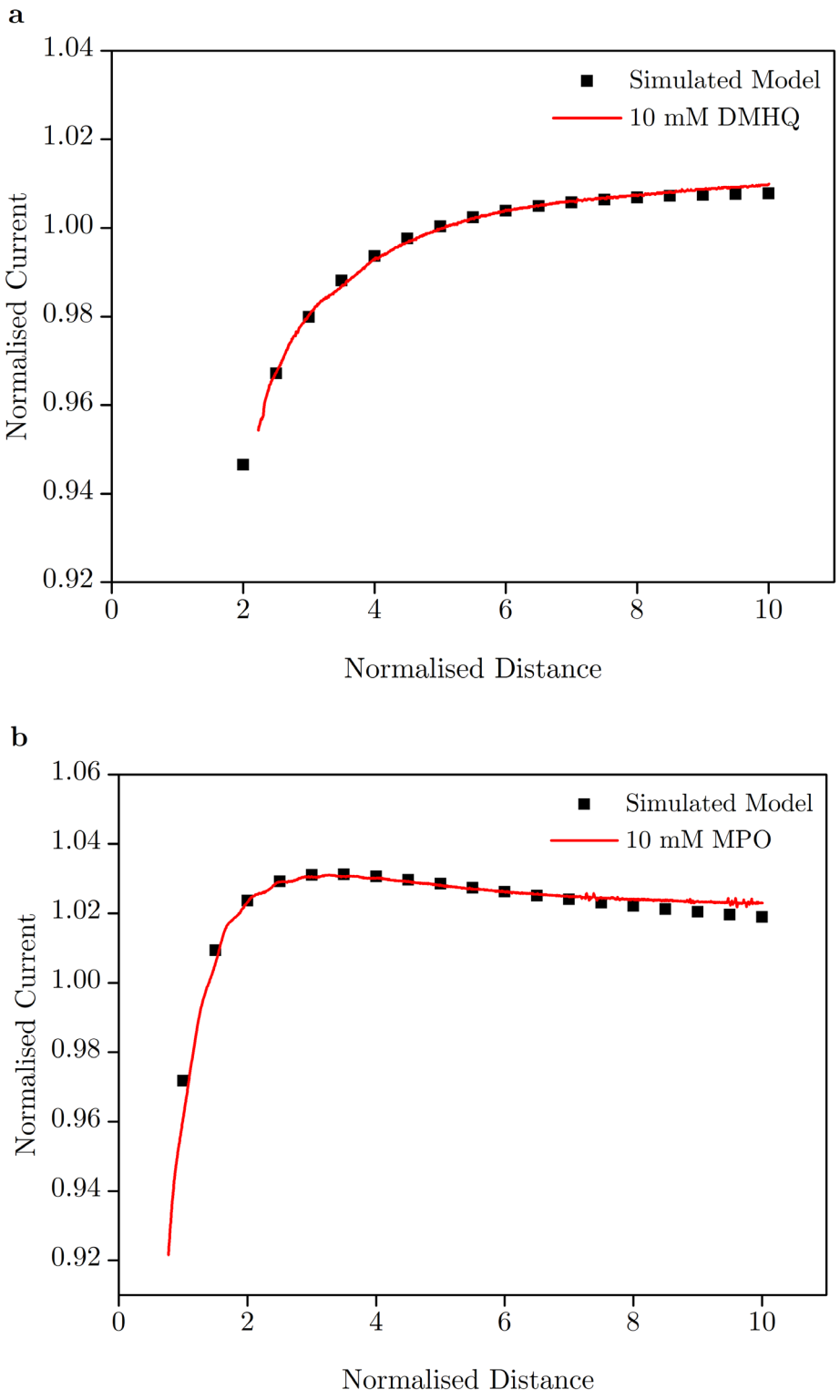

Fig. 4.22: Approach curves of **a.** DMHQ and **b.** MPO towards a Li_2O_2 pellet substrate using 10 mM RM concentration, with experimental conditions as described in **Section 4.2.11** (page 177). Simulated approach curves (black squares) obtained as described in **Section 4.3.8.2** (page 211). The number of displayed fitting points has been reduced in **Figure 4.22** to avoid obscuring the experimental data.

The corresponding expression for the current resulting from negative feedback, Ni_T^{ins}, where bringing the electrode tip closer to the substrate leads to a decrease in current, is given by **Equation 4.8**:

$$Ni_T^{ins} \approx \left(\frac{2.08}{R_g^{0.358}}\left(L - \frac{0.145}{R_g}\right) + 1.585\right)\left(\begin{array}{c}\frac{2.08}{R_g^{0.358}}\left(L + 0.0023R_g\right) + 1.57 \\ + \frac{lnR_g}{L} + \frac{2}{\pi R_g}\ln\left(1 + \frac{\pi R_g}{2L}\right)\end{array}\right)^{-1} \qquad \textbf{Eq. 4.8}$$

By combining **Equations 4.6** and **4.8** it is possible to construct a general equation for the first order irreversible reaction kinetics between a RM^+ and a substrate, given by **Equation 4.9** (overleaf), which, for the sake of simplicity, may be represented by **Equation 4.10**:

$$Ni_T\left(L, R_g, \kappa\right) \approx Ni_T^{cond}\left(L + \frac{1}{\kappa}, R_g\right) + \frac{Ni_T^{ins}\left(L, R_g\right) - 1}{\left(1 + 2.47R_g^{0.31}L\kappa\right)\left(1 + L^{0.006R_g + 0.113}\kappa^{-0.0236R_g + 0.91}\right)} \qquad \textbf{Eq. 4.10}$$

$$Ni_T(L,R_g,\kappa) \approx \alpha(R_g) + \frac{1}{\beta(R_g)}\frac{\pi}{4ArcTan\left(L+\frac{1}{\kappa}\right)} + \left(1-\alpha(R_g)-\frac{1}{2\beta(R_g)}\right)\frac{2}{\pi}ArcTan\left(L+\frac{1}{\kappa}\right)$$

$$+\frac{\left(\frac{2.08}{R_g^{0.358}}\left(L-\frac{0.145}{R_g}\right)+1.585\right)\left(\frac{2.08}{R_g^{0.358}}\left(L+0.0023R_g\right)+1.57+\frac{lnR_g}{L}+\frac{2}{\pi R_g}\ln\left(1+\frac{\pi R_g}{2L}\right)\right)^{-1}-1}{\left(1+2.47R_g^{0.31}L\kappa\right)\left(1+L^{0.006R_g+0.113}\kappa^{-0.0236R_g+0.91}\right)}$$

Eq. 4. 9

For this expression of the first order reaction kinetics, the dimensionless rate constant, $\varkappa$, contains the kinetic information for the reaction between the RM^+ and the substrate. The apparent rate constant, k_{app}, for the reaction may be extracted from $\varkappa$ through the following relationship:

$$\kappa = \frac{k_{app}a}{D} \qquad \textbf{Eq. 4.11}$$

Equation 4.11 highlights the importance of obtaining an accurate value for the diffusion constant. Even with a correction being applied to the cyclic voltammetry in **Figures 4.7** and **4.14** to account for the resistance of the TEGDME electrolyte, due to the large current being passed there is still a high ohmic drop resulting in peak separation of more than 59 mV (which is the expected peak separation for a reversible one-electron redox process).[17] Microelectrodes, on the other hand, exhibit a much lower Ohmic drop as they pass a much smaller current.[17] As such, the diffusion constant was calculated from the diffusion-limited current of the microelectrode as presented in **Figure 4.23**, with the results given in **Table 4.2**. It should be noted that within this analysis of the SECM data, only the diffusion of the RMs is considered, with both migration and convection omitted since they are considered to have a negligible contribution to the current.[41]

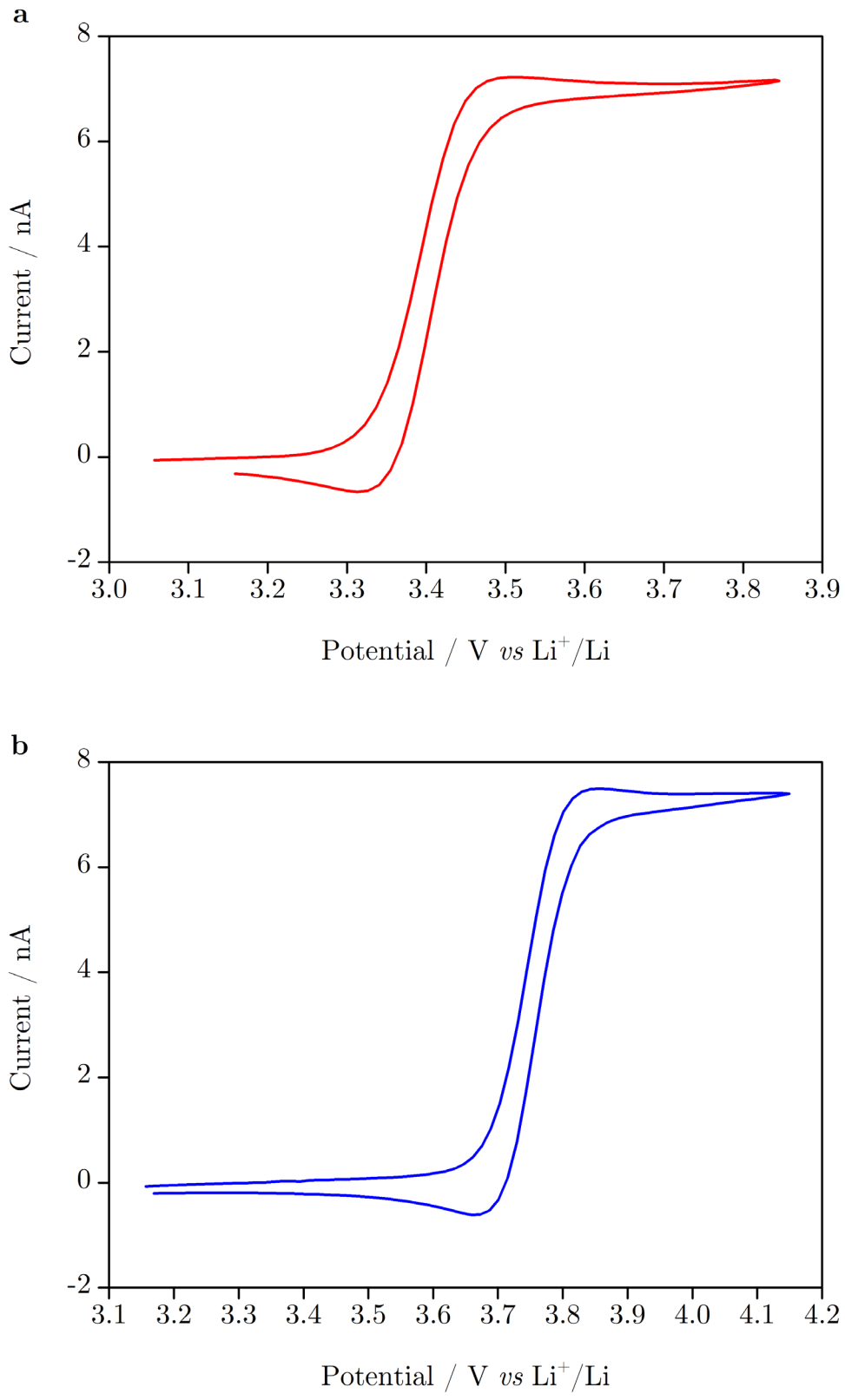

Fig. 4.23: Cyclic voltammetry of **a.** DMHQ and **b.** MPO at a microelectrode. Experimental conditions as described in **Section 4.2.11** (page 177).

The k_{app} for each RM was obtained by applying **Equation 4.9** to a set of simulated model SECM data and substituting β and L for the values obtained experimentally. Through an iterative process, the value of $\varkappa$ was varied until agreement between the model data and the experimental approach curves was obtained, with the simulated model data shown in **Figure 4.22**. Through rearrangement of **Equation 4.11**, the k_{app} for DMHQ and MPO were found to be 0.33×10^{-3} and 1.45×10^{-3} cm s^{-1} respectively. A summary of the key parameters used in determining k_{app} may be found in **Table 4.2**.

	β / dimensionless	R_g / dimensionless	D / cm^2 s^{-1}	k_{app} / cm s^{-1}
DMHQ	1.17	1.47	2.35×10^{-6}	0.33×10^{-3}
MPO	1.15	1.58	2.84×10^{-6}	1.45×10^{-3}

Table 4.2: Key parameters for the reaction kinetics between Li_2O_2 and the novel RMs, DMHQ and MPO.

4.3.9 Discussion of Novel RM Kinetics

While DMHQ and MPO may be considered in isolation, it is useful to put them in the context of other known RMs with similar structures, particularly with regards to two key parameters, formal oxidation potential and reaction kinetics with Li_2O_2.

4.3.9.1 DMHQ and DMPZ

DMHQ is analogous to DMPZ, with the exception that one of the connecting 1,2-disubstituted phenyl rings of DMPZ has been replaced by an ethylene bridge, as illustrated in **Figure 4.24**. This structural difference provides the reasoning for DMHQ having a slightly more positive redox potential at 3.38 V, compared to 3.29 V for DMPZ; phenyl substituents provide greater stabilisation for the nitrogen radical than alkyl moieties.[42]

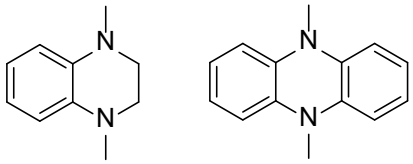

Fig. 4.24: Structures of DMHQ (left) and DMPZ (right).

Comparing the kinetics of DMHQ and DMPZ, generally it would be expected that a less sterically hindered centre would lead to a greater rate of reaction.[6] This is indeed what is observed with DMHQ and DMPZ, with the less sterically hindered DMHQ having a k_{app} that is almost twice that of DMPZ, at 0.33×10^{-3} cm s^{-1} and 0.18×10^{-3} cm s^{-1} respectively.[5] It follows, therefore, that DMHQ and TEMPO (**Figure 4.25**) should have somewhat similar values for k_{app}, given that they both are of similar molar mass (156 g mol^{-1} and 162 g mol^{-1} respectively) and both have similar groups around their redox-active sites. However, Chen *et al.* revealed that TEMPO has a k_{app} value of 3.6×10^{-3} cm s^{-1}, which is twenty times greater than the value for DMHQ.[5] Given the magnitude of the difference in kinetics between DMHQ and TEMPO, a

simple steric argument is insufficient to fully explain the difference in reaction kinetics of different RMs with Li_2O_2.

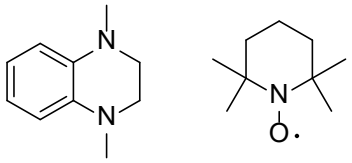

Fig. 4.25: Structures of DMHQ (left) and TEMPO (right).

4.3.9.2 MPO and MPT

MPO may be described as the oxygen analogue of MPT, which possesses a k_{app} of $2.36x10^{-3}$ cm s^{-1} and a redox potential of 3.84 V (a comparison of the structures of MPO and MPT may be found in **Figure 4.26**).[5] Substitution of the sulfur heteroatom for oxygen results in a decrease in the rate constant of the reaction with Li_2O_2 to $1.45x10^{-3}$ cm s^{-1} along with a decrease in the redox potential to 3.73 V. The lower redox potential of MPO compared to MPT indicates that it is easier to remove an electron from MPO than from MPT. This may be rationalised by considering the relative abilities of the heteroatoms to stabilise the resultant positive charge on the amine centre; there is more efficient overlap of the p-orbitals on the oxygen atom with the neighbouring pi-system than with the sulfur atom, allowing the oxygen to better donate electron density to stabilise the resultant positive charge on the nitrogen. This is despite the larger size of sulfur facilitating greater stabilisation of the positive charge by making it more diffuse; here the effect of the better orbital overlap by oxygen dominates.

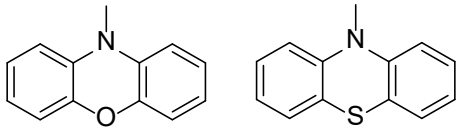

Fig. 4.26: Structures of MPO (left) and MPT (right).

The factors which result in a less positive redox potential do not also contribute to improved reaction kinetics, with MPO having a k_{app} of 1.45x10^{-3} cm s^{-1} relative to MPT's 2.36x10^{-3} cm s^{-1}. With the only structural difference between the two molecules being the identity of the non-nitrogenous heteroatom, this suggests that the heteroatoms may have a role to play in the reaction mechanism, perhaps through coordinating to the Li_2O_2 surface. However, given that oxygen would be expected to bind more strongly to a Li_2O_2 surface according to Pearson's Hard Soft Acid Base theory, this does not explain why MPT has a larger k_{app}.[43]

4.3.9.3 Marcus Kinetic Analysis of Redox Mediators

It has previously been assumed that the rate of the reaction between RMs and Li_2O_2 follows a classical Butler-Volmer kinetic regime, whereby any increase of the overpotential leads to an increase in the rate of reaction.[7] However, this argument does not satisfy the observations of this work or those of Chen *et al.*, where MPT and was found to have a lower k_{app} than TEMPO, despite the former operating at a more positive potential.[5] In addition, it is clear from comparison of DMHQ and TEMPO that a simple steric argument is also insufficient at providing an explanation for the observed trends.

Marcus theory of electron transfer provides an alternative description of kinetics to Bulter-Volmer, and takes into account the energy required for the reorganisation of the solvent (the outer sphere reorganisation energy) prior to the electron transfer step.[44] The reorganisation energy required for electron transfer, λ_{ET}, for each RM was calculated using the Born Equation:

$$\lambda_{ET} = \frac{e_0^2}{4\pi\epsilon_0}\left(\frac{1}{\epsilon_{op}} - \frac{1}{\epsilon_s}\right)\frac{1}{2a} \qquad \textbf{Eq. 4.12}$$

where e_0 is the electron charge, ϵ_0 is the permittivity of a vacuum, ϵ_{op} is the optical dielectric constant of the electrolyte (TEGDME = 2.05), ϵ_s is the static dielectric constant of the electrolyte (TEGDME = 7.78) and a is the radius of the RM molecule.[8] The radii of the RMs were determined by approximating each RM to a sphere and calculating their van der Waals volumes, V_{vdW}, as given by **Equation 4.13**:[45]

$$V_{vdW}(RM) = \left(\sum(all\ atoms' V_{vdW})\right) - 5.92N_B - 14.7R_a - 3.8R_{NR} \qquad \textbf{Eq. 4.13}$$

where N_B is the number of bonds, R_a is the number of aromatic rings and R_{NR} is the number of non-aromatic rings. The term $-(5.92N_B + 14.7R_a + 3.8R_{NR})$ acts as a correction, and the atomic V_{vdW} were obtained from published values.[45]

Equation 4.14 gives the electron transfer kinetics of a reaction governed by Marcus theory:

$$\ln k = \ln(KZ) - \frac{1}{RT}\frac{(\Delta_r G^\circ + \lambda)^2}{4\lambda} \qquad \textbf{Eq. 4.14}$$

as described in **Section 2.1.5** (page 83). The effect of the inner sphere reorganisation energy, that is to say the reorganisation energy associated with the change in bond lengths and angles of the RM, was assumed to be small compared to solution

reorganisation energy and so was neglected.[46-48] The solution reorganisation energy for lithium ion transfer was also expected to be independent of the RMs and so was omitted from the calculation. Finally, k_{ET} was taken to be the experimentally determined k_{app}.

The effect of the reorganisation energy can be acutely seen in **Figure 4.27**, where the use of SECM and application of **Equation 4.14** to a number of RMs results in the inverted parabola associated with Marcus electron transfer kinetics (the identity of the RMs included can be found in the Figure caption). DMHQ and MPO closely fit the trend, which was created without their inclusion to avoid overfitting of the trend to the data. Deviation from idealised Marcus kinetics is attributed to the different transmission coefficients and value of Z for each RM, along with their differing inner sphere reorganisation energies and any reorganisation energy attributed to the Li_2O_2, which has also been omitted from the calculations.

The implication of Marcus theory is that the rate of electron transfer is greatest when the reorganisation energy is equal to the negative of the free energy change of the electron transfer reaction, given by **Equation 4.15**:

$$\lambda = -\Delta G \qquad \textbf{Eq. 4.15}$$

As such, RMs with reorganisation energies that most closely match the free energy of the reaction will have the fastest k_{app}, providing an explanation for the trends observed in this work and by others.[5, 7]

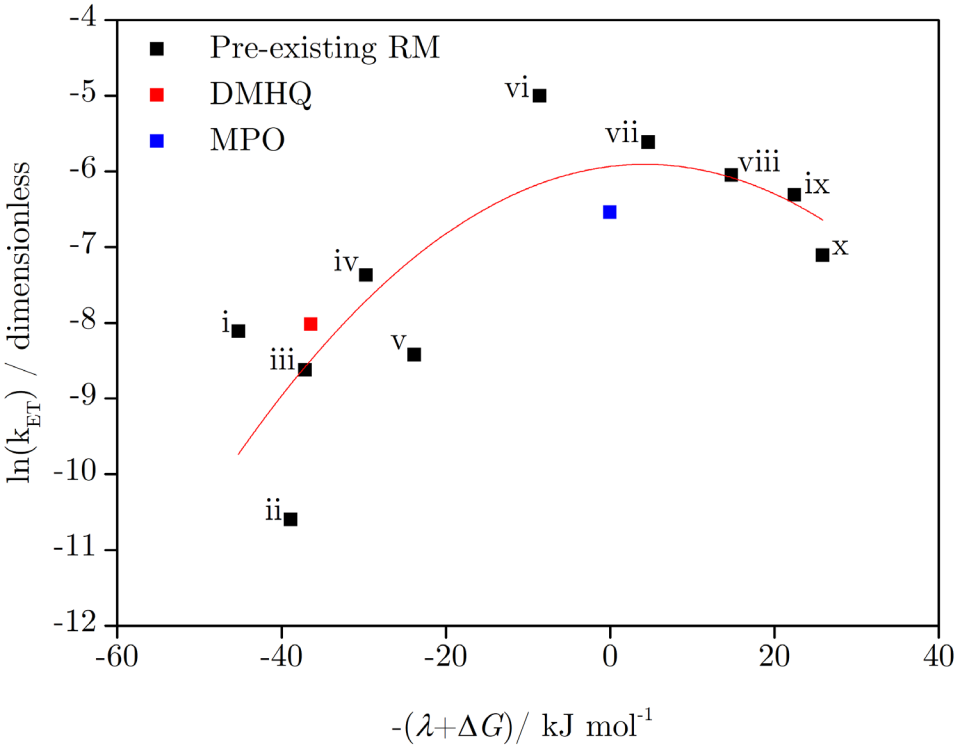

Fig. 4.27: Marcus plot of the k_{app} of a range of pre-existing RMs (black), DMHQ (red) and MPO (blue) with Li_2O_2 as a function of reorganisation energy. The pre-existing RMs are **i.** TMPD, **ii.** TDPA, **iii.** DMPZ, **iv.** TTF, **v.** ferrocene, **vi.** 1-Me-Azado, **vii.** TEMPO, **viii.** MPT, **ix.** 10-isopropylphenothiazine, and **x.** 10-(4-biphenylyl)phenothiazine. SECM data collection and analysis, with initial identification of Marcus kinetic behaviour, for RMs **i** – **x** was performed by Dr S. Ahn, with all experimental conditions as described in **Section 4.2.11** (page 177). The electrolyte was 0.1 M LiTFSI in TEGDME for all experiments.

4.3.9.4 Implications of Marcus Kinetic Behaviour of RMs

That the reaction between RM^+ and Li_2O_2 obeys Marcus kinetic theory has major implications for the Li-O_2 field. It demonstrates that, for a given concentration, there is a fundamental maximum rate achievable for RMs, which is dependent upon both the potential of the RM (through the Gibbs free energy) and the reorganisation energy of the solvent. In addition, it provides a satisfactory explanation for why RMs with

the nitroxyl functional group exhibit the greatest (known) k_{app} despite having an intermediate redox potential. Importantly, the Marcus dependency of the reaction between RM^+ and Li_2O_2 suggests that it is theoretically possible to have a low potential RM (*i.e.* one that operates below 3.45 V) operating with the maximum k_{app}, provided the equality in **Equation 4.15** be satisfied. Given that it is possible to calculate the reorganisation energy of solvents in the presence of RMs using DFT, as demonstrated by Ren *et al.* using TTF in acetonitrile, the work presented in this Chapter provides the key metric by which to screen candidate RM species in order to attain the greatest rate of reaction with Li_2O_2.[49]

4.4 Conclusions

Two novel RMs, DMHQ and MPO, were successfully synthesised and characterised, having been identified through logical computational screening. While DMHQ had a disappointing electron to O_2 ratio on charge, MPO was found to improve upon that of Li-O_2 cells without any RMs, with an electron to O_2 ratio of 2.69 and a k_{app} of 1.45×10^{-3} cm s^{-1}, comparable to that of the RM gold standard, TEMPO.

Investigation of the kinetics of the two novel RMs with Li_2O_2 found that no satisfactory answer could be established through general comparisons of their structure with other known RMs. Instead, application of Marcus kinetic theory found that the rate of reaction between RM^+ and Li_2O_2 is dependent upon the solvent reorganisation

energy. This realisation has profound implications for the field, providing an additional metric by which to screen molecules for their ability to act as RMs in Li-O_2 cells.

4.5 Appendices

4.5.1 Calculated Redox Potentials for Screened Compounds

Structure	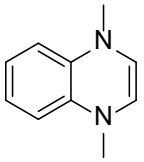	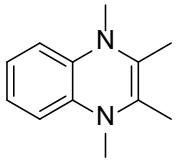	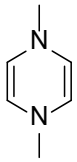
Calculated E^0 / V	2.63	2.95	2.08

Table 4.3: Calculated E^0 values for a selection of molecules, using the computational model described in **Section 4.2.1** (page 172).

Structure	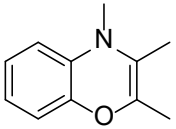	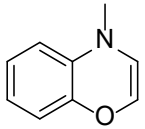	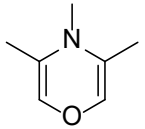	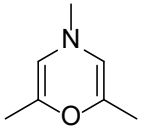	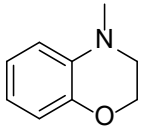	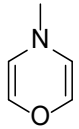
Calculated E^0 / V	3.18	3.51	3.42	3.24	3.98	3.42

Structure	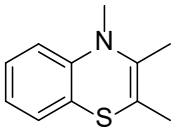	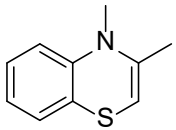	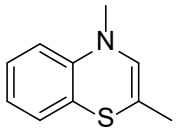	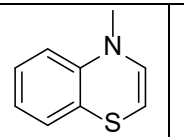	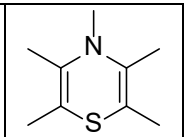	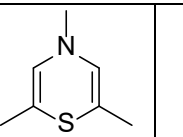	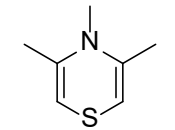	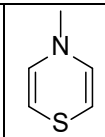	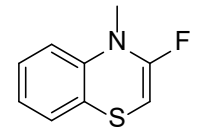
Calculated E^0 / V	3.25	3.27	3.28	3.34	2.76	3.33	3.50	3.55	3.14

4.5.2 FTIR of DMHQ and MPO

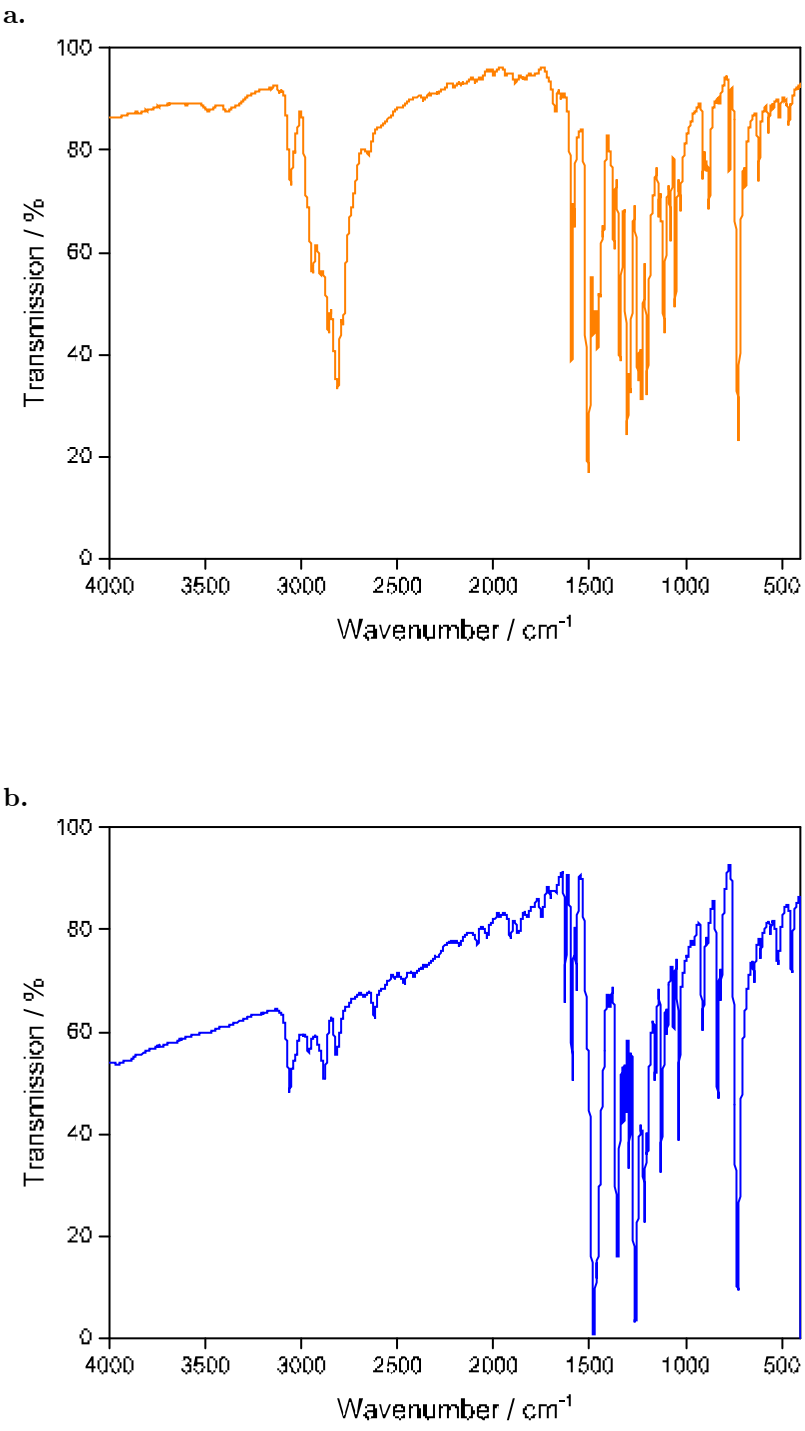

Fig. 4.28: FTIR of **a.** DMHQ and **b.** MPO. Assignments may be found in **Sections 4.2.2** (page 172) and **4.2.3** (page 173), respectively. Experimental conditions as detailed in **Section 4.2.5** (page 174).

4.5.3 ^{1}H NMR of DMHQ and MPO

a.

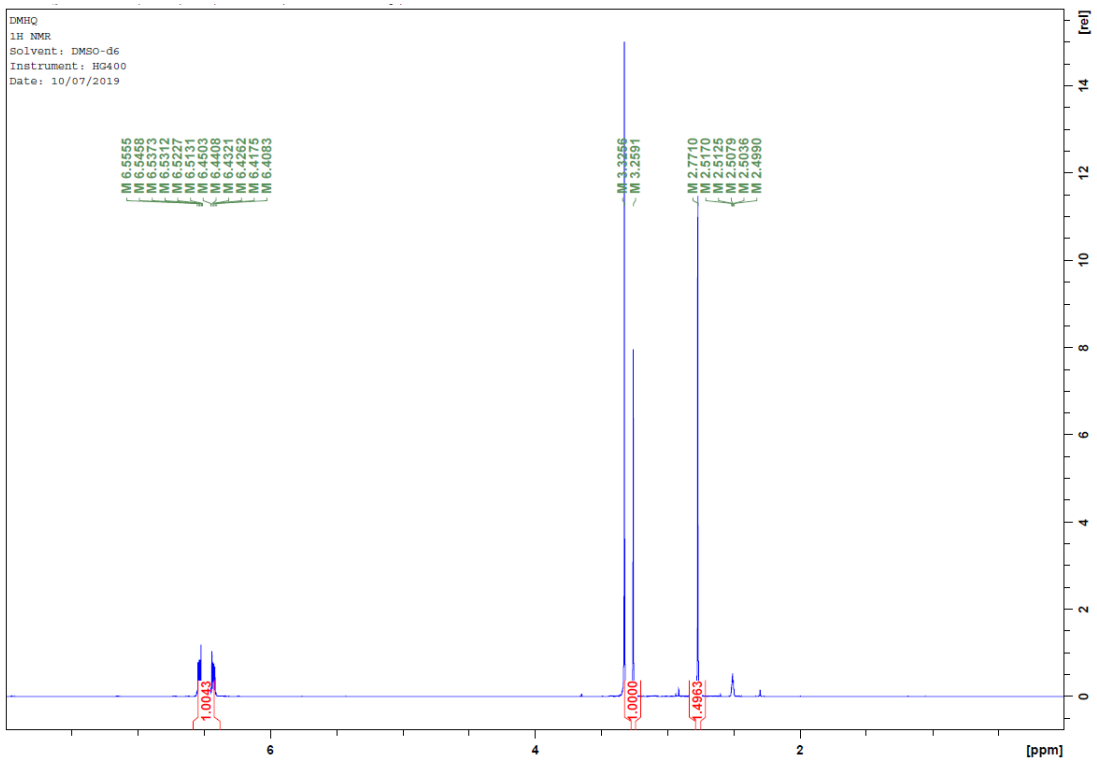

b.

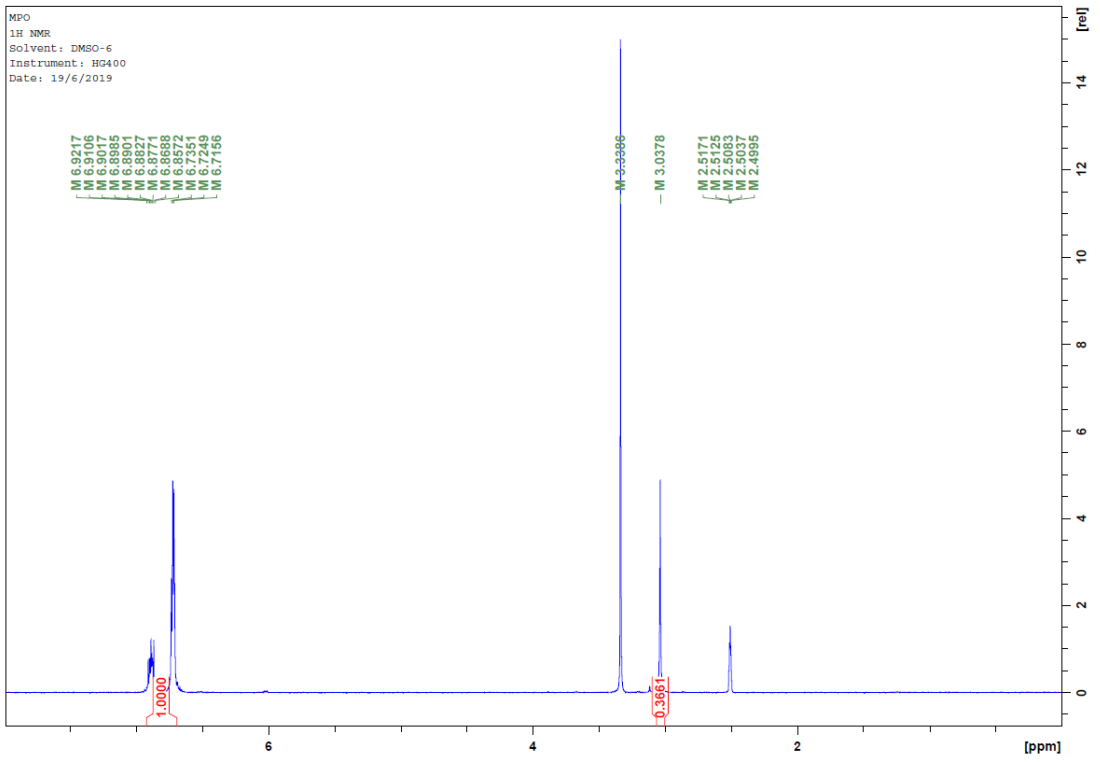

Fig. 4.29: ^{1}H NMR of **a.** DMHQ and **b.** MPO. Experimental conditions as detailed in **Section 4.2.6** (page 174).

4.5.4 Oxidation Stability of TEGDME

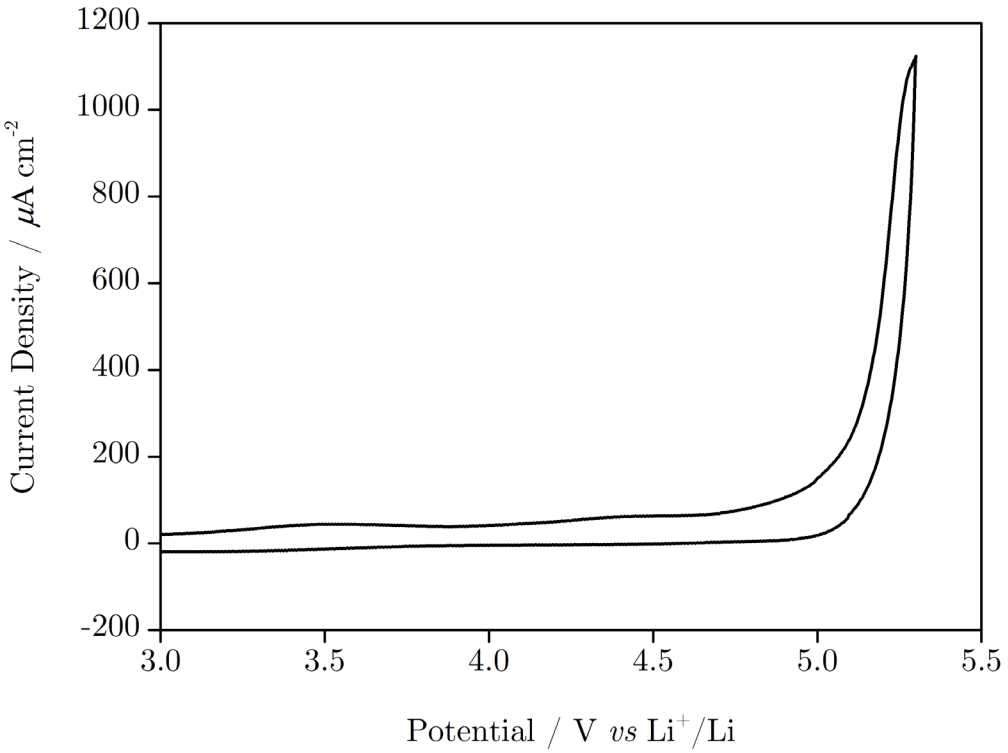

Fig. 4.30: Cyclic voltammogram demonstrating the oxidation stability window of TEGDME, with 1 M LiTFSI as the electrolyte at a scan rate of 100 mV s^{-1}. Experimental conditions as described in **Section 4.2.8** (page 175).

4.5.5 OEMS of 30 mM TEMPO

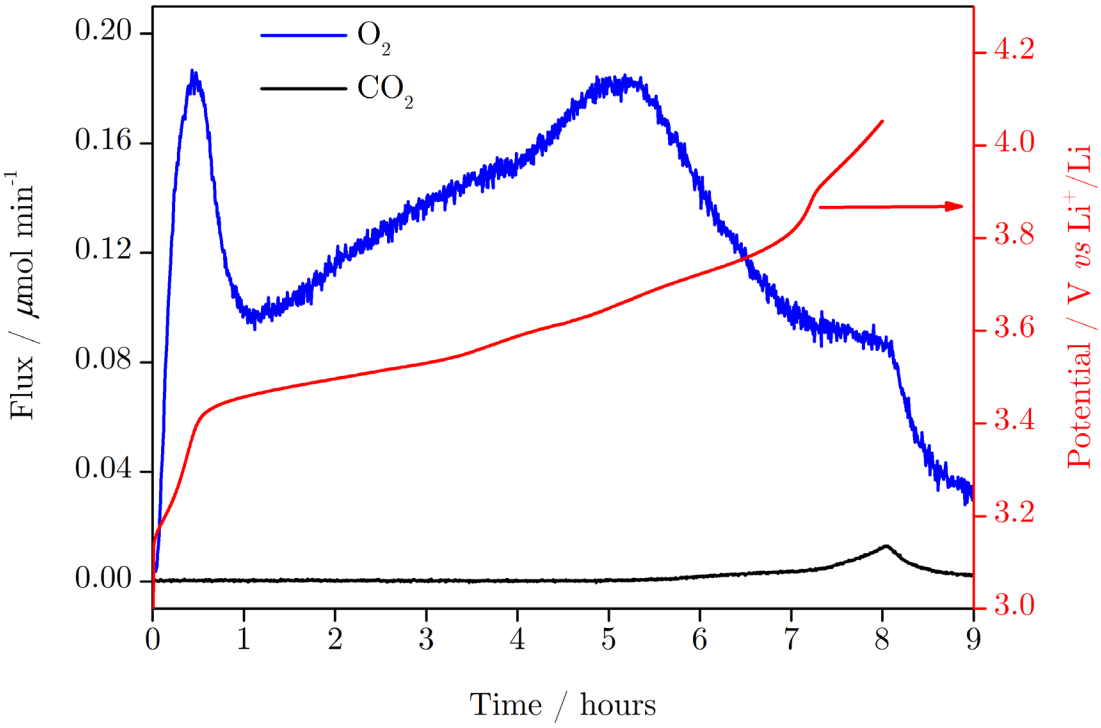

Fig. 4.31: OEMS (O_2 in blue and CO_2 in black) and charge profile (red) for a cell containing 30 mM TEMPO, charging at a constant current density of 100 μA cm^{-2}. Experimental conditions detailed in **Section 4.2.10** (page 177).

4.6 References

1. N. Feng, P. He and H. Zhou, *ChemSusChem*, 2015, **8**, 600-602.
2. H.-D. Lim, B. Lee, Y. Zheng, J. Hong, J. Kim, H. Gwon, Y. Ko, M. Lee, K. Cho and K. Kang, *Nat. Energy*, 2016, **1**, 16066.
3. X. Gao, Y. Chen, L. Johnson and P. G. Bruce, *Nat. Mater.*, 2016, **15**, 882–888.
4. X. Gao, Y. Chen, L. R. Johnson, Z. P. Jovanov and P. G. Bruce, *Nat. Energy*, 2017, **2**, 17118.
5. Y. Chen, X. Gao, L. R. Johnson and P. G. Bruce, *Nat. Commun.*, 2018, **9**, 767.
6. Y. Dou, R. Lian, G. Chen, Y. Wei and Z. Peng, *Energy Storage Materials*, 2020, **25**, 795-800.

7. Y. Ko, H. Park, B. Lee, Y. Bae, S. K. Park and K. Kang, *J. Mater. Chem. A*, 2019, **7**, 6491-6498.
8. C. F. Riadigos, R. Iglesias, M. A. Rivas and T. P. Iglesias, *J. Chem. Thermodyn.*, 2011, **43**, 275-283.
9. T. A. Dobrynina, N. A. Akhapkinn and V. F. Chauvaev, *Bulletin of the Academy of Sciences of the USSR, Division of Chemical Science*, 1969, **18**, 438-440.
10. T. Koopmans, *Physica*, 1934, **1**, 104-113.
11. S. Trasatti, *J. Electroanal. Chem.*, 1986, **209**, 417-428.
12. G. Gritzner, *J. Mol. Liq.*, 2010, **156**, 103-108.
13. D. Kundu, R. Black, B. Adams and L. F. Nazar, *ACS Cent. Sci.*, 2015, **1**, 510-515.
14. Y. Chen, S. A. Freunberger, Z. Peng, O. Fontaine and P. G. Bruce, *Nat. Chem.*, 2013, **5**, 489–494.
15. P. P. Bawol, P. Reinsberg, C. J. Bondue, A. A. Abd-El-Latif, P. Konigshoven and H. Baltruschat, *Phys. Chem. Chem. Phys.*, 2018, **20**, 21447-21456.
16. N. Feng, X. Mu, X. Zhang, P. He and H. Zhou, *ACS Appl. Mater. Interfaces*, 2017, **9**, 3733-3739.
17. D. Pletcher, *A First Course in Electrode Processes*, The Royal Society of Chemistry Cambridge, 2nd edn., 2009.
18. P. L. Arrechea, K. B. Knudsen, J. W. Mullinax, J. B. Haskins, C. W. Bauschlicher, J. W. Lawson and B. D. McCloskey, *ACS Applied Energy Materials*, 2020, **3**, 8812-8821.
19. Z. Liang, Q. Zou, J. Xie and Y.-C. Lu, *Energy Environ. Sci.*, 2020, **13**, 2870-2877.
20. K. P. C. Yao, J. T. Frith, S. Y. Sayed, F. Bardé, J. R. Owen, Y. Shao-Horn and N. Garcia-Araez, *J. Phys. Chem. C*, 2016, **120**, 16290-16297.
21. Y. Li, S. Dong, B. Chen, C. Lu, K. Liu, Z. Zhang, H. Du, X. Wang, X. Chen, X. Zhou and G. Cui, *J. Phys. Chem. Lett.*, 2017, **8**, 4218-4225.
22. W. H. Ryu, F. S. Gittleson, J. M. Thomsen, J. Li, M. J. Schwab, G. W. Brudvig and A. D. Taylor, *Nat. Commun.*, 2016, **7**, 12925.
23. G. Shen, L. Zhao, X. Zhao, X. Huangfu, Z. Li, R. Wang and T. Zhang, *Synlett*, 2017, **28**, 1111-1115.
24. H. D. Lim, H. Song, J. Kim, H. Gwon, Y. Bae, K. Y. Park, J. Hong, H. Kim, T. Kim, Y. H. Kim, X. Lepro, R. Ovalle-Robles, R. H. Baughman and K. Kang, *Angew.*, 2014, **53**, 3926-3931.
25. N. Mahne, S. E. Renfrew, B. D. McCloskey and S. A. Freunberger, *Angew.*, 2018, **57**, 19, 5529-5533.
26. H. Kim, W.-J. Kwak, H.-G. Jung and Y.-K. Sun, *J. Mater. Chem. A*, 2020, **8**, 5622-5628.
27. D. Cao, X. Liu, X. Yuan, F. Yu and Y. Chen, *ACS Appl. Mater. Interfaces*, 2021, **13**, 33, 39341-39346.
28. B. J. Bergner, A. Schurmann, K. Peppler, A. Garsuch and J. Janek, *J. Am. Chem. Soc.*, 2014, **136**, 15054-15064.

29. T. Zhang, K. Liao, P. He and H. Zhou, *Energy Environ. Sci.*, 2016, **9**, 1024-1030.
30. H.-D. Lim, Y. S. Yun, Y. Ko, Y. Bae, M. Y. Song, H. J. Yoon, K. Kang and H.-J. Jin, *Carbon*, 2017, **118**, 114-119.
31. B. Horstmann, B. Gallant, R. Mitchell, W. G. Bessler, Y. Shao-Horn and M. Z. Bazant, *J. Phys. Chem. Lett.*, 2013, **4**, 4217-4222.
32. L. Johnson, C. Li, Z. Liu, Y. Chen, S. A. Freunberger, P. C. Ashok, B. B. Praveen, K. Dholakia, J.-M. Tarascon and P. G. Bruce, *Nat. Chem.*, 2014, **6**, 1091-1099.
33. B. J. Bergner, C. Hofmann, A. Schurmann, D. Schroder, K. Peppler, P. R. Schreiner and J. Janek, *Phys. Chem. Chem. Phys.*, 2015, **17**, 31769-31779.
34. W. J. Kwak, H. Kim, Y. K. Petit, C. Leypold, T. T. Nguyen, N. Mahne, P. Redfern, L. A. Curtiss, H. G. Jung, S. M. Borisov, S. A. Freunberger and Y. K. Sun, *Nat. Commun.*, 2019, **10**, 1380.
35. O. Yurchenko, D. Freytag, L. zur Borg, R. Zentel, J. Heinze and S. Ludwigs, *J. Phys. Chem. B*, 2012, **116**, 30-39.
36. T. A. Hamlin, M. Swart and F. M. Bickelhaupt, *ChemPhysChem*, 2018, **19**, 1315-1330.
37. C. J. Cramer, *Essentials of Computational Chemistry: Theories and Models*, Wiley, 2nd edn., 2014.
38. C. Lefrou and R. Cornut, *ChemPhysChem*, 2010, **11**, 547-556.
39. C. Lefrou, *J. Electroanal. Chem.*, 2006, **592**, 103-112.
40. R. Cornut and C. Lefrou, *J. Electroanal. Chem.*, 2007, **608**, 59-66.
41. R. Cornut, S. Griveau and C. Lefrou, *J. Electroanal. Chem.*, 2010, **650**, 55-61.
42. J. Hioe, D. Sakic, V. Vrcek and H. Zipse, *Org. Biomol. Chem.*, 2015, **13**, 157-169.
43. R. G. Pearson, *J. Am. Chem. Soc.*, 1963, **85**, 22, 3533-3539.
44. R. A. Marcus, *J Chem. Phys.*, 1965, **43**, 679-701.
45. Y. H. Zhao, M. H. Abraham and A. M. Zissimos, *J. Org. Chem*, 2003, **68**, 7368-7373.
46. C. Costentin, D. H. Evans, M. Robert, J.-M. Saveant and P. S. Singh, *J. Am. Chem. Soc.*, 2005, **127**, 12490-12491.
47. G. Houchins, V. Pande and V. Viswanathan, *ACS Energy Lett.*, 2020, **5**, 6, 1893-1899.
48. S. Ghosh and S. Hammes-Schiffer, *J. Phys. Chem. Lett.*, 2015, **6**, 1-5.
49. H. S. Ren, M. J. Ming, J. Y. Ma and X. Y. Li, *J. Phys. Chem. A*, 2013, **117**, 8017-8025.

Chapter 5

The Effect of Phenol as a Phase Transfer Catalyst on the Oxygen Reduction Reaction in Potassium-Oxygen Batteries

Contents

5.1 Introduction

In contrast to LiO_2, which is a short-lived species that rapidly undergoes disproportionation to Li_2O_2, KO_2 is thermodynamically stable[a] and is the main discharge product in K-O_2 cells.[1, 2] NaO_2 is similarly stable, although in Na-O_2 cells a mixture of NaO_2 and Na_2O_2 can be observed given the close reduction potentials of the two oxygen species (2.27 V and 2.33 V, respectively).[3, 4] Furthermore, KO_2 has been found to be stable in contact with ether electrolytes, with minimal evidence of chemical reactions occurring between the two.[2, 5]

O_2 reduction in a K^+-containing ether solvent proceeds via the following surface mechanism:

$$O_{2(sol)} + e^- \rightarrow O_{2(sol)}^- \qquad \textbf{Eq. 5.1}$$

$$O_{2(sol)}^- + K_{(sol)}^+ \rightarrow KO_2^* \qquad \textbf{Eq. 5.2}$$

where * denotes surface adsorbed species.[1, 6] At sufficiently negative potentials, KO_2 may undergo a further one-electron reduction to form potassium peroxide, K_2O_2:[6-8]

$$KO_2^* + e^- + K^+ \rightarrow K_2O_2^* \qquad \textbf{Eq. 5.3}$$

However, discharging cells do not generally polarise beyond the potential plateau of KO_2 formation, and so K_2O_2 is infrequently observed. It should be noted that, unlike LiO_2, KO_2 does not undergo disproportionation to form K_2O_2.[6, 9, 10]

It is well established that the superoxides and peroxides of the alkali metals have poor solubility in ether solvents (and indeed in any low donor number solvent).[2, 11] Whilst KO_2 has been shown to have a greater level of electrical

[a] Under standard conditions of 298.15 K and 10^5 Pa.

conductivity in comparison to the discharge products in Li-O_2 and Na-O_2 cells, the formation of KO_2 and K_2O_2 films on the cathode surface leads to eventual cathode passivation and cell death.[1, 6, 12] As such, methods of facilitating solution-based growth of KO_2 are necessary, either through the use of high donor number solvents or through the use of additives, in order to increase the achievable discharge capacity.

Methods to mitigate passivation of the cathode on discharge of Li-O_2 and Na-O_2 cells include use of discharge RMs, such as DBBQ, and phase transfer catalysts, such as phenol and water (used to great success in Li-O_2 and Na-O_2 cells, respectively).[4, 13-15] The phase transfer catalysts[b] used thus far in M-O_2 cells are protic species that exchange H^+ ions with the alkali metal ions in MO_2 and M_2O_2 ($M = Li^+$, Na^+, K^+), to give the ether-soluble species HO_2 and MOOH, respectively, according to the reactions:[4, 9, 15]

$$MO_2 + H^+ \rightarrow M^+ + HO_2 \qquad \textbf{Eq. 5.4}$$

$$M_2O_2 + H^+ \rightarrow M^+ + MOOH \qquad \textbf{Eq. 5.5}$$

By causing the discharge product to dissolve into the electrolyte, phase transfer catalysts keep the cathode surface clear of passivating material, allowing for greater discharge capacities in comparison to cells without the proton source.[15]

This Chapter demonstrates the use of phenol as a phase transfer catalyst in K-O_2 cells, resulting in significantly increased discharge capacities and an electron to O_2 ratio that is close to unity, as expected for the formation of KO_2.[1, 16] However, it is

[b] A more general definition of a phase transfer catalyst would be a species that facilitates the movement of another chemical species from one phase to another.

further revealed that for successful use of phenol in a K-O_2 cell, a K^+-conducting solid electrolyte is essential, absence of which leads to KOH being the main discharge product.

5.2 Experimental

5.2.1 Cyclic Voltammetry

Cyclic voltammetry was performed using a planar gold disc (3 mm diameter) working and a platinum wire counter electrode, with $LiFePO_4$ (99.5%, TCI) in 1 M LiTFSI (99.95%, Sigma Aldrich) in distilled and dried TEGDME (>99%, Sigma Aldrich) behind a Vycor® glass frit serving as the reference electrode[c]. 0.5 M KTFSI (97%, Sigma Aldrich) in distilled, dried (over 4 Å molecular sieves) and degassed TEGDME served as the electrolyte, in a sealed 5-neck flask, with 30 mM phenol (>99%, Sigma Aldrich) when required. No *iR* correction was used. For oxygenated experiments, dried O_2 (99.999%, BOC) was bubbled through the solution for 5 minutes prior to each scan. Prior to each scan the gold working electrode was polished with alumina (particle size = 0.05 μm), cleaned by cycling in 0.1 M $HClO_4$ (Sigma Aldrich) and then dried under vacuum at 50°C. The scan rate used in each experiment is detailed in the relevant Figure caption. All experiments were conducted inside a N_2 glovebox (O_2 and H_2O < 0.1 ppm).

[c] The risk of contamination of the potassium electrolyte by Li^+ ions from the reference electrode was deemed to be minimal, given that the leak rate from a Vycor® glass frit was determined to be 3±1 nL h^{-1} (when using 10 mM KCl in ACN). M. P. S. Mousavi, S. A. Saba, E. L. Anderson, M. A. Hillmyer, P. Bühlmann, *Anal. Chem.*, 2016, **6**, 88, 8706-13.

For the cyclic voltammetry of $K_3[Fe(CN)_6]$ (99.98%, Sigma Aldrich), platinum working (5 mm diameter), platinum counter and Ag/AgCl in 3 M KCl reference electrodes were used, with a 1 M KOH (>99.95%, Sigma Aldrich) aqueous electrolyte. The platinum working electrode was polished and as described above.

5.2.2 Rotating Ring Disc Electrode Voltammetry

RRDE linear sweep voltammetry was performed using a platinum disc working electrode (5 mm diameter) with platinum also serving as the ring electrode (6.5 mm inner diameter, 7.5 mm outer diameter). The RRDE tip was assembled and then the entire unit was polished with alumina to ensure a planar surface. A platinum wire served as the counter electrode, and $LiFePO_4$ in 1 M LiTFSI in TEGDME behind a Vycor® glass frit acted as the reference. The electrolyte was 0.5 M KTFSI in TEGDME. For oxygenated experiments, dried O_2 was bubbled through the solution for 5 minutes prior to scan. As the vessel could not be sealed due to the rotation of the RRDE, O_2 was purged over the surface of the electrolyte providing a blanket for the duration of the experiment. All experiments were conducted under a N_2 atmosphere. For K-O_2 experiments a rotation rate of 250 rpm was used, with the disc being scanned at 5 mV s^{-1} and the ring potential held at 3.4 V.

To calculate the collection efficiency of the RRDE an electrolyte of 4 mM ferricyanide ($K_3[Fe(CN)_6]$) in 1 M KOH was used. The RRDE platinum disc and platinum ring were prepared as described previously, with a platinum wire serving as the counter electrode and Ag/AgCl in 3 M KCl as the reference. The rotation rate was

400 rpm and the disc scan rate was 50 mV s^{-1}. The ring potential was held at 0.6 V *vs* Ag/AgCl.

5.2.3 Discharge at a Gold Electrode

Experimental conditions as for cyclic voltammetry in **Section 5.2.1** (page 236) were used, with the gold electrode discharged at a constant current density of 50 μA cm^{-2}.

5.2.4 Swagelok Cells Assembly

Swagelok cells were assembled with potassium metal as the counter electrode, two stacked gas diffusion layers (GDLs, 4 mm diameter, H2315, Quintech) as the cathode, two glass fibre separators and 0.5 M KTFSI in TEGDME (300 μL) as the electrolyte, with 30 mM phenol as required. Cells were purged with dried O_2 for 5 minutes then left to equilibrate for 1 hour before discharge. All cells were constructed in an Ar-filled glovebox. GDLs were treated under a Ar:H_2 atmosphere (95:5 v/v, BOC) at 900°C for 3 hours and transferred into an Ar-filled glovebox without exposure to air prior to use.

For the OEMS cells, potassium β-alumina discs (Ionotec) of 10 mm diameter and 0.7 mm thickness were used as a K^+-conducting solid electrolyte (having an ionic conductivity of 0.5 mS cm^{-1} at 298 K, as quoted by manufacturer). The discs were polished using wet silica paper of increasing grades, followed by sonication in cyclohexane (99.5%, Sigma Aldrich). The discs were heat treated at 875°C under an Ar atmosphere overnight, before being stored under an inert Ar atmosphere prior to use.

5.2.5 *Operando* Electrochemical Mass Spectrometry

Cells were constructed as described in **Section 5.2.4** (page 238), with the addition of a K^+-conducting β-alumina solid electrolyte (Ionotec) and a separate potassium metal reference electrode. The cells were connected to a Thermo Scientific PrimaBT benchtop gas analyser and the potential was scanned at 0.1 mV s^{-1}. The cells were continually purged using a carrier gas of 20% O_2 in Ar (BOC) that was set to a flow rate of 0.6 mL min^{-1}. $^{16}O_2$ and $^{12}CO_2$ evolution was measured by monitoring the m/z 32 and 44 signals respectively, following industry-standard one-point calibration of the instrument using 0.1% O_2, 1000 ppm $^{12}CO_2$ and 500 ppm $^{13}CO_2$ made up to 100% with Ar (BOC).

5.2.6 X-Ray Diffraction Spectroscopy

Powder XRD data was obtained using a Rigaku Miniflex with Cu K_α radiation under a N_2 atmosphere. At the end of discharge the cells were disassembled and the cathode washed with DME (99.5%, Sigma Aldrich) and dried under vacuum to remove excess electrolyte. The cathodes were affixed to a stainless steel sample holder using vacuum grease as an adhesive, and measurements were taken in the range of $10^\circ < 2\Theta < 90^\circ$ at a scan rate of 0.9° min^{-1}. All samples were rotated during the measurements.

5.3 Discussion

5.3.1 Cyclic Voltammetry

5.3.1.1 Cyclic Voltammetry in the Absence of Phenol

The cyclic voltammetry presented in **Figure 5.1** demonstrates the reduction and oxidation of O_2 in the presence of K^+ ions in TEGDME. It can be seen that on the first scan there is a single cathodic peak, corresponding to the reduction of O_2, whilst on the reverse scan two oxidation peaks at 2.36 V and 2.55 V can be seen, corresponding to the sequential two-electron oxidation of K_2O_2 to O_2, as detailed in **Equations 5.1**, **5.2** and **5.3**. This reveals that the cathodic peak is a combination of the current densities for the sequential formation of both KO_2 and K_2O_2. The reduction peak is characteristic of the formation of a passivating layer on the electrode surface, with the current density rapidly tending towards zero once the peak current density has been passed.[17] This is expected, given the very poor solubility of both KO_2 and K_2O_2 in the low donor number solvent TEGDME.[18]

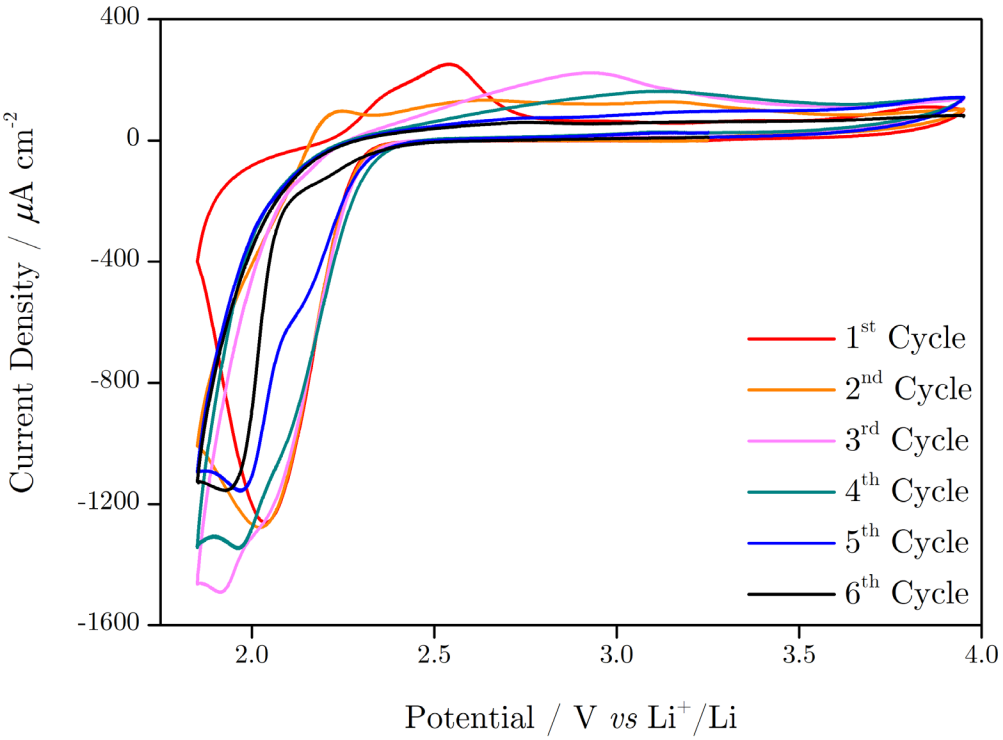

Fig. 5.1: Cyclic voltammetry of O_2 in a 0.5 M KTFSI in TEGDME electrolyte, at a scan rate of 100 mV s^{-1}. Experimental conditions as described in **Section 5.2.1** (page 236).

On successive scans the single cathodic peak splits into two distinct peaks related to KO_2 and K_2O_2 formation, occurring at 2.06 V and 1.91 V respectively. With each cycle, the peak current density resulting from KO_2 formation becomes smaller whilst the peak current density for K_2O_2 formation becomes more dominant. This is attributed to the incomplete oxidation of the KO_2 and K_2O_2 during each reverse scan, with some material remaining on the electrode surface at the end of each cycle. The presence of the pre-deposited film that is already on the electrode surface hinders further deposition of fresh KO_2. Instead, there is a swift reduction of remaining surface

adsorbed KO_2 from the previous cycle, leading to increasing K_2O_2 film thickness and resulting in surface passivation and a decrease in total cathodic current density by the 5^{th} and 6^{th} cycles.

From the 2^{nd} cycle onwards the oxidation peaks on the reverse scan become broader and move to a more positive overpotential. This is characteristic of an increasing passivating layer thickness, with increasing layer thickness leading to an increase in resistance, which drives an increase in required oxidation overpotential.[19]

5.3.1.2 Cyclic Voltammetry in the Presence of Phenol

The cyclic voltammetry presented in **Figure 5.2** demonstrates that the addition of 30 mM phenol to a solution of 0.5 M KTFSI in TEGDME results in an approximately two-fold increase in the reduction current density compared to systems without phenol, along with an apparent negative shift in the peak potential. In addition, the presence of phenol introduces current crossover, whereby the current density on the reverse scan is greater than the current density on the forward scan. Crossover is often observed in the deposition of metals or species from dilute solution onto a foreign substrate, that is to say deposition onto a material other than the species being deposited.[17] Further discussion of the current crossover will be take place at the end of this Section.

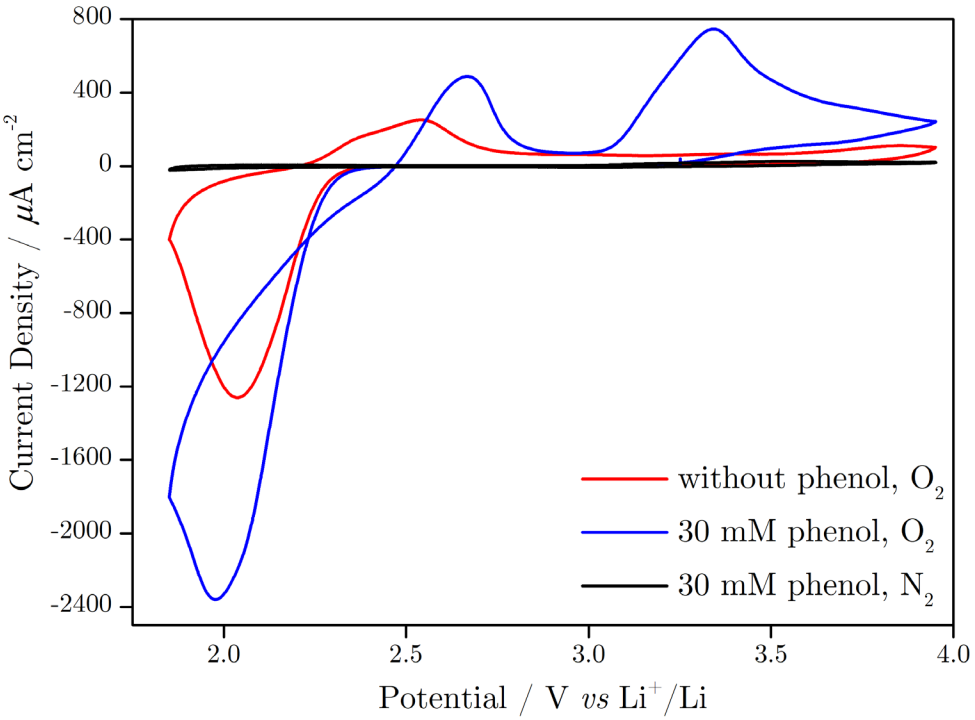

Fig. 5.2: Cyclic voltammetry of O_2 in a 0.5 M KTFSI in TEGDME electrolyte with (blue) and without (red) 30 mM phenol, at a scan rate of 100 mV s^{-1}. Experimental conditions as described in **Section 5.2.1** (page 236).

The presence of phenol also influences the oxidation reactions, with the two peaks for K_2O_2 and KO_2 oxidation replaced by a single peak at 2.67 V that has symmetry characteristic of the oxidation a surface adsorbed species. Given the more positive potential of this single peak, it is attributed to the one-electron oxidation of KO_2 to O_2, with no oxidation peak of K_2O_2 present. In addition, a new peak at 3.43 V is present on the reverse scan; this peak was observed in work by Gao *et al.* in a TBA^+-containing electrolyte, where it is attributed to the oxidation of HO_2 and/or H_2O_2.[15]

Ether-soluble HO_2 and H_2O_2 may be formed from reaction of both KO_2 (**Equations 5.6** and **5.7**) and K_2O_2 (**Equation 5.8**) with H^+, analogously to reactions observed in Li-O_2 and Na-O_2 cells:[4, 16, 20]

$$KO_2 + H^+ \rightarrow HO_2 + K^+ \qquad \textbf{Eq. 5.6}$$

$$2HO_2 \rightarrow H_2O_2 + O_2 \qquad \textbf{Eq. 5.7}$$

$$K_2O_2 + 2H^+ \rightarrow H_2O_2 + 2K^+ \qquad \textbf{Eq. 5.8}$$

KOOH is a further product that would be expected as an intermediate from the reaction in **Equation 5.8**, and will also have greater solubility in TEGDME.[9, 15, 21] It should be noted that the presence of phenol in the absence of O_2 results in no Faradaic processes within the potential window investigated (black trace, **Figure 5.2**), with the potential for phenol electrooxidation occurring in aprotic solvents at more positive potentials.[22]

The increasing peak separation between the cathodic peak at 1.98 V and the anodic peak at 2.67 V with increasing scan rate (**Figure 5.3**) (whereby the reduction peak (a) becomes more negative and the oxidation peak (b) becomes more positive) demonstrates that they are the reduction and oxidation peaks for the same irreversible redox couple.[17, 23] Increasing the scan rate leads to an increase in current density, which for irreversible reactions requires an increase in the overpotential, as given by **Equation 5.9**:

$$j_p = 3\text{x}10^5 n(n\alpha)^{\frac{1}{2}} D^{\frac{1}{2}} c v^{\frac{1}{2}} \qquad \textbf{Eq. 5.9}$$

Importantly, as the timescale of the experiment increases, the oxidation peak (b) current density decreases; this confirms that the KO_2 formed during the cathodic scan reacts chemically with another species in solution according to an *ec* mechanism.[17]

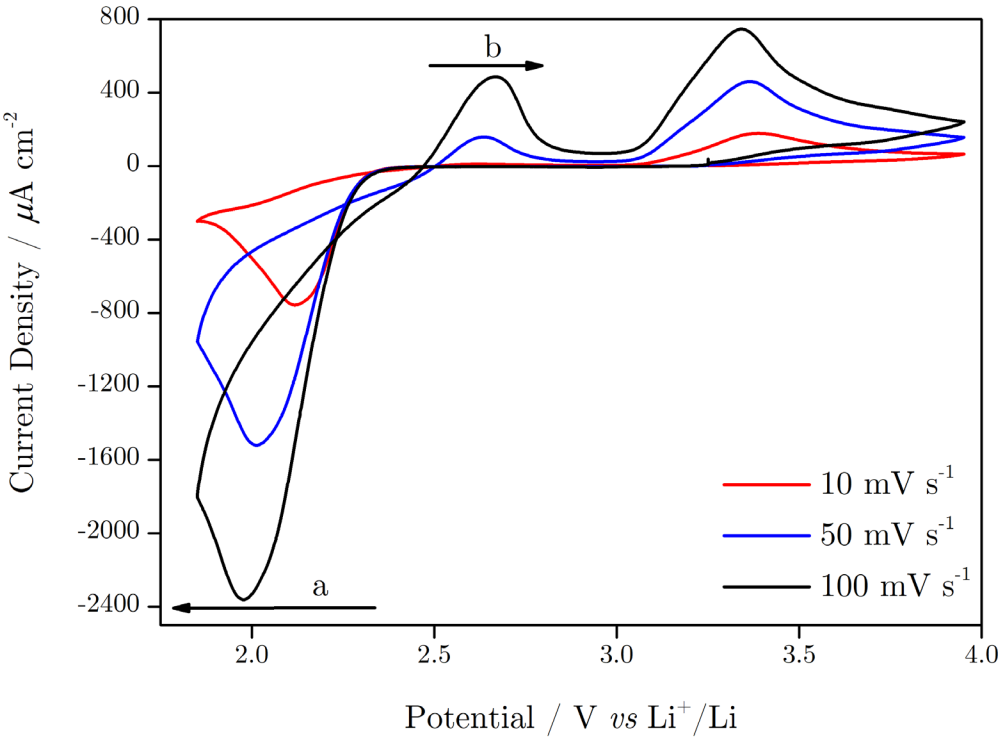

Fig. 5.3: Cyclic voltammetry of O_2 in a 0.5 M KTFSI in TEGDME electrolyte with 30 mM phenol, at a scan rate of 10 (red), 50 (blue) and 100 (black) mV s^{-1}. Experimental conditions as described in **Section 5.2.1** (page 236).

This reaction between the KO_2 and a species in solution can also be seen on successive cycles (**Figure 5.4**), where there is a total absence of any peaks associated with either KO_2 or K_2O_2 oxidation after the first cycle. This is attributed to the decrease in KO_2 forming on the electrode with each cycle; since a layer of incompletely oxidised K_2O_2 remains on the electrode surface after the first scan, less fresh KO_2 can

be deposited on each subsequent cycle. With any fresh KO_2 consumed through both further reduction and reaction with phenol, this means there are negligible quantities available for electrooxidation on the reverse scan. With each successive cycle the K_2O_2 surface film continues to thicken, such that by the third cycle the K_2O_2 film is sufficiently thick to prevent significant formation of KO_2, evidenced by the negligible presence of a KO_2 formation peak at 2.67 V. With less KO_2 available for reaction with phenol on each cycle, the oxidation peak of HO_2/H_2O_2 at 3.43 V has a corresponding decrease with each scan. The shift in the HO_2/H_2O_2 oxidation peak to a more positive potential is attributed to the increasing thickness of the K_2O_2 surface layer, which increases the charge transfer resistance and hence overpotential for the reaction.[22, 24]

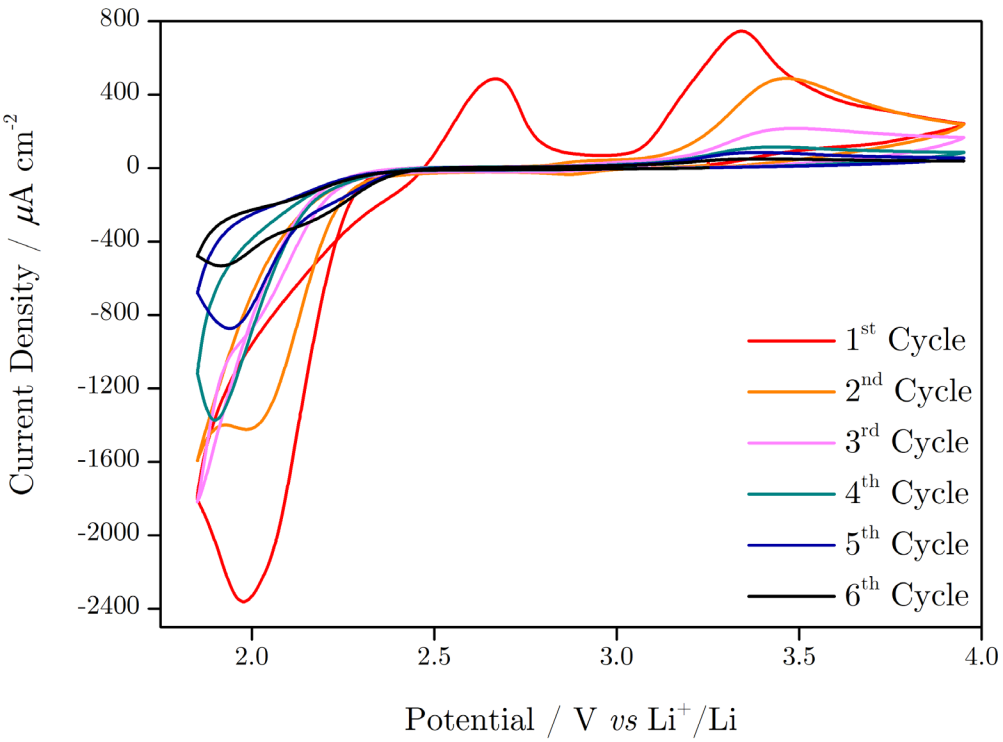

Fig. 5.4: Cyclic voltammetry of O_2 in a 0.5 M KTFSI in TEGDME electrolyte with 30 mM phenol, at a scan rate of 100 mV s^{-1}. Experimental conditions as described in **Section 5.2.1** (page 236).

As mentioned earlier, on the reverse scan of the first cycle a current crossover can be seen in phenol-containing cells. This feature arises from the need for an overpotential in order to form thermodynamically stable KO_2 nuclei on the gold surface, termed the nucleation overpotential.[17, 23] The nucleation overpotential is the difference between the potential required to deposit KO_2 onto a KO_2 surface compared to depositing KO_2 onto a foreign substrate. On the reverse sweep, there is already KO_2 nuclei onto which further KO_2 deposition can occur; as deposition is no longer occurring on a foreign substrate, the potential required for deposition is shifted in a positive direction. A second crossover potential exists at 2.47 V that corresponds to the equilibrium potential of the redox couple O_2/O_2^-, aiding the assignment of peak (b) in **Figure 5.3** as that for KO_2 oxidation.[17]

It is important to note that the crossover current is absent in systems not containing phenol. Without phenol, a passivating KO_2/K_2O_2 layer is deposited on the forward scan, which prevents further deposition on the reverse sweep. However, when phenol is present it acts as a proton source to facilitate the formation of soluble HO_2, which dissolves from the electrode surface. This reduces the thickness of the KO_2 film which, coupled with the slight conductivity of KO_2, allows further KO_2 deposition onto the KO_2 nuclei present (and at lower potentials).[6]

The lack of crossover current on subsequent cycles is attributed to the increasing thickness of the K_2O_2 passivating layer, which prevents further KO_2 deposition. This suggests an apparent inability of phenol to solubilise the K_2O_2 layer; it is therefore

suggested that the soluble species detected at 3.43 V originates primarily from reaction of KO_2 with H^+, according to **Equations 5.6** and **5.7**.

5.3.2 Rotating Ring Disc Electrode Voltammetry

To further verify the action of phenol in a KO_2 cell, a rotating ring disc electrode (RRDE) was used to detect any molecules formed during the cathodic linear potential scan that are also soluble in solution. The theory behind RRDE use is described in detail in **Section 2.1.3** (page 76). **Figure 5.5** illustrates the disc and normalised ring currents for systems with and without phenol. In line with the results obtained through cyclic voltammetry, the presence of phenol results in a larger disc current than the system without. Similarly, addition of phenol results in a significantly larger ring current than when phenol is absent, demonstrating the formation of an electroactive species at the disc electrode which is sufficiently soluble to move through convection to the ring.

Interesting, in the system without phenol there is a peak in the ring current at 2.10 V, followed by a decrease in observed current. This may be explained in the following manner: at 2.10 V KO_2 is being formed which, due to its slight solubility in TEGDME, is detected at the ring.[18, 25] However, once the potential has moved sufficiently negative the KO_2 formed is further reduced to K_2O_2. In common with the other alkali metal peroxides, K_2O_2 has an even lower solubility in TEGDME than KO_2, and so this transition leads to a decrease in the recorded current at the ring.[26] As a clarifying remark, the region of constant current due to mass transport limitations

which is typical of RRDE experiments is absent here due to the passivation of the disc, observed in similar studies.[4] Furthermore, the low scan rate of 5.0 mV s^{-1} was used to ensure sufficient time for KO_2 to be chemically converted to soluble HO_2/H_2O_2.

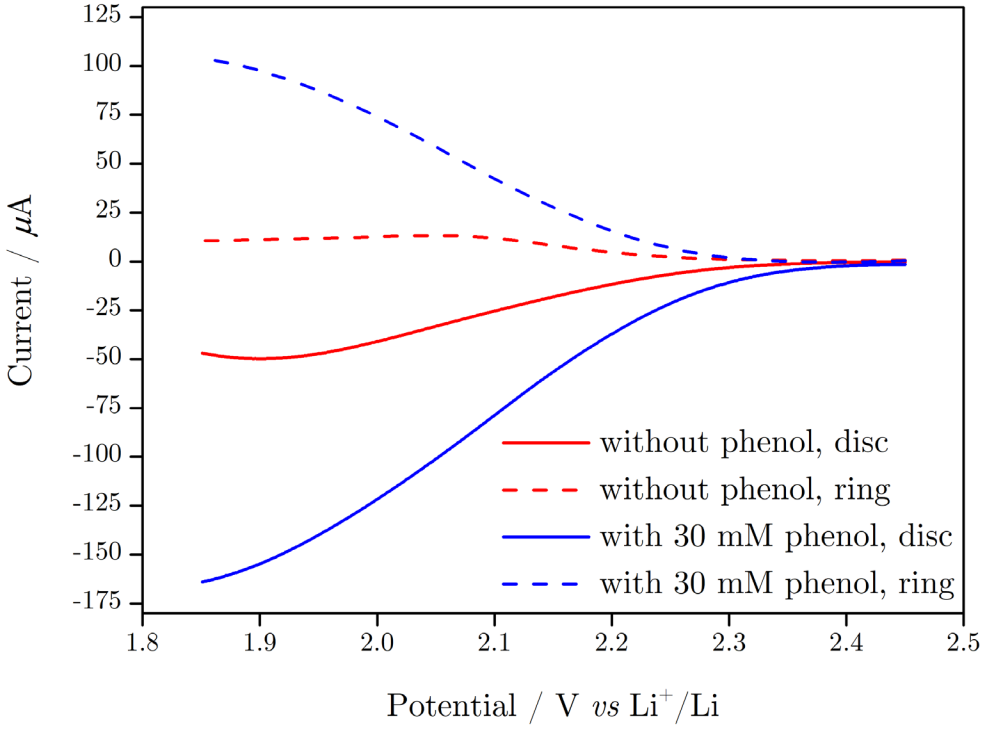

Fig. 5.5: RRDE linear sweep voltammetry of O_2 in a 0.5 M KTFSI in TEGDME electrolyte with (blue) and without (red) 30 mM phenol, with the RRDE rotated at 250 rpm. The scan rate of the platinum disc was 5.0 mV s^{-1}, and the platinum ring potential was held at 3.40 V. Ring currents corrected for collection efficiency of RRDE (N = 0.233) (further details in **Appendix 5.5.1** (page 259)). Experimental conditions as described in **Section 5.2.2** (page 237).

As discussed in **Section 2.1.3** (page 76), not all of the soluble products formed at the disc will reach the ring. The collection efficiency, N, of the RRDE was calculated using the ferrocyanide/ferricyanide redox couple, characterised in **Appendix 5.5.1**

Figure 5.11 (page 259). A collection efficiency of 0.223 was calculated from the limiting currents displayed in **Figure 5.12**. A correction was consequently applied to the ring currents measured in the K-O_2 system, to yield to values given in **Figure 5.5**.

5.3.3 OEMS: Monitoring O_2 Consumption on Discharge

Operando electrochemical mass spectrometry was conducted to ensure that O_2 was indeed being consumed during the discharge process, with **Figure 5.6** revealing this to be the case. The ratio of electrons to O_2 passed was found to be 1.02 e^-/O_2, close to the theoretical value of 1.00 that would be expected for the one-electron reduction to KO_2 and comparable with other studies.[2] Whilst the cell does polarise to a sufficiently negative potential to allow the formation of K_2O_2, this represents a small proportion of the discharge capacity, and so does not significantly alter the electron to O_2 ratio observed. It should be noted that no CO_2 was observed to evolve during discharge.

An electron to O_2 ratio of 1.02 further suggests that the soluble species detected through the cyclic voltammetry and RRDE is HO_2, since disproportionation of HO_2 to give H_2O_2 would result in the formation of O_2, resulting in a two electron process and an electron to O_2 ratio approaching 2.00.

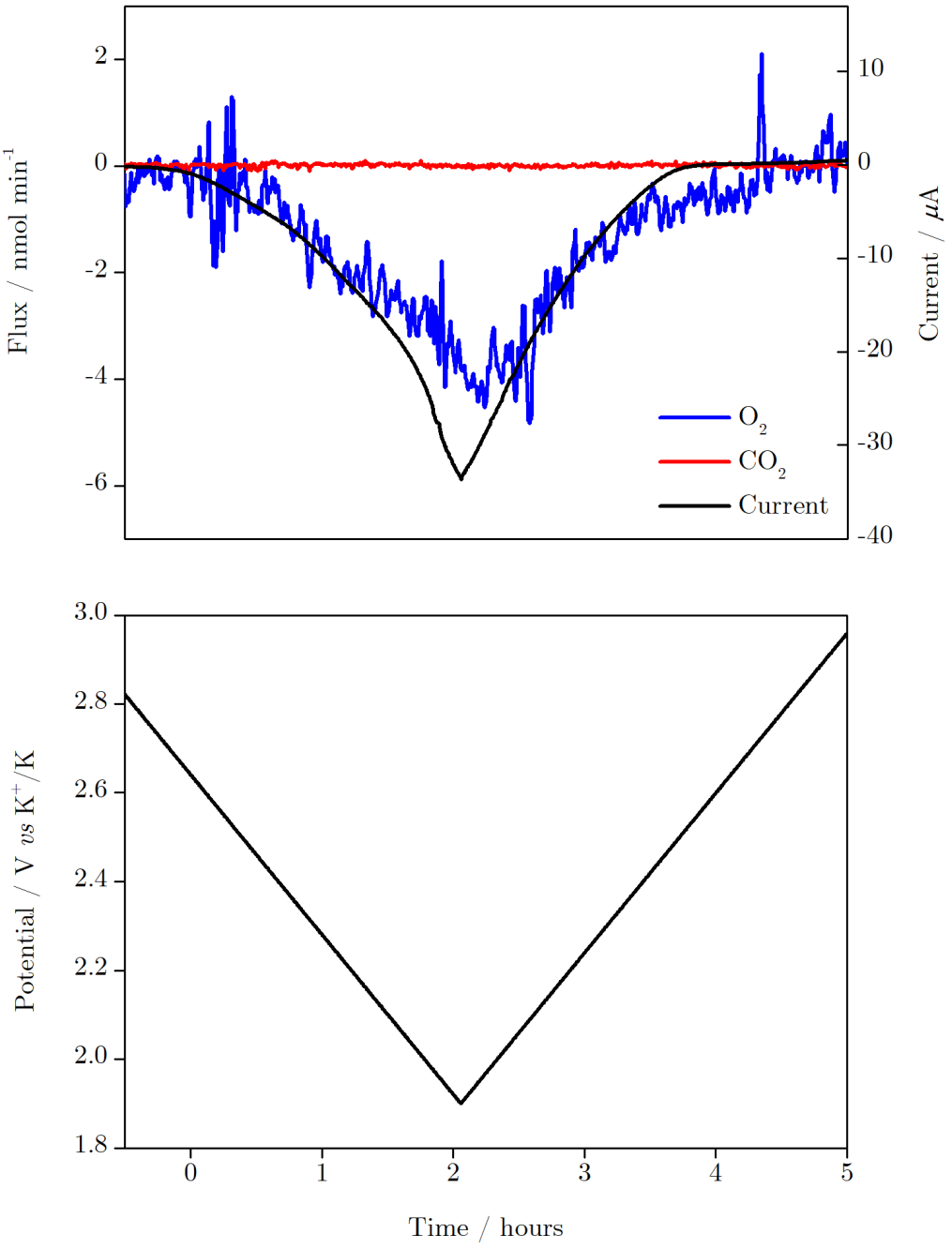

Fig. 5.6: OEMS during cyclic voltammetry of O_2 in a 0.5 M KTFSI in TEGDME electrolyte with 30 mM phenol, at a scan rate of 0.1 mV s^{-1}. The carrier gas was 20% O_2 in Ar with a flow rate of 0.6 mL min^{-1}. Experimental conditions as described in **Section 5.2.5** (page 239).

5.3.4 Discharge at a Planar Gold Electrode

Using the same planar gold electrode as for the cyclic voltammetry in **Sections 5.3.1** and **5.3.2** (pages 240 and 248, respectively), discharge at a constant current density of 50 μA cm^{-2} resulted in a ten-fold increase in the discharge capacity when phenol was present (**Figure 5.7**). Furthermore, phenol resulted in a decrease in the discharge overpotential by approximately 50 mV. Given that the cyclic voltammetry presented in **Section 5.3.1** (page 240) demonstrates that K_2O_2 formation is irreversible and results in cell passivation, the cut-off potential was set to 2.05 V, which is above the formal potential for K_2O_2 formation. As such, the discharge product was expected to be KO_2.

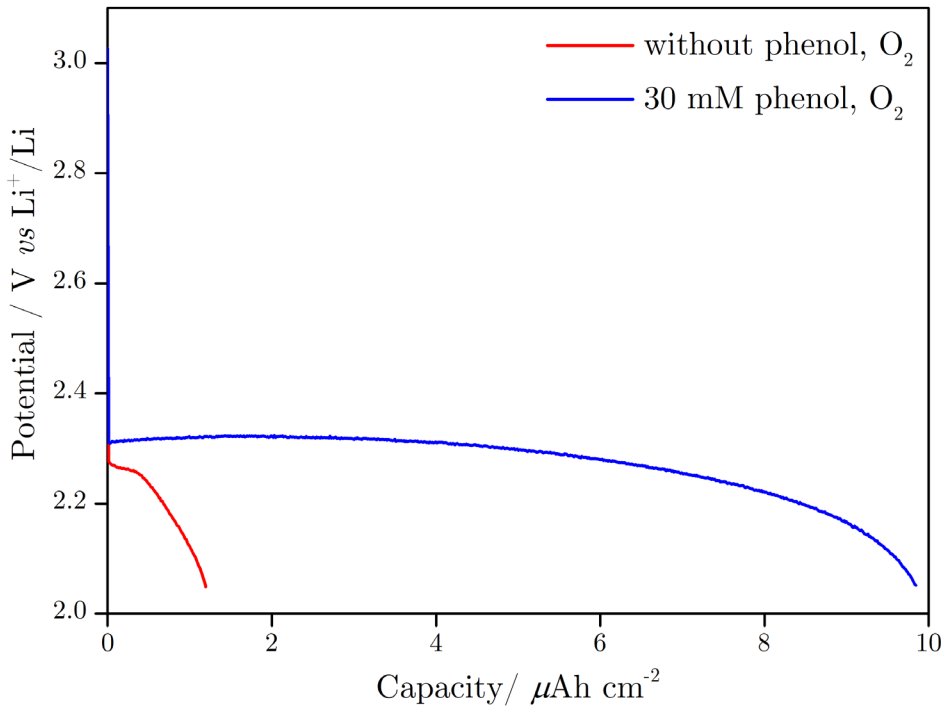

Fig. 5.7: Constant current density discharge of 50 μA cm^{-2} at a planar gold electrode, using an O_2-saturated 0.5 M KTFSI in TEGDME electrolyte with (blue) and without (red) 30 mM phenol. Experimental conditions as described in **Section 5.2.3** (page 238).

To confirm that phenol itself does not contribute to the discharge capacity, the gold electrode was discharged with phenol under N_2, with **Figure 5.8** showing an immediate polarisation of the electrode to approximately 1.65 V, far below the operational potential of a K-O_2 cell as presented in **Figure 5.7**.

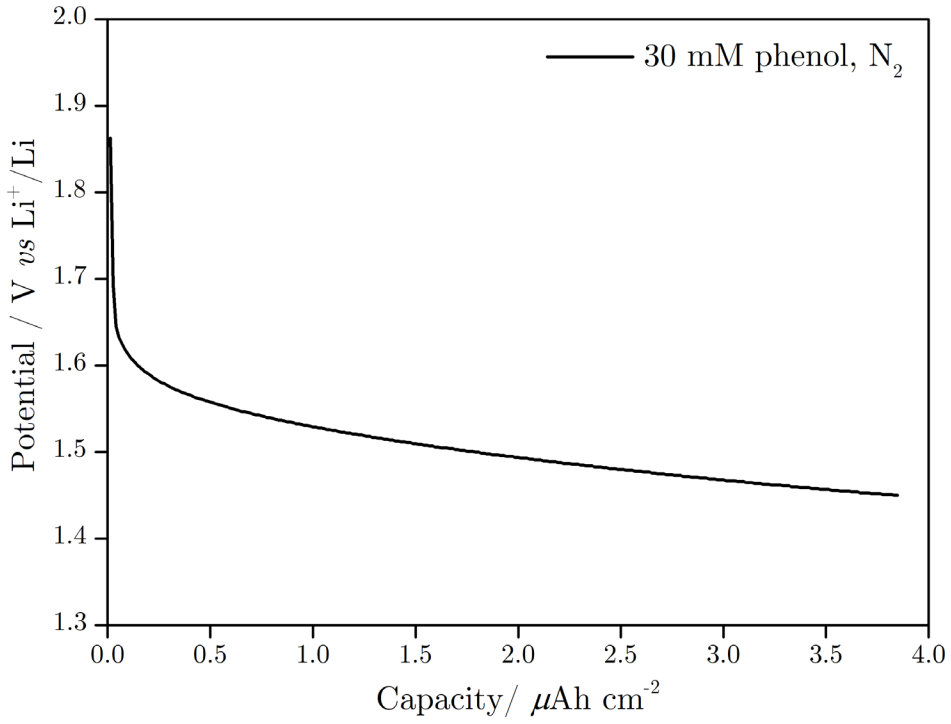

Fig. 5.8: Constant current density discharge of 50 μA cm^{-2} at a planar gold electrode, using a N_2-saturated 0.5 M KTFSI in TEGDME electrolyte with 30 mM phenol. Experimental conditions as described in **Section 5.2.3** (page 238).

5.3.5 Discharge at a GDL Cathode

Similarly to the discharge at a gold electrode, use of phenol resulted in a significant improvement to the discharge of cells with a GDL as the cathode (**Figure 5.9**). With phenol present the discharge capacity was increased by more than 300% and the

overpotential decreased by approximately 100 mV, compared to cells without phenol. These cells were constructed as detailed in **Section 5.2.4** (page 238), with a potassium metal counter electrode. As has been reported previously, the potassium metal underwent significant degradation during the course of discharge, demonstrating reaction with one or all of the electrolyte, phenol, O_2 and reduced O_2 species.[1, 16, 27] The decomposition of the counter electrode is discussed further in **Section 5.3.7** (page 256).

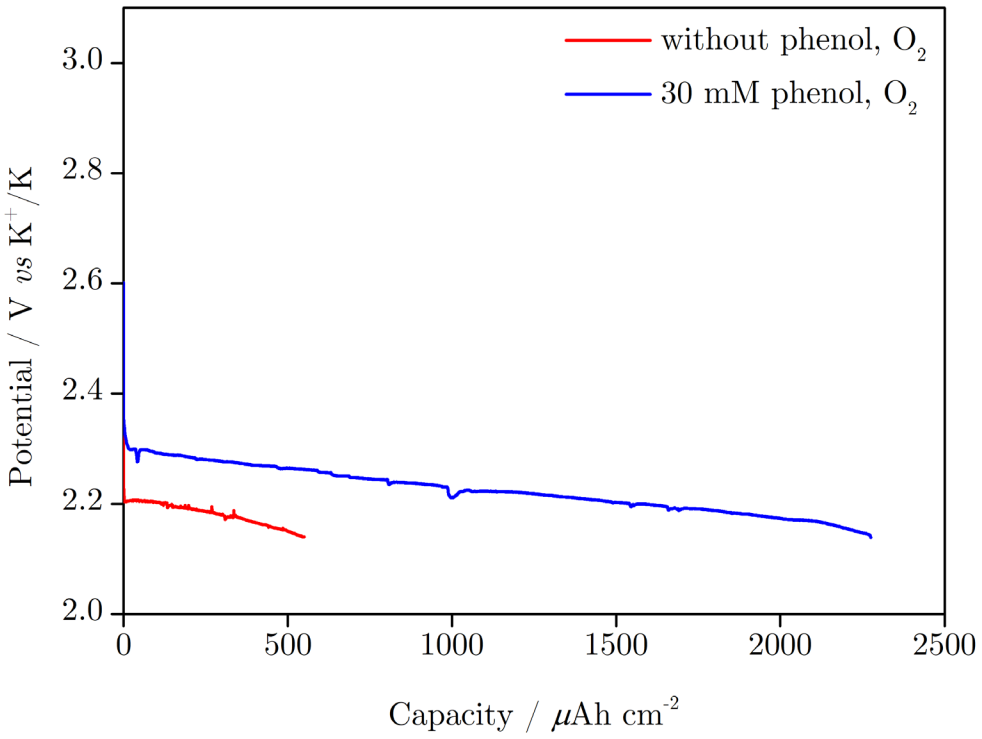

Fig. 5.9: Constant current density discharge of 100 μA cm^{-2} at a GDL electrode, using an O_2-saturated 0.5 M KTFSI in TEGDME electrolyte with (blue) and without (red) 30 mM phenol. Experimental conditions as described in **Section 5.2.4** (page 238).

5.3.6 XRD: Determining Identity of the Discharge Products

To confirm the identity of the discharge products, the discharged GDL cathodes were compared with standard samples of KO_2 and possible products of parasitic side reactions. However, rather than observing KO_2 as expected, the predominant discharge product can clearly be seen in **Figure 5.10** to be KOH, with an absence of any peaks that may be attributed to either KO_2 or K_2O_2 (to identify the presence of K_2O_2 a comparison was made with calculated powder patterns).[28] The peak variation between the KOH on the discharged GDL and the reference KOH is due to the latter containing a mixture of phases, whereas the KOH generated in the cell has greater phase purity.

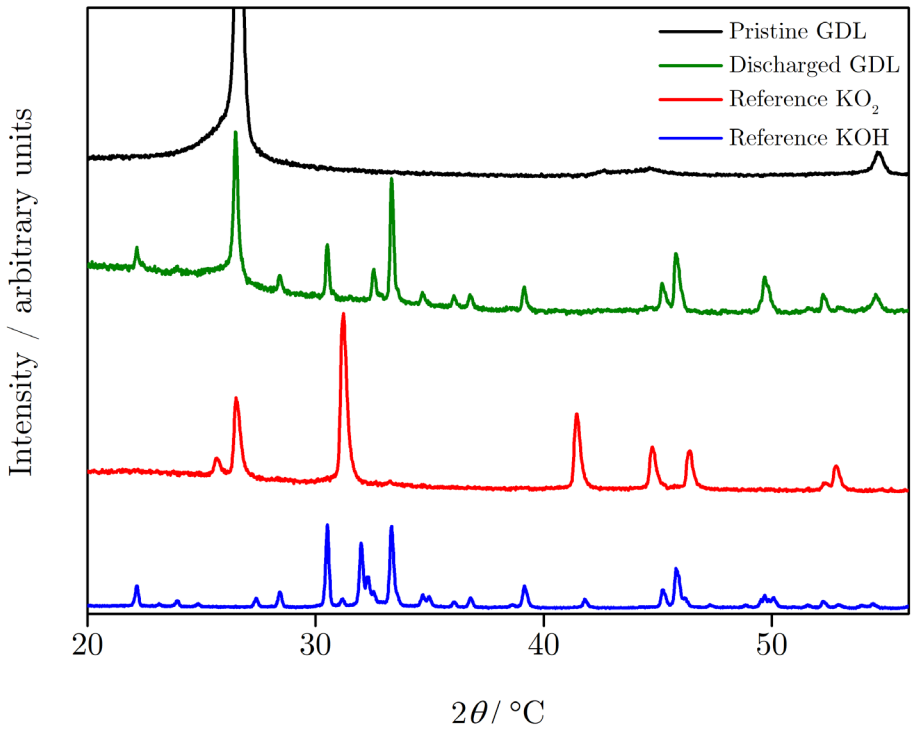

Fig. 5.10: Powder XRD pattern for K-O_2 cells discharged using 0.5 M KTFSI in TEGDME with 30 mM phenol as the electrolyte, and reference compounds. Experimental conditions as described in **Section 5.2.6** (page 239).

5.3.7 Discharge Mechanism in the Presence of Phenol

With XRD demonstrating that KOH is the main discharge product when phenol is employed in a K-O_2 cell, an explanation for its presence that is compatible with both the cyclic voltammetry and OEMS is required. For KOH to form from either KO_2 or K_2O_2, it is essential that H_2O is present within the cell, which itself may form through disproportionation of H_2O_2. Reaction of KO_2 and K_2O_2 with H^+ may form H_2O_2 according to the overall reactions:

$$2KO_2 + 2H^+ \rightarrow H_2O_2 + O_2 + 2K^+ \qquad \textbf{Eq. 5.10}$$

$$K_2O_2 + 2H^+ \rightarrow H_2O_2 + 2K^+ \qquad \textbf{Eq. 5.11}$$

The H_2O_2 may then undergo disproportionation, leading to the formation of H_2O:

$$2H_2O_2 \rightarrow 2H_2O + O_2 \qquad \textbf{Eq. 5.12}$$

The resultant H_2O can then react with both KO_2 and K_2O_2 to form KOH, according to **Equations 5.13** and **5.14**:[9, 16, 29]

$$2KO_2 + 2H_2O \rightarrow 2KOH + H_2O_2 + O_2 \qquad \textbf{Eq. 5.13}$$

$$K_2O_2 + H_2O \rightarrow KOOH + KOH \qquad \textbf{Eq. 5.14}$$

Given that the phenol-containing electrolyte was found to have an H_2O content of 6.4±1.0 ppm (compared to 6.9±0.7 ppm without phenol) via Karl Fischer titration (**Appendix 5.5.2, Table 5.1** (page 261)), the H_2O must be formed during cell discharge. However, the pathway to H_2O detailed above would lead to an electron to O_2 ratio much greater than the 1.02 observed through the OEMS. It is therefore unlikely that the entirety of this mechanism is operational.

A notable difference between the cells used for OEMS and those discharged for XRD analysis is the presence of a K^+-conducting solid electrolyte in the former. This was included to protect the potassium metal counter electrode from reaction with O_2 and the electrolyte. Potassium metal has been shown to react with DME to form a mixture of decomposition products including KOH, with 39.5 – 41.2% of the unprotected potassium counter electrode surface layer consisting of KOH after discharge.[16, 29, 30] KOH is insoluble in the ether solvent, and so does not appear in the spectroscopic analysis of the cathode in other works lacking protection of the counter electrode, since it cannot diffuse from the counter electrode to the cathode.[1] However, the presence of phenol (at relatively high concentration) allows KOH to be protonated to form soluble H_2O, which may then diffuse to the cathode and react with KO_2 according to **Equation 5.13**. With the K^+-conducting solid electrolyte in the OEMS cells preventing such reaction of the counter electrode with the electrolyte, this pathway to H_2O is closed down and so the one-electron reduction of O_2 to KO_2 proceeds.

5.3.8 Future Experiments

To verify the expectation that KO_2 is the true discharge product in a phenol-containing K-O_2 cell, discharge must occur with a potassium metal protection strategy in place, with any solid-electrolyte interphase formed by counter electrode reaction with the electrolyte found to be problematic in the presence of phenol.[27] Whilst the K^+-

conducting solid electrolyte as used for the OEMS in this work will be sufficient, an alternative counter electrode material may also be an appropriate approach.[31, 32]

The discharged cathodes in counter electrode-protected cells would require analysis via XRD, Fourier transform infrared spectroscopy and scanning electron microscopy to provide complete identification of the discharge products. Titration with $TiOSO_4$ followed by analysis via UV-vis spectroscopy will allow further quantification of the KO_2 formed. Comparison with cells discharged in the absence of phenol would be necessary to provide a benchmark against which to evaluate the effect of phenol.

5.4 Conclusions

In this Chapter, the effect of a protic phase transfer catalyst on the discharge of K-O_2 cells has been investigated, with the presence of phenol resulting in an increase in the discharge capacity of a GDL cathode by more than 300% compared to cells without. Furthermore, OEMS suggest that KO_2 is the main discharge product, with an electron to O_2 ratio of 1.02 demonstrating minimal side reactions when a K^+-conducting solid electrolyte is employed.

However, absence of a protective layer for the potassium metal counter electrode results in KOH being the main product on the cathode at the end of discharge when phenol is present. It is suggested that phenol protonates the KOH formed on the counter electrode surface through reaction of the potassium metal with the electrolyte, allowing the formation of H_2O that may diffuse to the cathode and react with the KO_2

on the surface to form KOH. Further investigation is required to confirm this hypothesis, along with spectroscopic analysis to confirm that, when the potassium metal counter electrode is adequately protected, the presence of phenol results in the formation of KO_2 as the main discharge product.

5.5 Appendices

5.5.1 Determining the RRDE Collection Efficiency

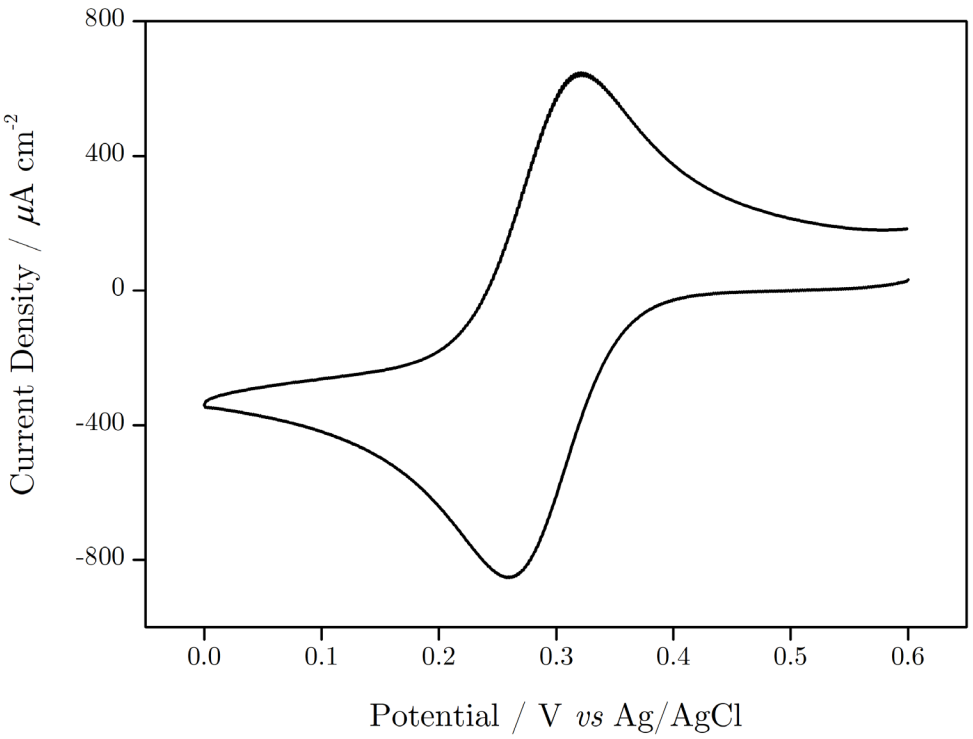

Fig. 5.11: Cyclic voltammetry of 4 mM $K_3[Fe(CN)_6]$ in 1 M $KOH_{(aq)}$, at a scan rate 100 mV s^{-1}. Experimental conditions as described in **Section 5.2.1** (page 236).

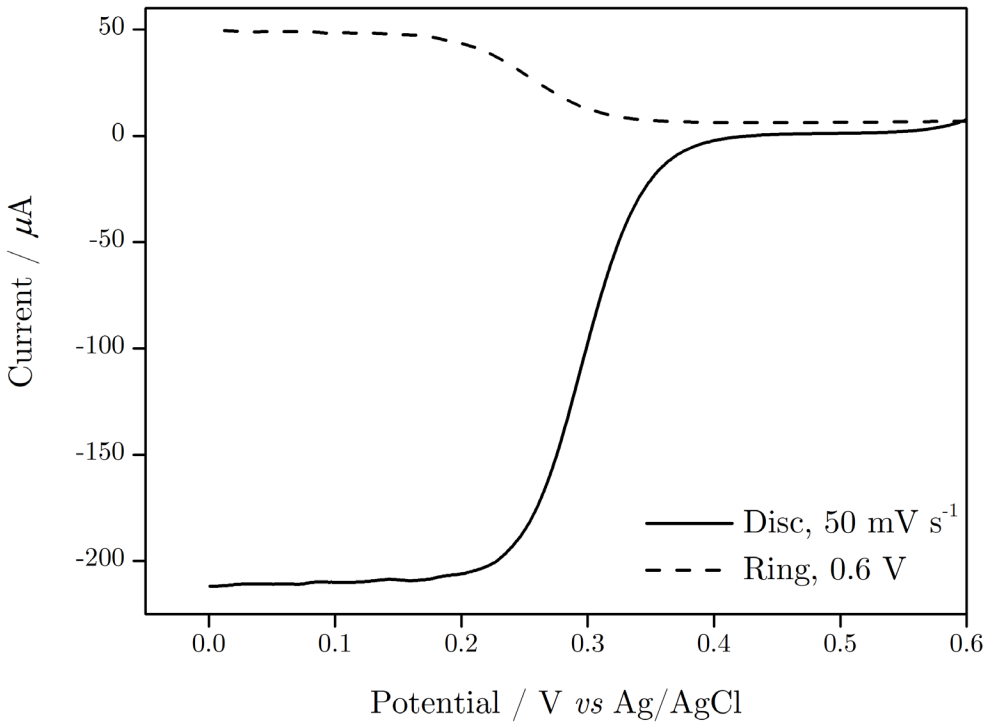

Fig. 5.12: RRDE linear sweep voltammetry (using the same RRDE tip as in **Figure 5.5**) of 4 mM $K_3[Fe(CN)_6]$ in 1 M $KOH_{(aq)}$ electrolyte, with the RRDE rotated at 500 rpm. The scan rate of the platinum disc was 50.0 mV s^{-1}, and the platinum ring potential was held at 0.60 V. Experimental condition as described in **Section 5.2.2** (page 237).

5.5.2 Karl Fischer Analysis of Electrolyte Water Content

Run	TEGDME / ppm	TEGDME + 30 mM Phenol / ppm
1	7.3	5.1
2	5.7	7.6
3	6.8	7.0
4	7.6	5.7
Mean	6.9	6.4
Std. Dev.	0.7	1.0

Table 5.1: Water content of TEGDME solvent with and without 30 mM phenol. TEGDME was distilled and dried as described in **Section 2.1.6.1** (page 86) and phenol was used as received. Solution containing phenol was prepared by dissolving 9.1×10^{-3} g of phenol in 3.0 mL TEGDME.

5.6 References

1. X. Ren and Y. Wu, *J. Am. Chem. Soc.*, 2013, **135**, 2923-2926.
2. N. Xiao, R. T. Rooney, A. A. Gewirth and Y. Wu, *Angew.*, 2018, **57**, 1227-1231.
3. L. Qin, L. Schkeryantz, J. Zheng, N. Xiao and Y. Wu, *J. Am. Chem. Soc.*, 2020, **142**, 27, 11629-11640.
4. C. Xia, R. Black, R. Fernandes, B. Adams and L. F. Nazar, *Nat. Chem.*, 2015, **7**, 496-501.
5. V. S. Bryantsev and F. Faglioni, *J. Phys. Chem. A*, 2012, **116**, 7128-7138.
6. Y. Chen, Z. P. Jovanov, X. Gao, J. Liu, C. Holc, L. R. Johnson and P. G. Bruce, *J. Electroanal. Chem.*, 2018, **819**, 542-546.

7. W. Wang, N. C. Lai, Z. Liang, Y. Wang and Y. C. Lu, *Angew.*, 2018, **57**, 5042-5046.
8. S. Sankarasubramanian and V. Ramani, *J. Phys. Chem. C*, 2018, **122**, 19319-19327.
9. P. H. Reinsberg, A. Koellisch and H. Baltruschat, *Electrochim. Acta*, 2019, **313**, 223-234.
10. E. Mourad, Y. K. Petit, R. Spezia, A. Samojlov, F. F. Summa, C. Prehal, C. Leypold, N. Mahne, C. Slugovc, O. Fontaine, S. Brutti and S. A. Freunberger, *Energy Environ. Sci.*, 2019, **12**, 2559-2568.
11. B. Lee, J. Kim, G. Yoon, H.-D. Lim, I.-S. Choi and K. Kang, *Chem. Mater.*, 2015, **27**, 8406-8413.
12. N. Xiao, X. Ren, M. He, W. D. McCulloch and Y. Wu, *ACS Appl. Mater. Interfaces*, 2017, **9**, 4301-4308.
13. X. Gao, Y. Chen, L. Johnson and P. G. Bruce, *Nat. Mater.*, 2016, **15**, 882–888.
14. X. Gao, Y. Chen, L. R. Johnson, Z. P. Jovanov and P. G. Bruce, *Nat. Energy*, 2017, **2**, 17118.
15. X. Gao, Z. P. Jovanov, Y. Chen, L. R. Johnson and P. G. Bruce, *Angew.*, 2017, **56**, 6539-6543.
16. X. Ren, K. C. Lau, M. Yu, X. Bi, E. Kreidler, L. A. Curtiss and Y. Wu, *ACS Appl. Mater. Interfaces*, 2014, **6**, 19299-19307.
17. D. Pletcher, *A First Course in Electrode Processes*, The Royal Society of Chemistry Cambridge, 2nd edn., 2009.
18. C. O. Laoire, S. Mukerjee, K. M. Abraham, E. J. Plichta and M. A. Hendrickson, *J. Phys. Chem. C*, 2009, **113**, 20127-20134.
19. A. M. Abd El-Halim, M. H. Fawzy and A. Saty, *J. Electroanal. Chem.*, 1991, **316**, 275-292.
20. Y. Qiao, S. Wu, J. Yi, Y. Sun, S. Guo, S. Yang, P. He and H. Zhou, *Angew.*, 2017, **56**, 4960-4964.
21. Y. G. Zhu, Q. Liu, Y. Rong, H. Chen, J. Yang, C. Jia, L. J. Yu, A. Karton, Y. Ren, X. Xu, S. Adams and Q. Wang, *Nat. Commun.*, 2017, **8**, 14308.
22. L. Kiss, D. Bősz, F. Kovács, H. Li, G. Nagy and S. Kunsági-Máté, *Polymer Bulletin*, 2019, **76**, 5849-5864.
23. X. Cao, L. Xu, C. Wang, S. Li, D. Wu, Y. Shi, F. Liu and X. Xue, *Coatings*, 2020, **10**, 1154.
24. P. Cea, M. C. Lopez, M. S, A. Villares, G. Pera and I. Giner, *J. Chem. Educ.*, 2009, **86**, 723-725.
25. M. S. Jung, S. Ha, D. Koo and K. T. Lee, *J. Phys. Chem. C*, 2020, **124**, 7644-7651.
26. P. H. Reinsberg, A. Koellisch, P. P. Bawol and H. Baltruschat, *Phys. Chem. Chem. Phys.*, 2019, **21**, 4286-4294.
27. X. Ren, M. He, N. Xiao, W. D. McCulloch and Y. Wu, *Adv. Energy Mater.*, 2017, **7**, 1601080.

28. K. Persson, Materials Data on K_2O_2 (SG:64) by Materials Project, https://materialsproject.org/materials/mp-2672/, (accessed 06/04/2021).
29. L. Qin, N. Xiao, S. Zhang, X. Chen and Y. Wu, *Angew.*, 2020, **59**, 10498-10501.
30. N. Xiao, J. Zheng, G. Gourdin, L. Schkeryantz and Y. Wu, *ACS Appl. Mater. Interfaces*, 2019, **11**, 16571-16577.
31. W. D. McCulloch, X. Ren, M. Yu, Z. Huang and Y. Wu, *ACS Appl. Mater. Interfaces*, 2015, **7**, 26158-26166.
32. L. Qin, S. Zhang, J. Zheng, Y. Lei, D. Zhai and Y. Wu, *Energy Environ. Sci.*, 2020, **13**, 3656-3662.

Chapter 6

Conclusion

Contents

6.1 Future Work

6.1.1 Avoiding Singlet Oxygen

Chapter 3 demonstrated that there is a potential window between 2.96 V and 3.31 V in which a Li-O_2 cell may be charged without the formation of $^1O_2$, with minimal quantities of $^1O_2$ formed between 3.31 V and 3.45 V. By suppressing the charging potential to below 3.45 V (and preferably 3.31 V) using RMs, the quantity of Li_2CO_3 formed during charge can be minimised. However, despite the main route to Li_2CO_3 through reaction of the electrolyte and carbon cathode with $^1O_2$ being shut down, other decomposition pathways continue to form Li_2CO_3. With the charging potential supressed below the 3.82 V required for direct Li_2CO_3 electrooxidation and with state-of-the-art low potential RMs shown to be incapable of chemically oxidising it, two further avenues of investigation present themselves. Firstly, attempts should be made to prevent formation of this residual Li_2CO_3, either through suppression of the reactive species involved or by using different electrolytes and cathode materials that have

greater stability. Secondly, other additives capable of reacting chemically with Li_2CO_3 should be considered (although inclusion of high concentrations of acid (for example) are likely to cause other issues within the Li-O_2 cell).

A third possibility might be to tailor the charge programme such that there is a short period at the end of charge, following complete oxidation of Li_2O_2, where the potential is held above 3.82 V to allow direct electrooxidation of Li_2CO_3. This may allow for the removal of Li_2CO_3 from the cathode surface whilst minimising the quantity of $^1O_2$ formed (although it should be noted that electrooxidation of Li_2CO_3 itself forms $^1O_2$). Future work should also look beyond the first cycle, to determine the extent of the positive effect of avoiding $^1O_2$ on repeated cycling.

6.1.2 Redox Mediator Kinetics

With the reaction kinetics between RMs and Li_2O_2 demonstrated in **Chapter 4** to follow Marcus theory, it is now possible to logically identify a RM to provide the greatest overall reaction rate. Future work should seek to identify the RM(s) that exhibit both a low oxidation potential and a $\Delta_r G^0$ that is equal to the negative of the reorganisation energy.

Given it is likely that RMs have different rates of reaction with Li_2O_2 and LiO_2, investigation of a tandem system that contains the two charge RMs that each provide the optimum rate for Li_2O_2 and LiO_2 oxidation, respectively, is recommended. This

would minimise the opportunity for LiO_2 disproportionation to occur, thereby further suppressing the formation of $^1O_2$ within Li-O_2 cells.

6.1.3 Additives for Potassium-Oxygen Cells

Further investigation as described in **Chapter 5** is required to verify that KO_2 is the discharge product in K-O_2 cells containing phenol. Furthermore, no work has yet been conducted on the inclusion of discharge or charge RMs in K-O_2 cells. This could provide a further way to increase the discharge capacity of K-O_2 cells, although it should be noted that of all the known alkali metal-oxygen systems, K-O_2 cells already have an exceedingly low overpotential on charge. Any charge RM would therefore only be needed in order to facilitate the oxidation of any electrically disconnected KO_2 arising from the action of a discharge RM.

6.2 Conclusion

Metal-oxygen batteries have the potential to supersede current Li-ion technology and make electric vehicles a truly viable alternative to those powered by petroleum. However, poor Li-O_2 cell stability, particularly during charge, has thus far proven a challenging problem to overcome. This thesis demonstrates that the main cause of parasitic side reactions, $^1O_2$, may be avoided on charge entirely through suppression of the charging potential below 3.31 V, with minimal levels of decomposition attributed to $^1O_2$ below 3.45 V (the presence of $^1O_2$ between 3.31 V and 3.45 V being the result

of LiO_2 disproportionation). This can be achieved through the use of RMs with sufficiently low redox potentials, such as TMPD and DMPZ, meaning $^1O_2$ does not have to be an inevitable consequence of charging Li-O_2 cells.

Two novel RMs have been demonstrated to successfully operate within Li-O_2 cells, with both DMHQ and MPO displaying improved cyclability compared to unmediated cells. MPO further displays reaction kinetics with Li_2O_2 comparable to TEMPO, the gold standard of RMs. Whilst no firm conclusions regarding reaction kinetics with Li_2O_2 can be made through comparison of the structural differences and similarities of these novel RMs with existing RMs, consideration of the solvent reorganisation energy reveals that reaction of DMHQ and MPO (along with other existing RMs) with Li_2O_2 follows Marcus kinetics. It is hoped that this new understanding of RM kinetics, along with the knowledge that RMs need to operate at a potential below 3.45 V to avoid significant levels of cell decomposition due to $^1O_2$, will lead to the optimal novel charge RM being identified and developed by the field.

Whilst this thesis makes great strides in providing solutions for the Li-O_2 system, it also provides exciting evidence of protic additives improving the discharge capacity of K-O_2 cells by approximately 300%. K-O_2 cells are inherently less prone to degradation than their lithium and sodium counterparts, due to the absence of the formation of $^1O_2$. This, along with their naturally low charging overpotential and the lower price of potassium metal (relative to lithium), makes K-O_2 cells a viable system that may be used synergistically with other metal-oxygen systems to satisfy our growing energy storage needs.

In summary, this thesis offers fresh understanding of the requirements for the development of Li-O_2 cells with both low levels of decomposition on charge and for the attainment of the maximum rate of reaction between RMs and Li_2O_2, and provides two novel RMs for use by the field. This work also demonstrates a strategy to improve the discharge performance of K-O_2 cells, which should be regarded as a complimentary battery system to Li-O_2 that is worthy of further study.